Activation analysis of heavy-ion accelerator constructing materials and validation of beam-loss criteria

Aktivierungsuntersuchungen von Schwerionenbeschleunigermaterialien und Strahlverlustkriterienvalidierung

Vom Fachbereich Physik der Technischen Universität Darmstadt zur Erlangung des Grades eines Doktors der Naturwissenschaften (Dr. rer. nat.) genehmigte Dissertation von Ing. Peter Katrík aus Beluša, Slowakei

July 2017 — Darmstadt — D 17

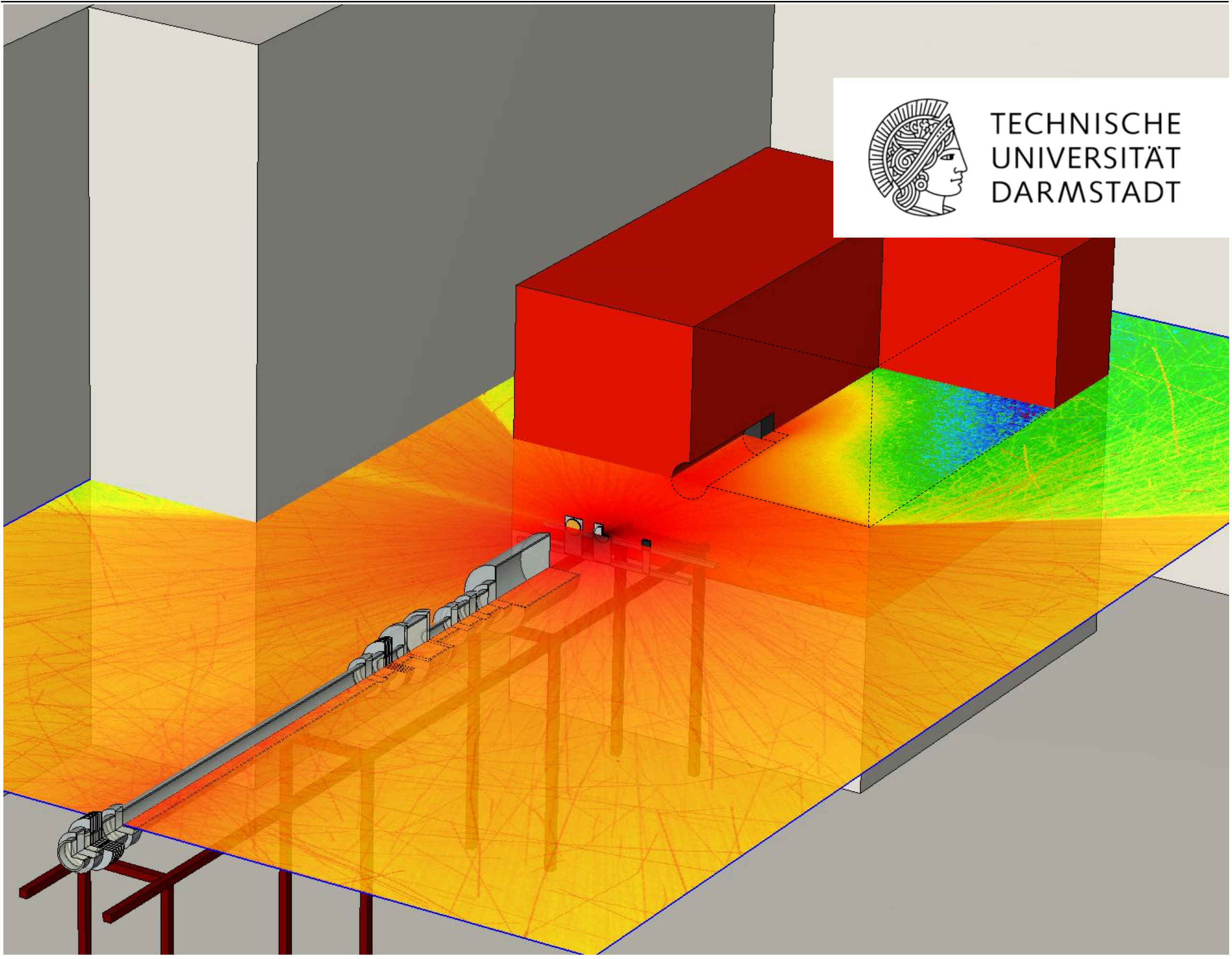

TECHNISCHE
UNIVERSITÄT
DARMSTADT

Bitte zitieren Sie dieses Dokument als:

URN: urn:nbn:de:tuda-tuprints-67924

URL: http://tuprints.ulb.tu-darmstadt.de/6792

DOI: 10.13140/RG.2.2.20430.97605

Aktivierungsuntersuchungen von Schwerionenbeschleunigermaterialien und Strahlverlustkriterienvalidierung

Vom Fachbereich Physik

der Technischen Universität Darmstadt

zur Erlangung des Grades

eines Doktors der Naturwissenschaften (Dr. rer. nat.)

genehmigte Dissertation von

Ing. Peter Katrík

aus Beluša, Slowakei.

1. Gutachten: Prof. Dr. Dr. h.c./RUS Dieter H.H. Hoffmann

2. Gutachten: Prof. Dr. Christina Trautmann

Tag der Einreichung: 14. 06. 2017

Tag der Prüfung: 17. 07. 2017

Darmstadt 2017

D 17

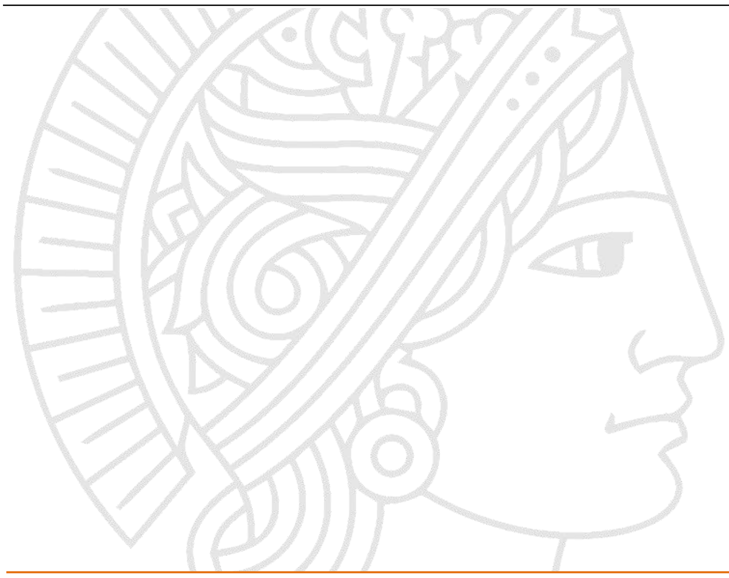

“A little inaccuracy sometimes saves tons of explanation”

H.H. Munro in *Short Stories of Saki*

AFFIDAVIT

LEGAL DECLARATION

I hereby confirm that my thesis entitled "Activation analysis of heavy ion accelerator constructing materials and validation of beam-loss criteria" is the result of my own work. I did not receive any help or support from commercial consultants. All sources and/or materials applied are listed and specified in the thesis.

Furthermore, I confirm that this thesis has not yet been submitted as part of examination process neither in identical nor similar form.

Darmstadt, 12th July 2017 *Peter KATRÍK*

ABSTRACT

Activation of high-intensity heavy-ion accelerators due to beam losses is a serious issue for accelerator parts like collimators, magnets, beam-lines, fragment separator components, etc. The quantification of the induced activity and the prediction of the radiation levels in an accelerator and its environment may have a positive impact on the decreasing of radiation hazards during "hands-on" maintenance as well as on the optimisation of the machine operation [1, 2]. Modern Monte Carlo simulation codes are often used at accelerator facilities for different scientific applications, including the preparation of experimental setup or even for a complete substitution of experiments exclusively by numerical calculations.

In the presented work the benchmarking of the FLUKA code was based on a comparison of simulated and experimental results gained by gamma-spectroscopic analysis of irradiated aluminium targets. The field of interest was the evaluation of simulation precision in the range of low energies, where new physical models are implemented. The Boltzmann Master Equation (BME) model is presented in the latest version of FLUKA 2011, and its calculation possibilities are expanded by the nucleus-nucleus interactions of heavy ions with energies below 100 MeV/u. The previous version of FLUKA 2008 uses the Relativistic Quantum Molecular Dynamics (RQMD) model which simulates transportation of heavy ions with energies lower than 100 MeV/u without considering their further interactions [3]. Different aluminium targets were irradiated by $^{124}\text{Xe}^{48+}$, $^{238}\text{U}^{73+}$ and $^{238}\text{U}^{89+}$ ion with energies of 300, 200 and 125 MeV/u, respectively. Using the so-called stacked-foils geometry was essential for the determination of induced activity as a function of the depth, known as depth profiles of residual activity. Acquiring gamma-spectra of each foil at different cooling-times guaranteed a reliable nuclide inventory of all accumulated nuclides. The depth profile collection of about 100 nuclides was a valuable source of experimental data for further verification of simulated results. FLUKA 2011 performs very precise estimation of the range of primary particles. It was shown that the discrepancy was only 0.5% for ^{238}U ions with an energy of 200 MeV/u. The imprecision of the simulated results caused by imperfect transition between the RQMD and the BME models is demonstrated on the depth profiles of ^{7}Be and ^{22}Na target-nuclei fragments. Other inaccuracies of FLUKA 2011 calculations were observed in the depth profiles of intermediate Z nuclides (e.g. ^{46}Sc, ^{48}V, ^{52}Mn, ^{54}Mn, ^{56}Co, ^{58}Co, ^{65}Zn), where an artificial increase of the induced activity close to the range of primary particles was predicted, but it was not confirmed by experimental data. Additional FLUKA calculations following the production rates of the problematic nuclides introduced an origin of this impreciseness, where inexplicable production increases appear at certain energies. All documented deficiencies were shared with the team of the FLUKA developers for their application in future code updates.

The second part of this dissertation is dedicated to a real-life application of the FLUKA 2011 version and a demonstration of the physical model development. The beam-loss criteria of 1 W/m for proton accelerators, known in a radiation safety community, are based on the empirical experiences; their equivalent for heavy-ion machines was determined by using the FLUKA 2008 [4]. The set of Monte Carlo simulations served to establish the scaling law which allows a comparison of the amount of induced activity by any heavy-ion beam and the proton beam, regardless of their mass number or energy. Tolerable beam losses, defined within this approach, are 5 and 60 W/m for uranium ions with energies of 1 GeV/u and 200 MeV/u, respectively. These energies are also the limits of applicability of FLUKA 2008 in this field. The fact that the criterion was calculated by this code version, which is considered as obsolete nowadays, as well as the fact that it covers only the situation of the first 100 days of a machine operation, was a great opportunity to validate the tolerable activation limits with FLUKA 2011. Additionally, an expansion of a criterion down to an energy of 25 MeV/u and simulation of a long-term operation of 20 years followed by a cooling time of 20 years was performed. As it was expected, the Boltzmann Master Equation model included in FLUKA 2011 influenced the final results of induced activity in constructing materials of accelerators. The beam-loss criteria became stricter for heavy-ion machines already for short-term operation. The limits do not change at an energy of 1 GeV/u, where the beam-loss value of 5 W/m remained for uranium ions, but the tolerable losses of uranium ions at an energy of 200 MeV/u decreased to a level of 40 W/m as compared to values predicted by FLUKA 2008. Long-term simulations revealed that an accumulation of the nuclides with longer half-life leads to an even stricter criterion. The beam losses of 4 W/m at 1 GeV/u are tolerable for uranium ions, but the importance of evaluation of the criterion by FLUKA 2011 is more visible at an energy of 200 MeV/u, where the tolerable beam losses are only 30 W/m, which is exactly half of the limits determined by FLUKA 2008. A complex set of calculations proved that the scaling law of the induced activity is not reliable for the heavy-ion beams with energies below 150 MeV/u and therefore, the use of the tolerable beam-loss criteria is not recommended anymore below this energy.

Key words: Activation, Induced radioactivity, Monte Carlo, FLUKA, Benchmarking, Beam-loss criteria.

ZUSAMMENFASSUNG

In hochintensiven Schwerionenbeschleunigern führen Strahlverluste zur Aktivierung von Beschleunigerteilen wie Kollimatoren, Magneten, Strahllinien, Fragmentseparatorkomponenten usw. Die Quantifizierung der induzierten Aktivität sowie die Vorhersage der Strahlungswerte im Beschleuniger und in seiner Umgebung können genutzt werden, von die Strahlungsgefahr zu verringern, da der Maschinenbetrieb und handwerkliche Wartungsarbeiten optimiert werden können [1, 2]. Moderne Monte-Carlo-Simulationen werden für verschiedene wissenschaftliche Anwendungen, die Vorbereitung von Versuchsaufbauten oder sogar für eine vollständige Substitution von Experimenten durch numerische Berechnungen verwendet. Die vorliegende Arbeit basiert auf dem Benchmarking der FLUKA-Code-Simulationen und experimentellen Ergebnissen.

Die Präzision von Simulationen in der Niedrigenergieregion wird bestimmt. Dazu wurde die neueste Version von FLUKA 2011 genutzt. In dieser ist das Modell der Boltzmann-Master-Gleichungsmodell (BME) implementiert und erlaubt somit die Simulation von Interaktionen von Atomkernen mit Energien unter 100 MeV/u. Im Gegensatz dazu nutzte die vorherige Version, FLUKA 2008, das Relativistische Quanten-Molekulardynamik-Modell (RQMD), welches einen Transport von schweren Ionen mit einer Energie unter 100 MeV/u ohne ihre Wechselwirkungen simuliert [3].

Im Experiment wurden Aluminium-Targets mit ^{124}Xe bei 300 MeV/u und mit ^{238}U bei 200 MeV/u sowie 125 MeV/u bestrahlt. Die Targets bestanden aus gestapelten Folien (Stapelfoliengeometrie), was die Bestimmung der induzierten Aktivität als Funktion der Tiefe, des sogenannten Tiefprofiles der Residualaktivität, ermöglichte. Die Messung der Gamma-Spektren der einzelnen Folien zu unterschiedlichen Abkühlzeiten garantierte die Inventur aller induzierten Nuklide. Insgesamt wurden etwa 100 Tiefenprofile der Radionuklide, die im bestrahlten Material erzeugt oder gestoppt werden, bestimmt.

Der Vergleich der experimentellen Daten mit den Simulationen zeigt, dass FLUKA eine sehr präzise Schätzung des Bereiches der Primärteilchen ermöglicht. Denn die Diskrepanz beträgt für ^{238}U-Ionen bei 200 MeV/u nur 0,5 %. Eine Ungenauigkeit der simulierten Ergebnisse, die durch einen unvollkommenen Übergang zwischen dem RQMD und dem BME-Modell verursacht wird, konnte anhand der Tiefenprofilen der Ziel-Kerne-Fragmente ^{7}Be und ^{22}Na nachgewiesen werden. Andere Ungenauigkeiten von FLUKA-Berechnungen wurden in den Tiefenprofilen von intermediären Z-Nukliden beobachtet (z. B. ^{46}Sc, ^{48}V,

^{52}Mn, ^{54}Mn, ^{56}Co, ^{58}Co, ^{65}Zn). Eine künstliche Zunahme der induzierten Aktivität nahe dem Bereich der Primärteilchen wurde durch die Simulationen vorhergesagt, aber nicht durch experimentelle Daten bestätigt. Zusätzliche FLUKA-Berechnungen, die sich auf die Produktionsraten der problematischen Nuklide konzentrierten, zeigten, dass hier eine unerklärliche Produktionszunahme der Nuklide bei bestimmten Energien auftritt. Alle dokumentierten Defizite wurden mit dem Team der FLUKA-Entwickler für ihre Anwendung in zukünftigen Code-Updates geteilt.

Der zweite Teil dieser Dissertation widmet sich einer realen Anwendung von FLUKA 2011 und demonstriert die Entwicklung der physikalischen Modelle. Für Protonenbeschleuniger sind die bekannten Strahlverlustkriterien 1 W/m, basieren auf empirischen Erfahrungen [2]. Die bisherigen tolerierbaren Strahlverlustkriterien für Schwerionenmaschinen wurden mit FLUKA 2008 ermittelt [4]. Der Satz von Monte-Carlo-Simulationen diente zur Festlegung des Skalierungsgesetzes der Aktivierungen des Materials, die durch den Protonenstrahl und durch den Schwerionenstrahl verursacht wurden. Hieraus ergaben sich tolerierbare Strahlverluste, von 5 W/m für Uranionen bei 1 GeV/u und 60 W/m bei 200 MeV/u. Die gewählten Energien sind auch die Grenzen für eine Anwendbarkeit von FLUKA 2008 in diesem Bereich [4]. Diese Kriterien decke nur die Situation der ersten 100 Tage des Maschinenbetriebs ab. In dieser Arbeit werden die tolerierbaren Aktivierungsgrenzen mit FLUKA 2011 validiert. Für Uranionen mit der Energie 1 GeV/u ergab sich mit FLUKA 2011 ein tolerierbarer Strahlverlust von 5 W/m. Dieser Wert wurde auch mit FLUKA 2008 bestimmt. Im Gegensatz dazu führte FLUKA 2011 in Niedrigenergieregion zu strengeren Strahlverlustkriterien für Schwerionenmaschinen denn die tolerierbaren Strahlverluste an Uranionen bei der Energie von 200 MeV/u sanken auf 40 W/m. Das heißt, dass das Boltzmann-Master-Gleichungsmodell, welches in FLUKA 2011 enthalten ist, die Ergebnisse der induzierten Aktivität in Baustoffen von Beschleunigern in der Niedrigenergieregion beeinflusst.

Darüber hinaus wurde die Simulation eines Langzeitbetriebs mit einer Dauer von 20 Jahren gefolgt von Abkühlzeit von 20 Jahren durchgeführt. Hier ergibt sich bei 1 GeV/u für Uranionen ein tolerierbarer Strahlverlust von 4 W/m. Bei 200 MeV/u belegt diese Wert 30 W/m, was eine Reduzierung um die Hälfte im Vergleich mit FLUKA 2008 bedeutet. Diese Langzeitsimulationen zeigen, dass eine Akkumulation der Nuklide mit längerer Halbwertszeit zu den strengeren Kriterien führt. Die Ausweitung der Berechnungen auf die Energie 25 MeV/u und ein komplexer Satz von Berechnungen zeigte, dass das Skalierungsgesetz der induzierten Aktivität für Schwerionenstrahlen mit Energien unter 150 MeV/u nicht zuverlässig ist und daher wird eine Verwendung der tolerierbaren Strahlverlustkriterien unter diese Energie nicht empfohlen.

Schlüsselwörter: Aktivierung, induzierte Radioaktivität, Monte Carlo, FLUKA, Benchmarking, Strahlverlustkriterien.

TABLE OF CONTENTS

Chapter One

Chapter Two

Chapter Three

Chapter Four

Chapter Five

CHAPTER ONE

INTRODUCTION

INTRODUCTION

Activation of accelerator components due to beam losses during normal machine operation is an important issue, especially for high-energy hadron accelerators. During the process of ion acceleration to high energies or during their transportation, controlled and un-controlled collisions with a matter of the components such as beam pipes, collimators and absorbers, beam-diagnostic equipment, magnets, target stations, etc. appear. Different accelerator component layout, operation and the amount of material close to the beam can result in a surprisingly wide variation of radiation levels and the subsequent production of secondary radiation [5]. Even if all the parameters affecting beam losses were known, a realistic assessment of all aspects of the activation, likewise the quantification of the induced radioactivity at any time in the accelerating facilities involving the different types of particles over a wide range of energies is a very complex task. Especially in cases of a long-term operation with permanent exchange of ion sources, the systematic build-up and decay of radioactivity make it extremely difficult to evaluate radioactivity levels in an absolute way. The residual activity induced by lost beam particles is a dominant source of exposure to personnel and one of the main access restrictions for "hands-on" maintenance. Effects in materials under irradiation may have a different impact on the properties as strain resistance, magnetic susceptibility, break-down voltage, etc., may degrade due to exposure to beam losses. Additionally, performance of electronic devices may change, as well as the lifetime of radiation-sensitive components of the accelerator may be reduced. The radiological history of all components is also very important at the last stage of the accelerator operational lifetime when they are considered as radioactive waste and the final disposal in repositories of radioactive waste has to be planned. Thus, a wrong assessment can have a significant influence on the costs for machine layout and maintenance. Using modern Monte Carlo codes at the design stage of an accelerator helps to incorporate radiation safety features in the infrastructure of the machine, predict the locations of possible radiation damages, and mitigate the impact of the radiation on the components and environment [5-9]. Indeed, all this is a strong motivation for activation studies of accelerator relevant materials which are performed at GSI Hemholtzzentrum für Schwerionenforschung GmbH (will be referred to as GSI) as a preparatory work for the Facility for Antiproton and Ion Research (FAIR).

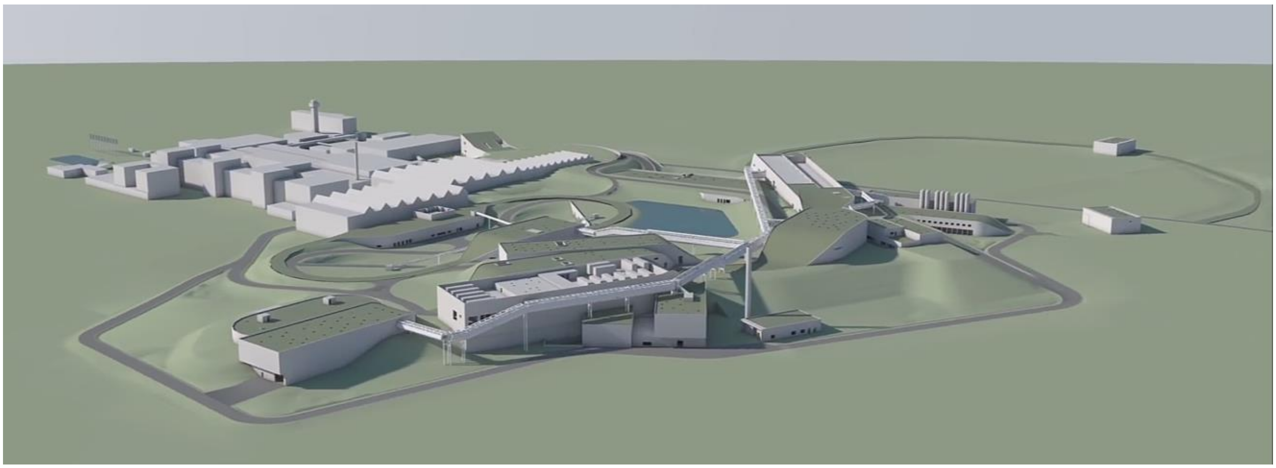

Figure 1: Visualisation of the world-wide unique particle accelerator facility FAIR [10].

The purpose of the FAIR accelerator project at GSI is to increase the intensity of accelerated beams of the existing facility infrastructure. This will allow a large variety of experimental possibilities for different scientific fields. There will be four main experiments at FAIR called APPA (Atomic and plasma physics, and applied sciences in the medical and material sciences), CBM (Physics of hadrons and quarks in compressed nuclear matter), NuSTAR (Structure of nuclei, nuclear astrophysics and radioactive ion beams) and PANDA (Physics with antiproton beams). Expected limits for the new synchrotron SIS-100 are the U^{28+} beams energies up to 2.7 GeV/u and intensities of 3×10^{13} ions per pulse and the proton beams energies up to 29 GeV and intensities of 2.5×10^{13} protons per pulse. This will be possible only after upgrading the intensities of SIS-18 and reaching the beam parameters required for the injection into SIS-100 [11, 12]. Nevertheless, experimental areas belonging to SIS-18 already offered worldwide unique conditions for purposes of activation studies [13]. The main purpose of experiments was to accumulate valuable data about the residual activity induced in the material, the list and amount of the radioactive nuclides as well as their depth distribution in the target. The obtained experimental results are compared with results of simulations and used for verification of the Monte Carlo transport codes. Possible discrepancies provide interesting information for further development of the physical models in terms of completeness and precision.

1.1 STATE OF THE ART

Depth-profiling of an induced activity as a benchmarking tool

In the frame of the activation studies at GSI Darmstadt, the activation of about 30 targets made of materials as aluminium, copper, stainless steel, lead, graphite, and carbon-composite irradiated by uranium, xenon, tantalum, nitrogen or argon beams with energies in the range from 100 MeV/u to 1 GeV/u was studied (e.g. Ref [4, 21, 23, 24]). Thanks to the so-called stacked-foils geometry of the experimental targets, the technique of depth-profiling of the residual activity was applicable in this study. Results of different combinations of target material and beam species with various beam energies were reported in several publications, where the discrepancies between calculation and experimental results were discussed [17-30]. Some updates of the FLUKA code were initiated by GSI researchers after the observation of discrepancies between the experimentally measured and the simulated range of heavy ions [23, 39].

Beam-loss criteria

After validation of the Monte Carlo codes and assessment of the uncertainties of the numerical experiments, it was possible to use simulations for providing data for real applications. The beam-loss criteria based exclusively on numerical calculations are an example of appropriate and professional solution for situations where it would be very difficult to obtain the same results by classical experimental approaches. The scientific community agreed on the tolerable beam losses of 1 W/m for proton accelerators based on the empirical experiences available in 1999, when the 7th ICFA Mini-workshop on high intensity high brightness hadron beams was held and the first criterion for proton machines was established [2]. A set of calculations provided by FLUKA 2008 delivered data of the activation of the standard constructing materials of accelerators by different heavy-ion beams. This study proved that the same amount of beam losses leads to a lower activation for heavier ions and also for ions with higher energy. This dependency of the mass number and the energy of the primary particles on the tolerable beam losses were described as the scaling law [4]. It is also important that this complex set of simulations is adequate to 81 individual experiments (for each studied constructing material) with minimal duration of about 400 days for data acquisition, without considering the time necessary for data analysis. Therefore, using the Monte Carlo simulations for determination of the scaling law and the tolerable beam-loss criteria is a time-saving approach with a great benefit of reduction of radioactive waste production.

Available Monte Carlo simulation codes

Modern Monte Carlo (MC) codes are a fast and reliable source of knowledge used in continuous evolving of particle accelerators. Existing as well as facilities under construction are benefiting from them during the processes of modernization or fine-tuning of efficiency and stability of machine operation. Increasing the intensities to new limits in combination with complex ion sources and new technologies and applications in material research, medicine or physics study are creating unprecedented types of radiation in close environment of accelerators. Accordingly, new collimators and radiation shielding have to be developed in order to minimize radiation hazards for all workers. Nowadays, due to accelerated CPU performance, a significant amount of difficulties and uncertainties can be predicted or even solved by several Monte Carlo codes with a sufficient range of accuracy. Some of the available codes developed by different research centres and collaborations are listed here:

- FLUKA (a multi-particle transport code) – collaboration INFN-CERN [41, 42]
- MARS15 – Fermi National Accelerator Laboratory [43-46]
- SHIELD (universal Monte Carlo hadron transport code) – Institute for Nuclear Research of Russian Academy of Science, Moscow [47, 48]
- PHITS (Particle and Heavy Ion Transport code System) – collaboration JAEA, RIST, KEK [49-51]
- MCNP (Monte Carlo N-Particle code) – Los Alamos National Laboratory [52, 53]
- GEANT4 (an object-oriented Monte Carlo toolkit) – GEANT4 collaboration [55, 56]

It is natural that the mentioned Monte Carlo codes have diverse nuances according to their specifications and purposes of the fields of interest of their developers. Nevertheless, the amount of experimental data needed as a calibration tool for physical models is very often limited. Hence, an inter-comparison of results obtained by several MC codes became an exploited alternative. Several codes use similar routines for specific parts of calculations or share some physical models, approximations or databases [43, 57, 58]. Results of individual MC codes are therefore compatible with each other. In short, choosing an adequate code is mostly depending on goals and field of interest of users. However, other aspects as CPU requirements, licence terms and conditions or flexibility of user interface are not negligible.

An essential motivation to use exclusively the FLUKA code in all parts of this work is based on the outcomes of referred studies [18] and [19]. The first investigation presents unique data obtained by using FLUKA 2008. The later advertises the newer version FLUKA 2011 and its added features with important physics improvement. The authors of FLUKA multi-particle transport code released notes for FLUKA 2011 where they declared older versions being obsolete and no longer adequate for research purposes [3]. The same statement can be applied to results of older versions of the FLUKA code as a matter of course. New features of FLUKA 2011 which can increase reliability of activation studies of constructing materials of accelerators compared to older versions are presented in the following list as a state-of-art of engaged Monte Carlo code:

- > Stopping power models have been redesigned and expanded by higher order corrections. In particular, the Barkas (z^3), Bloch (z^4), and Mott corrections have been implemented.
- > Nuclear stopping power calculation of heavy ions at low energies is possible.
- > Several improvements in the hadron-nucleus event generators have been implemented.
- > New evaporation model for residual nuclei production or heavy fragments production is available for ion beam interactions.
- > The model for heavy ion interactions at low-medium energies called Boltzmann Master Equation (BME) has been included. All primary particles (with the mass number $A \geq 4$) with projectile energies lower than 125 MeV/u are treated by BME. (Note: authors warn the users that BME has been extended and improved very recently and possible bugs can appear).
- > The transport and interaction of heavy ions is controlled via a new IONTRANS card [3].

1.2 GOALS AND STRUCTURE OF THIS WORK

Goals

The activation studies and the validation of the Monte Carlo codes have been performed at GSI Darmstadt in form of individual experiments or as a complex work package covered by research topics. Therefore, the goals of the present work were focused on issues which were not discussed yet or on statements which needed to be redefined:

- > Collecting new experimental data for the activation of material by heavy ions with energies from low-medium energy range.

- Evaluating the Monte Carlo simulation code precision based on the results of the benchmarking calculated and experimentally obtained data.
- Using the new FLUKA 2011 to repeat the calculations performed by the previous version FLUKA 2008, which served for establishing the beam-loss criteria for heavy-ion accelerators.
- Expanding the beam-loss criteria for hadron accelerators with operating energies below 200 MeV/u by using the FLUKA 2011.
- Testing the applicability of the beam-loss criteria for long-term operation of heavy-ion facilities.

Structure of this work

The present work focused on two separate topics, which are (1) benchmarking of the FLUKA code and (2) determination of beam-loss criteria based on the simulations. The experiments performed for benchmarking purposes were not used for the estimation of the beam-loss criteria. In other words, the FLUKA code is the common element which connects these two topics. Some of the observations from the first topic need to be used in the second one too. This may seem like duplicity, but improves the clearness of explanations of both topics.

The work consists of five chapters starting with the current chapter called introduction, where the explanation of the importance of the activation study and the benchmarking of the simulation codes was placed. The second chapter is devoted to a brief presentation of the most common mechanisms of heavy-ion interactions as well as to a theoretical description of the simulation codes used in the following chapters. The third chapter is addressed to activation experiments and is internally split into six subsections. The first two are describing common experimental techniques and simulation models used for all experiments. Each of the next three subsections covers the process of activation, analysis and presents result of individual irradiations of experimental targets. The last subsection of the third chapter summarizes the benchmarking and covers the discussion about the observed discrepancies and their possible origin. The forth chapter is devoted to validation and the extension of the existing beam-loss criteria for short-term usage of heavy-ion accelerators and creation of the criterion for long-term operation. That corresponds to the first two subsections of the forth chapter and one more subsection is summarising the limits of tolerable beam losses. The fifth chapter presents the outcome and the main observations of the work.

CHAPTER TWO

THEORY

2 THEORETICAL BACKGROUND

2.1 ACTIVATION

Activation is the process during which a previously stable material is becoming radioactive due to inducing the radioactivity by exposure to specific radiation. The induced radioactivity was studied for the very first time by Irène Curie and Frédéric Joliot-Curie who received the Nobel Price for this discovery in 1935 [59].

In terms of the activation of accelerator components by high energetic heavy ions, the interaction of the accelerated hadrons with nucleus of static accelerator materials leads to the emission of neutrons, protons, nuclear fragments and other kinds of radiation [5]. The activation by the secondary particles is the major mechanism induced by heavy-ion beams. This is experimentally manifested by its presence far beyond the range of the primary particles [17, 20, 24, 40]. While hitting the target, the heavy ion projectiles are fragmented and remain implanted in the target. This process can be separated into several steps and result in the activation of the target. At high energy, the ions interact mostly with the electronic cloud of the target which results in the acceleration of secondary particles also called delta rays (electronic energy loss regime, described in section 2.1.3). At lower energy, the accelerated ions interact directly with the nucleus of the target which leads to the fragmentation of both the accelerated nucleus and the target nucleus (nuclear energy loss regime, described in section 2.1.4). The activation of the sample thus result for the sum of the activation induced along the complete energy loss process of the accelerated ion into the target, that is to say: activation induced by ionization, delta ray, fragmentation of target and projection nuclei. It is noted that the contribution to the total residual activity of high-energy heavy-ion projectile fragments is significantly bigger compared to the contribution of the target-nuclei fragments [17, 20, 24]. The struck nucleus may convert to a different isotope, very likely a different element, with high probability of being radioactive. According to the energy of projectile particles, it is also possible that the secondary particles may be emitted with the energy, which would be high enough for causing further spallation interactions. Also, they can be captured by other nuclei and lead to production of radioactive isotopes [5]. The products of the interaction may have an atomic weight of anything up to that of target material nucleus due to fragmentation or it may even be higher in the case of capture reactions. As it may be seen, the interactions of lost heavy ions with the accelerator structures introduce a great variability of activation processes. The overall induced radioactivity depends on the primary particle (projectile) loss; the probability of isotope production depends on the composition of the activated (target) material, the spectrum of the secondary particles and the cross section of the isotope. A quantification of the amount of individual isotopes also depends on their half-life times and the operation time of accelerator as well as the cooling time since operation stopped. The precise estimation is rather a complex task, especially in cases of repeated operations of machine with certain breaks, where the systematic build-up and decay of induced radioactivity should be taken in account [5].

2.1.1 INTERACTION OF HEAVY-IONS, NEUTRONS AND PHOTONS WITH MATTER

The activation process consists of various types of nuclear interactions. The most important interactions are high-energy inelastic hadron interactions (spallation reactions), neutron radiative capture, and photonuclear reactions [7].

The spallation reaction is a process in which a light projectile (proton, neutron, or light nucleus) with a high kinetic energy ranging from several hundreds of MeV to several GeV interacts with a heavy nucleus and causes the emission of many hadrons (mostly neutrons) and fragments.

The radiative capture is a reaction, in which the incident neutron is entering the target nucleus, which leads to forming of a compound nucleus. The active nucleus is returning to its ground state by gamma emission. This process can occur at all incident neutron energies, and the probability of the interaction strongly depends on the incident neutron energy, the target excitation as well as the temperature [14].

The photonuclear reaction corresponds to the absorption of a gamma-ray photon (γ) by a target nucleus accompanied by the ejection of protons (p), neutrons (n), alfa particles (α) or heavier particles (F) from the nucleus. The (γ, p) and (γ, n) photonuclear reactions are limited by the energy of the photon which must exceed the binding energy of the nucleon in the nucleus. The total cross section for all possible photonuclear reactions (e.g.: (γ, γ'), (γ, n), (γ, 2n), (γ, p), (γ, α), (γ, F)) is called the gamma-ray absorption cross section for a nucleus [15].

Interactions of different particles may lead to the production of isomeric nuclei. A metastable state of atomic nucleus is a particular excited state of an atom that has a longer half-life time than is a half-life time of a nucleus in an ordinary excited state and also it is shorter than a half-life time of a nucleus in a lowest energy state called the ground state. A metastable state may be interpreted as a temporary energy trap where a nucleus can remain in this state for a sufficient time. It may then be regarded as separate nucleus and are denoted with a superscript "m" (i.e. ^{120}Sb and ^{120m}Sb). These nuclides are called nuclear isomers because they fulfil a definition of isomers as the same nuclei with the same atomic number (Z) and the same mass number (A), even though they disintegrate following different decay schemes. The metastable nuclei have their own decays period and decay in the processes called isomeric transition (IT) [72, 73], presented by following equation:

$$IT: {}^{Am}_{Z}P = {}^{A}_{Z}P + \gamma \tag{1}$$

2.1.2 STOPPING POWER AND RANGE OF CHARGED PARTICLES

The major atomic process undergone by charged particles when going through a media consist of Coulomb scattering with both atomic electrons and nuclei. It should be emphasized that these interactions are identically described by the fundamental law of electrostatic for both electrons and nuclei, but the result differs because of their difference in masses. Two district models are used to describe the Coulomb scattering process:

- Inelastic collisions – are the interactions with the target electrons (also referred to as electronic stopping power). They are by far the dominant source of charged particle energy losses for high energy projectile (> 1 MeV/u), while they give a contribution proportional to the atomic number Z of target atoms to angular deflections.
- Elastic collisions – are the interactions with target nuclei, usually referred to as nuclear stopping power. They result in negligible energy losses at the high energies; however, the nuclear stopping power is important for low-energy heavy particles. The angular deflection is proportional to Z^2. As a consequence, angular deflections are associated mostly with scattering on atomic nuclei, but for the lightest elements where the two contributions become comparable.

Energy losses of charged particles are commonly expressed as an average energy loss per unit path length. The slowing down of energetic protons and ions in matter is governed by collisions with the target electrons and leads to the characteristic shape of the depth–dose profile of heavy charged particles with a peaking energy deposition, the so-called Bragg peak. [18]. The nuclear stopping power contribution to the total energy loss of protons and ions in the energy range of relevance for the activation studies of the accelerators is rather negligible [9]. The stopping power S(E) is defined as the average energy lost by the particle per unit distance.

$$S(E) = -\frac{dE}{dx}, \tag{2}$$

with E is kinetic energy of the particle and the x is the path length.

Due to a random occurrence of the energy loss events, the average must be taken over a large number of particles at given energy. A particle with an initial kinetic energy E is slowed-down to kinetic energy E(x) at path length x due to both Coulombic interactions with (target) electrons and nuclei, and radiation losses. The distance the particle travels before they complete kinetic energy loss is defined as the projectile range, R. It is possible to derive it as of the sum of the reciprocal values of the stopping power integrated over their kinetic energy deceleration range. It is also known as the Continuous Slowing Down Approximation (CSDA):

$$R(E) = \int_0^{E_0} \left(\frac{dE}{dx}\right)^{-1} dE \tag{3}$$

Thus from the equation it is deduced that, the higher the stopping power is, the shorter the projectile range is. The stopping power increases toward the range and reaches a maximum, the Bragg peak, shortly before the energy drops to zero. The stopping range was defined as the depth in the target where the half-maximum on the descending part of the Bragg peak is located [19].

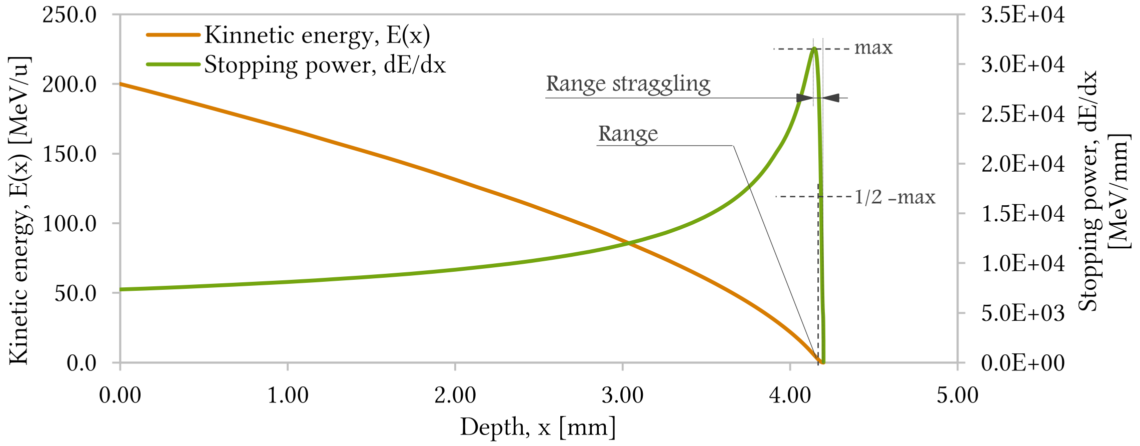

Figure 2: Calculated stopping power and energy decrease as function of penetration depth by SRIM code for 200 MeV/u uranium beam in aluminium. The typical "Bragg curve" shape is presented as green curve and decreasing of the kinetic energy as orange curve.

2.1.3 ELECTRONIC STOPPING POWER - BETHE-BLOCH FORMULA

The Bethe-Bloch formalism is often used for electronic stopping power computation [9, 60, 61, 76]. The energy loss of the projectile per unit distance in the target material is called the stopping power. The standard formulation has been modified and refined by several correction parameters (such as density, shell, Barkas, Bloch and Mott corrections). The precision of the equation at the lowest energies was improved by Ziegler [65] and its complemented version was implemented in FLUKA and explained in detail in Ref. [9]. All these possible corrections and their dependency on the experimental conditions also explain the variety of Bethe-Bloch formula that can be found in literature. The formula for the average energy loss of particles much heavier than electrons and with charge "z" can be expressed by:

$$\left(\frac{dE}{dx}\right)_0 = \frac{2\pi n_e r_e^2 m_e c^2 z_{eff}^2}{\beta^2}\left[ln\left(\frac{2m_e c^2\beta^2 T_{max}}{I^2(1-\beta^2)}\right) - 2\beta^2 - \delta(\beta) - 2\frac{C(\beta)}{Z} + 2zL_1(\beta) + 2z^2L_2(\beta) + K_M(z,\beta)\right], \quad (4)$$

$$n_e = \frac{\rho N_{AV} Z}{A}, \quad (5)$$

$$T_{max} = \frac{2m_e c^2\beta^2\gamma^2}{1 + 2\gamma\frac{m_e}{M} + \left(\frac{m_e}{M}\right)^2}, \quad (6)$$

$$\gamma = \frac{1}{\sqrt{1-\beta^2}}, \quad (7)$$

for spin 0 particles and similarly for spin ½ particles where [9]:

- r_e is the classical electron radius,
- m_e is the mass of the electron,
- n_e is the target material electron density,
- ρ is the target material density,
- N_{AV} is Avogadro's number,
- A is mass number,

- Z is atomic number,
- z_{eff} is the projectile effective charge and z is the electron charge,
- β is the velocity relative to the speed of light (β = v/c),
- I is the logarithmic average over all ionization and excitation levels of the target material,
- T_{max} is the maximum energy transfer to a stationary electron,
- M is the projectile mass.

The terms δ, C/Z, L_1, L_2 and K_M are included in Bethe-Bloch formalism due to individual corrections:

- δ is the density correction for the dielectric polarization of the target
- C is the shell correction which takes into account the effect of atomic bonds if particle velocity is close to orbital velocity of electrons [75]
- L_1 is the Barkas correction ($\sim z^3$) accounts the differences between the stopping power of particles and anti-particles [66, 67]
- L_2 is the Bloch correction ($\sim z^4$) is important for high-velocity particles to secure collisions with minimal impact parameters by adoption of the exact scattering amplitude [68]
- K_M is the Mott correction associated to (electron-ion scattering cross-section) Rutherford cross-section deviations important in the case of medium-heavy projectiles with the relativistic velocities [69, 70].

The Bethe-Bloch formula introduced in the equation (4) gives the mean loss rate as the function of the particle speed and the charge and of the relevant material properties. Moreover, with high-Z projectiles it is necessary to evaluate their effective charge - z_{eff}, which takes into account the partial neutralization of the projectile charge, when the particle speed is not much larger than the speed of the atomic electrons (since electron capture becomes important at low energies) [8, 9]. Particularly, the FLUKA code also assume that $z_{eff} = z$ effective charge is equal to charge of projectiles with sufficiently large velocities or to the charge of very light ions (e.g. protons and alphas), otherwise FLUKA makes use of the semi-empirical procedure of the effective charge parametrization (proposed in Ref. [71]) deduced from set of about 600 experiments [9].

2.1.4 NUCLEAR STOPPING POWER

The nuclear stopping is much smaller compared to the electronic stopping power and it is often considered to be negligible in cases of high-energy heavy ions. Nevertheless, the nuclear stopping power is important for low-energy heavy particles. A calculation of the nuclear stopping power is possible if the form of the repulsive potential between two atoms is known. Many different models have been proposed over the years, some determined semi-empirically, others from theoretical calculations [65]. Thus different forms of the stopping power may be found in available literature. For example, nuclear stopping in FLUKA is given by following equation [16]:

$$S_n(E) = \frac{5105.3\, Z_1 Z_2 \hat{S}_n(\varepsilon)\rho}{\left(1+\frac{M_1}{M_2}\right)\left(Z_1^{0.23}+Z_2^{0.23}\right)A}\ [MeV/g/cm^2]\ , \qquad (8)$$

where ε is the reduced energy and calculated from:

$$\varepsilon = \frac{32.536\,E}{Z_1 Z_2 \left(1 + \frac{M_1}{M_2}\right)\left(Z_1^{0.23} + Z_2^{0.23}\right)} \,, \tag{9}$$

where E is the energy in keV, and M_1, M_2 are the masses of projectile and target atom, respectively. The charges of the interacting nuclei are labelled as Z_1, Z_2. The reduced nuclear stopping is then given by

$$\hat{S}_n(\varepsilon) = \frac{0.5 ln(1 + 1.1383\varepsilon)}{[\varepsilon + 0.01321\varepsilon^{0.21226} + 0.19593\varepsilon^{0.5}]} \quad for\ \varepsilon\ < 30\ , \tag{10}$$

$$\hat{S}_n(\varepsilon) = \frac{ln(\varepsilon)}{2\varepsilon} \qquad for\ \varepsilon\ \geq 30\ . \tag{11}$$

2.2 BEAM-LOSS CRITERIA

With the necessity of using particle accelerators for various scientific, nuclear and military applications, the importance of the tolerable beam-loss criteria became of major importance arose. The radiation protection policies define limits of workers exposure by the radiation emitted by the accelerator and its environment, as well as limits of the access time to radioactive areas. Usually, the interlock radiation detectors are deployed to ensure adherence to radiological standards in sensitive locations around the machine. Unfortunately, it is not technically possible to achieve a complete coverage of whole area due to finite number of the detectors array. An alternative method to estimate the radiation levels in accelerator tunnels and close region around beam-lines was investigated and the relationship between beam-losses and the production of radiation was observed [2].

2.2.1 PROTON MACHINES

The beam loss criteria for proton machines have been defined for the very first time on the 7th ICFA Mini-workshop on high intensity high brightness hadron beams in September 1999. Experienced accelerator users and researchers from the European Organisation for Nuclear Research (CERN), the Los Alamos National Laboratory (LANL), the Lawrence Berkeley National Laboratory (LBNL), the Brookhaven National Laboratory (BNL), the Fermi National Accelerator Laboratory (FNAL), the High Energy Accelerator Research Organisation (KEK) and the Japan Atomic Energy Research Institute (JAERI) collaborated within the beam loss working group. The radiation-protection policies in the US, Japan and at the CERN were taken as a base for discussion about the practical limits on residual radioactivity to allow for hands-on maintenance of accelerator components. Beam loss working group came to an agreement that a measurement on operating facilities indicate acceptable dose levels if beam loss can be kept to 1 W/m or less [2]. A following statement was published in the work group report and it can be considered as the first beam-loss criteria for proton machines: *"To allow hands-on maintenance of accelerator components without unreasonable constraints, dose levels should be below 1 mSv/h (measured 30 cm from component surface). This corresponds to beam loss of about 1 W/m along the beam enclosure; this figure is roughly independent of* *beam energy, for energies above 100 MeV. Thus a greater number of particles can be lost at lower energies, as activation is less efficient."* [2].

2.2.2 HEAVY-ION MACHINES

Establishing of a universal criterion for different heavy-ion beams is complicated, because the induced residual activity depends on the amount, energy and mass of the lost particles as well as on the irradiated material and its composition. Nevertheless, the operation of heavy-ion accelerators must satisfy the same radiological regulations as the proton machines and the dose-level in accelerator environment must be the same even though the activation by heavy-ions differs from the activation by protons [5]. Strašík et al. presented the beam-loss criteria for heavy ions based on the normalization of the induced activity by unit beam power of 1 W [4]. They claimed that a list of the fragments obtained from the radionuclide inventory, as well as a representation of their relative activities accumulated in targets, is almost identical for all heavy ions (see Figure 3). Authors supported their allegation by a study of the 100 days long activation of copper and stainless steel targets (a beam-pipe and a bulk target) by heavy ions (^{1}H, ^{4}He, ^{12}C, ^{20}Ne, ^{40}Ar, ^{84}Kr, ^{132}Xe, ^{197}Au and ^{238}U) with the energies between 200 MeV/u and 1 GeV/u.

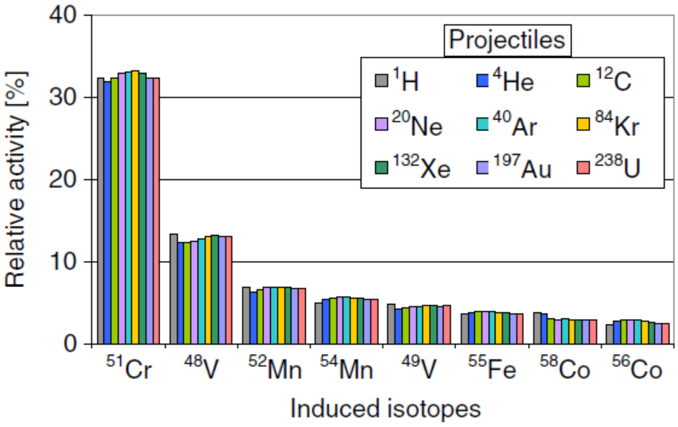

Figure 3: Relative activities of the nuclides induced by different beams with an energy of 1 GeV/u at the cooling time of 1 day after irradiation in the beam-pipe made of stainless steel [4].

Since the relative activities of the most contributing fragments are very similar for all projectiles, the time evolution of the total activities must be also comparable for all ion species. A normalization of the activities to the activity at certain time (the end of the irradiation was chosen by authors) and following calculation of their mean value can be used for obtaining of a generic curve which is independent from projectile mass [4], see Figure 4.

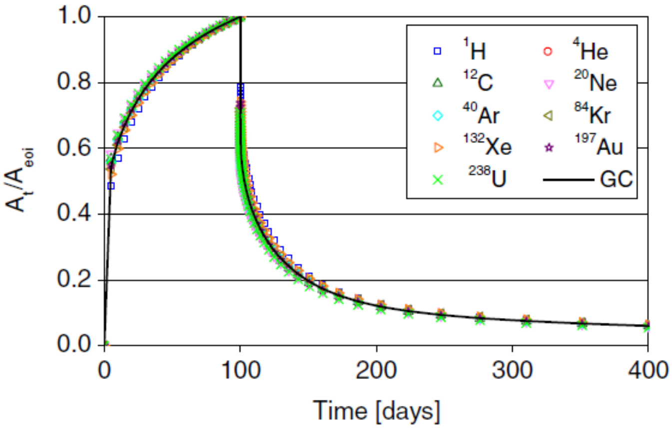

Figure 4: Time evolution of the relative activity induced in the beam pipe made of stainless steel by different projectiles at 500 MeV/u. A_t is the induced activity as a function of time; A_{eoi} is the induced activity at the end of the irradiation. The generic curve is obtained by averaging the data points of the individual curves corresponding to different primary ions [4].

The generic curve (GC) can be constructed as:

$$A_{GC} = \langle\, {}^{j}A \rangle \ , \tag{12}$$

where A_{GC} is the activity given by the generic curve at a certain time point and ${}^{j}A$ is the activity induced by the jth projectile at the same time point. The generic curve has two separate parts corresponding to activation before the end of the irradiation, Eq. (13) and decay after the end of the irradiation, Eq. (14). Fitting the generic curve is only possible using two different functions for the activation and decay, respectively [4].

$$A(t_a) = \sum_{i=1}^{N} g_i \left[1 - exp\left(\frac{-\ln 2}{T_i} t_a\right)\right] \ , \tag{13}$$

where $A(t_a)$ is the total activity at the time t_a after the beginning of the irradiation, g_i are the production rates of individual nuclides, T_i are the half-life of nuclides, and N is the total number of induced nuclides [4].

$$A(t_d) = \sum_{i=1}^{N} A_i \cdot exp\left(\frac{-\ln 2}{T_i} t_d\right) \ , \tag{14}$$

where $A(t_d)$ is the total activity at the time t_d after the end of the irradiation, A_i are the activities of the individual nuclides at the end of the irradiation, T_i are the half-life of the nuclides and N is the total number of induced nuclides. The equations (13) and (14) are not taking in account a presence of daughter nuclides, but as the authors proved in several experimental studies [17, 20, 24], their contribution to total activity can be neglected [4]. Thus the three main observations were:

- The inventory of the isotopes induced in the stainless-steel beam pipe does not depend strongly on the projectile species.
- The time evolution of the induced activity correlates to the generic curve.
- The activity induced by 1 W/m of beam losses is decreasing with increasing ion mass and with decreasing energy [4].

Under these conditions, it was possible to define the scaling law for heavy-ion beam-loss criteria based on the accepted limit of 1 W/m for protons fulfilling the radiological limits. The scaling factor is calculated as:

$$SF = \frac{A_p(1GeV)}{A_i(E)} \ , \tag{15}$$

where $A_p(1GeV)$ is the normalised activity produced by a proton beam with an energy of 1GeV during 100 days of continuous irradiation and that was scored at 1 day after the end of the irradiation. The activity $A_i(E)$ is produced by any of the particle beams of defined energy E. Activation by such a heavy-ion beam corresponds to the beam losses with the beam power of 1 W. The activity is measured 1 day after the irradiation [4]. It was demonstrated that the normalized activity is decreasing with the increasing ion mass. The tolerable beam losses for heavy ions were specified by scaling the existing value of 1 W/m for protons. The scaling law yields the beam-loss tolerances for uranium beam of 12 W/m (5 W/m) at 1 GeV/u, 23 W/m (12 W/m) at 500 MeV/u, and 75 W/m (60 W/m) at 200 MeV/u in the case of the beam-pipe (and bulk target) geometry. To conclude on the present criterion, the authors of the reference [4] claimed that an influence of the energy-threshold of 100 MeV/u for heavy-ion inelastic interactions carried by FLUKA 2008.3.6 can appear in their results. The re-evaluation of the beam-loss limitations by FLUKA 2011 version was performed for copper and iron targets and presented in the thesis of Dr. Chetvertkova (see Ref [19]). The calculations considered the same set of the primary projectiles (^{1}H, ^{4}He, ^{12}C, ^{20}Ne, ^{40}Ar, ^{84}Kr, ^{132}Xe, ^{197}Au and ^{238}U) with an energy of 200, 100 and 50 MeV/u. Difficulties to derive accurate beam-loss criteria for the ion beam energies below 100 MeV/u were also reported. Therefore, the criteria should be determined also for longer irradiation times. At low energies, the stopping range of the heavy ions becomes shorter than the nuclear mean free-path. Thus, the number of the produced target fragments would be approximately the same as the number of projectile fragments. In case extended machine operation, the accumulation of long-lived projectile fragments becomes a significant part of the total activity induced in the bulk target structure. In both cases the nuclide inventory in the target would differ for different projectiles [19].

2.3 SOFTWARE

Three different computer programs were used for ion-beam transportation calculations. A description of their specifications is located in following subsections.

2.3.1 FLUKA

The FLUKA (a multi-particle transport code) is a fully integrated particle physics Monte Carlo program developed within INFN-CERN collaboration (INFN – Italian National Institute of Nuclear Physics and CERN - The European Organization for Nuclear Research) [86]. It is a general purpose tool for many scientific fields and enables calculations of particle transport and their interactions with matter. Results of the FLUKA calculations are often used for designing accelerators shielding parts, target preparations, the dosimetry and radioprotection, the radiation damage prediction, the ADS (Accelerator Driven Systems) controlling, the waste transmutation and repository time-planning, the particle physics study (calorimetry, tracking and detector simulations), the medical applications in hadron therapy, etc. The final predictions are obtained with a minimal set of free parameters, fixed for all combinations of energies, targets, and projectiles. One of the main goals is to provide the solid predictions where no experimental data are directly available [9, 41, 86].

Table 1: Transport limits of the FLUKA code [41].

Particles	Secondary particles	Primary particles
Charged hadrons	1 keV – 20 TeV *	100 keV – 20 TeV $^{*\,\#}$
Neutrons	Thermal – 20 TeV *	Thermal – 20 TeV *
Antineutrons	1 keV – 20 TeV *	10 MeV – 20 TeV *
Muons	1 keV – 1000 TeV	100 keV – 1000 TeV $^{\#}$
Electrons	1 keV – 1000 TeV	70 keV – 1000 TeV $^{\#}$ (low-Z materials) 150 keV – 1000 TeV $^{\#}$ (high-Z materials)
Photons	100 eV – 10000 TeV	1 keV – 1000 TeV
Heavy ions	< 10000 TeV/u	< 10000 TeV/u
* - upper limit 10 PeV with the DPMJET	$^{\#}$ - lower limit 10 keV in single scattering mode	

The FLUKA can simulate with high accuracy the transportation and interaction of about 60 different particles, including polarised photons and optical photons, electrons, neutrinos, muons, hadrons and all corresponding antiparticles, as well as neutrons and heavy ions within a wide range of the energies, see Table 1. Time evolution and tracking of emitted radiation from decaying residual nuclides can also be simulated. FLUKA can administrate the transportation processes through the complex geometries even with the effect of the electric and magnetic fields. Thanks to improved Combinational Geometry package [93], FLUKA can be used for preparing of various geometry configurations and for optimizing the prototypes of probe design before performing experiment. The principle of the Monte Carlo method is based on the generation of successive random samples (so-called seeds) and on the statistical interpreting of the global results after numerous iterations of each particle along its path through the target material. At each step, the occurrence and the outcome of the interactions of the projectile are chosen by random selection from the appropriate probability distribution. In such an approach all the possible channels of the reaction are treated and all the conservation laws, typical for an occurring interaction, are hold for all the individual reaction products. All the secondary particles issued from the primary projectile interactions are transported before a history of next primary particle is recorded. For this reason, it is possible to simulate the accumulation of some particles or continuous effects in the matter. The statistical accuracy of the results depends on the number of the seeds of the simulation. FLUKA is using the biasing technique for statistical convergence of the results [94].

Boundaries and specifications of the FLUKA physical models are described in the user manual, several journal and conference papers [87]. Naturally, it is not an intention of this thesis to introduce all physical models used by FLUKA in detail. On other hand, it is convenient to pay some attention to the ones that have a special influence on the results computed in the conditions presented in later chapters, i.e. the transport modules and interaction modules. As well as to the models which have undergone a significant improvement between the two program versions, namely FLUKA 2008 and FLUKA 2011, and they have a sense for the presented research.

The transport of the charged particles

FLUKA is using the Continuous slowing down approximation (CSDA) (demonstrated on the page 19) for the transportation of the particles and calculation of their range. The basic CSDA model is taking into account two effects: (a) ionisation fluctuations and (b) production of the secondary electrons ("δ" rays) with the sufficient energy for further ionisation. FLUKA allows users to activate either one of them, both of them or none of them by setting their thresholds [89]. This approach is made to exploit the statistical properties of the cumulant of the probability distribution (in particular the Poisson distribution), which return very satisfactory results compared to the previous classical approaches (the Landau [91] and Vavilov [92] distribution) [89]. The moments of the energy loss up to the 6th order are calculated and the approach can account for an arbitrary threshold for the explicit production of secondary electrons, for arbitrary step-lengths, and for the contribution of distant collisions to energy loss fluctuations. The effect of the Mott correction on energy loss fluctuations is included as well. Consideration of an energy-loss fluctuation impact on the range determination and also on the shape of the Bragg peak increased the precision of the results with minimal CPU effort [88, 89]. An original approach of multiple Coulomb scattering of charged particles based on the Molière's theory [62, 88, 97] has been specially developed for FLUKA. The stopping power of charged particles is calculated using the Bethe-Bloch theory with the following parameters involved: mean excitation energy (material dependent), density correction, shell correction, and maximum energy transfer to an electron [60, 61]. A detailed explanation of all parameters, extensions and corrections (Barkas, Bloch, Mott corrections) was given in subsection 2.1.3 (page 20).

Interaction models

FLUKA has several models describing the interactions between different hadrons, hadrons and nuclei, and different nuclei. Each model is applicable within a certain energy range, as shown in Table 2. A detailed explanation of all of them is not possible in the thesis however, the results of the experimental part of the present work will use two of them, which are shortly introduced below.

The Boltzmann master equation (BME) is available in the FLUKA code since releasing of the version 2011. The BME theory afforded opportunity to simulate interaction of heavy ions ($A > 1$) below 100 MeV/u, since previous versions of FLUKA could only simulate their transportation [3]. The simulation of the primary particles with the target nuclei is described by the two-component Fermi gases model. It is assumed that the interaction scheme has two steps, where in the first step, the interaction of the projectile and target nucleons occurs and also it may further cause the cascade of another interaction in the target. An emission of nucleons is possible at this stage, but the majority of all emitted particles (e.g. nucleons, gammas and clusters) are yielded during the second step of interaction, when the excited nuclei relaxation [3].

The Relativistic quantum molecular dynamics (RQMD) is the microscopic model using the Fermi gas approximation for treating of projectiles and target nuclei. An issue of the energy-momentum conservation is covered by using the experimental binding energies of interacting particles. The model is combining the classical propagation of hadrons and the stochastic scattering within whole energy range between 100 MeV/u and 5 GeV/u.

Table 2: Hadron interaction models used by FLUKA [41].

Interaction	Energy	Model
Hadron - hadron	5 GeV/c – 20 TeV/c < 5 GeV/c	Dual Parton Model (DPM) Resonance production and decay model
Hadron - nucleus	5 GeV/c – 20 TeV/c < 5GeV/c	Glauber-Gribov multiple scattering and GINC PEANUT model
Nucleus – nucleus	> 5 GeV/u 0.1 – 5 GeV/u < 0.1 GeV/u	DPMJET RQMD (Relativistic Quantum Molecular Dynamics) BME (Boltzmann Master Equation)

2.3.2 SRIM

Stopping and **R**ange of **I**ons in **M**atter (SRIM) is a group of several programs calculating the interactions, the stopping and the range of ions (with initial energy 10 eV – 2 MeV/u) in matter [74, 75, 98, 99]. Detailed descriptions of all parameters and formulas are available in SRIM textbook "SRIM – The Stopping and Range of Ions in Matter" [99] including a routines optimization according to experimental data. It is practical to pay careful attention to the principles of stopping power modules used by SRIM and their suitability for the activation study of constructing materials. The calculations of a stopping power of high energy ($E > 1$ MeV/u) heavy ions ($Z > 3$) contain two components. The first one, the Brandt-Kitagawa approximation [100] of the charge state of heavy ions is substituting the average charge state of heavy ions known from the Bohr's theory [101]. A second component is covering several high velocity effects influencing the heavy ion stopping. A Bethe - Bloch formula contains a mean ionisation potential and a shell corrections for elimination of the dependency on the target material, as well as a density corrections or the Barkas and Bloch corrections [102]. Another crucial specification of SRIM package is the compilation of available collision models. There are merely elastic nuclear collisions and inelastic electronic collisions considered, but no inelastic nuclear collisions are considered in the calculations. The elastic nuclear collisions generate an angular deflection combined with the stopping of the ions and the inelastic nuclear collisions are represented as a continuous slowing-down process. For this reason, the fragmentation of the primary ions along their trajectory is not possible and such a process is absolutely excluded from ion transportation in target material. Users can choose between two individual approaches of SRIM package:

> Table of the Stopping and Range of ions in Matter (so-called Stopping/Range Tables) provides quick calculations of ion transportation in one-layer targets. Table of Ion ranges with range straggling are calculated using transport equations included in the **P**rojection **RA**nge **AL**gorithm (PRAL). Accuracy of these ranges is usually within 5% of the TRIM Monte Carlo code (more accurate calculation from SRIM developers). Table of stopping powers are reported as nuclear energy loss (to the target nuclei) and as electronic energy loss (to the target electrons).

> **TR**ansport of **I**ons in **M**atter (TRIM) Monte Carlo module was developed for more complicated amorphous targets simulations. Complex targets made of compound materials up to eight layers (each of different material) are accepted. TRIM uses a statistical algorithm which allows the ions to make jumps between singular collisions and then averaging the collision results over the intervening gap. The Coulomb collisions and interactions between the overlapping electron shells are calculated as well as the electron excitations and plasmons creations caused by the transported

ions within the target. There are available 3D distributions of target damages and displacements, sputtering yield, ionization profiles, phonon production in addition to the range and range straggling. All target atom cascades in the target are followed in detail. [74, 75]

2.3.3 ATIMA

Another software used in some parts of the experimental study, to prepare the targets and to validate the primary particle range, is ATIMA. A specialisation of this program is the calculation of the stopping power, energy loss and energy-loss straggling, the angular straggling, the range and range straggling of the ions interacting with the target material. In addition, the beam parameters as well as the magnetic rigidity, the time-of-flight or the velocity of particles are determined for slowing-down process of the protons and heavy ions with kinetic energy from 1 keV/u to 450 GeV/u [103]. The stopping power of ions with the energy higher than 30 MeV/u is obtained from the theory by Lindhard and Soerensen [105], where a precise quantum mechanical calculation of the energy transfer in the interaction process of projectiles with target electrons is needed. The shell corrections [106], a Barkas term [107, 108] and the Fermi-density effect [109] are also included in the calculations. The projectiles are treated as ions with the size of a nucleus with a mean charge according to reference [110]. ATIMA is using an older version of SRIM [75] in the case of ions with an energy below 10 MeV/u. The Bethe formula [111] considers the nuclear size effect for very relativistic ions. The energy-loss straggling calculation is based on the Firsov [112] and Hvelplund [113] theory.

The functioning of the ATIMA code is described in several articles written by the developers. The stopping-power and energy-loss straggling calculations were crosschecked with an experimental data from FRS at GSI [114, 115]. According to permanent refinement of the code the effects of charge-exchange straggling [119, 120] or the charge dependence of dE/dx [121] were studied. One can find some more results obtained by ATIMA listed in the references [116, 117, 118]. ATIMA code is developed at GSI Darmstadt as software for Linux operating system, but there are also a Windows version (implemented in LISE++) and so-called "WWW-interface" [103, 104].

CHAPTER THREE

EXPERIMENTS

3 ACTIVATION EXPERIMENTS

This chapter presents the results of activation experiments and their comparison to simulations. As it was already mentioned before in the introduction chapter, the experiments were focused on studying the inducing of the radioactivity as a function of depth, providing the nuclide inventory of induced radionuclides and determining the range of primary particles. In order to collect high-quality data, many aspects have been taken into account and the configuration of targets and irradiation properties have been adjusted for each activation experiment. It has to be stressed at this place that the preparation of the experiments was challenged by coordinating many aspects and conditions, which often contraindicated each other. For example, in order to present the depth profile of the residual activity with a sufficient depth resolution a large amount of foils is needed in the target. Gamma spectra of each foil should be measured for some minimal-time necessary to obtain sufficient statistic. The total measuring time disqualifies directly some of the short-lived isotopes, simply because they decay before the measurement of whole target is finished. Thus, a reasonable balance between the depth-resolution and the amount of the short-lived nuclides, which is acceptable to sacrifice due to the total time of the data acquisition, was necessary to saddled. This was an example of one single problem, but there were many others complications related to the target preparation, the beam monitoring, the transportation of the activated samples, etc. They are described in the first section of this chapter. It is important for the reader to keep in mind that many compromises were made for achieving the experimental data.

The present chapter is divided into six sections. The first one (section 3.1) is devoted to the detailed explanation of the target preparation, experimental setup and used methods. The general model designed for the FLUKA simulations is described in the part 3.2. Sections 3.3, 3.4 and 3.5 present results of several experiments. The methodology and analysis of all experiments were identical. For this reason, similar examples and explanation of a data processing is included only in the section presenting the first experiment (section 3.3). This may help to minimize a repetition of the same illustrations in the cases similar observations difficulties in more than one experiment. Individual occurrences and circumstances are described continuously in each section. The last section (3.6) of this chapter summarizes the conclusions of the activation experiments.

3.1 EXPERIMENTAL PREPARATION, REALIZATION AND ANALYSIS

3.1.1 EXPERIMENTAL AREA AND LIMITS FOR THE TRANSPORTATION OF IRRADIATED SAMPLES

The experiments presented in this work were performed at GSI Helmholtzzentrum für Schwerionenforschung GmbH in Darmstadt. The cave HHD hosting the beam dump of SIS-18 synchrotron was chosen as experimental area adequate for our studies (Figure 5). Production of a great amount of secondary particles spreading like a shower is specific for this kind of experiment. Massive radiation shielding around the extraction and beam dump was specially constructed to safely intercept high-intensity heavy-ion beams and guarantee appropriate conditions [26]. The ionizing radiation is produced during normal accelerator operation on many places along the beam-pipe, magnets, etc. Therefore there are three classified regions for better protecting of people working at GSI:

- Not controlled area – allowed effective dose is lower than 1 mSv/year
- Controlled area – allowed effective dose is lower than 6 mSv/year
- Inaccessible area – the dose rate is higher than 3 mSv/h

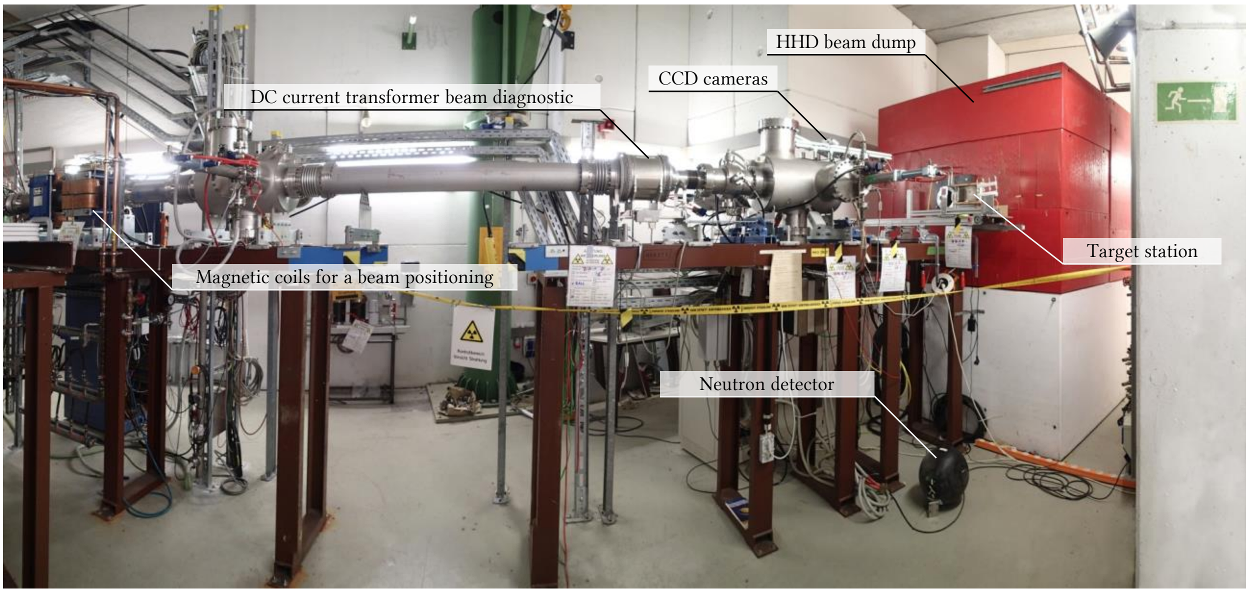

Figure 5: Photo of HHD beam dump at GSI Helmholtzzentrum für Schwerionenforschung GmbH.

Each of the areas has specific rules defined by radiation protection ordinance [125]. Conditions for operation, storing and transportation of radioactive material inside of the area or between different areas are defined and controlled by the radiation safety group at GSI. The dose rates of the irradiated targets allowed for transportation from cave HHD (controlled area) to the gamma spectroscopy station (not controlled area) in the laboratory are typically below 20 µSv/h.

The cooling-time necessary for decreasing the radioactivity to tolerable level was estimated by a dose-rate simulation [19]. The time dependency of radioactivity is described by the decay law (see Eq. 16). It can be used for activity calculation of some radioactive nuclides:

$$A(t) = A_0 \cdot exp\left(\frac{-\ln(2).t}{T_{1/2}}\right) , \qquad (16)$$

where A(t) is the activity at some specific time t, A_0 is the activity at t=0 and $T_{1/2}$ is the half-life time of the radioactive nuclide [5].

The production of the radioactive nuclides is directly proportional to the number of primary particles interacting with the material. This is why the study of short-lived isotope production is possible only if the gamma spectroscopy measurements start soon after the end of the irradiation. Preliminary FLUKA calculations and experiences from previous experiments (see Ref. [4-26]) were used to set a lower and an upper limit of the total number of primary ions. The meaning of these limits can be explained as range for acceptable activation between which it is possible to measure an irradiated sample in a short time after the end of the irradiation and in which sufficiently high count-rates for gamma spectra are obtained. The total number of ions accumulated during irradiation ranged between 1 x 10^{12} and 5 x 10^{13}. In these cases, the experimental targets were available for an initiation of gamma spectroscopic measurements between 5 and 12 days after the end of the irradiation. Radioactive nuclides with half-life time shorter than 1 day were automatically omitted from further analysis.

3.1.2 RANGE OF THE PRIMARY IONS IN ALUMINIUM TARGETS

The determination of the range was also used for an effective setting of the target dimensions. The total thickness was set to the double length of the primary particles range, because the targets of this size are sufficient for recording of complete depth profiles of primary particles and also majority of all produced fragments. The range of the primary particles was determined from the energy loss calculations. The curve describing the stopping power of the projectiles is known as the Bragg peak curve. Three independent codes were used to calculate the range-area position:

> ATIMA

> SRIM (with Monte Carlo module TRIM)

> FLUKA

Simulations were following the ion beam path very closely from the moment of extraction from the accelerator. The beam with nominal energy measured at SIS-18 is extracted through a 100 µm-thick vacuum window made of stainless steel. Also it passed through a 60 cm air gap between the beam-pipe and the target station. The energy loss in the air gap and vacuum window depends on the primary particles species and also on their nominal energy. For this reason, the range calculation was performed for every experiment individually. The input file for the FLUKA code requires beam settings and irradiation parameters. The beam profile was estimated to be circularly shaped with a Gaussian distribution and a full width at half maximum (FWHM) of 1.5 cm. The targets were cylinders with a diameter of 5 and 10 cm and different thicknesses between 0.5 cm and 5 cm. Since the energy loss is a statistical phenomenon, fluctuations (also called straggling) of primary-projectile ranges are expected [75]. Results of ion-transport programs are shown in the following Table 3.

Table 3: The range and the range straggling of uranium and xenon beams of different energies in aluminium targets. Energy losses of the primary particles in the vacuum window and in the air gap were taken into account.

		ATIMA	SRIM	FLUKA
Range [mm]	^{238}U 200 MeV/u	3.722 ± 0.003	3.874 ± 0.010	3.442 ± 0.004
	^{238}U 125 MeV/u	1.621 ± 0.002	1.716 ± 0.008	1.382 ± 0.001
	^{124}Xe 300 MeV/u	10.300 ± 0.011	10.382 ± 0.026	10.070 ± 0.001

An important difference between the employed software is the interaction apparatus, where only the FLUKA code calculates the influence of inelastic nuclear collisions. For this reason, results provided by FLUKA are considered as most reliable [87].

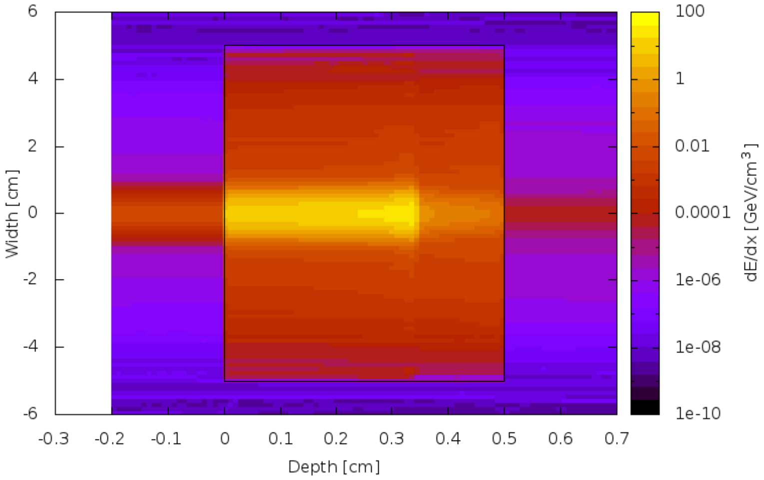

Figure 6: An example of the stopping power distribution in the horizontal plane calculated by FLUKA for the case of ^{238}U ions with the nominal energy of 200 MeV/u penetrating through the air gap and the aluminium target.

3.1.3 EXPERIMENTAL TARGETS

The study of nuclide production as a function of depth is possible only if the measurement of the radioactivity at different positions along the trajectory of the incident ions in the target is possible. Slicing of the target into a number of foils allows measuring gamma spectra of individual layers. From the stopping power calculations it is known that most of the primary ions penetrate into the range area (see Figure 7). The region around the Bragg peak has priority in our research because some of the fragments are detectable only in the narrow depth interval. For this reason, thinner foils are placed in range areas. The residual activities do not change drastically in downstream and upstream regions of the range area and, thus, the high-resolution is not necessary for the entire target [23].

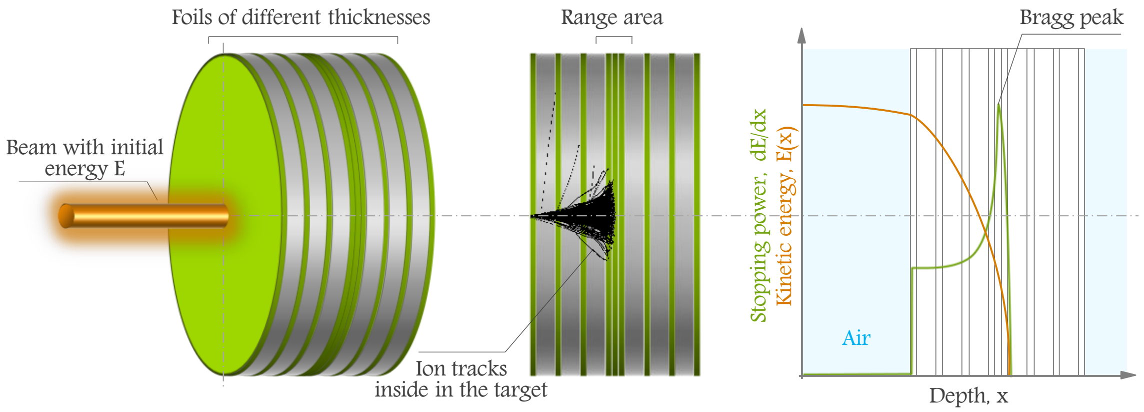

Figure 7: Schematic representation of the experimental targets used for activation study. The foils with different thickness were used for better resolution of the depth profiles and precise location of the range area. The diagram on the right side is showing the kinetic energy of the primary ions as a function of depth, as well as the maximal stopping power (Bragg peak) located in the range area.

High-purity materials were used as targets to avoid additional production of nuclei by the interaction of the heavy-ion primary particles with elemental impurities. The targets were made of 99.95% natural aluminium (ρ = 2.70 g/cm^3 at 20 °C) and were designed as cylinders with a diameter of 5 cm and 10 cm. The bigger target size has been chosen for the activation by uranium beam in order to avoid possible beam-focusing issues of the uranium beam which have been observed in the first experiment. This update of the target geometry was considered as an indispensable step for preventing the same problems in the case of the repeated experiment. The targets were assembled from many foils of different thicknesses or foils of equal thickness organized in groups of a few foils. The thickness of the foils was chosen in a way that the activation depth profiles had a good resolution in the range area and that the self-absorption of the gamma quanta in the foil could be neglected. The same aspects were taken into account for sampling the foils by arranging them into small groups made of 3-5 individual foils. In further analysis such a group of samples were perceived as another individual foil with a thickness equal to a sum of thicknesses of all grouped foils in those samples.

The high number of activation foils in the target can be unsuitable for other analysis. The capacity of the one HPGe detector is restricting the total number of samples possible to measure successfully because there is only a limited time before the nuclides decay. For example, 73 activation foils, used in the experiment of irradiation of the aluminium target by xenon beam, were decreased by grouping them into 41 samples.

3.1.4 IRRADIATION OF THE TARGETS

All experiments were performed from the main control room at GSI. A couple of CCD cameras and two movable platforms with remote control options installed at HHD cave allow a complete irradiation experiment without entering the radiation controlled area. A schematic representation of the experimental area is displayed in Figure 8 and photography is shown in Figure 5. During all experiments, the synchrotron SIS-18 was working in the fast-extraction regime with the beam pulse repetition time of 2-3 seconds [127]. The irradiation of targets was scheduled as parasitical beam-time experiments at SIS-18 which means that beam pulses were addressed to different experimental stations and individual pulses were distributed in a certain ratio controlled by the operators of the synchrotron. Energy and stability of beam were controlled permanently and parameter as beam intensity was recorded after each beam pulse.

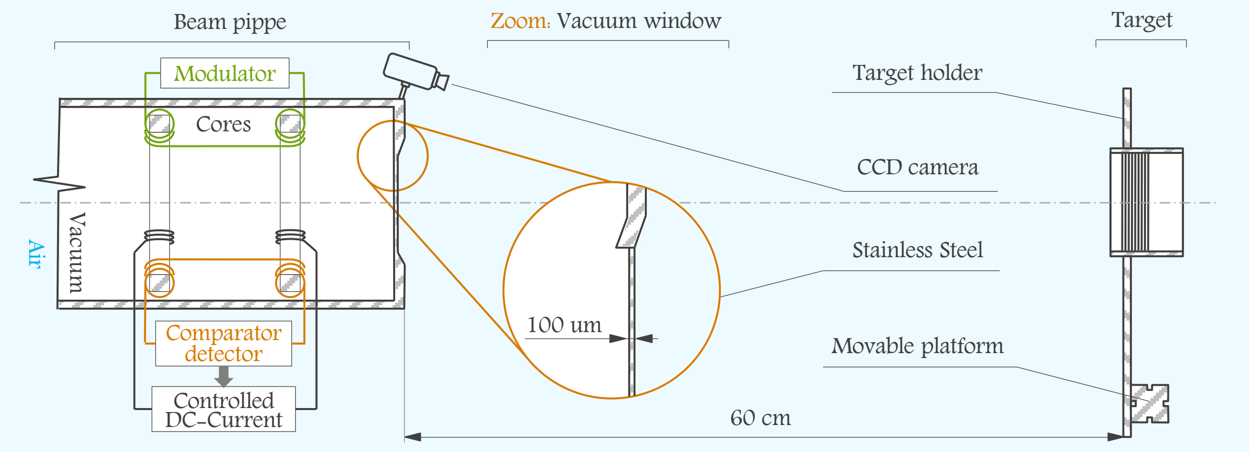

Figure 8: A schematic of the irradiation area with installed control and diagnostic tools. (Side view)

MEASUREMENT OF THE TOTAL NUMBER OF IONS

The beam intensity is crucial parameter for a precise repetition of experiments by simulations. The direct measurement of the number of ions in each beam pulse is technologically not possible without damaging the beam. One of the available options is the measurement of the beam charge of each pulse. The total number of ions can be easily calculated by using the measured value of the accumulated charge Q_{acc} at the end of the irradiation and by the following Equation (17):

$$N_{TOI} = \frac{Q_{acc}}{q_e \cdot q_{ion}} , \tag{17}$$

where N_{TOI} corresponds to the Total number of Ions, q_e is the electron charge and q_{ion} is the charge state of the ion beam [126].

At GSI, ion beam intensities are usually observed and measured using various types of DC current transformers (DCCT), adjusted to the special requirements at their location in accelerator facilities. DCCTs can be used for beam monitoring during the acceleration process, as well as for measurements of intensity decreases during the extraction. A DCCT includes two ring cores with a set of opposite windings with a frequency modulation (see Figure 8). The induced signal is detected by the secondary winding. When a DC ion beam penetrates the two toroids with identical magnetic characteristics, the hysteresis curves of the ring cores become asymmetric, because of the magnetic field around the ion beam. This asymmetry is corrected for by a feedback loop, and the compensation current is a measure for the beam current. The uncertainty of the DCCT is estimated to about 3% [126, 128, 129]. Data from DCCT are available during irradiation via NODAL code [130], where the intensity of the beam is displayed as charge after each pulse. The time of the pulse detection, the charge of ion beam per pulse and the accumulated charge were recorded during the entire beam-time. Recorded values were converted to the number of ions per pulse and the accumulated number of ions by using the Eq. (17). An example of the irradiation history of one of the experimental targets is given in Figure 9 and the irradiation parameters of all experiments are summarized in Table 4.

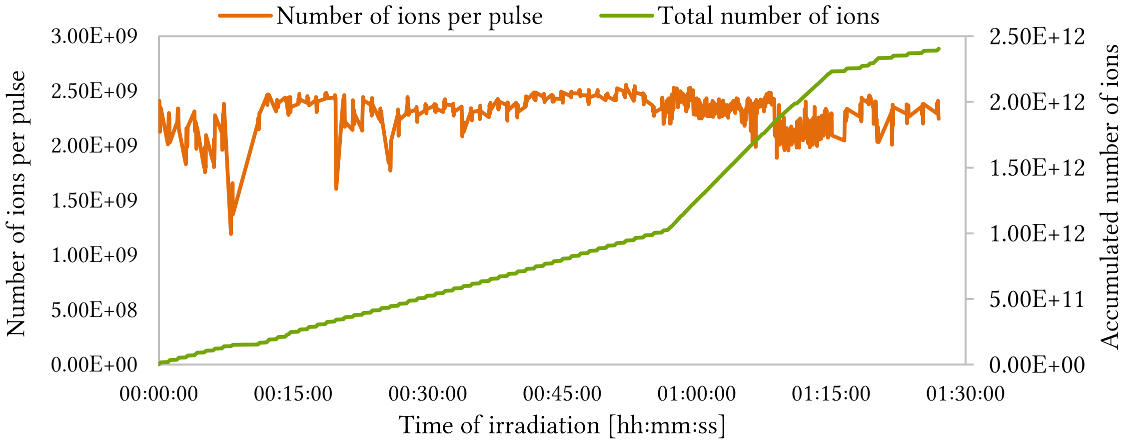

Figure 9: An example of the beam current measurement (after recalculation into a number of ions) recorded during irradiation of the aluminium target by $^{124}Xe^{+48}$ ions beam with an energy of 300 MeV/u.

Table 4: Irradiation parameters obtained by CD current transformer measurements during irradiation

		Beam charge state	Irradiation time hh:mm:ss [sec]	Accumulated charge [C]	Total number of ions
Beam	^{238}U 200 MeV/u	+73	03:58:33 [14313 s]	3.34×10^{-5}	2.86×10^{12}
	^{238}U 125 MeV/u	+89	02:13:57 [8037 s]	1.69×10^{-5}	1.18×10^{12}
	^{124}Xe 300 MeV/u	+48	01:27:00 [5220 s]	1.91×10^{-5}	2.49×10^{12}

MEASUREMENT OF THE BEAM SPOT SIZE

The measurement of beam parameters such as beam position, shape irregularity and strength of focusing is important for a precise setting of the values in the simulation input files. There are several locations within the beam line where beam diagnostics equipment is installed. Nevertheless, the distance between the last diagnostic point and the experimental target is several meters. In addition, the ion beam is extracted through the vacuum window and is transported through the air gap which results in a defocusing of the beam. Under these circumstances, an additional beam diagnostic at the target position is required. Two different techniques were used:

- Imaging of the beam on an inorganic scintillator monitor
- Capturing of the beam spot on an organic foil

THE SCINTILLATION SCREENS

A scintillating screen was used as a first step of the relative beam-spot size and position monitoring. The monitor principle relies on the fact that charged particles crossing the screen material deposit energy which is converted into detectable light. The resulting photon emission leads to a direct image of the spatial distribution of the particle beam (beam spot) and can be measured with standard optical techniques

[134, 135]. The beam profile monitors are made of alumina (Al_2O_3) ceramic material and they are fabricated with a grid structure (a profile-meter) on the surface with the resolution of 1 cm (see Figure 10). The live view on the scintillating screens is provided by two CCD cameras placed on the top of beam-pipe in the HHD cave as shown in the Figure 8. The Bosch NBC-455 Dinion Color Camera is used for a detailed view of the scintillating screen or experimental target during irradiation. The second CCD camera CONRAD-420TVL with broad view angel is monitoring big part of the beam-dump area and all positions of the movable platform supporting the target holders. The signal from both cameras was transited to the main control room via cabling network system at HHD cave.

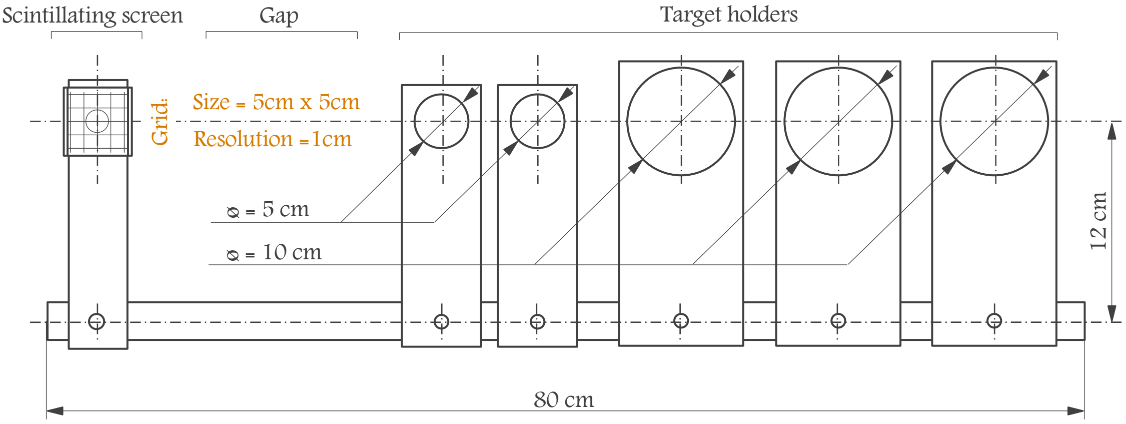

Figure 10: Schematic picture of the installation layout of targets on the movable platform. (Front view).

The calibration of the beam focusing was performed in the accelerator mode of low-intensity beam, where the intensity reaches only small fraction of the actual setting used during target activation. Using the full intensity of the beam the number of photons produced by the scintillating screen causes the CCD sensors to saturate, which is preventing any observation of the beam. The inaccuracy of this method is rather big as it is concerning the naked eye observation of fast events. The beam spots measured with this technique differ about 0.5 - 1.0 cm compared to the values measured using organic foils, as it is shown in Table 5. However, it would be impossible to align the centre of the ion beam to that of the experimental targets without using the scintillation screen.

THE ORGANIC FOILS:

The advantage of using organic foils to analyse the beam parameters lies in the permanent capturing of the spatial distribution of the beam. 20 μm thick polyimide (Kapton) foil 10 μm thick polycarbonate (Pokalon) foils were used because of their radiation resistance attribute. Organic foils are changing colour proportionally to a dose of radiation they absorb [136, 137]. The precise location of a beam spot is visible as a dark area. Organic foils were attached to the surface of the first foil. The importance of this technique was proven during the first experiment, where focusing of the beam changed during the irradiation due to a fluctuation of the strength of magnetic field in focusing magnet. The beam spot on the Pokalon foil was the only available evidence of an expansion of the beam spot, which was earlier controlled by the scintillating screen. Figure 11 – Foil B shows that the size of the beam was bigger than the size of the target.

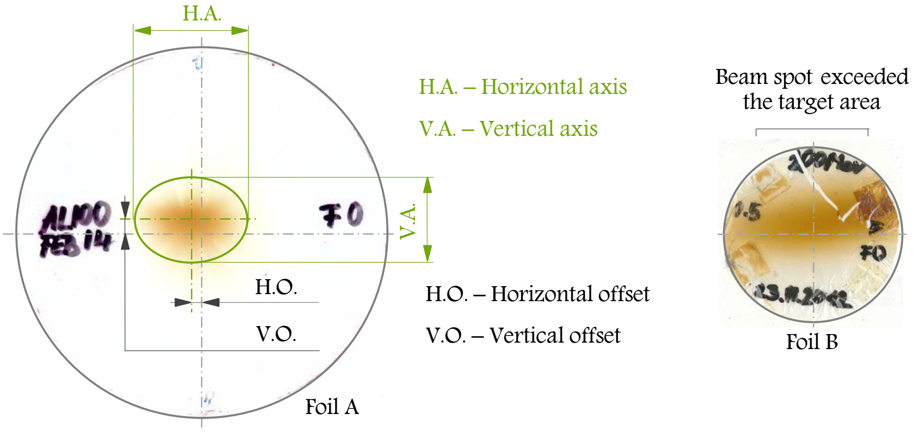

Figure 11: Organic foils used for beam spot measurement. Foil A is showing the real beam spot of ^{238}U with an energy of 125 MeV/u. Foil B is the organic foil from the activation of target by ^{238}U with an energy of 200 MeV/u.

The measured sizes of the beam spots from several experiments are collected in the following Table 5. An offset of the beam spots is defined as the distance from the centre of the target which is located in the plane origin.

Table 5: Beam spot measured on the scintillation screen and on the organic foils as well as the offset of the beam spot from the centre of the targets measured on the organic foil.

		Horizontal axes x Vertical axes [cm]		
		Scintillation screen	Organic foil	Offset from the centre
Beam	^{238}U 200 MeV/u	4.0 x 2.0	3.4 x 3.0	0.3 x 0.1
	^{238}U 125 MeV/u	2.5 x 2.5	3.3 x 2.5	-0.3 x 0.3
	^{124}Xe 300 MeV/u	1.0 x 1.0	1.5 x 1.0	0.7 x -0.2

3.1.5 GAMMA SPECTROSCOPY

Gamma spectroscopy methods were used to identify fragments produced in the experimental foils and to determine their residual activities [138]. A great number of gamma-ray spectra were measured. In particular, about 1000 spectra were acquired for the purposes of the activation study presented in this work. A well-structured database with an unambiguous naming of the gamma-ray spectra was established. A unique and an immutable name was assigned to each spectrum. For instance, "Al300MeVXe-F5-7cm_2.spe" represents an Aluminium target irradiated by a xenon beam with an energy of 300 MeV/u. The spectrum belongs to foil No. 5 and was measured in distance of 7 cm from the detector surface in the 2nd set of measurement. There will be several examples of gamma spectra with such abbreviated names introduced on the following pages.

The semiconductor detector (Canberra® HPGe – GC3518) is powered by a high-voltage power supply (Ortec HV-Supply) at an operating voltage of 4000 V. The energy resolution of this detector was estimated as the full width of maximum (FWHM) of 1.8 keV at the 1332 keV ^{60}Co gamma-line. The detector was coupled to a spectrometer (ORTEC® DESPEC LF ™) using 8192 channels. The detector was mounted in a vacuum chamber which was attached to a Dewar flask (cooling medium was liquid nitrogen at 77 °K), in order to protect the sensitive detector surface from moisture and contamination [139, 140]. The graphical interface of the GammaVision® software (Model A66-B32) was used to control the multi-channel analyser and to record the measured spectra from 30 keV up to 2.5 MeV [141].

The energy and efficiency calibration of the detector were frequently repeated every 2-4 months, usually on beginning of the measurement of each set of samples. A set of calibration sources (^{22}Na, ^{60}Co, ^{137}Cs, ^{133}Ba, ^{152}Eu, ^{210}Pb and ^{241}Am) with certified accuracy ≤ 2 % was supplied by the radiation safety department at GSI. All calibration sources and foils were measured at a distance of 7 cm from the detector surface. Several efficiency curves measured within the past four years are shown in Figure 12 clearly showing the stability of the detector performance. The residual activity was studied at several time points after the end of the irradiation. The downtime between two measurements was often several months. Non-stability of the high-purity germanium crystal structure, the electronic power supply or the control equipment may contribute to uncertainties of the measurements.

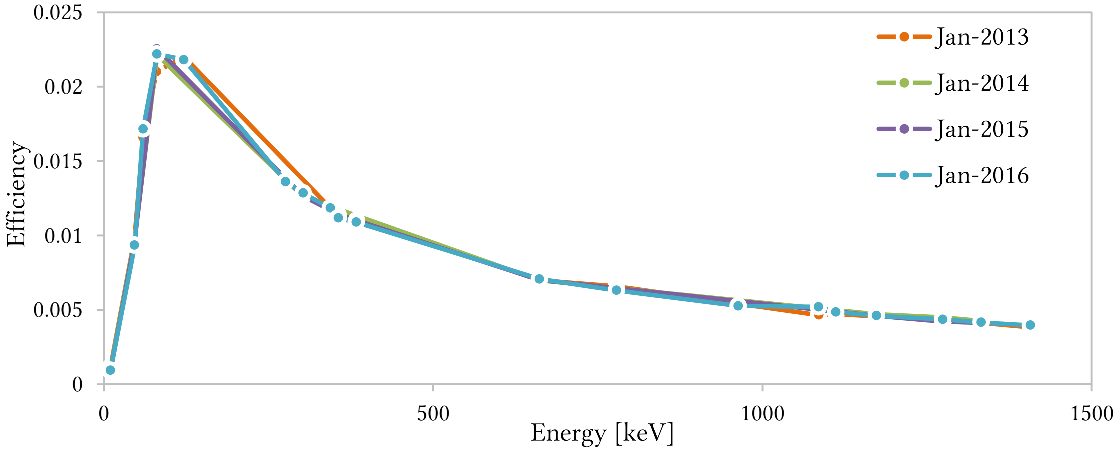

Figure 12: Examples of efficiency calibration curves. There is no noticeable change of efficiency after 4 years permanent usage of the detector Canberra HPGe – GC3518.

The gamma-ray spectra were measured in the low-background chamber shielded by iron walls. Nevertheless, the background spectra were measured every six months for a minimum of three days to have an overview of its influence on the gamma spectra. A background extraction procedure was either done manually within the spectra analysis or automatically by the competent analysis features included in the GammaVision software [141]. An example of how the background influences the measurement of the samples is presented in Figure 13. The picture shows the count-rate of the gamma spectra, which allows comparing peaks even their acquisition times differ significantly. Several peaks marked in the rectangles are the typical cases when the background peak is pronounced in the spectrum without affecting the count-rate caused by any radioactive nuclide induced in the sample. Thus, the gamma peaks of the background (orange) are overlapping the gamma peaks recorded from the sample (green). In the same figure are shown also examples of the ^{133}Ba and the ^{103}Ru nuclides, where the gamma peaks from the sample's gamma spectra are higher than the gamma peaks with the same energies (or very similar energies) obtained from the background measurement. In such cases it is necessary to adjust the number of counts in the Net-Peak-Area before the measured data may be used for the quantification of the radioactivity.

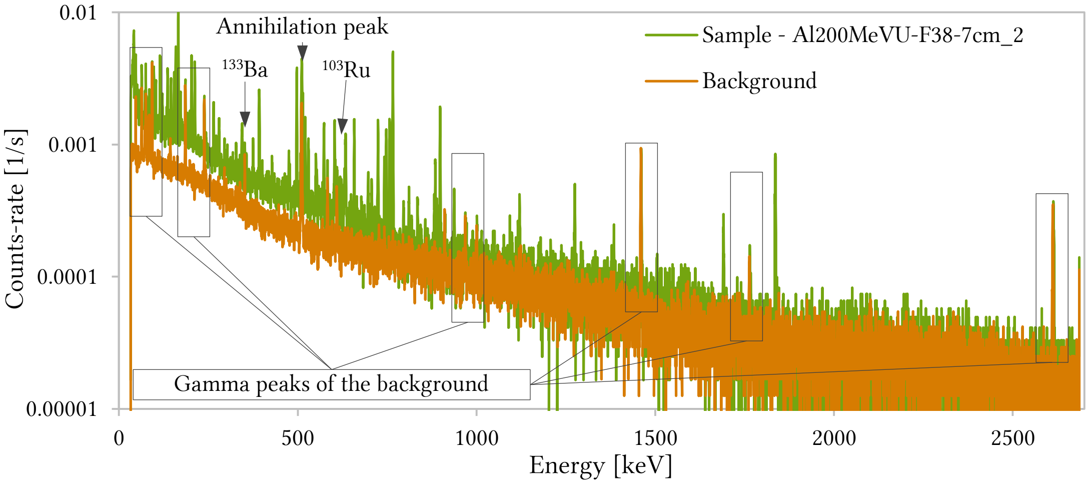

Figure 13: Gamma spectra of foil no. 38 consisting of an Aluminium target irradiated with a 200 MeV/u uranium beam measured the second time after irradiation (green) compared to the background gamma spectrum (orange).

The gamma-ray spectra were recorded as soon as the dose rate allowed for the safe handling of the samples and the access to the beam dump area was granted. Wipe tests of each target were executed to check for a possible contamination of the surface. In order to distinguish between short-lived and long-lived isotopes in gamma spectra analysis as well as to increase the recording precision, the gamma-ray spectra were recorded at different time-points. For this reason, the samples were measured multiple times: several days and a few months after the end of the irradiation (Table 6). The acquisition time of the gamma-ray spectra fluctuated between several hours up to a few days depending on count-rate detected from a sample.

Table 6: The time period between the end of the irradiation and the recording of the gamma-ray spectra for foils irradiated with different beams.

		Time after the end of the irradiation [days]		
		1st set	2nd set	3rd set
Beam	^{238}U 200 MeV/u	6 - 22	133 - 180	
	^{238}U 125 MeV/u	16 - 34	128 - 144	260 – 285
	^{124}Xe 300 MeV/u	9 - 38	218 - 293	378 – 505

Long-lived nuclides are often not well pronounced in those gamma-ray spectra that are obtained shortly after the end of the irradiation because of a large number of short-lived nuclides. Nuclides are not distinguishable by a spectrometer and pile up into a single peak within the gamma spectrum when the difference between the energies of detected gamma quanta is smaller than the energy resolution of the detector. The ratio of individual contributions of two or more nuclides in one peak is difficult to calculate. In the case of very complex spectra it is also possible that several peaks are produced by many nuclides. Assuming that the nuclides under investigation have different half-life times, a measurement of the one sample at several decay times is a feasible solution. The count-rate of the background is decreasing with time according to the short-lived nuclides decay. For this reason, some of the long-lived nuclides are observed only in later recorded spectra. Figure 14 demonstrate the importance of the repetition of the gamma-ray measurements, where a number of the gamma-ray peaks is significantly decreasing due to the longer cooling-time of the later acquired spectrum. The life-time of the data acquisition of both gamma spectra was about 14 hours and they differ only about 15 minutes, which is a negligible time period in respect to the cooling-time between the sets recorded 20 and 415 days after the irradiation. For this reason it is possible to compare the number of the counts of gamma peaks without any additional correction factor.

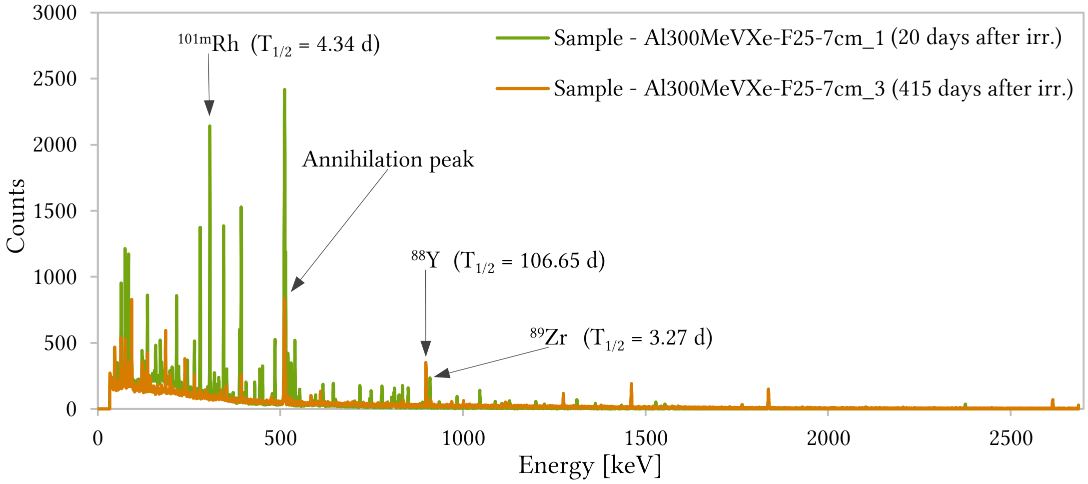

Figure 14: Two representative gamma-ray spectra of foil no. 25 from Aluminium target irradiated by 300 MeV/u ^{124}Xe beam measured after 20 days (green) and after 415 days (orange) after the end of the irradiation. There are noticeably fewer peaks in the orange spectrum because of the decay of short-lived nuclides.

Figure 14 shows two gamma peaks produced by the ^{89}Zr ($T_{1/2}$ = 3.27 d, E_γ = 908.6 keV, I_γ = 100 %) short-lived nuclide and the ^{88}Y ($T_{1/2}$ = 106.65 d, E_γ = 898.6 keV, I_γ = 93.7 %) long-lived nuclide. They are located close to each other which influenced the earlier set of the measurement (green). For this reason it is possible to use the acquired data of the ^{88}Y nuclide only from the later set of the measurement (orange). In similar manner, a well pronounced peak produced by the ^{101m}Rh ($T_{1/2}$ = 4.34 d, E_γ = 306.85 keV, I_γ = 81.0 %) nuclide is visible in the earlier spectrum. The number of counts recorded in the first set of the measurement is about 2000 in the channel corresponding to the maximum of the gamma peak, but it is completely missing in the later measured set. Such a fast disintegration of the short-lived radionuclides is noticeable in the case of many other short-lived nuclides with gamma lines from the energy range between 0 and 500 keV. The last example presented in this picture is the case of the annihilation peak whose number of counts is about two-thirds smaller for the later measured spectrum compared to the earlier measured spectrum.

The target foils were separated into two regions according to the position of the foils within the target. The first region is defined as the foils upstream of the range of the primary particles and the second region contains the foils downstream of the range of the primary particles. Examples of gamma-ray spectra of one foil from the region upstream and downstream of the range of the primary particles are shown in Figure 15 and Figure 16, respectively. It is noticeable that the number of peaks is different for both spectra (the effect of short-lived nuclides is negligible because both spectra were measured with a time difference of only 9 hours). A spectrum of the foil from the first region (Figure 15: foil F1, located at 3.2 mm upstream of the range) contains fewer peaks compared to spectrum obtained from a position behind the projectile range (Figure 16: foil F38, located at 0.3 mm downstream of the range).

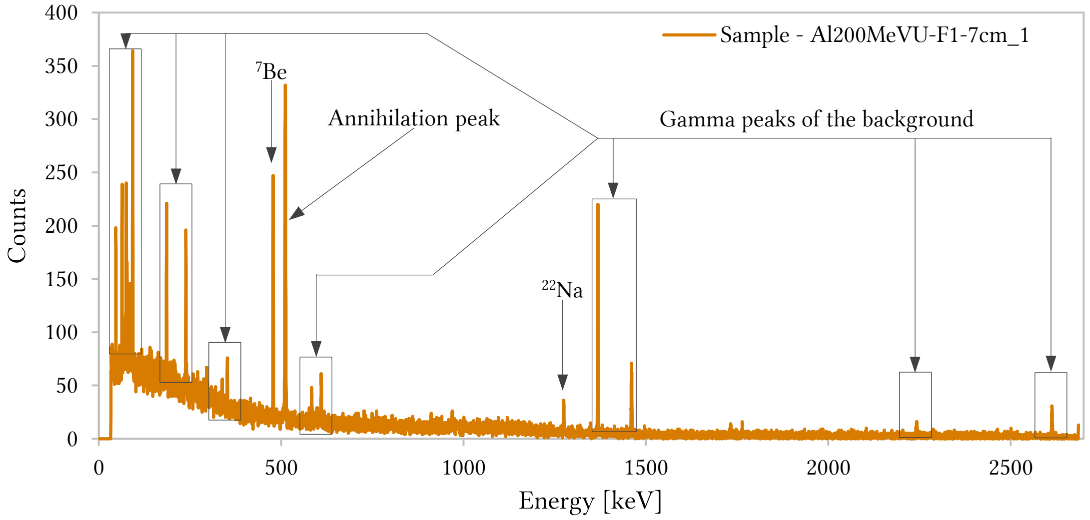

Figure 15: The gamma-ray spectrum of aluminium foil no. 1 located at 3.2 mm upstream of the range of ^{238}U ions with an energy 200 MeV/u (depth in the target = 0.25 mm)

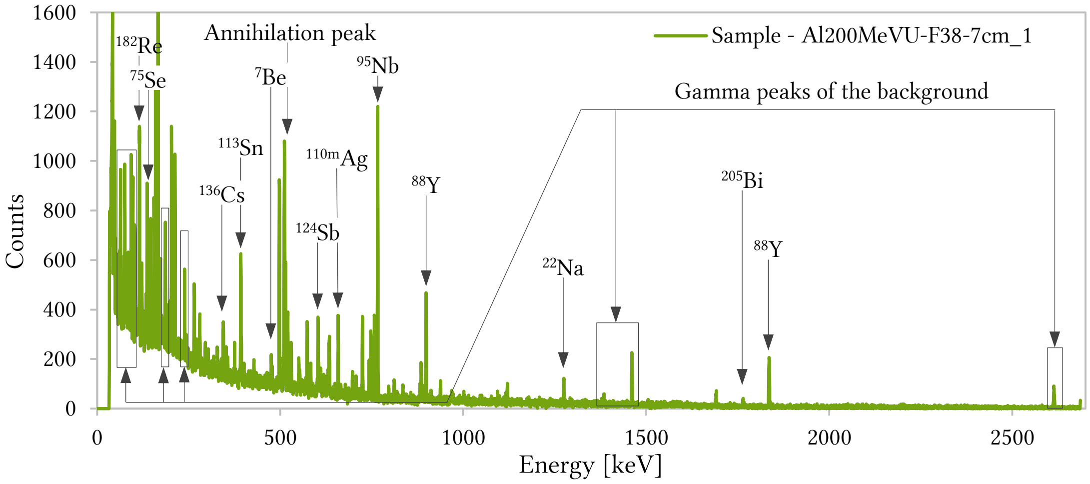

Figure 16: The gamma-ray spectrum of aluminium foil no. 38 located at 0.3 mm downstream of the range of ^{238}U ions with an energy 200 MeV/u (depth in the target = 3.75 mm)

The region upstream of the range contains products of the target activation (^{7}Be and ^{22}Na), the annihilation peak and the gamma peaks of the background as it is displayed in Figure 15. Whereas the region downstream of the range contains both products of the target activation by secondary particles (^{7}Be and ^{22}Na) as well as the projectile fragments (e.g. ^{75}Se, ^{88}Y, ^{95}Nb, ^{110m}Ag, ^{113}Sn, ^{136}Cs, ^{182}Re and ^{205}Bi) together with the annihilation peak and the gamma peaks of the background, see Figure 16. The comparison of those two figures is representing a different number of induced nuclides in the foils upstream and downstream of the range area at the first place. But it is also possible to follow the increase in the background radiation due to greater amount of the induced nuclides. The level of the background radiation yields to 100 counts in the first case, but it is about a factor 6 higher in the second case. It is also interesting to compare the ratio between the gamma peaks produced by the ^{7}Be nuclide and the electron-positron annihilation. The maximum value of the gamma peaks of the ^{7}Be nuclide and the annihilation peak amount to 247 and 332 counts, respectively, in the gamma spectra of the foil no. 1. Whereas the same gamma peaks achieve 218 and 1080 counts, respectively, in the gamma spectra of the foil no. 38.

ANALYSIS OF THE GAMMA-SPECTRA

Gamma-spectroscopy analysis [138, 141] was performed in order to define types and to quantify amounts of the produced nuclei after the irradiation. It was the most time-consuming part of the present study. The evaluation of the gamma spectra is a complicated task because of an enormous complexity of the measured spectra. In some recorded spectra, several hundred gamma lines were found in some of the spectra. This is a typical situation for heavy-ion beams interacting with constructing materials of accelerators. It was reported that more than 600 different radioactive nuclides were produced by the fragmentation of a ^{238}U beam [28]. A combination of radioactive projectile fragments and radioactive target nucleus fragments creates a very extensive distribution of gamma lines in spectra. A great number of short-lived nuclides with multistep decay schemes are detectable shortly after the end of the irradiation. Although the spectra become less complicated after the decay of short-lived nuclides, but the complexity of the investigated spectra remains still rather high because of long-lived nuclides. Often, they have various decay schemes or decay further to short-lived daughter nuclides decaying in a similar manner as the parent nuclide [6]. Here, each gamma-line in every single spectrum was studied as a unique peak. In many cases, there were several nuclide candidates producing a gamma-quantum with similar energy, but not necessarily with the same depth distribution. For this reason, the identification of nuclide producing one gamma-peak was not straightforward for all spectra of the same experimental target and repetitive identification of possible gamma-line producers was needed.

The identification of the radioactive nuclides was done in several steps based on the following aspects:

> FLUKA simulations of each experiment have been provided in order to gain an overview about the nuclides produced in the target. There was a great number of 1500 to 2000 radioactive nuclides predicted by Monte Carlo simulations. The list of possible radioactive nuclides was reduced significantly after neglecting those with very short half-life time with respect to the start of earliest possible measurement and after exclusion of those which are not emitting gamma-quanta. The results of the simulations were about 300 radioactive nuclides candidates detectable by the chosen experimental technique.

> The identification of the nuclides was based on the energy of the gamma line, its half-life and the relations of the gamma emission probabilities using several databases and libraries of radioactive nuclides and decay schemes [142-145].

> The list of nuclides as possible producers of each gamma line in spectra was elaborated. For those candidates which have several gamma lines with different energies, peaks of all significant gamma quanta in the same gamma spectrum were searched for. If only some of the gamma lines were observed (e.g. 3 out of 5), those nuclides were removed from the list of the candidates.

- An induced activity of some long-lived nuclides was determined only from the latest set of the gamma-spectra measurements if the earliest experimental data were affected by another nuclide and if it was confirmed that no other nuclide is contributing to the production of the gamma peak. This allowed for determining the contribution of such a nuclide in earlier measured spectra and extracting a number of counts in the gamma peak if this was issued by the contribution of the nuclides with different half-life times. Thus, the quantification of the residual activity of a short-lived nuclide was also possible under these circumstances.
- Radioactive nuclei are produced not only directly in nuclear reactions, but also through decays of other radioactive nuclei or de-excitation of isomeric states. A number of radioactive daughter nuclei of interest could not be calculated at the end of the irradiation using the Eq. (18)

QUANTIFICATION OF THE RESIDUAL ACTIVITY INDUCED INSIDE THE TARGET

For each foil, the partial activity of each isotope was obtained from the Peak-Net-Area (PNA) determined by the GammaVision software, including uncertainties [141]. Each spectrum was measured at a different time after the end of the irradiation due to availability of only one HPGe detector. For a better comparability of the presented results, all measured activities were extrapolated backward to the end of the irradiation by using exponential decay curves available for each nuclide with known half-life time. Due to the non-zero probability of nuclide creation by the decay of nuclides into daughters, the real residual activity is lower by about the activity of the daughter nuclides, which were produced and measured during the cooling time and they had not been present in the target before the measurement. Consequently, the assumption that all nuclides are produced exclusively by primary projectiles during ion irradiation leads to an overestimation of the induced radioactivity. Nevertheless, this simplification is tolerable for the purpose of our study, because an acceptable overestimation of residual activity in developing materials for accelerator parts is increasing the radiation safety. Generally speaking, an overestimation is preferred to an underestimation in terms of safety.

The activity of the accurately identified nuclide at the end of irradiation A_{EOI} is calculated from the radioactivity decay law [146] by

$$A_{EOI} = \frac{PNA(E_\gamma)}{T_L \cdot I_\gamma(E_\gamma) \cdot Eff(E_\gamma)} \cdot D_C \qquad [Bq]\,, \tag{18}$$

where PNA(E) corresponds to Peak-Net-Area of the peak of gamma spectrum at the energy E_γ, T_L is the Live-Time of the acquisition, $I_\gamma(E_\gamma)$ is the probability of a gamma quantum emission of E_γ according to the decay scheme of the investigated nuclide, $Eff(E_\gamma)$ is the absolute detector efficiency (at E_γ) and D_C is the decay correction factor. $Eff(E_\gamma)$ is supposed to specify the number of the full-energy deposition of E_γ in the detector per gamma-quantum of E_γ emitted by a sample. D_C essentially converts the nominal count rate to the count rate at the end of the irradiation and is derived assuming the dead time is constant during the counting period. As such, it is an approximation that is valid only for materials whose half-life is long with respect to the live time of the measurement [146].

$$D_C = e^{\lambda \cdot T_{TM}} \cdot \frac{e^{\lambda \cdot T_R}}{1 - e^{-\lambda \cdot T_R}} \tag{19}$$

The decay correction contains two different adjustments. The first one is projecting the measured activity of the radioactive nuclide back to the moment at the end of the irradiation by considering the Time-To-Measurement T_{TM} as an exponent of the exponential function. A precise value of T_{TM} is calculated for each gamma spectrum as the time interval between the end of irradiation and start of a gamma spectroscopic measurement of the chosen spectrum. The second part of the correction is accounting for the correct admittance of the nuclei decayed during the data acquisition to the total number of decayed nuclei by using the Real-Time T_R of the measurement of the given gamma spectra as an exponent of the decay function [146]. The decay constant λ is another variable changing for each nuclide and it is calculated as

$$\lambda = \frac{ln(2)}{T_{1/2}}, \tag{20}$$

with $T_{1/2}$ being the half-life of the decaying radionuclide.

The unit of residual activity calculated by equation (18) is the Becquerel (Abbreviation - "Bq"). It is necessary to use a unit which will make the calculated values independent of the different properties of each foil (in the case of comparing of samples from the same target) and of the individual irradiation settings (in the case of comparing between different experiments). For this reason, an additional normalization of the residual activity at the end of the irradiation, $A_{EOI-NORM}$, is reasonable for further comparison of experimental results. It writes as

$$A_{EOI-NORM}\,[Bq/mm/ion] = \frac{A_{EOI}\,[Bq]}{N_{ION}\cdot T_C}, \tag{21}$$

where T_C is the thickness of the sample and N_{ION} is the total number of primary ions accumulated during the irradiation of the sample. The residual activity of each observed nuclide was calculated. The resulting activity is assumed to be located in the centre of the corresponding target samples. Collecting these information for each sample, detailed depth profile of the residual activity of each investigated radioactive nuclide is obtained. A representative depth profile is presented in Figure 17 showing the residual activity of samples as orange circles. The dark green line is a curve fitting the activities acquired from the samples and represents the activity as a function of depth. The light green area represents the induced activity in the target.

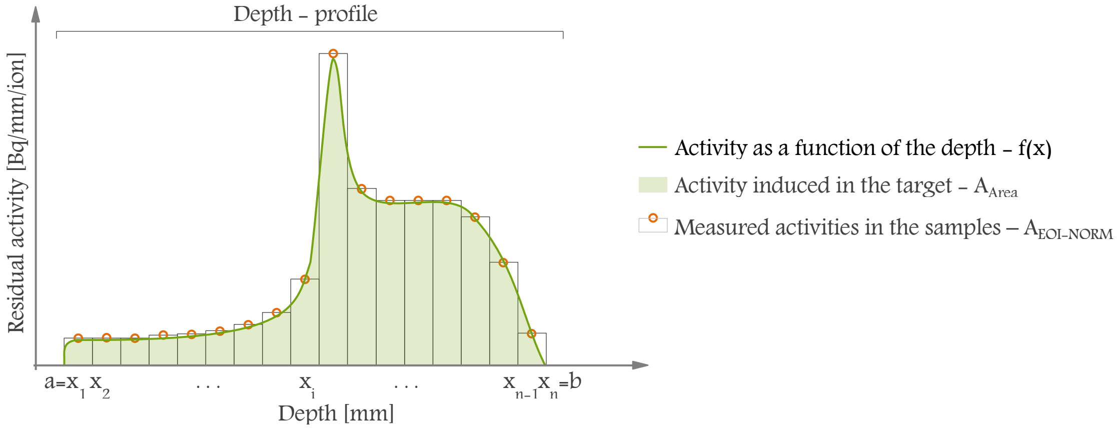

Figure 17: A representative depth profile of the residual activity as a function of target depth. The area under the green curve evaluated by numerical integration corresponds to the induced activity in the target.

The depth profiles of the residual activity induced by an ion beam in the material have various shapes. The integration of a function describing the distribution of an activity in the target is applicable for the quantification of the total residual activity of individual radioactive nuclides:

$$A_{Area} = \int_a^b f(x)\, dx \qquad (22)$$

The rectangular integration method of the depth profile shape was used to approximate the area of a function on a graph. This method was inspired by the (Midpoint rule) Riemann sum. The sum is calculated by dividing the region up into rectangular shapes that together form an area that is similar to the region being measured experimentally. The width of rectangles is determined by the interval of integration which corresponds to the thickness of the measured samples. The height of rectangles corresponds to the measured value of the residual activity in the middle of the sample and is defined as the value of the function at the midpoint of its base.

$$A_{Area} = \int_a^b f(x)\, dx \approx \sum_{i=1}^{n-1} (x_{i+1} - x_i) \cdot f\left(\frac{x_{i+1} + x_i}{2}\right) \qquad (23)$$

Within a fixed interval, the approximation of the integration becomes more accurate as narrower rectangles are used which better represent the values of the function [147, 148]. This confirms that assembling of many thin foils in an experimental target is an adequate approach for quantifying and reconstructing of the residual activity.

It should be emphasised that the determination of the residual activity was not possible in cases of all identified radioactive nuclides (or in cases of all energy lines of investigated nuclides). The short-lived isotopes exhibit radioactivity below a minimum detectable activity (MDA). This situation occurs for some isotopes which were quantified in the early measured sets of gamma spectra, but which were not present after the end of the irradiation. . Another example for an impossible quantification of the residual activity beyond possibilities of the experimental setup is the case of gamma peaks corresponding to long-lived nuclide, but that are corrupted by a great number of gamma peaks belonging to short-lived nuclides. For this reason, the determination of their activities is possible only in gamma spectra that are not affected by short lived-nuclides.

3.1.6 UNCERTAINTY ASSESSMENT

The accuracy of the experimental method used for studying the residual activity induced in accelerator materials is determined by the accuracy of all parts of the experiment and by the devices used to record experimental data. Several factors play roles that are summarized as follows:

- The thickness of the activation foil. The thickness is measured with an uncertainty of less than 0.5%.
- The total number of ions accumulated during the irradiation was measured by DC current transformers with an uncertainty of 3 % (specific for this instrument at GSI Darmstadt).
- The absolute efficiency of the HPGe detector used for recording all gamma spectra. In the process of efficiency calibration the uncertainties of several components are considered.
    - The uncertainty of the calibration source with a certified relative standard-uncertainty of less than 2 %
    - The uncertainty of the peak net area of less than 2%
    - The Uncertainty of the curve fitting which depends on the energy and varies from 1% to 7%.
- The uncertainty of the Peak-Net-Area was estimated by the Gamma-Vision 32 software and it depends on the number of counts recorded in the peak area and on the peak-to-Compton ratio (the ability of detector to distinguish low energy peaks in the presence of the high-energy gamma quants the Compton background) [149].
- The half-life and the probability of a gamma quant emission. These values and their uncertainties were obtained from the databases in references [142-144].
- The depth uncertainty is interpreted as the uncertainty of the foil position in the target. It can be measured with 0.05 mm precision. The resolution of the experiment is defined by the thickness of an activation foil and its uncertainty, which is measured to be less than 0.5 %.

3.2 SIMULATION OF THE RESIDUAL ACTIVITY DEPTH PROFILES

Monte Carlo calculations provided by the FLUKA code focused on the precise determination of the residual activity. Naturally, the calculation model was simplified in order to decrease the CPU-time. The activation of the irradiated target is affected by anything that is influencing the energy of ions as well as the shape and the focus of the beam. Since the vacuum window and targets are the first high-Z materials the primary particles are colliding with, a shower of secondary particles is expected to be produced mainly within these objects. Consequently, the activation of the target foils by fragments of materials of the target holders and other nearby objects is very improbable and such components are negligible.

A schematic of the applied geometry model is displayed in Figure 18. This image is not scaled because of the wide range of object dimensions between a few micrometers (vacuum window thickness) and a few meters (distance between vacuum window and target). The parameters of the ion beam measured during the experiments were applied at this position. The vacuum window made of the austenitic stainless steel has a thickness of 100 μm and is directly separating the vacuum and the air region. The beam source is located at a distance of about 1 cm from vacuum window within the vacuum. The target is exposed to the irradiation at a distance of 60 cm, analogous to experimental setup. The whole geometry was surrounded by a 10 m diameter spherical region called "Blackhole", which is a fictitious material used to terminate particle trajectories [41].

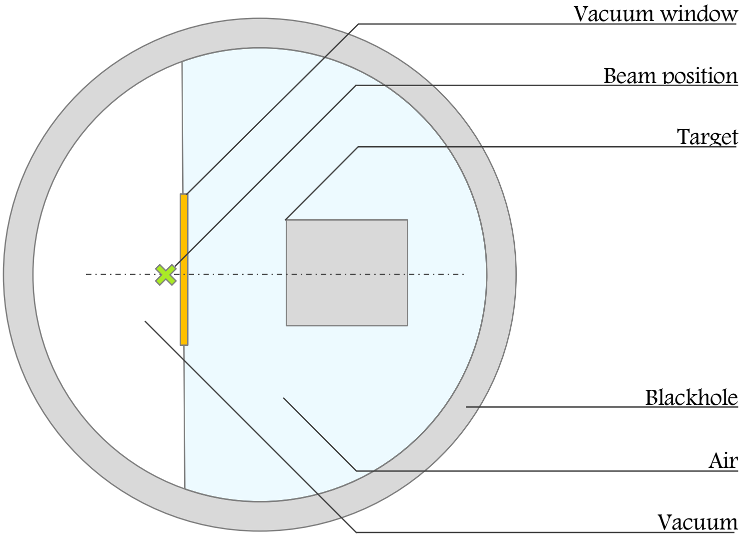

Figure 18: A schematic (not-scaled) of the assigned regions used for the FLUKA calculations. The X-Z plane and the Y-Z plane are identical due to the symmetry of the cylindrical bodies.

In the FLUKA simulations were set in a way that the heavy-ion transport with nuclear interactions and the electromagnetic dissociation was activated for primary ions and for target nuclei. The new evaporation model with heavy-fragment evaporation was also used. Emission of the high-energy light fragments through the coalescence mechanism was considered. The main calculations were provided with a rather high statistics of about 50 million initial seeds. Nevertheless, some of the simulations used as a support of unique observations (e.g. production rate of intermediate-Z fragments, see section 3.5.3) requested an even a higher statistical precision.

3.3 ACTIVATION OF THE ALUMINIUM TARGET BY THE 200 MeV/u URANIUM BEAM

The aluminium target was irradiated in the stacked-foil geometry by a $^{238}U^{73+}$ beam with an energy of 200 MeV/u. The length of the experimental target was designed to approximately double the stopping range of the primary ions in a longitudinal direction which was determined from preliminary calculations (Section 3.1.2). The stopping range of 200 MeV/u uranium ions in aluminium amounts to 3.442 ± 0.004 mm according to the FLUKA simulations, 3.722 ± 0.003 mm according to ATIMA and 3.874 ± 0.007 mm according to SRIM. Thus, the length of the target was chosen to yield 7.0 mm and altogether 70 target foils were used for the depth-profiling of the residual activity. Some of the individual foils were merged in groups of 4-5 pieces and they were considered as individual samples during the whole process of an investigation (grouping of the foils is recorded in Table 7). The aluminium foils had a diameter of 10 cm, a purity of 99.95 % and a density of 2.7 g/cm^3 at 20°C. The beam of primary particles was provided by the heavy-ion synchrotron SIS-18 for about 4 hours and the accumulated charge was 3.34×10^{-5} C, which corresponds to 2.86×10^{12} ions delivered to the target (see Table 4 on the page 37). The target was irradiated in the fast-extraction regime with repetition rates of 2-3 s. An impact of 60 cm long air-gap and 100 μm of the stainless steel vacuum window were taken into account according to the experimental area layout (Figure 8).

Table 7: Configuration of the aluminium experimental target

	Aluminium target irradiated by 200 MeV/u ^{238}U									Thickness [mm]	Diameter [mm]
[Foil number] Foil thickness [mm]	[1-5]	[6-10]	[11-15]	[16-20]	[21-25]	[26-30]	[31]	[32]	[33]	7.0	100.0
	0.5	0.5	0.5	0.5	0.5	0.5	0.1	0.1	0.1		
	[34]	[35]	[36]	[37]	[38]	[39]	[40]	[41]	[42]		
	0.1	0.1	0.1	0.1	0.1	0.1	0.1	0.1	0.1		
	[43]	[44]	[45]	[46]	[47-51]	[52-56]	[57-61]	[62-66]	[67-70]		
	0.1	0.1	0.1	0.1	0.5	0.5	0.5	0.5	0.4		

The target samples were gamma spectroscopically measured in a low-background housing of the high-purity germanium (HPGe) detector. The gamma-ray spectra were recorded in two series of measurements: (1st) 6 – 22 days and (2nd) 133 – 180 days after the end of the irradiation. The experimental data were compared to the Monte Carlo simulations, provided by the FLUKA 2011.2c.0 code [19]. An autonomous detector scoring residual nuclei produced in inelastic interactions was assigned to each foil. Residual activities of produced nuclides were detected 6 days after the end of the simulated irradiation. This approach has been chosen in order to keep similarity to the real experimental conditions at the highest possible level. An influence of a great number of short-lived nuclides with a half-life time of a few microseconds up to a few minutes, which are not detectable with our experimental setup, was avoided. Also a functionality of the radioactive decay calculations of FLUKA can be applied and tested in this fashion. An extrapolation of the simulated residual activities backward in the time to the end of the irradiation was necessary since all foils of the experimental and simulated target should be compared at the same time point. After the time-normalization of the residual activities, the normalization per one incident ion was made. The results of this study became independent from the special experimental constrains and they can be compared with any other results of aluminium material irradiated by uranium beams with identical energy.

3.3.1 THE DEPTH PROFILES OF NUCLIDES OBSERVED IN EXPERIMENT

There were more than 350 depth profiles created based on the gamma spectra of experimental samples. In total, about 150 candidates were identified as possible producers of investigated depth profiles according to the analysis technique explained in chapter 3.1.5. A significant number of all candidates are gamma-ray emitters with complex decay schemes and they are represented by gamma-quants of different energies. Due to the massive complexity, almost 300 depth profiles were not fulfilling the requirements of our study. The final compilation of 56 depth profiles of radioactive nuclides induced in the aluminium target are presented in the "Appendix 1", starting from the Figure 56 to the Figure 112 (on the pages 111 - 125). Those are the depth profiles of nuclides which unambiguously identified. As an example of some characteristic cases of the depth profiles, the residual activity of ^{7}Be, ^{22}Na, ^{88}Y, ^{113}Sn, ^{127}Xe, ^{139}Ce, ^{146}Eu, ^{206}Bi, and ^{237}U are discussed in this chapter. Those nuclides have been chosen in order to illustrate and to explain the differences between the depth profiles produced by radioactive nuclides with different mass numbers (starting from the light target-nuclei fragments up to heavier fragments with a mass close to the primary particles).

The nuclides induced in the target can be classified into two groups:

- target-nuclei fragments
- projectile fragments

The characteristic shapes of the depth profiles of these two groups are clearly distinguishable. The target-nuclei fragments are present starting from the 1st target foil and they are significantly detectable even beyond the range of the primary projectiles. For this reason, the lighter secondary particles contribute significantly to the target activation which is thus not only caused by the primary projectiles. The range of the ions in matter is proportional to A/Z^2 (where A is the mass number and Z is the atomic number). Thus, the lower the Z of the secondary particles the longer is their penetration range compared to the range of the primary particles. In our experiments, we observed that the projectile fragments are detectable starting from the range of the primary particles. This can be explained by the fact that the projectile gets fragmented at the very end of its track in the target. In opposite to that, if a fragmentation of primary particle is happening at the very beginning of its track, the resulting lower-Z fragments have longer stopping ranges, and they are penetrating beyond the range of the primary projectiles. Representative measured and simulated depth profiles of the residual activity of ^{7}Be, ^{22}Na, ^{88}Y, ^{113}Sn, ^{139}Ce, ^{127}Xe, ^{146}Eu and ^{206}Bi are displayed in Figure 19 to Figure 26. Experimental data from the 1st and the 2nd set of measurements are labelled as "(1st)" and "(2nd)", respectively.

DEPTH PROFILES OF TARGET-NUCLEI FRAGMENTS:

The nuclides ^{7}Be and ^{22}Na are typical examples for target-nuclei fragments. Their experimentally measured depth profiles of the residual activity are shown in Figure 19 and Figure 20, respectively.

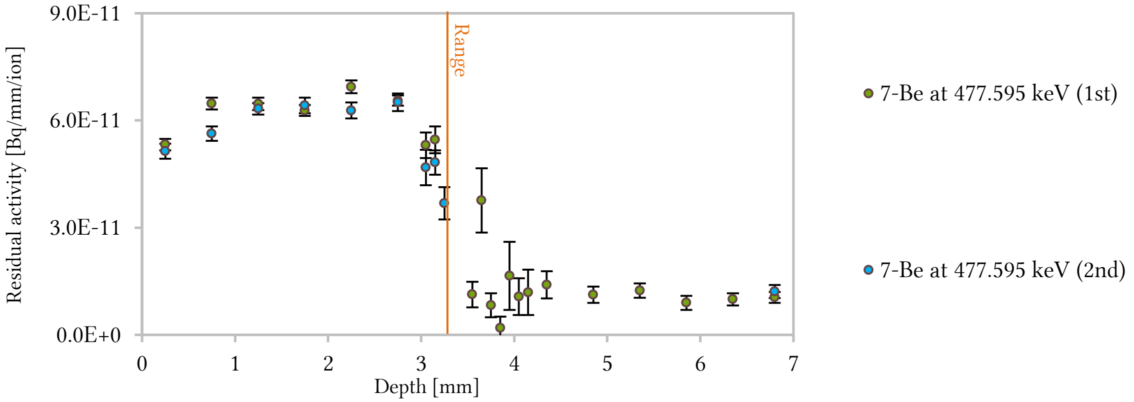

Figure 19: The depth profile of ^{7}Be in the aluminium target irradiated by 200 MeV/u ^{238}U beam.

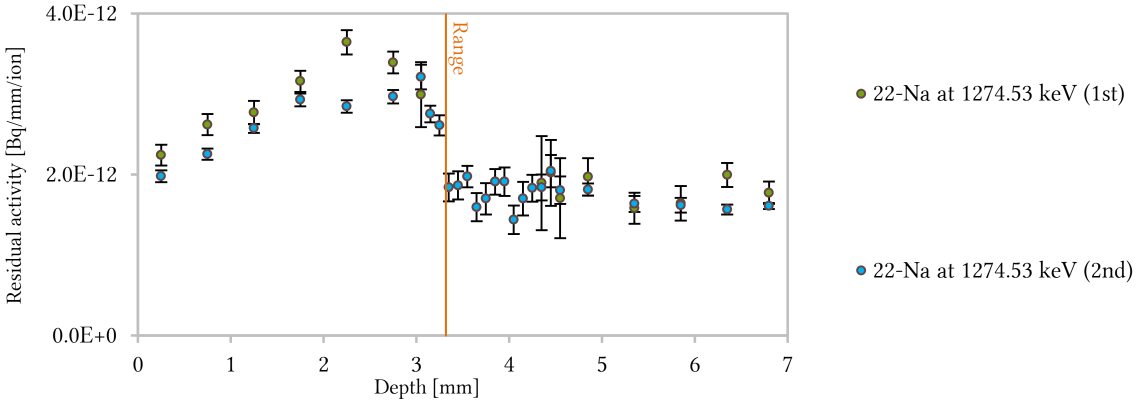

Figure 20: The depth profile of ^{22}Na in the aluminium target irradiated by 200 MeV/u ^{238}U beam.

The depth profiles of the ^{7}Be and ^{22}Na displayed in Figure 19 and Figure 20, respectively, are containing data points upstream of the range area because the fragmentation of the target nuclei is possible starting from the first foil. The produced fragments do not have to necessarily gain a kinetic energy (from the colliding primary particles) sufficient for exiting the foil in which the interaction took place. For this reason it is possible to detect an induced activity of target-nuclei fragments also in the first experimental foil.

It should be clarified that some adjustment based on the gamma-spectra analysis was made in the case of both depth profiles presented in Figure 19 and Figure 20. In particular, several experimental data points from the range area recorded during the 1st set of the measurement were excluded because of their overlapping with other short-lived nuclides. For instance, the gamma peak of ^{7}Be ($T_{1/2}$ = 53.12 d, E_γ = 477.595 keV, I_γ = 10.52 %) is located close to that of ^{188}Ir ($T_{1/2}$ = 1.73 d, E_γ = 477.99 keV, I_γ = 15.0 %), while in the case of the ^{22}Na ($T_{1/2}$ = 949.69 d, E_γ = 1274.53 keV, I_γ = 99.94 %) the contribution of ^{200}Tl ($T_{1/2}$ = 1.08 d, E_γ = 1273.497 keV, I_γ = 3.31 %) has to be considered. Both short-lived nuclides are significantly heavier than the examined target-nuclei fragments and therefore their depth profiles are placed only in a very narrow region close to the range of the primary particles. Besides that, the 2nd set of the measurement was not affected because of the large difference of the half-life times of concerned nuclides (and the appropriately chosen cooling time between the sets of the measurement). These facts allowed us to remove the data points of overlapping depth profiles from the 1st set in order to preserve their uninfluenced parts downstream and upstream of the range.

THE DEPTH PROFILES OF PROJECTILE FRAGMENTS:

The depth profiles of the residual activity of ^{88}Y, ^{113}Sn, ^{127}Xe, ^{139}Ce, ^{146}Eu and ^{206}Bi are shown in Figure 21-Figure 26 as an example for the typical shapes of projectile fragment depth profiles.

A typical shape of the depth profiles of projectile fragments is starting from the range of the primary particles and data points are obtained for the foils downstream of the range area. This is caused by the fact that projectile fragments may be created in the first target foil. The kinetic energy of such fragments may be very similar to the kinetic energy of the primary projectile at the moment of the interaction and this allows the produced fragment to penetrate through the target material. Moreover, the projectile fragments are lighter than the primary projectiles and for this reason they may be detected also in the foils located far behind the range area. There is an evident dependence of the "width" of the depth profiles on the mass of the fragment and it may be concluded that the lighter the fragment the wider is the depth profile. This statement is in agreement with theory of the stopping power explained in the chapter 2.1.2. The back side of the depth profile corresponds to the range of the projectile fragment which was created on the target surface. The front side of the profile was created by the projectile which was fragmented at the very end of its track. The chosen examples in this chapter are ordered with respect to the atomic mass (from lightest to heaviest nuclides), which may help to see better how the depth profiles get narrower with higher mass of the projectile fragments.

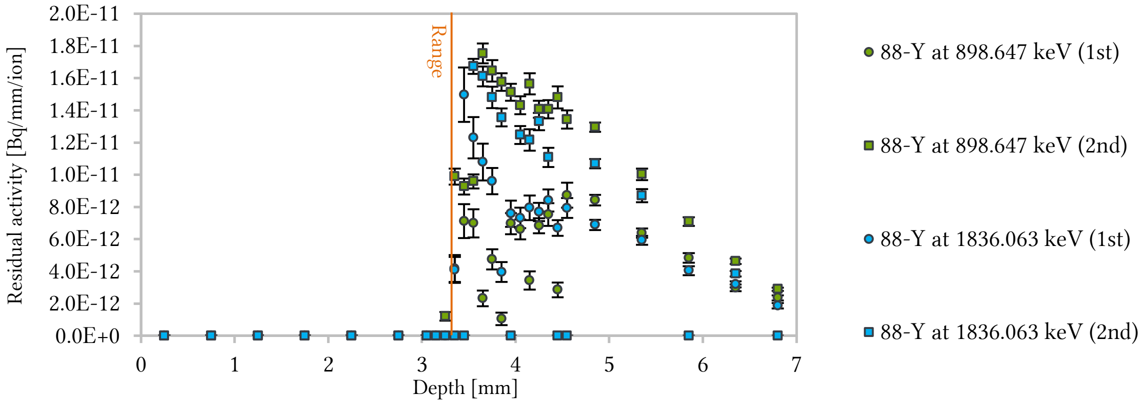

Figure 21: The depth profile of ^{88}Y in the aluminium target irradiated by 200 MeV/u ^{238}U beam.

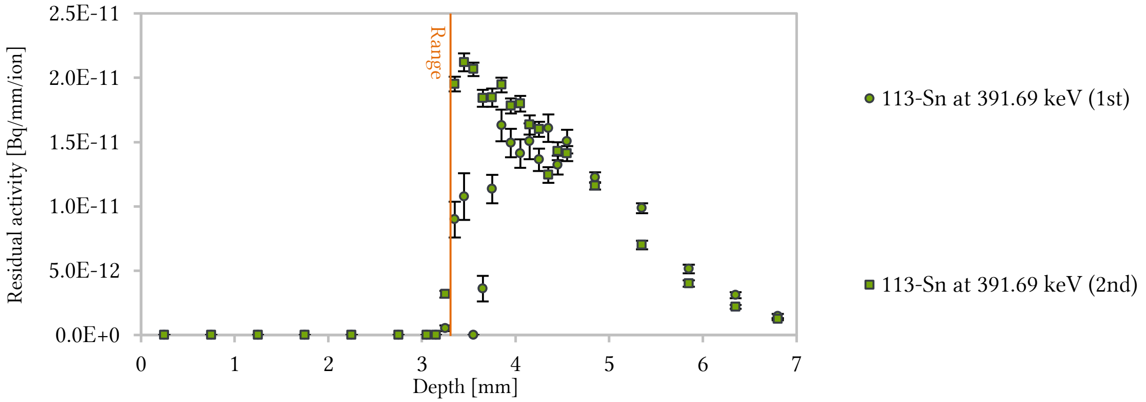

Figure 22: The depth profile of ^{113}Sn in the aluminium target irradiated by 200 MeV/u ^{238}U beam.

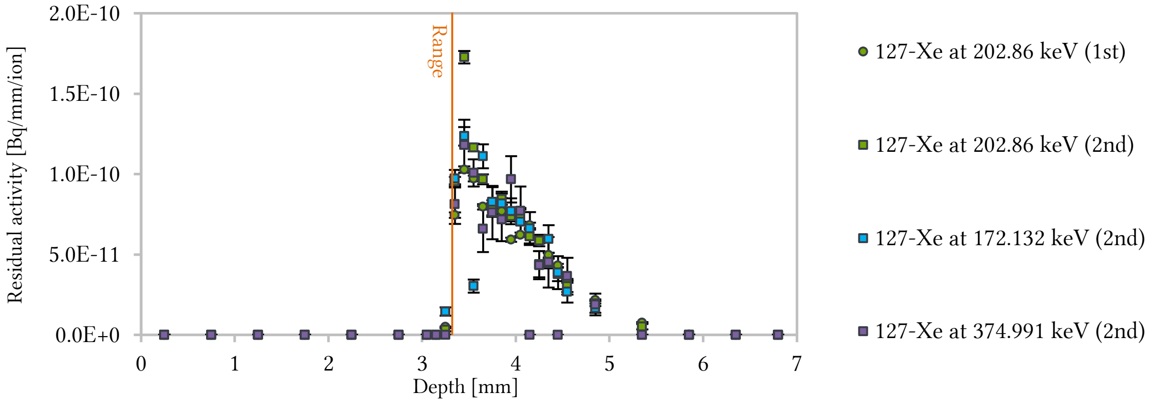

Figure 23: The depth profile of ^{127}Xe in the aluminium target irradiated by 200 MeV/u ^{238}U beam.

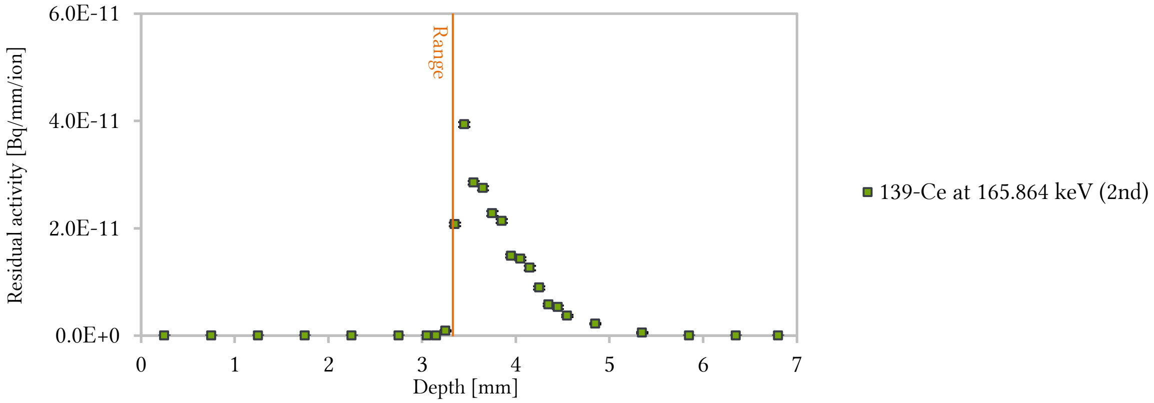

Figure 24: The depth profile of ^{139}Ce in the aluminium target irradiated by 200 MeV/u ^{238}U beam.

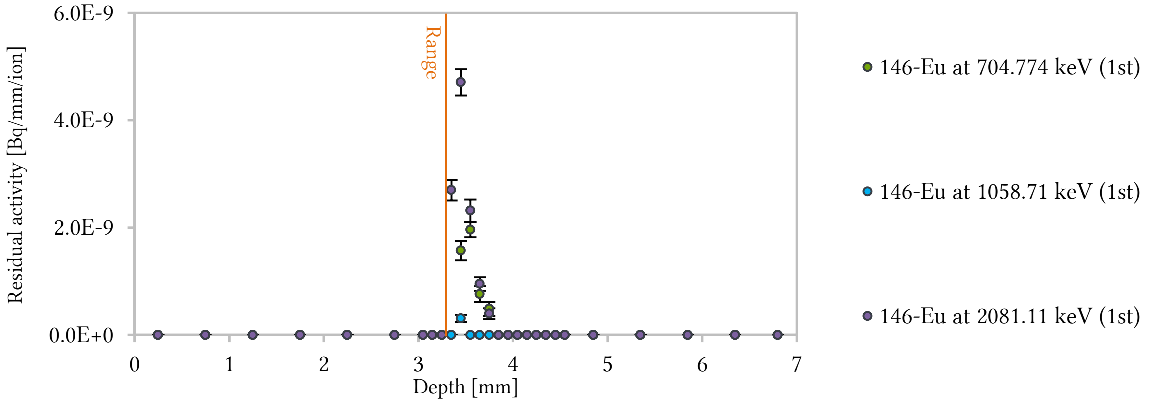

Figure 25: The depth profile of ^{146}Eu in the aluminium target irradiated by 200 MeV/u ^{238}U beam.

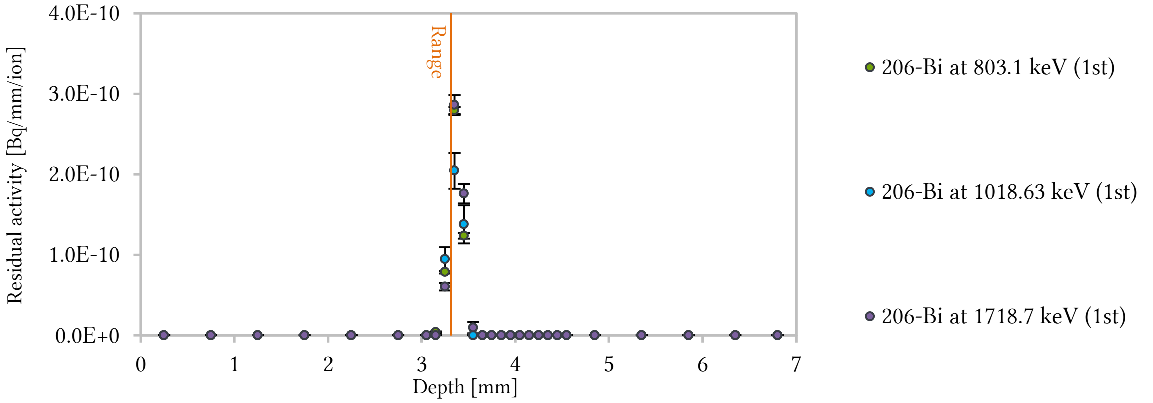

Figure 26: The depth profile of ^{206}Bi in the aluminium target irradiated by 200 MeV/u ^{238}U beam.

3.3.2 QUANTIFIED RESIDUAL ACTIVITIES OF THE OBSERVED NUCLIDES

The determination of the residual activity of produced radioactive nuclides is an essential part of the comparison of the experimental data and the results of the FLUKA simulations. The residual activity of each nuclide was obtained by numerical integration of the depth profiles as described before in chapter 3.1.5. In the cases of depth profiles exhibiting significant differences between the residual activities calculated from the 1st and the 2nd set of measurement, an additional analysis was needed for the error reduction of the quantified residual activities. Considerable amounts of experimental data have been excluded completely for further analysis because of an affection of gamma peaks by complex decay schemes of accumulated nuclides. In order to ensure the non-interchangeability of the data kept for further analysis, a labelling system was established to guarantee transparency and understandability. Quantified residual activities are presented in Table 8, where the problematic data were replaced by an abbreviation indicating the reason for the data exclusion, as explained below.

The abbreviation "INFL" was used in cases of an influenced measured data by indistinguishable gamma-emitters. An example of a corrupted depth profile by several nuclides induced in the aluminium target is shown in Figure 27. Three different nuclides are contributing to the production of a single gamma peak with an energy of about 603 keV in the case of the depth profile from the 1st set of measurement. An elaborated list of candidates (potential producers) emitting the investigated gamma peak contains ^{124}Sb ($T_{1/2}$ = 60.2 d, E_γ = 602.729 keV, I_γ = 98.26 %), ^{127}Sb ($T_{1/2}$ = 3.85 d, E_γ = 603.5 keV, I_γ = 4.45 %) and ^{124}I ($T_{1/2}$ = 4.176 d, E_γ = 602.729 keV, I_γ = 63 %) [143]. The difference between the energies of their gamma quants is about 0.7 keV, which is beyond the energy resolution of the corresponding experimental setup and the used HPGe detector. It should be emphasised that all three projectile fragments are truly present in the target foils because their other expected gamma lines were observed too. The depth profile based on the 2nd set of measurement can be assigned to ^{124}Sb with respect to the half-life times of candidates and the time point of the gamma spectra recording. The simulated depth profile is in good agreement with the experimental data obtained after the decaying of the short-lived nuclides. Note that the residual activity of ^{127}Sb ($T_{1/2}$ = 3.85 d, E_γ = 685.7 keV, I_γ = 37 %) was calculated from another measured gamma line of this nuclide and is included in Table 8. In contrast to that, the determined residual activity of ^{124}I is missing even 4 energy lines with the highest probability of emission. All of those lines are contributing to the production of gamma peaks with other short-lived or long-lived nuclides. Considering this, the complexity of the spectra analysis due to an enormous number of radioactive nuclides is evident.

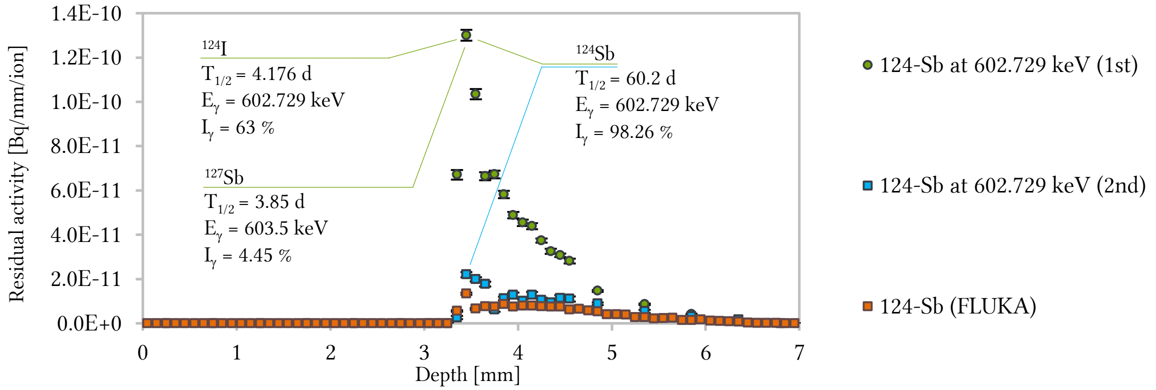

Figure 27: The depth profile of ^{124}Sb in the aluminium target irradiated by 200 MeV/u ^{238}U beam, where the 1st set of measurement was overlapping by ^{124}I and ^{127}Sb.

In opposite to the example shown above, the determination of the activities of some long-lived and short-lived nuclides was not reliable because of the large number of peaks belonging to short-lived nuclides emitting gamma quants of different energies. The difference between the energy lines is bigger than the energy resolution of the experimental setup. Such gamma quants can be distinguished as separated peaks of the spectra, but they appear only as a background (i.e., shown in Figure 14). The background decreases with the time as the short-lived nuclides disintegrate and the determination of the residual activities of the long-lived nuclides becomes possible for the later measured sets of gamma spectra.

The abbreviation "MDA" was used when the determination of the residual activity was not possible in the case of some nuclides when their activities were below a minimum detectable activity in the spectra. This issue was mostly observed in the case of the nuclides whose residual activity was quantified in the early-measured spectra, but it was not possible in the later-measured spectra. It was because they already decayed completely or they disintegrated in the way which allowed pronouncing the gamma peaks in spectra, but not sufficiently enough for the gamma-spectroscopic analysis.

The last abbreviation used in the table of the determined residual activities is "AVRG" and it was used in the case when different gamma lines of the same nuclide were observed. The average value of the residual activity was calculated separately for each set of the measurement.

Table 8: Identified nuclides and their activities induced in the aluminium target irradiated by 200 MeV/u uranium beam. A_1, A_2 – activity, σ_1, σ_2 – uncertainty of the measured activity including detector-efficiency calibration uncertainty and net-peak-area uncertainty. Activities are extrapolated to the end of the irradiation. Subscript "1" and "2" are related to the spectrum measured 6-22 and 133-180 days after the end of the irradiation, respectively. The abbreviation "INFL" is used for nuclides whose activity determination was restraint due to the influence of another nuclide, "MDA" is marking a missing value of the residual activity due to decaying below the minimum detectable activity. "AVRG" corresponds to an average residual activity determined from several gamma lines of the same radioactive nuclide.

Nuclide	Half-time [d]	Energy [keV]	A_1 [Bq/ion]	σ_1 [%]	A_2 [Bq/ion]	σ_2 [%]
^{7}Be	53.12	477.6	3.17E-10	5.76	2.09E-10	5.03
^{22}Na	949.69	1274.53	3.28E-11	6.67	1.49E-11	4.45
^{54}Mn	312.3	834.85	INFL		2.89E-12	11.46
^{58}Co	70.86	810.78	INFL		1.20E-11	11.46
^{69}Ge	1.63	1107.01	2.24E-10	27.03	MDA	
^{74}As	17.77	595.35	6.88E-11	5.57	MDA	
^{75}Se	119.78	136	1.09E-11	9.21	1.61E-11	4.51
		264.66	1.26E-11	9.9	1.84E-11	6.7
		AVRG	1.18E-11		1.73E-11	
^{82}Br	1.47	554.35	2.54E-10	12.06	MDA	
		1317.47	2.54E-10	17.06	MDA	
		AVRG	2.54E-10			
^{83}Rb	86.2	520.39	3.12E-11	9.51	4.09E-11	6.83
		529.63	INFL		4.18E-11	9.52
		AVRG	3.12E-11		4.14E-11	
^{87}Y	3.33	484.81	3.82E-10	9.52	MDA	
^{88}Y	106.65	898.65	1.92E-11	7.7	3.66E-11	3.67
		1836.06	2.17E-11	7.79	2.26E-11	3.98
		AVRG	2.05E-11		2.96E-11	

Nuclide	Half-time [d]	Energy [keV]	A_1 [Bq/ion]	σ_1 [%]	A_2 [Bq/ion]	σ_2 [%]
^{89}Zr	3.27	908.96	9.08E-10	4.5	MDA	
^{95}Nb	34.98	765.79	1.17E-10	2.53	8.94E-10	1.84
^{95}Zr	64.02	756.73	9.13E-11	3.96	1.01E-10	4.02
^{96}Tc	4.28	554.35	2.54E-10	12.06	MDA	
^{101}mRh	4.34	306.86	5.48E-10	3.25	MDA	
^{103}Ru	39.26	497.08	INFL		2.72E-10	2.96
^{106}mAg	8.28	540.97	3.20E-11	12.31	MDA	
		616.17	8.05E-11	14.21	MDA	
		717.24	9.40E-11	10.29	MDA	
		824.79	5.12E-11	21.76	MDA	
		1199.39	1.73E-10	12.31	MDA	
		AVRG	8.61E-11			
^{110}mAg	249.79	657.76	6.69E-12	14.32	8.33E-12	6.2
		706.68	INFL		3.96E-12	24.3
		884.69	6.48E-13	20.53	4.95E-12	9.37
		937.49	INFL		6.84E-12	15.34
		1384.3	INFL		3.44E-12	19.24
		AVRG	3.67E-12		5.50E-12	
^{111}In	2.8	171.28	1.40E-09	2.74	MDA	
^{113}Sn	115.09	391.69	3.11E-11	6.92	3.59E-11	3.86
^{115}Cd	2.23	336.24	1.80E-09	16.4	MDA	
^{119}mTe	4.7	270.53	1.70E-10	10.31	MDA	
^{120}mSb	5.76	1023.1	2.58E-10	3.32	MDA	
		1171.3	2.67E-10	3.25	MDA	
		AVRG	2.63E-10			
^{121}mTe	154	212.19	2.99E-11	4.21	1.05E-11	5.1
^{124}Sb	60.2	602.73	INFL		2.54E-11	9.34
^{126}Sb	12.46	414.81	9.04E-11	3.77	MDA	
		720.64	6.19E-11	6.84	MDA	
		695.03	9.50E-11	4.35	MDA	
		AVRG	8.24E-11			
^{127}Sb	3.85	685.7	6.51E-10	7.47	MDA	
^{127}Xe	36.4	172.13	INFL		1.01E-10	11.68
		202.86	1.04E-10	2.4	1.15E-10	5.44
		374.99	INFL		9.07E-11	19.9
		AVRG	1.04E-10		1.02E-10	
^{131}Ba	11.5	123.81	1.75E-10	2.44	MDA	
^{131}I	8.02	364.49	5.62E-10	1.56	MDA	
^{136}Cs	13.16	818.51	4.03E-11	5.77	MDA	
^{139}Ce	137.64	165.86	6.45E-12	8.26	2.40E-11	2.34
^{140}La	1.68	487.02	Daughter product of ^{140}Ba		Daughter product of ^{140}Ba	
		815.77				
		925.19				
		2521.4				
^{143}Pm	265	741.98	INFL		4.50E-12	9.29

Nuclide	Half-time [d]	Energy [keV]	A_1 [Bq/ion]	σ_1 [%]	A_2 [Bq/ion]	σ_2 [%]
^{144}Pm	363	618.01	INFL		4.32E-13	24.8
		696.51	INFL		1.49E-12	11.91
		AVRG			9.61E-13	
^{145}Eu	5.93	653.51	1.55E-10	8.52	MDA	
		1658.53	1.82E-10	7.15	MDA	
		AVRG	1.69E-10			
^{146}Gd	48.27	114.71	1.72E-11	6.47	5.49E-11	3.27
^{147}Gd	1.59	396	5.31E-10	6.1	MDA	
		1069.35	3.97E-10	17.85	MDA	
		AVRG	4.64E-10			
^{148}Eu	54.5	550.28	3.29E-12	20.27	2.18E-12	27.88
		629.99	1.61E-11	9.79	1.87E-12	28.01
		AVRG	9.70E-12		2.03E-12	
^{149}Gd	9.28	298.63	1.31E-10	6.79	MDA	
		346.65	7.71E-11	5.2	MDA	
		788.88	4.19E-11	16.28	MDA	
		AVRG	8.33E-11			
^{155}Tb	5.32	105.31	1.42E-10	3.32	MDA	
^{165}Tm	1.25	242.92	8.48E-10	4.71		
^{169}Lu	1.42	960	1.34E-09	5.53	MDA	
		1449.74	1.23E-09	9.62	MDA	
		AVRG	1.29E-09			
^{169}Yb	32.03	109.78	1.39E-11	9.17	5.06E-11	10.53
		130.52	2.90E-11	11.72	2.90E-11	14.3
		177.21	3.87E-11	9.35	3.99E-11	9.4
		307.74	INFL		5.35E-11	20.74
		AVRG	2.72E-11		4.33E-11	
^{170}Lu	2.01	1054.28	6.97E-10	13.3	MDA	
		1280.25	7.62E-10	7.51	MDA	
		1341.2	1.42E-09	12.4	MDA	
		1955.65	3.98E-10	25.3	MDA	
		2041.88	1.01E-09	8.94	MDA	
		2126.11	8.30E-10	7.25	MDA	
		2364.1	3.29E-10	26	MDA	
		AVRG	7.78E-10			
^{182}Re	2.67	100.11	1.70E-08	0.16	MDA	
		113.67	1.20E-08	0.44	MDA	
		AVRG	1.45E-08			
^{185}Os	93.6	874.81	3.52E-11	11.44	5.02E-12	22.89
^{188}Ir	1.73	672.51	3.80E-09	8.72	MDA	
		1209.83	1.10E-10	27.01	MDA	
		1944.08	3.18E-10	21.49	MDA	
		2214.62	4.38E-10	6.48	MDA	
		AVRG	1.17E-09			

Nuclide	Half-time [d]	Energy [keV]	A_1 [Bq/ion]	σ_1 [%]	A_2 [Bq/ion]	σ_2 [%]
^{188}Pt	10.2	423.34	1.55E-10	21.17	MDA	
		381.43	7.16E-11	7.68	MDA	
		AVRG	1.13E-10			
^{190}Ir	11.78	557.97	1.45E-11	13.08	MDA	
		569.31	7.83E-12	19.34	MDA	
		AVRG	1.12E-11			
^{191}Pt	2.8	409.44	6.26E-11	14.07	MDA	
^{200}Tl	1.09	1205.72	1.19E-09	8.22	MDA	
^{205}Bi	15.31	987.62	1.76E-11	16.24	MDA	
		1764.36	3.12E-11	5.67	MDA	
		AVRG	2.44E-11			
^{206}Bi	6.24	803.1	4.85E-11	2.17	MDA	
		1018.63	4.37E-11	13.96	MDA	
		1718.7	5.32E-11	6.86	MDA	
		AVRG	4.85E-11			
^{206}Po	8.8	522.47	5.99E-11	9.82	MDA	
		807.38	4.16E-11	5.03	MDA	
		860.93	1.07E-10	12.9	MDA	
		980.23	5.37E-11	10.6	MDA	
		1032.26	6.77E-11	2.95	MDA	
		AVRG	6.60E-11			
^{227}Th	18.72	50.13	7.26E-11	4.9	MDA	
^{228}Pa	0.92	964.77	3.78E-09	15.69	MDA	
		968.97	1.21E-08	2.39	MDA	
		AVRG	7.94E-09			
^{230}Pa	17.4	454.95	3.45E-11	6.58	MDA	
		918.48	2.86E-11	18.93	MDA	
		951.95	1.47E-11	9.27	MDA	
		AVRG	2.59E-11			
^{237}U	6.75	208	6.74E-09	0.2	MDA	

3.3.3 COMPARISON OF EXPERIMENTAL DATA TO THE SIMULATION

The residual activities of the individual nuclides were determined by numerical integration of depth profiles and were compared to the results of the FLUKA simulation. The depth profiles of very different shapes can have a similar area. For this reason, the comparison of residual activities is meaningful only after the depth profile analysis and excluding of all experimental data containing inexplicable deviations. The deviations between the experimentally measured, A_E, and the simulated residual activities, A_S, are indicated in terms of their ratio, as shown in Figure 28. The average value of the experimentally measured residual activity was taken into account if the concerned nuclides exhibit more gamma-lines with different energies and/or at the different time of measurement. All values of residual activity employed here are time-independent of the experimental data acquiring and the scoring setting of simulation because they all are extrapolated to the end of the irradiation.

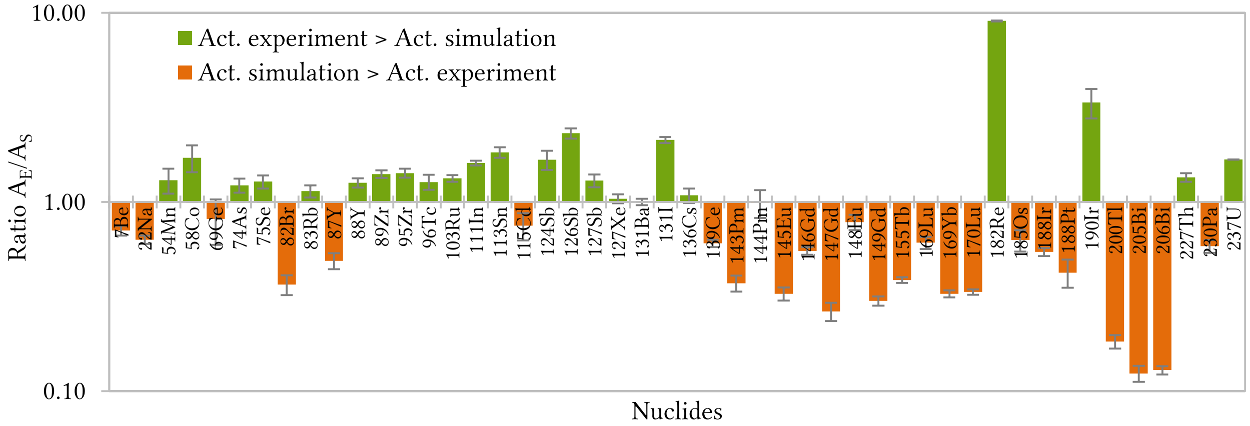

Figure 28: Ratio A_E/A_S of the residual activities of nuclides induced in the aluminium target after the irradiation by ^{238}U beam with an energy of 200 MeV/u, where A_E denotes the calculated value from the experimental data and A_S that calculated by the FLUKA code. Nuclides which have not displayed any bar, have a very good agreement ($A_E/A_S = 1$).

The ratios of the residual activities are sorted from low Z to high Z and they are displayed as colour bars using the logarithmic scale. A closer look at the data indicates that the FLUKA code underestimates more likely a production of lighter nuclides (the green bars in Figure 28) and the average discrepancy amounts to factor of about 2. At the same time, the FLUKA code overestimates a production of heavier fragments (the orange bars in Figure 28), similarly with the average discrepancy of a factor of about 2 (the reciprocal of the "A_E/A_S" ratio is $1/0.47 \approx 2$). In a concise manner, the residual activities calculated by FLUKA are bigger or smaller than the measured value by a factor of two. The discrepancies between measured and calculated residual activities of all other nuclides vary from the factor of 0.12 ± 0.01 to 9.06 ± 0.04. The A_E/A_S ratio of ^{182}Re yielding 9.06 ± 0.04 is an extreme incident, where FLUKA is significantly underestimating the production of this nuclide and it may be seen also in the depth profile illustration in Figure 100 on page 122. On the contrary, an example of an excellent match between experiment and simulation is ^{133}Ba, where the residual activities ratio is 1.00 ± 0.04. In a similar manner, ^{144}Pm ($A_E/A_S = 0.99 \pm 0.04$) and ^{127}Xe ($A_E/A_S = 1.04 \pm 0.04$) have a very impressive agreement. Figure 28 is not representing all nuclides listed in Table 8 because of the excluded data in the case of metastable nuclides, where the employed FLUKA version reports a limited competence [41]. Another reason for excluding nuclides from this comparison was an extraordinary mismatch between experimental and simulated data. For example, nuclides ^{165}Tm and ^{206}Po have been confidently identified by gamma-spectra analysis, but there was no prediction of their presence by FLUKA. Therefore, a calculation of the ratio of the residual activities was not possible.

3.3.4 RANGE OF THE PRIMARY PARTICLES

A benchmarking of experimentally measured and calculated ranges is a relevant validation technique of heavy-ion interaction-models exploited by simulation codes, which was presented in several publications [23, 95, 96]. Choosing an adequate thickness of the foils is very important, especially within the range region, because the precision of this technique is strongly limited by this parameter. Each foil is represented in the depth profile by the position of its centre, and similarly, a determined residual activity of the whole foil is referenced to the same position.

This study assumes that the measured and the calculated ranges of the ^{238}U primary beam are available. Unfortunately, there was not a sufficient amount of ^{238}U ($T_{1/2} = 4.468 \times 10^9$ y | $E_{\gamma 1} = 49.55$ keV, $I_{\gamma 1} = 0.064$ % | $E_{\gamma 2} = 113.5$ keV, $I_{\gamma 2} = 0.0102$ %) gamma-quants emitted during the gamma spectra acquirement. The activity of the ^{238}U was low due to the great half-life time with respect to the time of the gamma-spectroscopic measurement making the detection of none of its two gamma-lines possible. A similar issue resulted in the development of the positron emission tomography (PET) imaging. In that case, the spatial distribution of the primary ions (i.e. ^{12}C) inside the patient's body is not possible to be monitored directly. In the contrary, the fragments of the primary particles (^{11}C) are detectable positron emitters and their spatial distribution correlates with the distribution of the primary ions. This is possible because the penetration range of heavy ions is roughly proportional to $R \sim A/Z^2$. Since Z and A of the primary ions and its projectile-fragment nuclides are almost identical and their initial energies are the same, the ranges of both nuclides should be also very similar. Thus, imaging of the projectile fragments corresponds to the spatial distribution of the primary ions [122-124]. In a similar fashion, the measurement of the ^{237}U projectile fragments depth profile is an essential matter for a range-verification technique of the ^{238}U primary beam. The ^{237}U ($T_{1/2} = 6.75$ d, $E_\gamma = 208.0$ keV, $I_\gamma = 21.2$ %) is emitting several gamma-quants with different energies, but only one was not interfering with gamma emitters of other nuclides and provide a satisfactorily high abundance at the same time. One can expect that the range of the ^{237}U (A = 237, Z = 92) nuclides is slightly shorter than that of the ^{238}U (A = 238, Z = 92) nuclides. Considering the fact that the fragmentation events occur in different depths of the target, the determination of the maximum possible difference between lengths of the trajectories of both nuclides is essential. Such an extreme case corresponds to the scenario where the ^{238}U primary beam is directly fragmented on the surface of the experimental target. Subsequently, the produced ^{237}U projectile fragments penetrate the sample with the highest possible energy. Accordingly, estimated difference between the range of the ^{237}U ($237/92^2 = 0.02800$) projectile fragments and the ^{238}U ($237/92^2 = 0.02812$) primary ions is about 0.5%, which is less than the experimental uncertainty. Conclusively, the experimentally measured range of the ^{237}U fragments substituted the missing experimental data of the ^{238}U primary particles.

An estimation of the calculated values of range and range straggling was provide by computer codes FLUKA 2011.2c.4, ATIMA and SRIM-2013 introduced in sections 2.3.1, 2.3.2 and 2.3.3, respectively. The range is usually determined as the position of the Bragg peak. Unfortunately it was not possible to measure the stopping power experimentally, therefore, fitting the narrow depth profile of the ^{237}U to Gaussian curve served for determination of the range and the range straggling. The calculated and experimentally measured range as well as the range straggling are presented in Table 9. The experimental data are compared to the calculations in the Figure 29.

Table 9: Range and range straggling of the ^{238}U primary ions and ^{237}U fragments in the aluminium target calculated by ATIMA, SRIM and FLUKA and obtained experimentally. The initial energy of the primary particles was 200 MeV/u and their energy losses in vacuum window and in the air gap were taken into account in the calculations.

	ATIMA	SRIM	FLUKA	EXPERIMENT
		Range ± range straggling [mm]		
^{238}U	3.722 ± 0.003	3.874 ± 0.007	3.442 ± 0.004	-
^{237}U	3.569 ± 0.003	3.713 ± 0.007	3.423 ± 0.007	3.46 ± 0.09

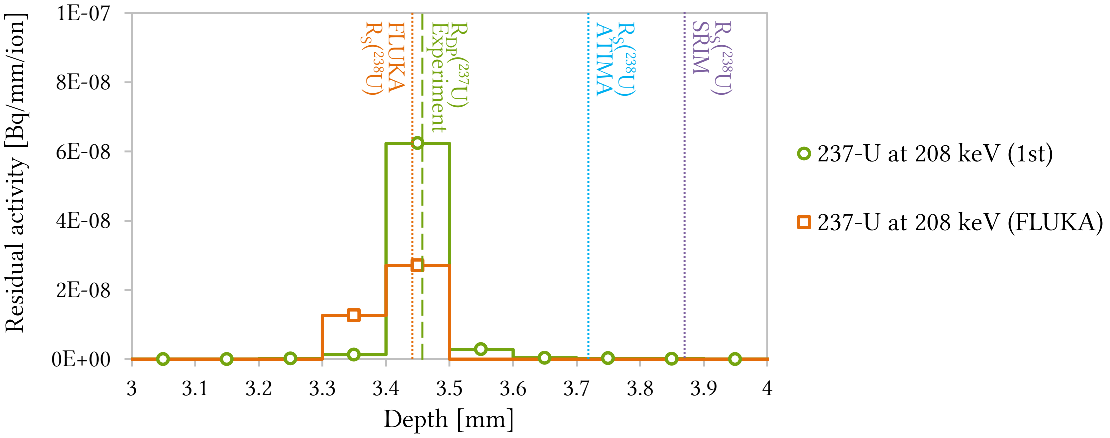

Figure 29: Experimentally measured range (R_{DP}) of the ^{237}U and simulated range (R_S) of the ^{238}U ions in the aluminium target irradiated by ^{238}U with an energy of 200 MeV/u displayed in zoomed depth profile. The vertical lines represent the ranges of the ^{238}U ions calculated by FLUKA, ATIMA and SRIM and the experimentally measured range of the ^{237}U fragments. Energy losses of the primary particles in the vacuum window and in the air gap were taken into account.

The FLUKA code predicted the presence of the ^{237}U in two foils only (No. 34 and No. 35), but we identified it in the foil No. 36 as well. The range and range straggling of the ^{237}U ions calculated by FLUKA is 3.423 mm ± 0.007 mm, whereas the range determined experimentally is 3.46 mm ± 0.09 mm.

Relative deviations of the ^{237}U range obtained by depth-profiling method from the ^{238}U ranges calculated by the available software were determined. The relative deviations, δ, were calculated according to:

$$\delta \quad = \frac{|R_S - R_{DP}|}{R_{DP}} \cdot 100 \qquad [\%], \tag{24}$$

where R_{DP} is the range obtained from the depth profiling of the residual activity of ^{237}U and R_S is the range of the ^{238}U primary ions calculated by FLUKA, ATIMA and SRIM software. ATIMA and SRIM are overestimating the range calculation of the ^{238}U compared to the measured range of ^{237}U and their relative deviations are 7.7 % and 12.1 %, respectively. At the same time, FLUKA is predicting a shorter range of the primary projectiles, but the relative deviation amounts to 0.5% only.

The range straggling calculated by ATIMA is identical for both ^{237}U and ^{238}U fragments and the same statement is valid for the SRIM results as well. A logical explanation of this difference is that ATIMA and SRIM have not implemented inelastic interactions in its calculations (nor TRIM, a Monte Carlo module of SRIM code). Thus, they predict that the fragmentation is happening only on the surface of the target. On the other hand, the FLUKA calculations presented the range straggling of the ^{237}U fragments about two times larger than the range straggling of the ^{238}U primary projectiles. The FLUKA code is more complex software and the inelastic nuclear collisions are involved in the process of primary ion beam transportation. For this reason, the fragmentation processes may occur along the whole length of ion trajectories, which naturally influences the range and the range straggling. Additional to this, SRIM and ATIMA are considering a mono-energetic beam. On the contrary, the beam parameters such as the beam size and momentum spread were set in the FLUKA calculations according to the experimental values which causes also an impact on the range straggling as it has been shown in the Ref [23].

3.3.5 OBSERVED DISPARITIES BETWEEN EXPERIMENTAL AND SIMULATED DATA

The investigation of the depth profiles of the residual activity revealed significant discrepancies between the measured and calculated residual activity of the target-nuclei fragments, namely ^{7}Be and ^{22}Na. (see Figure 30 and Figure 31). The simulated data predicts the experimental data correctly only within the first foil of the target. In order to explain the deviations of the FLUKA prediction at certain depths in the experimental target, their possible coherence with the FLUKA policy of the interaction models was studied. The production of radioactive nuclides is depending on the interactions of primary projectiles with the target material. The energy of the primary particles decreases due to these interactions and therefore, a study of the energy as a function of the depth was used to identify target regions in which different interaction models were assumed by the FLUKA code. The FLUKA user manual states that the nucleus-nucleus interactions of heavy ions are calculated by three different models [41]:

- DPMJET-II and DPMJET-III (Dual Parton Models) for projectiles with an energy above 5 GeV/u
- RQMD (Relativistic Quantum Molecular Dynamics) for projectiles with an energy between 5 GeV/u and 100 MeV/u
- BME (Boltzmann Master Equation) for projectiles with an energy below 100 MeV/u

The first models (DPMJETs) were not relevant for our simulations since none of the projectiles reached such high energies. The energy range of our experiments is suitable to be described by both, the Relativistic Quantum Molecular Dynamics (RQMD) and the Boltzmann Master Equation (BME) physics models. This fact motivated us to test for an influence of the transition between RQMD and BME by changing of different threshold settings. The FLUKA manual explains the way of changing between RQMD and BME models. The code does not have to be strictly fixed to the threshold value of 100 MeV/u, since there is no theoretical knowledge or an empirical experience evidencing that this value is a constant and both models are qualitatively comparable at this energy region. Thus, a default setting of FLUKA allows using both models within the energy band of 125 ± 25 MeV/u and for each seed of simulation it is choosing one of them [41].

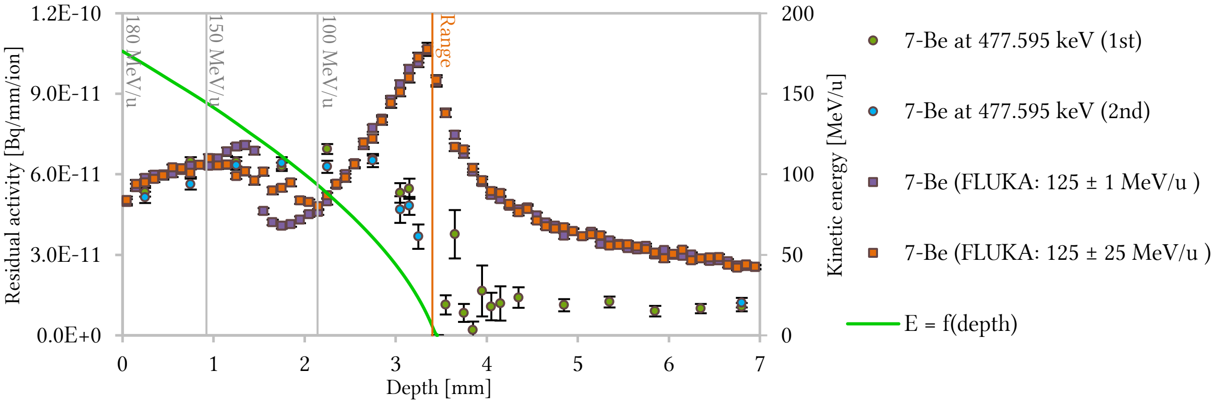

Figure 30: Examples of the FLUKA simulations with different settings of the energy band of RQMD and BME physics models transition applied in the case of the depth profile of ^{7}Be in the aluminium target irradiated by a 200 MeV/u ^{238}U beam. The energy losses in the vacuum window and in the air gap were taken into account in the calculations.

Figure 30 shows the depth profiles of ^{7}Be analogous to Figure 19 from before with results of the FLUKA simulation added in orange and purple. There are two depth profiles of the ^{7}Be, simulated by FLUKA employing different settings for the energy band for the transition between BME and RQMD models are displayed together with a depth profile of the measured residual activity. The depth profile of the measured activity has a rather simple shape, where the residual activity achieves about 5.69 x 10^{-11} Bq/mm/ion in the first foil. From that point on the residual activity slowly increases up to the maximal value of 6.94 x 10^{-11} Bq/mm/ion at the depth of 2.25 mm. Following the experimental residual activity is permanently decreasing to about1.05 x 10^{-11} Bq/mm/ion at the last experimental foil, at the depth of 6.8 mm. On the contrary, the two profiles calculated by FLUKA are characterized by a dominant peak in the range region of the primary particles (where the highest residual activity is about 1.07 x 10^{-10} Bq/mm/ion at the depth of 3.35 mm) and by a steady decrease of the residual activity through all foils downstream of the range (where the lowest calculated activity is about 2.55 x 10^{-11} Bq/mm/ion). The parts of the calculated depth profiles upstream of the range undergo remarkable changes depending on the nucleus-nucleus model energy-threshold. As it was already mentioned, the default setting of the transition between BME and RQMD models is 125 ± 25 MeV/u, thus both models are used from 100 MeV/u up to 150 MeV/u [41]. In this particular case, a local maximum of the calculated residual activity of 6.60 x 10^{-11} Bq/mm/ion is located at the depth of 0.95 mm and the local minimum of 4.80 x 10^{-11} Bq/mm/ion is at the depth of 2.15 mm. A comparison of the positions of these local extremes with the E=f(depth) calculation showed that they are corresponding very closely to the depths where the energy of the primary projectiles is approaching 150 MeV/u and 100 MeV/u, respectively. This fact motivated us to change the default settings used by FLUKA. The energy band was set to 125 ± 1 MeV/u in order to see an influence of the transition between the interaction models on the shape of the depth profile. Indeed, there is a noticeable change of the positions of the local maximum and local minimum downstream of the range. Under these conditions, the local maximum of 7.08 x 10^{-11} Bq/mm/ion is at the depth of 1.35 mm and the local minimum of 4.07 x 10^{-11} Bq/mm/ion is at the depth of 1.75 mm. Based on these results, we assume that the FLUKA calculations and the experimental data is correlated with the energy of the primary projectiles and the exchange of RQMD and BME nucleus-nucleus interaction models does affect the results of the residual activity calculations. Unfortunately, none of the chosen settings improved the mismatch between the experimental and calculated data.

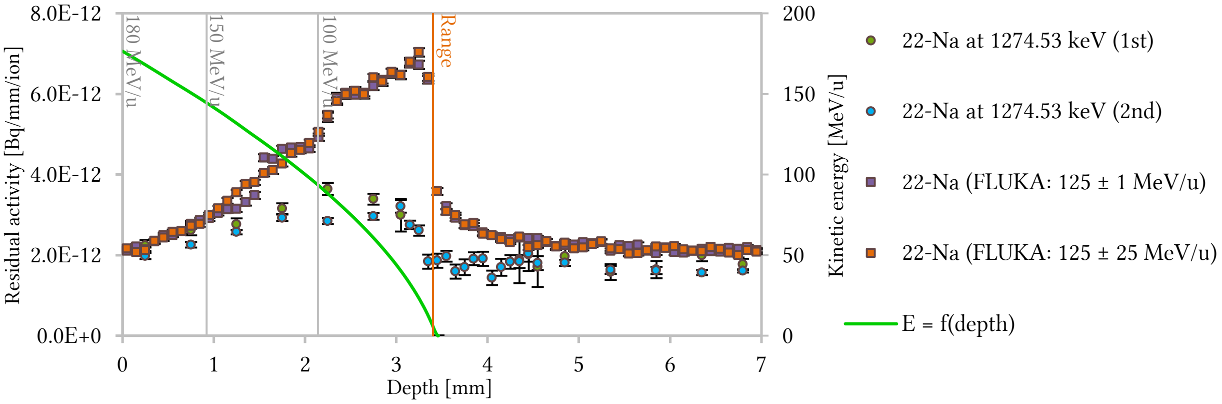

Figure 31: Examples of the FLUKA simulations with different settings of the energy band of RQMD and BME physics models transition applied in the case of the depth profile of ^{22}Na in the aluminium target irradiated by a 200 MeV/u ^{238}U beam. The energy losses in vacuum window and in the air gap were taken into account in the calculations.

Figure 31 shows the depth profiles of ^{22}Na analogous to Figure 20 from before with results of the FLUKA simulation. Similarly to the case of the ^{7}Be, an investigation of the ^{22}Na as another target-nuclei fragment was executed. The depth profile created from experimentally measured residual activities has a very similar shape as it was in the case of ^{7}Be, where higher activities were observed in the foils upstream of the range compared to activities downstream of the range. The value of about of 2.12 x 10^{-12} Bq/mm/ion is corresponding to the residual activity accumulated in the first foil and is identical for both experimental and simulated data. The highest residual activity of about of 3.64 x 10^{-12} Bq/mm/ion was measured again in the foil placed at the depth of 2.25 mm. Residual activities decrease as the depth increases and the lowest residual activity of 1.77 x 10^{-12} Bq/mm/ion was observed again in the very last foil of the target. The depth profile of the simulated residual activity achieves the highest activity of about 7.03 x 10^{-12} Bq/mm/ion at a depth of 3.15 mm for both settings of FLUKA. Any local maximum or local minimum did not appear in the region upstream of the range, in the case of the ^{22}Na nuclide. Nevertheless, similarities to the simulated depth profile of the ^{7}Be are visible in the comparison of two different settings of the energy band used for transition between BME and RQMD model. Both simulated depth profiles are overlapping each other everywhere except the region where the primary particles exhibit an energy between 100 and 150 MeV/u, which corresponds to a depth range between 0.95 and 2.25 mm. The results calculated including the transition of BME and RQMD models with the energy band of 125 ± 25 MeV/u have a rather monotonous behaviour. On the other hand, the results calculated using the energy band of 125 ± 1 MeV/u present a noticeable step in the middle of this region. Initially, the activities are slightly lower than those calculated employing the default FLUKA setting. In opposite to that, at a depth of 1.55 mm they start to be higher, but only until a depth of 2.25 mm, where the BME nucleus-nucleus interaction model is solely used and the results of the different FLUKA settings are overlapping again. Although the difference between the two FLUKA settings is not massive; the similar behaviour as it was observed in the case of ^{7}Be is noticeable. It should be stressed at this place that the FLUKA simulations were performed with an enormously high statistic of 50 000 000 initial seeds for each setting of the energy bands, but it was necessary in order to provide indisputable results. In this fashion, we obtained calculated values with high precision, where the error bars of the residual activities are smaller than the size of the data points in their graphical interpretation.

Another discrepancy of the FLUKA code observed from the comparison of the experimentally measured and the simulated results concerns the estimation of the activity produced by the metastable nuclides. The recent version of the FLUKA code does not offer any features for the residual activity calculation produced by nuclides in such an excited state, since the present models do not distinguish among ground state and isomeric states [41]. For this reason, it was not possible to add the FLUKA results to the existing experimental depth profiles of ^{101m}Rh, ^{106m}Ag, ^{110m}Ag, ^{119m}Te, ^{120m}Sb nuclides. Nevertheless, the recorded depth profiles of these nuclides are valuable for a possible crosschecking with some of the future versions of the FLUKA code, therefore, they are included in the APPENDIX part. An example of the depth profile of the metastable nuclide ^{120m}Sb is presented in Figure 32.

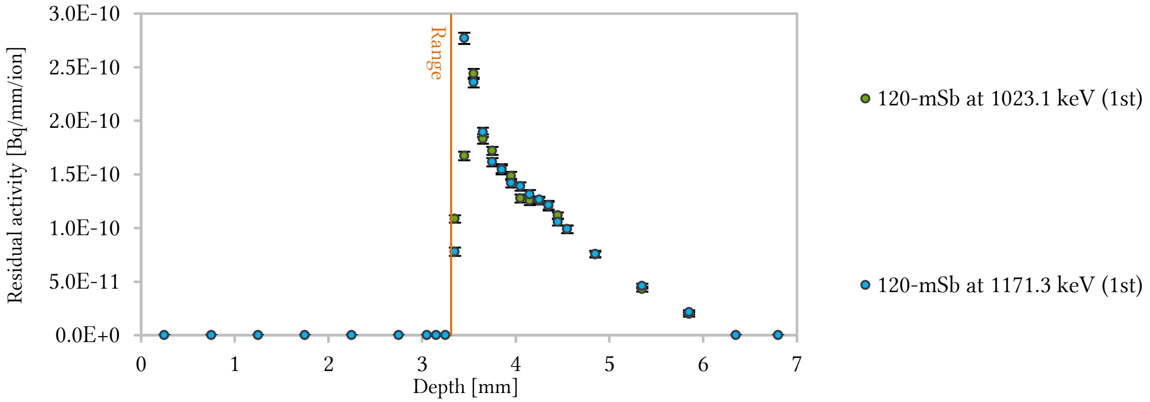

Figure 32: The depth profile of ^{120m}Sb in the aluminium target irradiated by 200 MeV/u ^{238}U beam.

3.4 ACTIVATION OF THE ALUMINIUM TARGET BY THE 125 MeV/u URANIUM BEAM

The purpose of irradiating a second aluminium target was to identify induced nuclides and quantify their residual activity. Analogous to the previous, experimental data were intended to be used for the validation of the simulated results provided by the FLUKA code. Recent observations of the impact of the transition between the interaction models were considered as an additional perspective of this study on which it was necessary to focus. With this in mind, an approach of a detailed study of the application of the Boltzmann master equation as the only nucleus-nucleus interaction model used in the calculations was chosen. For this reason, the initial energy of the uranium beam used for the irradiation of the second aluminium target was planned to yield 100 MeV/u. This initial energy was considered also for the experimental target designing and the preparation of all foils used in stacked-foils geometry (as listed in Table 10). Unfortunately, technical complications on the SIS-18 caused an unstable operation of the synchrotron at the desired energy, resulting in the lowest possible energy of 125 MeV/u. SRIM and ATIMA were used for a quick estimation of the new range of the primary particles, including the energy losses in the vacuum window and in the air gap. These calculations assured us that the total thickness of the target of 1.6 mm is still sufficient to stop the entire beam inside the target, although the initial energy of the primary particles increased by 25 MeV/u. Using only experimental foils of 0.1 mm thickness each to construct the target has proven to be the appropriate design since the good resolution in the range region was not lost in spite of the longer range of the particles with higher energy. On this basis, the irradiation of the target was performed even though it was evident that a significant part of the residual activity depth profiles downstream of the range will be missing. On the other hand, the most important evidence of the transition difficulties between the nucleus-nucleus interaction models was previously observed in the region upstream of the range and this part of the depth profiles is also available considering the changed conditions.

Table 10: Configuration of the aluminium experimental target

	Aluminium target irradiated by 125 MeV/u ^{238}U								Thickness [mm]	Diameter [mm]
[Foil number] Foil thickness [mm]	[1] 0.1	[2] 0.1	[3] 0.1	[4] 0.1	[5] 0.1	[6] 0.1	[7] 0.1	[8] 0.1	1.6	100.0
	[9] 0.1	[10] 0.1	[11] 0.1	[12] 0.1	[13] 0.1	[14] 0.1	[15] 0.1	[16] 0.1		

The experimental target was irradiated by ^{238}U^{89+} beam with an energy of 125 MeV/u. As before the target was made of 99.95% pure aluminium with a density of 2.7 g/cm^3 at 20°C. Bunches of primary ions were delivered from the synchrotron SIS-18 in the fast-extraction regime for about 2 hours. In total, an accumulated charge of 1.69×10^{-5} C, which corresponds to 1.18×10^{12} ions, was induced into the target. The gamma-spectroscopic measurements were performed in three sets: (1st) 16 – 34 days, (2nd) 128 – 144 days and (3rd) 260 – 285 days after the end of the irradiation. Contrary to the experiment, the 1.6 mm thick target used for the simulated residual activities consisted of 70 equally thick foils instead of 16. This higher number of foils in the simulation provides a better depth resolution compared the experimental target.

3.4.1 QUANTIFIED RESIDUAL ACTIVITIES OF OBSERVED NUCLIDES

The depth profiles of about 180 gamma lines were constructed from the three sets of recorded gamma spectra and about 90 possible candidates for their production were identified. Unfortunately, the high complexity of the decay schemes of the identified nuclides in combination with the influence of technical complications during the irradiation allowed us to confidently analyse only a small fraction (8 out of 180) of the total number of the depth profiles. The residual activities of 8 nuclides are presented in Table 11. The values of the activity were determined by numerical integration of the depth profiles, which are collected in Appendix 2 (Figure 113–Figure 120).

Table 11: Identified isotopes and their activities in the aluminium target irradiated by 125 MeV/u uranium beam. A_1, A_2, A_3 – activity, σ_1, σ_2, σ_3 – uncertainty of the measured activity including detector-efficiency calibration uncertainty and net-peak-area uncertainty. Activities are extrapolated to the end of the irradiation. Subscript "1", "2" and "3" are related to the spectrum measured 16-34, 128-144 and 260-285 days after the end of the irradiation, respectively. The abbreviation "INFL" is used for nuclides whose activity determination was restraint due to the influence of another nuclide, "MDA" is marking a missing value of the residual activity due to decaying below the minimum detectable activity. "AVRG" corresponds to an average residual activity determined from several gamma lines of the same radioactive nuclide.

Nuclide	Half-time [d]	Energy [keV]	A_1 [Bq/ion]	σ_1 [%]	A_2 [Bq/ion]	σ_2 [%]	A_3 [Bq/ion]	σ_3 [%]
^{7}Be	53.12	477.6	7.88E-11	8.47	7.38E-11	22.35	MDA	
^{22}Na	949.96	1274.53	2.62E-12	18.04	3.99E-12	15.78	3.71E-12	19.28
^{46}Sc	83.79	889.28	1.03E-12	17.11	6.48E-13	28.8	MDA	
^{113}Sn	115.09	391.69	7.65E-12	4.96	9.23E-12	6.27	7.31E-12	9.43
^{124}Sb	60.2	602.73	8.41E-12	4.59	5.79E-12	10.99	MDA	
		1690.98	INFL		5.38E-12	22.02	MDA	
		AVRG	8.41E-12		5.59E-12			
^{127}Xe	36.4	202.86	3.82E-11	1.4	3.66E-11	5.58	4.22E-11	19.35
		374.99	2.94E-11	5.89	4.76E-11	17.58	MDA	
		AVRG	3.38E-11		4.21E-11		4.22E-11	
^{139}Ce	137.64	165.86	7.98E-12	2.09	1.10E-11	2.52	9.25E-12	3.1
^{144}Pm	363	696.51	INFL		1.05E-12	14.89	1.03E-12	16.85

3.4.2 COMPARISON OF EXPERIMENTAL DATA TO THE SIMULATION

A method of the numerical integration of the depth profiles of the residual activity was used for both experimentally measured and numerically determined by the FLUKA code. An average value of the residual activity was taken into account in the cases of those nuclides with several depth profiles obtained from different gamma peaks or from different sets of the measurements. A validation of the simulation code is based on the comparison of the measured and the calculated residual activity values. Their ratio provides a practical solution for getting a fast overview about the simulation overestimate or underestimate of the experimental data as presented in Figure 33.

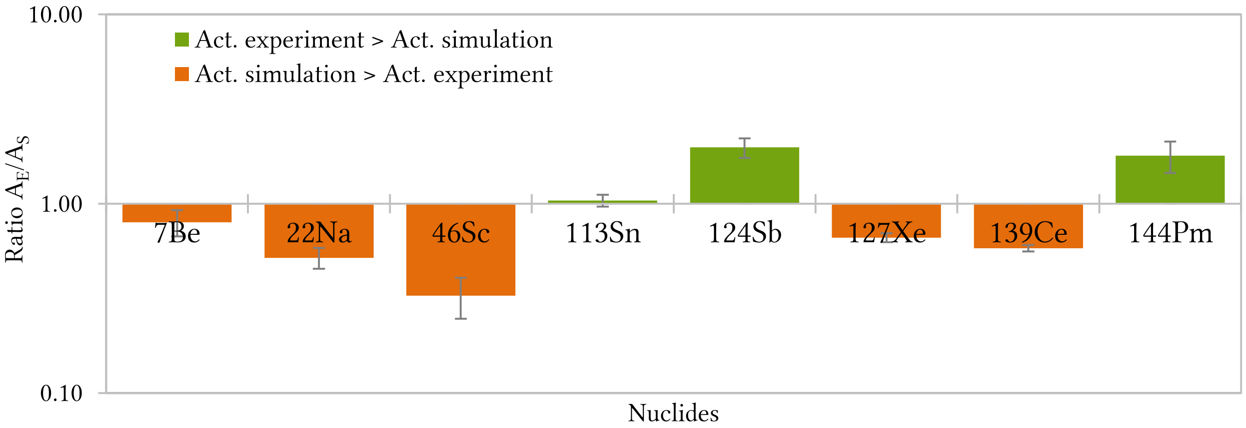

Figure 33: Ratio A_E/A_S of the residual activities of nuclides induced in the aluminium target after the irradiation by ^{238}U beam with an energy of 125 MeV/u, where A_E denotes the calculated value from the experimental data and A_S that calculated by the FLUKA code.

An enormous amount of the depth profiles were affected by the significant change of the range of the uranium ions with the energy of 125 MeV/u, compared to previously planned 100 MeV/u, and therefore their application in practice was no longer possible. Discrepancies between the residual activities of the remaining nuclides vary by factors ranging between 0.33 ± 0.08 and 1.98 ± 0.24, where these extreme values correspond to the ^{46}Sc and ^{124}Sb, respectively. On the other hand, a very good agreement was found in the case of ^{113}Sn, where the "A_E/A_S" ratio is equal to 1.04 ± 0.08.

3.4.3 OBSERVED DISPARITIES BETWEEN EXPERIMENTAL AND SIMULATED DATA

As it was already mentioned, after the observation of the influence of the transition between the nucleus-nucleus interaction models used in the code on the numerically determined results, special attention was paid to the analysis of the ^{7}Be and ^{22}Na nuclides. Their residual activity depth profiles were not possible to capture completely due to the shifting of the range of the primary ions caused by the increase of the initial uranium beam energy. Nevertheless, the parts of the depth profiles upstream of the range are sufficient and we can study the precision of the prediction of inducing these nuclides. The production of the radioactive nuclei corresponds to the fragmentation of the primary ions and target atoms. Therefore, the precision of the simulation results is limited by the Boltzmann master equation providing nucleus-nucleus interactions of primary and secondary particles on their penetration path until they lose their entire energy and finally stop in the target.

The depth profiles of the residual activity of the ^{7}Be and ^{22}Na induced in the aluminium target irradiated by 125 MeV/u uranium ions are presented in Figure 34 and Figure 35, respectively. The shapes of both depth profiles are similar; starting from the first foil, the residual activity increases monotonously until a depth of about 1.25 mm, at which the ^{7}Be, as well as the ^{22}Na reached their maximum. From that point on, the residual activity decreases until the end of the experimental target. Unfortunately, the technical problems during irradiation, as well as by the time limitation for the gamma spectroscopic measurement of the experimental foils (which did not allow to detect enough decay events of the nuclides). Thus, all complications together resulted in error bars as large as about 20 % of the experimental data points. Under these circumstances, a quantitative analysis would not be appropriate, but a qualitative comparison of the shapes of the depth profiles is sufficient. The residual activity of the investigated nuclides is mostly uniform in the whole area upstream of the range. In contrary to the calculated results, the measured results present a decrease of the residual activity whenever the simulated depth profiles reached their maximum. It is obvious from this comparison that the depth profiles determined from the experiment and provided by the FLUKA code have not a common behaviour. With this in mind, we can propound the conclusion that BME interaction model should be improved by FLUKA developers.

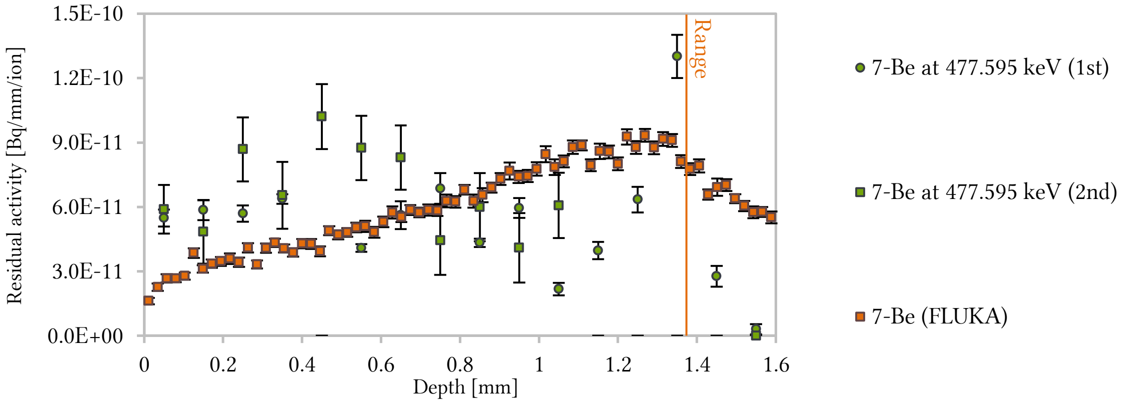

Figure 34: The depth profile of ^{7}Be in the aluminium target irradiated by 125 MeV/u ^{238}U beam.

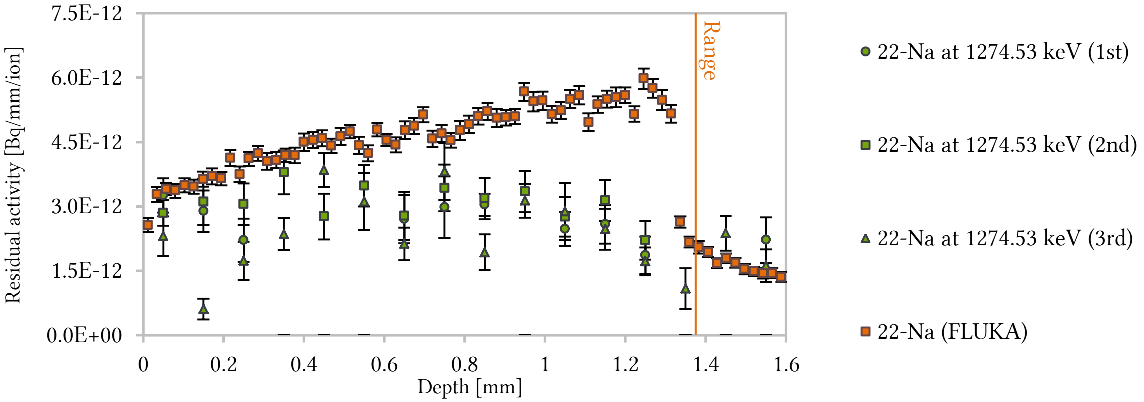

Figure 35: The depth profile of ^{22}Na in the aluminium target irradiated by 125 MeV/u ^{238}U beam.

3.5 ACTIVATION OF THE ALUMINIUM TARGET BY THE 300 MeV/u XENON BEAM

Along similar lines, a third aluminium target was irradiated. The main aim of this experiment was to study the activation of the constructing materials by different kinds of heavy-ion beams. In the light of the previously found evidences questioning the precision of the FLUKA calculations, the purpose of this experiment was extended to investigate the creditability of the nucleus-nucleus interaction models.

The experimental target was activated by a $^{124}Xe^{48+}$ beam with an energy of 300 MeV/u. The irradiation took one and half hour and this time was sufficient to collect 2.49×10^{12}, which corresponds to an accumulated charge of 1.91×10^{-5} C. The used target material was the same as in previous experiments (aluminium, 99.95% purity, 2.7 g/cm^3 density at 20°C). The stopping range of 300 MeV/u xenon ions in aluminium amounts to 10.070 ± 0.001 mm according to the FLUKA simulations, 10.300 ± 0.011 mm according to ATIMA and 10.382 ± 0.026 mm according to SRIM. The foils with the thickness of 1.0 mm were placed at the beginning and at the end of the experimental target. A good depth-resolution in the range area was ensured by 0.1 mm thick foils (see Table 12).

Table 12: Configuration of the aluminium experimental target

	Aluminium target irradiated by 300 MeV/u ^{124}Xe									Thickness [mm]	Diameter [mm]
[Foil number] Foil thickness [mm]	[1]	[2]	[3]	[4]	[5]	[6]	[7]	[8]	[9]	25.3	50.0
	1.0	1.0	1.0	1.0	1.0	1.0	1.0	1.0	1.0		
	[10-14]	[15]	[16]	[17]	[18]	[19]	[20]	[21]	[22]		
	0.5	0.1	0.1	0.1	0.1	0.1	0.1	0.1	0.1		
	[23]	[24]	[25]	[26]	[27]	[28-32]	[33-37]	[38-42]	[43-47]		
	0.1	0.1	0.1	0.1	0.1	0.5	0.5	0.5	0.5		
	[48-52]	[53-57]	[58-62]	[63]	[64]	[65]	[66]	[67]	[68]		
	0.5	0.5	0.5	1.0	1.0	1.0	1.0	1.0	1.0		
	[69]	[70]	[71]	[72]	[73]						
	1.0	1.0	1.0	1.0	1.0						

Three complete sets of gamma-spectroscopic measurements of all experimental samples were acquired: (1st) 9 - 38 days, (2nd) 218 - 293 days and (3rd) 378 – 505 days after the end of the irradiation. The simulated residual activities were obtained from the irradiation of an equally long aluminium target (25.3 mm) consisting of 70 equally thick foils (0.36 mm).

3.5.1 QUANTIFIED RESIDUAL ACTIVITIES OF OBSERVED NUCLIDES

The acquisition of three sets of gamma spectra was sufficient for observing about 120 different gamma lines. The subsequent analysis identified 42 nuclides with the different energy of the produced gamma lines, the radionuclide abundance and the half-life time. Unfortunately, some of the nuclides should have been excluded due to their complicated decay schemes of identical or overlapping gamma peaks. At the end of the evaluation, depth profiles of residual activity of about 30 nuclides were chosen for future investigations. They are collected in Appendix 3, starting from Figure 121 up to Figure 159. As before the numerical integration was used for determination of the residual activity of all gamma quants of each nuclide, see Table 13.

Table 13: Identified isotopes and their activities in the aluminium target irradiated by 300 MeV/u xenon beam. A_1, A_2, A_3 – activity, σ_1, σ_2, σ_3 – uncertainty of the measured activity including detector-efficiency calibration uncertainty and net-peak-area uncertainty. Activities are extrapolated to the end of the irradiation. Subscript "1", "2" and "3" are related to the spectrum measured 9-38, 218-293 and 378-505 days after the end of the irradiation, respectively. The abbreviation "INFL" is used for nuclides whose activity determination was restraint due to the influence of another nuclide, "MDA" is marking a missing value of the residual activity due to decaying below the minimum detectable activity. "AVRG" corresponds to an average residual activity determined from several gamma lines of the same radioactive nuclide.

Nuclide	Half-time [d]	Energy [keV]	A_1 [Bq/ion]	σ_1 [%]	A_2 [Bq/ion]	σ_2 [%]	A_3 [Bq/ion]	σ_3 [%]
^{7}Be	53,12	477,6	9,05E-10	2,77	5,56E-10	6,83	MDA	
^{22}Na	950,32	1274,5	8,43E-11	3,39	4,67E-11	2,61	4,63E-11	2,5
^{46}Sc	83,79	889,28	2,58E-11	6,53	5,02E-12	20,97	MDA	
		1120,55	2,76E-11	6,97	2,98E-13	21,07	MDA	
		AVRG	2,67E-11		2,66E-12			
^{48}V	15,97	944,1	9,33E-11	15,88	MDA		MDA	
		983,52	1,44E-10	4,51	MDA		MDA	
		1312,1	1,46E-10	4,58	MDA		MDA	
		AVRG	1,28E-10					
^{52}Mn	5,59	744,23	2,68E-10	11,73	MDA		MDA	
		935,54	2,81E-10	10,38	MDA		MDA	
		1434,07	2,61E-10	10,55	MDA		MDA	
		AVRG	2,70E-10					
^{54}Mn	312,3	834,85	INFL		4,40E-12	11,26	4,62E-12	8,78
^{56}Co	77,27	846,77	8,82E-12	8,16	1,09E-12	37,06	MDA	
		1238,28	1,13E-11	12,11	MDA		MDA	
		AVRG	1,01E-11		1,09E-12			
^{58}Co	70,86	810,78	4,38E-11	3,11	1,62E-11	13,1	8,12E-12	27,57
^{65}Zn	244,26	1115,55	1,41E-11	12,11	1,25E-11	12,49	1,13E-11	12,68
^{75}Se	119,78	96,73	1,85E-11	20,51	MDA		MDA	
		121,12	8,83E-11	4,28	6,59E-11	4,54	MDA	
		136	5,19E-11	3,18	3,30E-11	3,34	4,29E-11	4,53
		264,66	5,24E-11	3,82	3,74E-11	4,09	4,35E-11	5,95
		400,66	5,08E-11	9,85	4,30E-11	13,08	4,47E-11	17,76
		AVRG	5,24E-11		4,48E-11		6,00E-11	
^{77}As	17,77	595,85	6,21E-11	6,46	MDA		MDA	
		637,78	4,43E-11	16,07	MDA		MDA	
		AVRG	5,32E-11					
^{83}Rb	86,2	520,39	1,09E-10	2,94	9,26E-11	5,21	9,98E-11	9,39
		529,64	1,57E-10	3,12	9,33E-11	7,29	9,60E-11	14,06
		552,63	1,00E-10	5,92	8,54E-11	11,96	7,31E-11	23
		AVRG	1,22E-10		9,04E-11		8,96E-11	
^{84}Rb	32,77	881,61	1,55E-11	10,62	MDA		MDA	
^{87}Y	3,33	484,81	4,45E-09	3,02	MDA		MDA	
^{88}Y	106,65	898,04	2,48E-11	4,94	1,52E-10	2,2	2,13E-10	2,48
		1836,06	2,40E-11	5,75	1,59E-10	2,67	2,08E-10	2,78
		AVRG	2,44E-11		1,56E-10		2,11E-10	
^{95m}Tc	61	204,12	1,31E-11	8,83	3,38E-12	37,16	MDA	
^{95}Nb	34,98	765,79	8,85E-13	25,42	MDA		MDA	

Nuclide	Half-time [d]	Energy [keV]	A_1 [Bq/ion]	σ_1 [%]	A_2 [Bq/ion]	σ_2 [%]	A_3 [Bq/ion]	σ_3 [%]
^{96}Tc	4,28	778,22	5,67E-10	5,49	MDA		MDA	
		849,93	5,06E-10	6,17	MDA		MDA	
		AVRG	5,37E-10					
^{97}Ru	2,9	215,72	3,31E-09	3,69	MDA		MDA	
		324,48	1,57E-09	17,54	MDA		MDA	
		AVRG	2,44E-09					
^{97}Y	3,33	388,53	3,54E-09	3,69				
^{99}Rh	16,1	175,43	3,66E-10	15,94	MDA		MDA	
		353,05	8,57E-11	10,39	MDA		MDA	
		AVRG	2,26E-10					
^{100}Pd	3,63	75	2,20E-09	2,38	MDA		MDA	
		84	4,25E-09	6,95	MDA		MDA	
		AVRG	3,23E-09					
^{100}Rh	0,87	539,51	1,71E-03	5,12	MDA		MDA	
		588,34	4,49E-04	21,43	MDA		MDA	
		822,65	1,96E-04	35,21	MDA		MDA	
		1107,22	9,98E-04	11,38	MDA		MDA	
		1362,15	1,05E-03	12,28	MDA		MDA	
		1553,35	1,05E-03	8,33	MDA		MDA	
		1929,81	1,09E-03	11,44	MDA		MDA	
		AVRG	9,35E-04					
^{101m}Rh	4,34	306,86	4,06E-09	1,28	MDA		MDA	
		454,4	2,45E-09	9,93	MDA		MDA	
		AVRG	3,26E-09					
^{101}Rh	1205,29	127,23	INFL		8,11E-13	15,39	9,51E-13	9,81
		197,99	1,89E-12	22,86	1,35E-12	16,31	1,62E-12	12,09
		AVRG	1,89E-12		1,08E-12		1,29E-12	
^{105}Ag	41,29	63,98	3,49E-10	4,04	6,92E-11	7,47	7,96E-11	6,57
		331,51	3,33E-10	7,35	MDA		MDA	
		344,52	3,79E-10	1,29	3,05E-10	7,76	2,34E-10	32,97
		360,66	4,90E-11	22,45	MDA		MDA	
		370,17	2,74E-10	20,72	MDA		MDA	
		443,37	2,63E-10	3,89	2,30E-10	14,99	MDA	
		644,55	3,16E-10	3,48	1,81E-10	21,67	MDA	
		650,72	3,07E-10	8,7	MDA		MDA	
		673,21	2,55E-10	16,06	MDA		MDA	
		1087,94	3,20E-10	7,75	7,21E-11	51,11	MDA	
		AVRG	2,85E-10		1,71E-10		1,57E-10	
^{106m}Ag	8,28	221,7	2,47E-10	13,91	MDA		MDA	
		228,63	1,30E-10	27,86	MDA		MDA	
		406,17	2,66E-10	8,62	MDA		MDA	
		429,64	2,84E-10	8,65	MDA		MDA	
		450,97	2,70E-10	4,6	MDA		MDA	
		616,17	3,07E-10	6,72	MDA		MDA	
		703,11	2,08E-10	22,93	MDA		MDA	
		717,24	2,93E-10	4,97	MDA		MDA	
		748,44	2,73E-10	5,36	MDA		MDA	
		793,3	2,47E-10	18,04	MDA		MDA	
		804,34	1,72E-10	13,67	MDA		MDA	
		808,37	2,10E-10	14,85	MDA		MDA	
		1045,83	2,32E-10	6,82	MDA		MDA	
		1119,39	2,63E-10	10,99	MDA		MDA	
		1128	3,83E-10	8,81	MDA		MDA	
		1222,88	2,64E-10	17,56	MDA		MDA	
		1527,65	2,63E-10	9,63	MDA		MDA	
		1572,35	1,51E-10	18,57	MDA		MDA	
		AVRG	2,48E-10					

Nuclide	Half-time [d]	Energy [keV]	A_1 [Bq/ion]	σ_1 [%]	A_2 [Bq/ion]	σ_2 [%]	A_3 [Bq/ion]	σ_3 [%]
^{110m}Ag	249,79	573,36	7,86E-06	0,35	3,22E-08	6,81	2,37E-08	6,79
^{111}In	2,8	171,28	7,75E-09	1,48	MDA		MDA	
		245,39	8,70E-09	1,55	MDA		MDA	
		AVRG	8,23E-09					
^{113}Sn	115,09	255,05	1,63E-10	15,66	1,60E-10	8,66	1,51E-10	16,26
		391,69	2,10E-10	1,03	1,75E-10	1,01	1,45E-10	1,37
		AVRG	1,87E-10		1,68E-10		1,48E-10	
^{117m}Sn	13,6	158,56	1,28E-11	12,23	MDA		MDA	
^{119m}Te	4,7	153,59	1,03E-09	1,45	MDA		MDA	
		270,53	1,02E-09	3,46	MDA		MDA	
		942,21	9,42E-10	10,07	MDA		MDA	
		976,37	2,46E-10	38,42	MDA		MDA	
		1013,2	6,49E-10	26,16	MDA		MDA	
		1081,35	1,00E-09	18,59	MDA		MDA	
		1095,75	1,05E-09	18,41	MDA		MDA	
		1136,75	1,00E-09	7,24	MDA		MDA	
		1212,73	1,05E-09	2,16	MDA		MDA	
		2089,57	9,65E-10	9,35	MDA		MDA	
		AVRG	8,95E-10					
^{120m}Sb	5,76	89,9	7,28E-11	6,53	MDA		MDA	
		1171,3	5,97E-12	29,1	MDA		MDA	
		AVRG	3,94E-11					
^{121m}Te	154	212,19	5,81E-12	7,34	6,37E-12	6,22	6,41E-12	7,01
^{121}Te	16,78	470,47	2,25E-09	3,35	MDA		MDA	
		507,59	8,82E-10	1,16	MDA		MDA	
		AVRG	1,57E-09					
^{124}I	4,18	602,73	1,24E-10	10,24	MDA		MDA	

3.5.2 COMPARISON OF EXPERIMENTAL DATA TO THE SIMULATION

In a similar manner as it was done in previous experiments, a comparison of the experimentally measured and the simulated residual activity of individual nuclides are displayed as a graphical interpretation of their ratio in Figure 36. The residual activity of some nuclides was only acquired from gamma spectroscopic measurements, while the FLUKA simulations did not predict any activity. In particular, this was the case of all isometric nuclides ^{95m}Tc, ^{101m}Rh, ^{106m}Ag, ^{110m}Ag, ^{117m}Sn, ^{119m}Te, ^{120m}Sb, ^{121m}Te. A validation of the FLUKA code revealed an incident of the nuclide ^{100}Rh, during which several gamma lines of this gamma source were confidently detected and identified, but the simulation estimates its activity about three magnitudes lower. For this reason, these nuclides were excluded from Figure 36. It is apparent that FLUKA overestimates the residual activity of the majority of all observed nuclides. Nevertheless, the ratios of several nuclides indicate a good agreement between measured and simulated activities by their value close to unity: ^{100}Pd ($A_E/A_S = 1.02 \pm 0.06$), ^{113}Sn ($A_E/A_S = 0.91 \pm 0.02$), ^{111}In ($A_E/A_S = 1.10 \pm 0.02$) and ^{87}Y ($A_E/A_S = 1.14 \pm 0.04$). The ratios between experimental and numerical residual activities of all other nuclides vary between 0.11 ± 0.01 and 4.94 ± 0.24. These extreme values caused by the overestimation and the underestimation of the activity by the FLUKA code belong to ^{101}Rh and ^{88}Y nuclides, respectively.

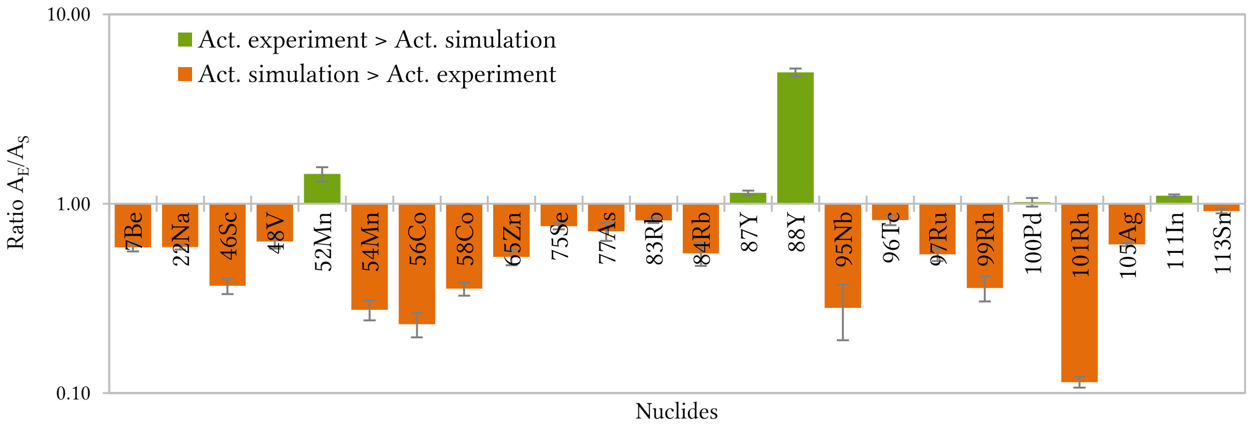

Figure 36: Ratio A_E/A_S of the residual activities of nuclides induced in the aluminium target after the irradiation by ^{124}Xe beam with an energy of 300 MeV/u, where A_E denotes the calculated value from the experimental data and A_S that calculated by the FLUKA code.

3.5.3 OBSERVED DISPARITIES BETWEEN EXPERIMENTAL AND SIMULATED DATA

Special attention was paid to the investigation of the depth profiles of ^{7}Be and ^{22}Na since significant discrepancies of the simulated residual activities of the target-nuclei fragments have been observed in previous experiments. The previous findings suggest that the precision of the FLUKA code is lower when it comes to the calculation of heavy-ion interactions with energies from energy band, employing both the Relativistic Quantum Molecular Dynamics (RQMD) and the Boltzmann Master Equation (BME) nucleus-nucleus interaction models as well as when the interactions are controlled only by BME below this energy band. Simulations were executed with the default settings of FLUKA; in other words, an RQMD-BME changeover was realized within energy band of 125 MeV/u ± 25 MeV/u. The depth profiles of the residual activity of ^{7}Be and ^{22}Na are displayed in Figure 37 and in Figure 38. For the sake of clarity, the simulations were coupled with the SRIM calculation providing the kinetic energy dependency of the primary particles on the penetration depth. Its graphical interpretation is included in both depth profiles as an additional green curve, labelled E = f(depth). Experimentally measured residual activities of all sets of measurement are exceptionally matching each other in the cases of both nuclides. Measured depth profiles of ^{7}Be and ^{22}Na have a very similar shape. The residual activity is homogenously increasing starting from the depth of 0.5 mm (the first target foil) until the foil placed in the depth of 9.55 mm, at which the highest activities were induced. Specifically, the residual activity of ^{7}Be is 8.80×10^{-11} Bq/mm/ion and ^{22}Na achieved 5.68×10^{-12} Bq/mm/ion at this depth. A great depression of the residual activity on the length of just a few hundredths of micrometres (about three foils) was captured by the thinnest foils located in the range region between the depth of 9.75 and 10.05 mm. Afterwards, the residual activity is almost constant in all foils in the region downstream of the range. The simulated residual activities of both nuclides have some common contours with the experimental depth profiles. They both are in good agreement with the experimental values in the foils located in the region upstream of the range. The FLUKA simulation reliably follows the trend of the residual activity increase within the region upstream of the range. A similar conclusion is valid also for the region downstream of the range, where the simulated depth profiles display a comparable shape as the experimental ones, but the calculated values are slightly overestimated. Comparing the depth profile range regions of both nuclides, the overestimating of the residual activity is less than a factor of 2 for both.

At this stage of the FLUKA code validation is possible to identify the origins of the simulation difficulties. FLUKA provided an almost ideal prediction of the residual activity as long as only the RQMD interaction model is used. The discrepancies between the simulated and experimental depth profiles appear at the depth of about 6.5 mm in the case of ^{22}Na and about of 8.5 mm in the case of ^{7}Be. These locations correspond to the depth where the primary xenon ions achieve the kinetic energy of 150 MeV/u and 100 MeV/u, respectively. The kinetic energy as a function of the depth was calculated by the SRIM code and it is displayed as the green curve in Figure 37 and in Figure 38. Further evidence supports the assumption based on the findings of previous experiments, because these energies are again identical to the border values of the energy band of 125 MeV/u ± 25 MeV/u used for the transition between RQMD and BME interaction models.

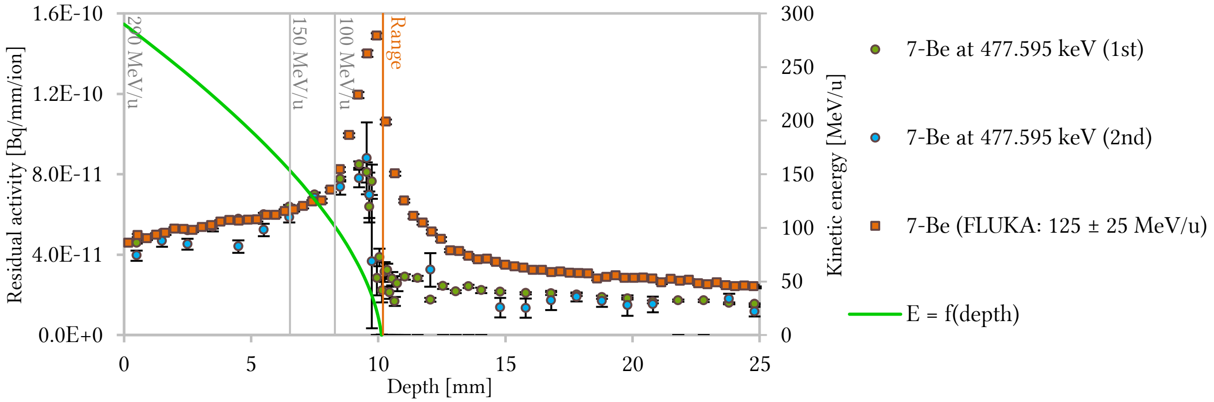

Figure 37: The depth profile of ^{7}Be in the aluminium target irradiated by 300 MeV/u ^{124}Xe beam and the kinetic energy of the primary particles as a function of the depth calculated by SRIM code.

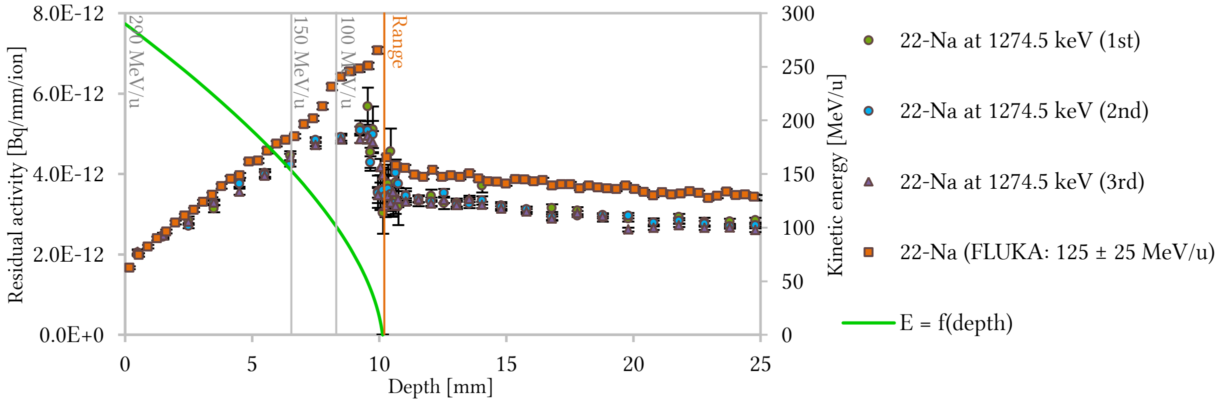

Figure 38: The depth profile of ^{22}Na in the aluminium target irradiated by 300 MeV/u ^{124}Xe beam and the kinetic energy of the primary particles as a function of the depth calculated by SRIM code.

The analysis of the depth profiles of nuclides induced in the aluminium target irradiated by 300 MeV/u ^{124}Xe beam discovered also unusual deviations between the simulated results and the measured data. FLUKA predicts an artificial increase of the residual activity in a small region downstream of the range of the primary particles. An observation concerns the depth profiles of ^{46}Sc, ^{48}V, ^{52}Mn, ^{54}Mn, ^{56}Co, ^{58}Co, ^{65}Zn. Previous experimental studies of the primary particle range showed that the peaks located in the range region are produced by those projectiles that get fragmented shortly before they lose all their kinetic energy

[21, 23]. This motivated us to study the production rates of the fragments produced by ^{124}Xe passing through an aluminium foil. The production rate of about 30 fragments with mass numbers between 46 and 124 was simulated as the number of the fragments exiting the back surface of the foil. A study was performed as a set of several simulations of the xenon beam of the same intensity, but with different energies from a range between 25 MeV/u and 300 MeV/u. In order to ensure identical conditions for all beams with different energies, the thicknesses of the foil had to be set individually for each simulation. The stopping power calculation served for the determination of the depth causing the loss of 10 % of the kinetic energy of the primary particles in the aluminium material. The main practical reason to do so was the elimination of the influence of the foils size on the production rate. In this manner, any fluctuation of the production of the studied nuclides could be judged as a product of the physical models only.

Indeed, the monitoring of the production rate of the different fragments showed that FLUKA is calculating a significant increase of the fragments production at low energies. Figure 39 displays graphs of the production of three projectile fragments. All three curves exhibit a similar behaviour; production rates are almost constant for beams with energies between 200 MeV/u and 300 MeV/u. Another interesting observation is the fact that an increase of the production appears in case of all investigated fragments. The highest production rate of ^{46}Sc is created by the beam with an energy of 80 MeV/u and in the case of ^{88}Y it is close to the beam energy of 30 MeV/u. The peak of the production-rate of ^{105}Ag is not completely pronounced because the simulations were not done below 25 MeV/u, but the figure shows that the production rate is increasing for beams with the lowest simulated energies. It can be concluded that the FLUKA calculations are affected by the artificial increase of the fragment production, with the production rate peak depending on the mass number. The higher Z the more the production-rate peak is shifted to lower energies.

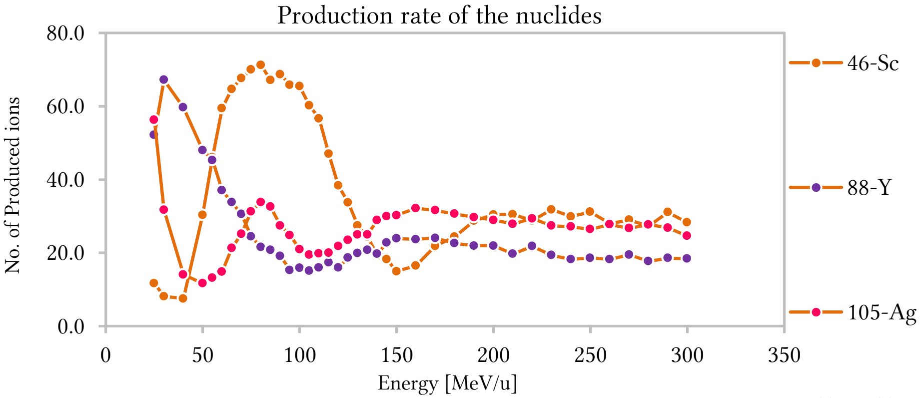

Figure 39: The production rates of the fragments with different mass number (^{46}Sc, ^{88}Y and ^{105}Ag) calculated by FLUKA.

The available observations seem to suggest that the depth profiles of all projectile fragments are affected. Therefore, it should be explained, why the artificial peaks of the residual activity are only visible in the case of intermediate Z fragments. A possible interpretation can be demonstrated by the nuclide ^{48}V (see Figure 40). Firstly, it should be clarified that the production rates were calculated for beams with the energy up to 300 MeV/u. After taking into account the energy losses of the primary ions in the vacuum window and in the air gap, it was determined that the xenon beam is colliding with the target with an energy of about

280 MeV/u. This point is represented by a green cross in Figure 40. The graphical interpretation of the number of produced fragments as a function of the initial energy uncovered an explicit justification. There is a significant increase of the production rate of the ^{48}V fragments by the xenon beam with an initial energy of 75 MeV/u (a data point is marked as an orange cross). A closer look at the depth profile of the residual activity shows that the artificial peak is located at the depth of about 10.6 mm. If all presented assumptions are correct, we should be able to reconstruct the depth position as the combination of the thickness of the aluminium necessary for slowing down the primary xenon ions with an energy of 280 MeV/u down to 75 MeV/u (where the ^{124}Xe ions get fragmented and the ^{48}V are produced) and the range of the ^{48}V with an energy of 75 MeV/u in aluminium. From the stopping power calculations provided by ATIMA, it is possible to determine that the ^{124}Xe ions lose that amount of energy in 8.38 mm of aluminium and the range of the 75 MeV/u ^{48}V ions is 2.16 mm (which is an almost perfect match, because 8.38 + 2.16 = 10.54 mm). Consequently, the range of the 280 MeV/u ^{48}V (corresponds to situation when the ^{124}Xe ions get fragmented in the first target foil) in aluminium amounts to 19.67 mm. As we can see, the difference between the position of the artificial peak of residual activity and the longest possible penetration depth of ^{48}V is about 9 mm. This distinction is big enough to let the artificial residual activity to be pronounced as the peak in the depth profile. On the basis of the knowledge currently available, it is legitimate to presume that the overestimating of the residual activity by FLUKA is mostly noticeable in the case of intermediate Z nuclides (^{46}Sc, ^{48}V, ^{52}Mn, ^{54}Mn, ^{56}Co, ^{58}Co, ^{65}Zn) because the shape of the depth profile of the real induced activity is significantly wider than the depth profile of heavier nuclides. In the same manner, FLUKA is predicting an increase of the production of heavier fragments (^{73}As, ^{75}Se, ^{77}As, ^{83}Rb, ^{84}Rb, ^{88}Y, ^{89}Zr, ^{105}Ag, ^{111}In), but the deviation of the depth profiles is not so remarkable, because the heavier nuclides have a narrower shape. That leads to the disabling of a possibility to see the artificial residual activity as an individual peak of the depth profile.

Examples of three depth profiles of residual activity coupled with the graph of the production rate of the corresponding nuclides ^{48}V, ^{54}Mn and ^{58}Co are presented in Figure 40 up to Figure 42.

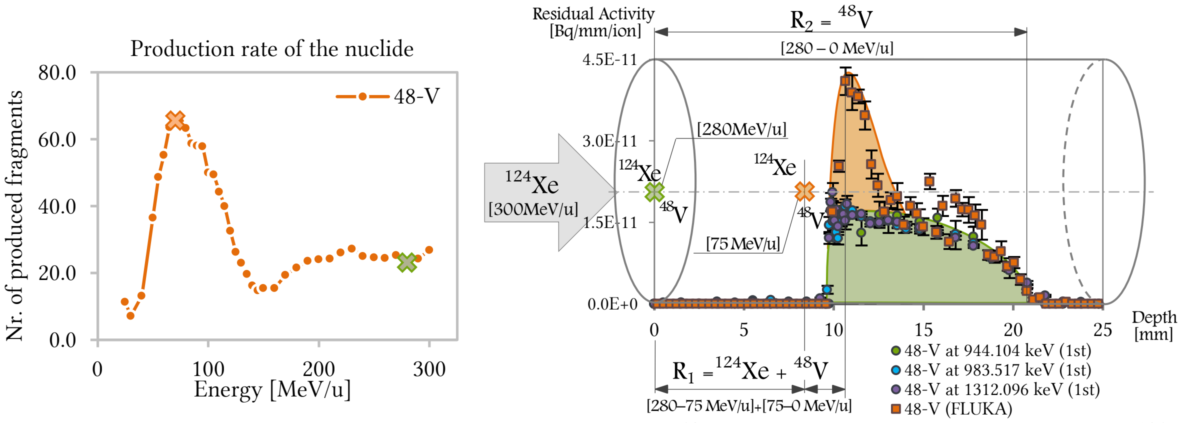

Figure 40: The depth profile of the residual activity of the ^{48}V in aluminium target irradiated by ^{124}Xe with an energy of 300 MeV/u (on the right side, inserted in a scheme of the target) and the production rate of the nuclide in thin foil (on the left side).

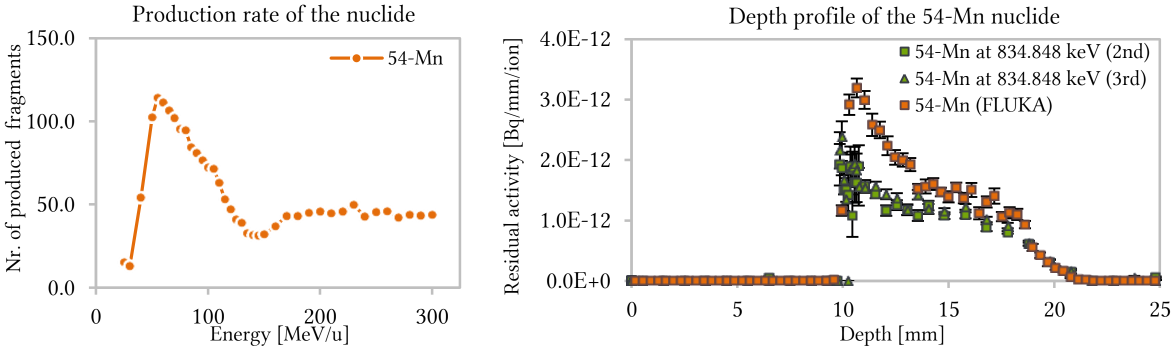

Figure 41: The depth profile of the residual activity of the ^{54}Mn in aluminium target irradiated by ^{124}Xe with an energy of 300 MeV/u (at the right) and the production rate of the nuclide in thin foil (at the left).

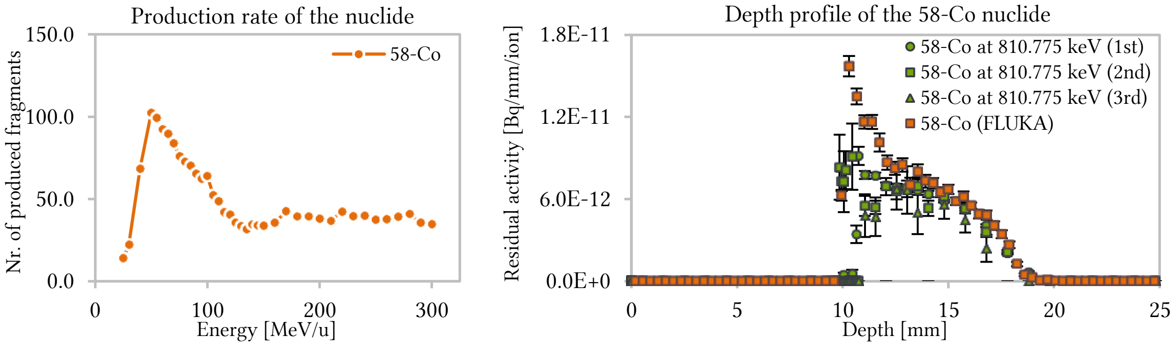

Figure 42: The depth profile of the residual activity of the ^{58}Co in aluminium target irradiated by ^{124}Xe with an energy of 300 MeV/u (at the right) and the production rate of the nuclide in thin foil (at the left).

3.6 SUMMARY OF THE ACTIVATION EXPERIMENTS

The irradiations of three aluminium targets by 200 MeV/u uranium ions, 125 MeV/u uranium ions and 300 MeV/u xenon ions were performed at SIS-18 at GSI Darmstadt. The gamma-spectroscopic measurements of the targets consisting of thin aluminium foils and their analysis were used as reference for the validation of the FLUKA simulation of the same experiments. It was demonstrated that the characteristic shape of the depth profiles contains valuable information about the physics of the activation processes. The depth profiles of residual activity of all identified nuclides induced in aluminium targets are presented in Appendix 1, 2, 3.

The detailed comparison of the measured to the simulated depth profiles of the residual activity of the ^{7}Be induced in aluminium target irradiated by 200 MeV/u revealed an imperfect transition between the nucleus-nucleus interaction FLUKA models. The shape of the depth profile of ^{7}Be contains some deformations pronounced as a local maximum and a local minimum of the residual activity in the region upstream of the range. These local extremes appeared at the depths which are identical to the depths at which the transition between the interactions models of the FLUKA code takes place. Following the study of the ^{22}Na showed the same observations of the influence of transition between Relativistic quantum molecular dynamics (RQMD) and Boltzmann master equation (BME) nucleus-nucleus interaction models on the calculated residual activity. The simulated residual activities of both nuclides are overestimated in the range region, insinuating a causation of abnormal results by BME interaction model also below the transition energy-band. In order to confirm the presented observations, a second aluminium target was irradiated by 125 MeV/u uranium ions. Compared to the shape of the depth profiles of the same nuclides gathered from the foregoing experiment, any local maximum or local minimum of the residual activity in the region upstream of the range did not appear. In fact, this result was expected since the highest kinetic energy of the primary ions at the surface of the first target foil is about 100 MeV/u due to energy losses in the vacuum window and the air gap. Therefore, the RQMD-BME transition is not influencing the shape of the depth profiles and only the BME model was in charge of executing the interactions happening in the whole target. Thus, an overestimation of the calculated residual activities of both nuclides in the range region is caused by the BME interaction model, similarly as it was in the previous experiment. The irradiation of third aluminium target by 300 MeV/u xenon ions have been performed in order to ensure the assumptions based on previous experiments. Thanks to the higher initial energy of primary ions it was possible to monitor the influence of the RQMD-BME transition on the simulated depth profiles. There were no local extremes in the region upstream of the range found in the case of ^{7}Be. Nevertheless, the discrepancies of the calculated residual activities are getting significantly bigger at the borders of the RQMD-BME transition energy-band. In particular, the shape of the ^{7}Be is affected by the depth where the xenon ions reach the kinetic energy of 100 MeV/u and 150 MeV/u in the case of ^{22}Na. FLUKA overestimates the residual activities of both nuclides also in the range region, where only BME nucleus-nucleus interaction is used. These observations brought us to the conclusion, that the Boltzmann master equation modulus of FLUKA is introducing discrepancies into the simulation. The differences between the experimental and calculated residual activities of both ^{7}Be and ^{22}Na are about a factor of 2 at the depth of the primary particles range. Similar results were enumerated for all three experiments. A closer look at the shapes of the depth profile of ^{7}Be from the 1st and the 3rd experiment (where imperfect transitions between

RQMD and BME interaction models were observed) rose up the question: Why do the local extremes appear only in the 1st experiment. Unfortunately, it is not possible to construct a satisfying answer out of the acquired data. On other hand, it was proven beyond any doubts, that the shape of the depth profiles of ^{7}Be and ^{22}Na are influenced by the transition between RQMD and BME interaction models. Moreover, it was shown that the appearance of the simulated data deviation is dependent on the transition energy-band settings. Nevertheless, the default settings of the FLUKA physics models or any of the user-specified settings, which were tested in this study, did not eliminate the discrepancies between experimental and calculated values of the residual activities of the target-nuclei fragments. On the basis of the evidences currently available, it is suggested that the transition between RQMD and BME interaction models, as well as BME interaction model must be inspected and improved by the FLUKA developers.

Another important observation of FLUKA imprecision is also related to the last experiment. Simulated depth profiles of several nuclides induced in the target by the xenon beam contain a peak-like deformation in the range region, which was not confirmed by experiment. A common parameter of all nuclides is their nuclide numbers which is between 40 and 70 (in particular: ^{46}Sc, ^{48}V, ^{52}Mn, ^{54}Mn, ^{56}Co, ^{58}Co, ^{65}Zn). The issue of the artificial peaks of the residual activity are caused by a wrong prediction of the production of nuclides, which was also found in another set of simulations. Production rates of all nuclides observed in the experiment were studied for various energies of xenon ions penetrating the aluminium foils of normalized thicknesses. These FLUKA calculations brought to light very clear explanation of the inaccurate energetic dependency of the production-rates of a problematic group of nuclides. For instance, FLUKA calculates the uniform production-rate of all nuclides by primary ions with the high kinetic energy. The situation changes when the xenon ions lose their energy down to about 100 MeV/u. The production-rate calculated by FLUKA below that energy is about the factor of 3 higher. An important observation is the fact that the increase of the production rate of each nuclide is caused by primary ions with different kinetic energies and also within a small energy range. Nevertheless, these nuclides are produced with the kinetic energy equal to the kinetic energy of the primary ions at the depth, where the fragmentation occurred. They appear in the depth profile of the residual activity as the peak at the point at which they lose their remaining energy. This is why, the observed artificial peaks of residual activity in the region downstream of the range. It should be clarified, that the increase of the production rate was found also in cases of heavier nuclides (^{73}As, ^{75}Se, ^{77}As, ^{83}Rb, ^{84}Rb, ^{88}Y, ^{89}Zr, ^{105}Ag, ^{111}In), but any special deformation of their depth profiles is not visible. This can be explained by the fact that the heavier the fragment, the narrower s the depth profile. In these particular cases, it seems like the real depth profile (measured and simulated) and the artificial peak of residual activity (simulated) has a similar width and it is not distinguishable as a deformation of the shape. Under these circumstances, it can be seen only as overestimating of the residual activity by FLUKA. This assumption is supported by the comparison of the numerically integrated areas of the experimentally acquired and the simulated depth profiles of the residual activities. Hence we can conclude that the FLUKA is providing the affected simulation results of the residual activity in the case of intermediate-Z fragments and also in the case of other heavier fragments.

Chapter Four

Simulations

4 Beam-loss Criteria for Heavy-ion Accelerators

The main concern of the accelerator operation is the hands-on maintenance of accelerator components, which requires a residual dose below a certain level, allowed by regulatory requirements for radiation exposure, before any reparation work may launch. The only available information suitable for heavy-ion accelerators are based on an empirical evaluation of the activation of the proton-machine components, where the uncontrolled beam losses of 1 W/m are considered as an acceptable threshold for the hands-on maintenance [2, 150]. An approach of scaling the existing limitations of the tolerable proton losses was used to specify the tolerable beam losses of heavy ions. The scaling factor was obtained as a ratio of the normalized activity induced by 1 GeV proton beam to the normalized activity induced by losses of hadron beams equivalent to a beam power of 1 W [4]. It is necessary to clarify that the main motivation for this work was to evaluate the first beam-loss criteria for heavy ions established by FLUKA 2008 as well as to expand the existing scaling law for lower energy ranges by the new version of the FLUKA code. An identical approach as chosen by the authors of the first beam-loss criteria for heavy ion machines was used. According to the release notes for FLUKA 2011 an updated version includes interactions of all projectiles with $A \geq 4$ on all targets at low-medium energies below 100 MeV/u [3]. This is possible due to an implementation of the Boltzmann Master Equation model for projectiles with energies lower than 125 MeV/u [3, 41]. In all other cases, settings and physical models were set identically to the calculations used for the first determination of the beam-loss criteria. The evaporation model with heavy-fragment evaporation was used. Emission of the high-energy light fragments through the coalescence mechanism was activated. The heavy-ion transport with nuclear interactions was switched on. Low-energy neutron transport was simulated down to thermal energies (10^{-5} eV), and residual nuclei from low-energy neutron interactions were scored. The FLUKA versions, which were released during the time of the performance of all calculations, were considered as a suitable computing tool to increase the precision of the beam-loss criteria. Code versions from FLUKA 2011.2b.5 up to 2011.2c.4 were used, but in order to dispel any doubts about correctness of presented results, an upgrade of installed code was done exclusively in-between the individual simulation packages (a simulation package can be understood as a set of calculations, where the combination of a target material and irradiation time are constant).

Accumulation and decay of an activity induced by different projectiles (^{1}H, ^{4}He, ^{12}C, ^{20}Ne, ^{40}Ar, ^{84}Kr, ^{132}Xe, ^{197}Au and ^{238}U) with energies between 1 GeV/u and 200 MeV/u were recalculated in the same fashion as it was done in the case of establishing of the first beam-loss criteria. Technical capabilities of FLUKA 2011 were exploited for a further expansion of the studied range of energies down to 25 MeV/u. A short-term activation of copper and stainless steel and long-term activation of copper were studied. The geometry of targets was designed as a 60 cm long cylinder with the diameter of 20 cm. This corresponds to the parameters of the bulk target used for determination of the first criteria. The beam-pipe calculations were not repeated since the first results introduced a less strict criterion for this kind of geometry. For example, the tolerable levels of the beam losses were enumerated as 75 W/m for 200 MeV/u and 12 W/m for 1 GeV/u uranium beams in the stainless steel pipe, while the criteria for the same beams were 60 W/m for 200 MeV/u and 5 W/m for 1 GeV/u in the bulk target. In reality, the structure of accelerator facilities is made of a combination of both target models, where the beam-pipes as well as magnet yokes and shielding should be taken into account. In terms of ALARA principle (As Low As Reasonable Achievable [81]) of a radiation protection, it makes more sense to focus on a stricter limitation, which is, in this particular case, the bulk-target geometry.

Table 14: Intensities of different beams equivalent to the beam power of 1 W.

[Number of particles per second]							
	1GeV/u	900 MeV/u	800 MeV/u	700 MeV/u	600 MeV/u	500 MeV/u	400 MeV/u
^{1}H	6.24×10^{9}	6.94×10^{9}	7.80×10^{9}	8.92×10^{9}	1.04×10^{10}	1.25×10^{10}	1.56×10^{10}
^{4}He	1.56×10^{9}	1.73×10^{9}	1.95×10^{9}	2.23×10^{9}	2.60×10^{9}	3.12×10^{9}	3.90×10^{9}
^{12}C	5.20×10^{8}	5.78×10^{8}	6.50×10^{8}	7.43×10^{8}	8.67×10^{8}	1.04×10^{9}	1.30×10^{9}
^{20}Ne	3.12×10^{8}	3.47×10^{8}	3.90×10^{8}	4.46×10^{8}	5.20×10^{8}	6.24×10^{8}	7.80×10^{8}
^{40}Ar	1.56×10^{8}	1.73×10^{8}	1.95×10^{8}	2.23×10^{8}	2.60×10^{8}	3.12×10^{8}	3.90×10^{8}
^{84}Kr	7.43×10^{7}	8.26×10^{7}	9.29×10^{7}	1.06×10^{8}	1.24×10^{8}	1.49×10^{8}	1.86×10^{8}
^{132}Xe	4.73×10^{7}	5.25×10^{7}	5.91×10^{7}	6.76×10^{7}	7.88×10^{8}	9.46×10^{7}	1.18×10^{8}
^{197}Au	3.17×10^{7}	3.52×10^{7}	3.96×10^{7}	4.53×10^{7}	5.28×10^{7}	6.34×10^{7}	7.92×10^{7}
^{238}U	2.62×10^{7}	2.91×10^{7}	3.28×10^{7}	3.75×10^{7}	4.37×10^{7}	5.25×10^{7}	6.56×10^{7}

[Number of particles per second]						
	300 MeV/u	200 MeV/u	150 MeV/u	100 MeV/u	50 MeV/u	25 MeV/u
^{1}H	2.08×10^{10}	3.12×10^{10}	4.16×10^{10}	6.24×10^{10}	1.25×10^{11}	2.50×10^{11}
^{4}He	5.20×10^{9}	7.80×10^{9}	1.04×10^{10}	1.56×10^{10}	3.12×10^{10}	6.24×10^{10}
^{12}C	1.73×10^{9}	2.60×10^{9}	3.47×10^{9}	5.20×10^{9}	1.04×10^{10}	2.08×10^{10}
^{20}Ne	1.04×10^{9}	1.56×10^{9}	2.08×10^{9}	3.12×10^{9}	6.24×10^{9}	1.25×10^{10}
^{40}Ar	5.20×10^{8}	7.80×10^{8}	1.04×10^{9}	1.56×10^{9}	3.12×10^{9}	6.24×10^{9}
^{84}Kr	2.48×10^{8}	3.72×10^{8}	4.95×10^{8}	7.43×10^{8}	1.49×10^{9}	2.97×10^{9}
^{132}Xe	1.58×10^{8}	2.36×10^{8}	3.15×10^{8}	4.73×10^{8}	9.46×10^{8}	1.89×10^{9}
^{197}Au	1.06×10^{8}	1.58×10^{8}	2.11×10^{8}	3.17×10^{8}	6.34×10^{8}	1.27×10^{9}
^{238}U	8.74×10^{7}	1.31×10^{8}	1.75×10^{8}	2.62×10^{8}	5.25×10^{8}	1.05×10^{9}

The theoretical premise behind scaling of the beam losses for protons to heavy-ions is that the unit beam-power of 1 W is defined as a number of the lost-particles hitting the accelerator structures each second [31]. This is important for all simulations; therefore, intensities of losses were calculated for each beam of interest. For instance, the loss of 6.24 x 10^9 protons per second with an energy of 1 GeV/u deposit the same energy to material as the loss of 1.05 x 10^9 uranium ions per second with an energy of 25 MeV/u, because both beams are equivalent to the beam power of 1 W (see Table 14).

4.1 BEAM-LOSS CRITERIA CALCULATED FOR A SHORT-TERM OPERATION

The induced activities of produced fragments in bulk targets were scored at several time points during and after the irradiation, in Table 15. The activation part took 100 days and it was monitored every 5 days. The decay time points were denser after the end of the irradiation in order to capture the decay of short-lived nuclides and their possible influence on the applicability of the scaling law after short cooling time. Two different target materials were studied, and the corresponding results are presented in the following subsections 4.1.1for copper and in 4.1.2 for stainless steel targets.

Table 15: The list of irradiation (0-100 days) and decay times (100.05-400 days) chosen for simulation of short–term operation.

Scoring time points [day]										
0.0	5.0	10.0	15.0	20.0	25.0	30.0	35.0	40.0	45.0	50.0
55.0	60.0	65.0	70.0	75.0	80.0	85.0	90.0	95.0	100.0	100.05
100.06	100.07	100.09	100.10	100.12	100.14	100.17	100.21	100.25	100.29	100.35
100.42	100.50	100.60	100.71	100.85	101.02	101.22	101.45	101.74	102.08	102.48
102.96	103.54	104.22	105.04	106.02	107.20	108.59	110.26	112.26	114.64	117.49
120.89	124.95	129.80	135.59	142.51	150.78	160.65	172.44	186.52	203.33	223.42
247.41	277.32	310.29	351.17	400.0						

4.1.1 COPPER BULK TARGET

As a first step of the beam-loss criteria evaluation the comparison of the nuclide inventory of induced fragments in identical bulk targets after an identical irradiation procedure was chosen. An example of the difference in results provided by FLUKA 2008 and FLUKA 2011 is displayed on Figure 43. Both nuclide inventories are representing the relative activities of most contributing fragments to total activity induced by different beams species during 100 days of irradiation and measured after 1 day of cooling. A quantitative observation is showing that the list of the main sources of radioactivity is the same for both FLUKA versions. Indeed, this was an expected impact of the code update on the simulated results since the parts of the code which underwent changes have expanded the calculation range of the nucleus-nucleus interactions into the range of the lower energies, but the probabilities of the interaction itself remained unchanged [3]. This is proven also by the analysis, where a closer look at the simulation results shows that the values of the relative activity of all nuclides are lower in the case of FLUKA 2011 version, whereas the nuclide production ratios of the different beams are almost identical to those observed by FLUKA 2008. For example, the relative activity of ^{64}Cu is about 5% lower in the case of all ion beams calculated by FLUKA 2011 as compared to FLUKA 2008. Similar assessment can be stated also for other fragments presented in the nuclide inventory in

Figure 43. This can be explained as follows, the lower threshold for the nucleus-nucleus interactions in FLUKA 2011 leads to higher induced activities due to the increased contribution from projectile fragments.

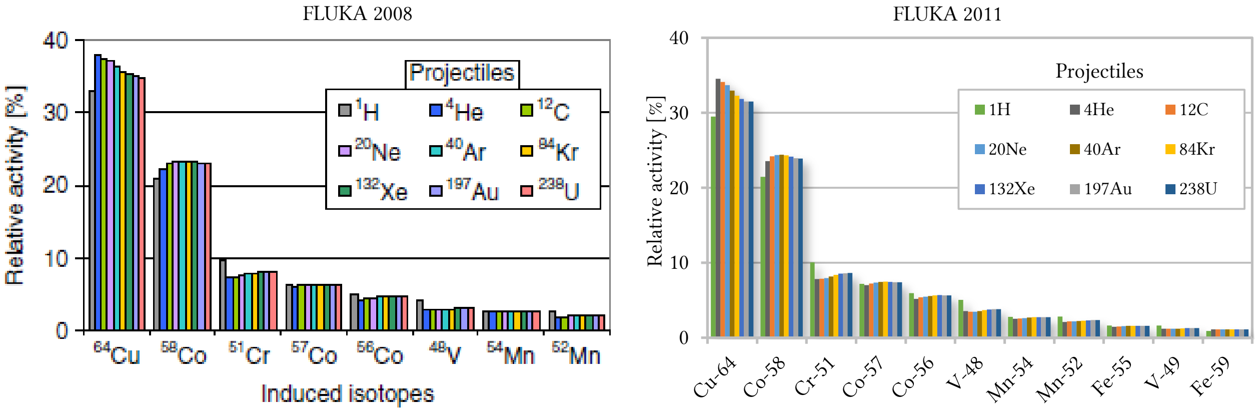

Figure 43: Nuclide inventories of a copper target activated for 100 days by different heavy-ion beams with an energy of 500 MeV/u. Relative activities were calculated by FLUKA 2008 [4] (left) and FLUKA 2011 (right).

The previous comparison was useful for a quick inspection, to ensure that the accumulated activities differ significantly and thus, it is reasonable to expect an influence of the tolerable levels of the beam losses.

Establishment of the scaling law between proton and heavy-ion beam-loss criteria is possible only after constructing the time evolution of induced activity. The time evolution and the nuclide inventory for activations caused by a beam with energies of 1 GeV/u and 200 MeV/u, corresponding to boundary energies of the first criteria, are displayed in Figure 44 and Figure 45, respectively. The example of activation by 25 MeV/u beams, as the boundary of expanded range for new criteria, is shown in Figure 46. The time evolution is illustrated as a ratio of the induced activity, A_t, and the normalized by the activity at the end of the irradiation, A_{eoi}. If there is no big difference in the time evolution of the activities induced by different beams, a generic curve (GC) can be created by averaging the individual curves. In such a case, the generic curve is representing the time evolution of the induced activity independently from the primary beam particles. Possible differences in the shapes of the time-evolution curves can be explained by the diverse nuclide composition in the nuclide inventory.

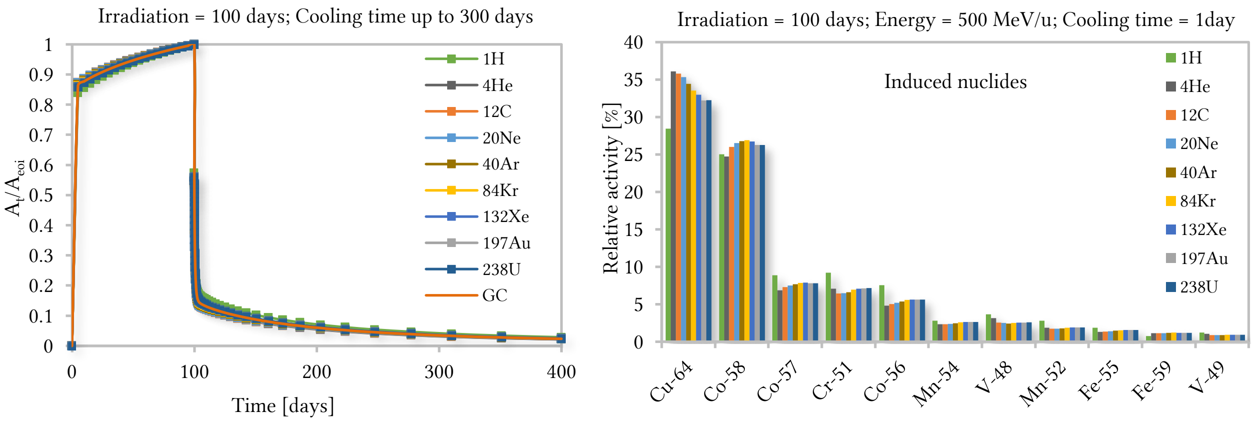

Figure 44: Time evolution of the induced activity in a copper bulk target irradiated by different projectiles with an energy of 500 MeV/u (left) and the relative activities of the most contributing nuclides (right).

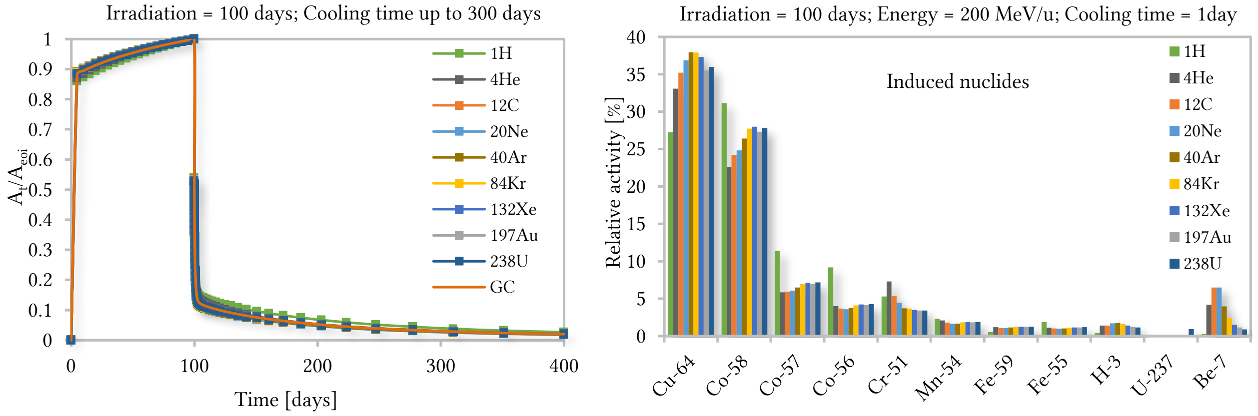

Figure 45: Time evolution of the induced activity in a copper bulk target irradiated by different projectiles with an energy of 200 MeV/u (left) and the relative activities of the most contributing nuclides (right).

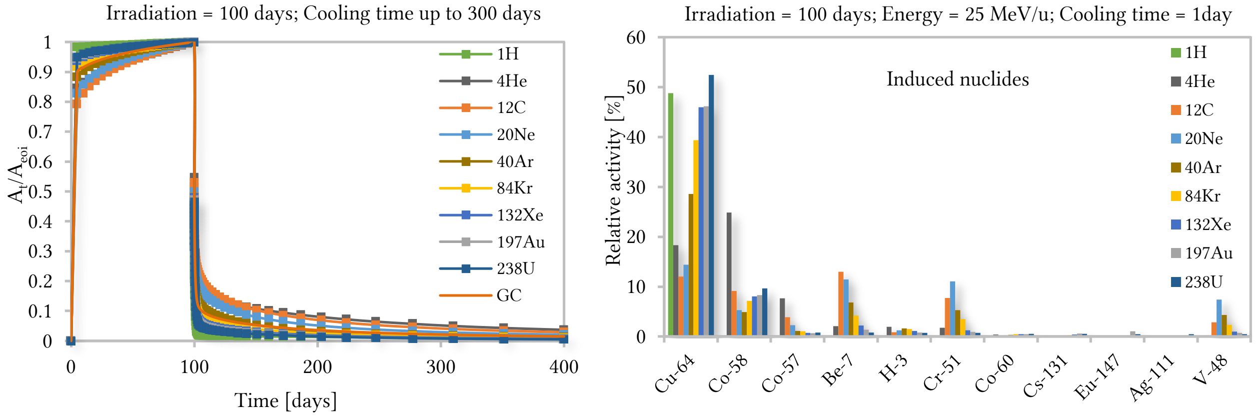

Figure 46: Time evolution of the induced activity in a copper bulk target irradiated by different projectiles with an energy of 25 MeV/u (left) and the relative activities of the most contributing nuclides (right).

From these presented examples it is noticeable, that the partial relative activities are almost the same for all nuclides independently from the projectile mass at energies from 1 GeV/u down to 200 MeV/u. This suggests that radioactive nuclides are produced mostly by secondary particles. More precisely, this study shows that the time evolution of the activity induced by 200 MeV/u ion beams is still following the shape of the generic curve. But the partial relative activities are no longer identical at energies below 150 MeV/u and their behaviour is similar to the case of 25 MeV/u ion beams (see Figure 46). Some nuclides were not produced by the ion-beams of all species. Moreover, the activation starts to be driven also by the projectile fragments and not only by the target-nuclei fragments as it was in the cases of higher energies. Different nuclide compositions should also have an influence on the decay-curve of the total residual activity. The deviation of a shape of individual curves starts to be noticeable shortly after the start as well as the end of the irradiation. They differ from each other significantly and they do not follow the generic curve shape. Hence, an employment of the data below this energy is inappropriate for the scaling-law definition.

Three conditions for an applicability of the scaling law were defined in the previous beam-loss criteria: (1) the induced-nuclide inventory does not depend strongly on the projectile species; (2) time evolution of the induced activity correlates to a generic curve, and (3) the total activity induced by beam losses of 1 W/m (the normalized activity) is decreasing with the increase of the ion mass and the decrease of the energy. The scaling factor under these circumstances can be expressed as a ratio of the normalized activity induced by 1 GeV proton beams, $A_p(1\text{ GeV})$, to the normalized activity induced by the particles of interest at given energy, $A_i(E)$. The graphical representation of the calculated scaling factors is displayed in Figure 47.

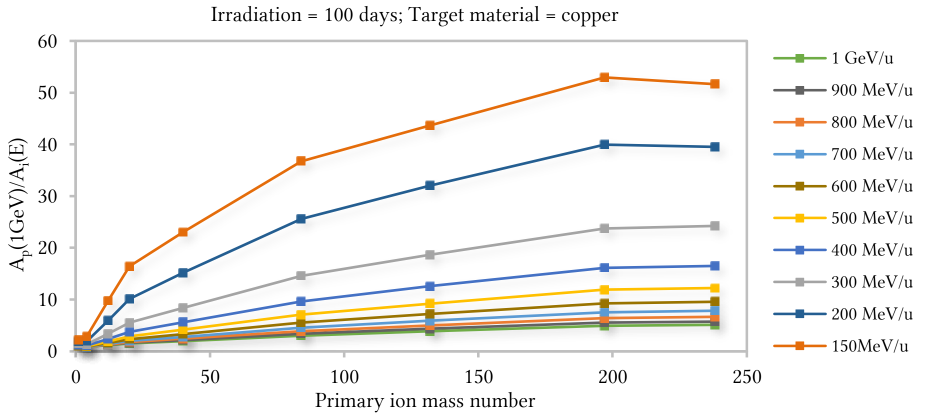

Figure 47: Scaling factors for the tolerable beam losses as a function of the ion mass

The tolerable beam losses based on the FLUKA 2011 simulations are collected in Table 16. The scaling factors calculated for the ion beams with energies of 100, 50 and 25 MeV/u are inserted with the strikethrough values. It is because we observed that the reliable expansion of the universal scaling law is not possible in this range of energies. The recent study uncovered the significant difference between the beam-loss criteria determined by FLUKA 2008 and FLUKA 2011. The results provided by the newer version of the calculation code are stricter, and a smaller amount of beam losses is allowed compared to the previous versions. For example, the tolerable beam losses are 40 W/m for uranium beam with an energy of 200 MeV/u according to FLUKA 2011 instead of 60 W/m according to FLUKA 2008.

Table 16: Tolerable beam-loss criteria for the short-term (100 days)using heavy-ion accelerators based on the investigated activation of the copper bulk target. (The strikethrough values are improper for use)

	Scaling factor [W/m]												
Beam energy	1 GeV/u	900 MeV/u	800 MeV/u	700 MeV/u	600 MeV/u	500 MeV/u	400 MeV/u	300 MeV/u	200 MeV/u	150 MeV/u	100 MeV/u	50 MeV/u	25 MeV/u
^{1}H	1.00	1.01	1.02	1.05	1.09	1.15	1.27	1.47	1.90	2.25	~~2.76~~	~~4.11~~	~~7.90~~
^{4}He	0.87	0.87	0.87	0.88	0.91	0.97	1.09	1.33	1.98	2.85	~~4.59~~	~~9.29~~	~~19.87~~
^{12}C	1.18	1.23	1.30	1.41	1.60	1.88	2.37	3.35	5.94	9.77	~~17.09~~	~~35.25~~	~~74.27~~
^{20}Ne	1.50	1.62	1.77	1.99	2.33	2.87	3.77	5.53	10.15	16.41	~~28.35~~	~~60.41~~	~~138.25~~
^{40}Ar	1.96	2.17	2.42	2.78	3.34	4.20	5.62	8.42	15.20	23.04	~~37.23~~	~~76.72~~	~~194.57~~
^{84}Kr	3.02	3.39	3.87	4.58	5.56	7.07	9.65	14.61	25.59	36.75	~~54.64~~	~~107.19~~	~~254.84~~
^{132}Xe	3.84	4.34	4.98	5.90	7.21	9.20	12.59	18.65	32.03	43.68	~~62.98~~	~~116.93~~	~~262.30~~
^{197}Au	4.90	5.56	6.40	7.55	9.25	11.90	16.14	23.73	39.96	52.94	~~73.35~~	~~124.94~~	~~263.11~~
^{238}U	5.11	5.75	6.63	7.83	9.59	12.20	16.48	24.23	39.55	51.68	~~70.19~~	~~113.37~~	~~246.10~~

4.1.2 STAINLESS STEEL BULK TARGET

The motivation for a study of the activation of a stainless steel bulk target during 100 days was to ensure an independence of the scaling law on the target material. The assumed composition of the used stainless-steel was C (0.07%), Mn (2.0%), Si (1.0%), Cr (18%), Ni (9.5%), and S (0.03%) in addition to iron (also known as stainless steel 304). The time evolution and the nuclide inventory of the induced nuclides by heavy-ion beams with the energies of 500, 200 and 25 MeV/u in the bulk target made of stainless steel are shown in Figure 48, Figure 49 and Figure 50, respectively.

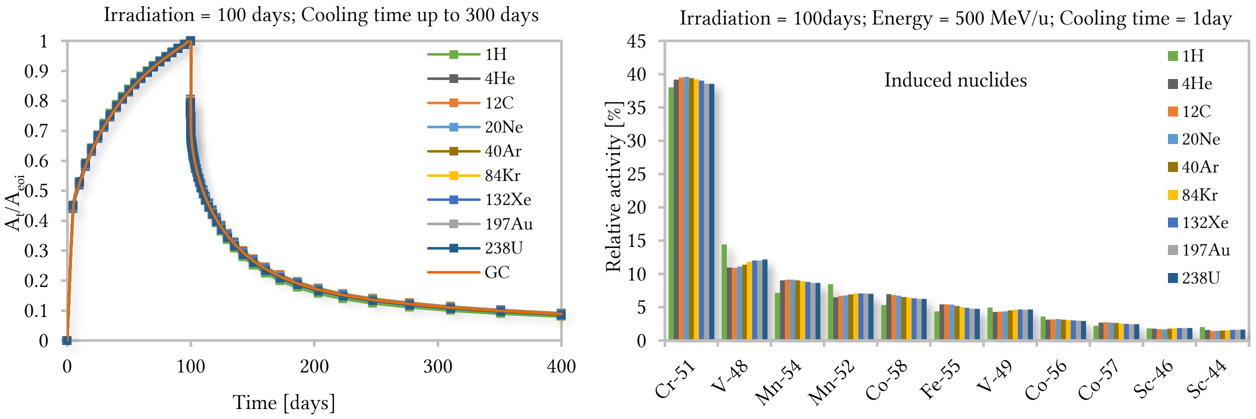

Figure 48: Time evolution of the induced activity in a stainless steel bulk target irradiated by different projectiles with an energy of 500 MeV/u (left) and the relative activities of the most contributing nuclides (right).

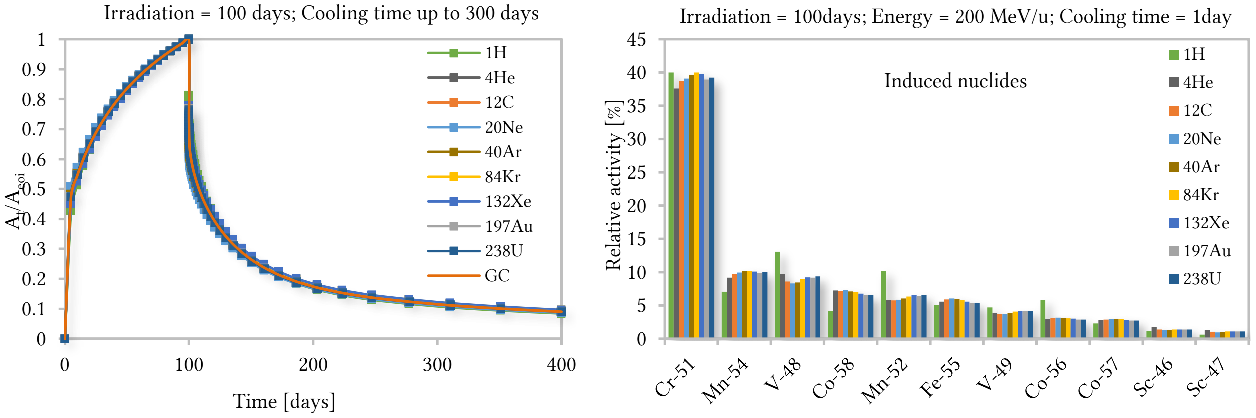

Figure 49: Time evolution of the induced activity in a stainless steel bulk target irradiated by different projectiles with an energy of 200 MeV/u (left) and the relative activities of the most contributing nuclides (right).

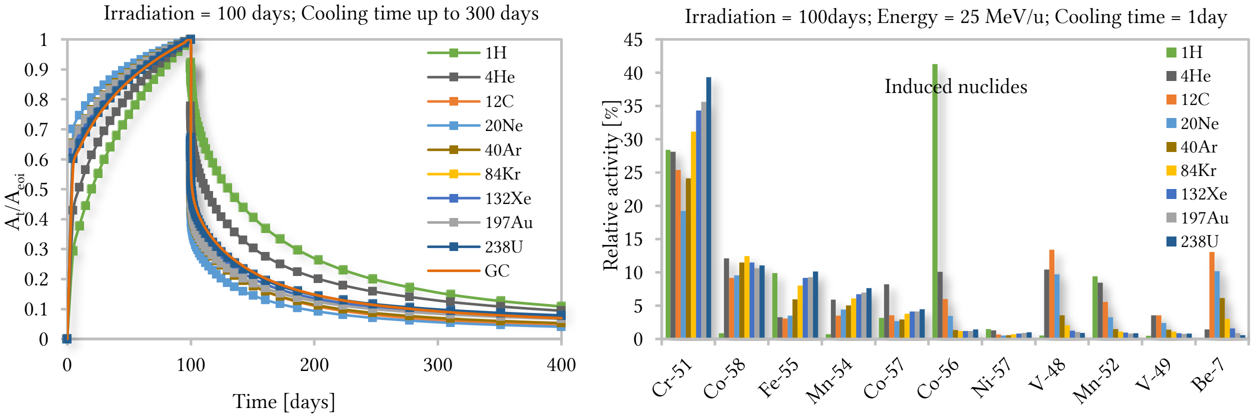

Figure 50: Time evolution of the induced activity in a stainless steel bulk target irradiated by different projectiles with an energy of 25 MeV/u (left) and the relative activities of the most contributing nuclides (right).

These results reveal the same observations as it was in the case of the copper target. The time evolution of the activity induced by different heavy ions is following the shape of the generic curve in the case of the primary projectiles with the energy above 150 MeV/u. The only remarkable difference compared to the copper-target results is the manner how rapidly the activity accumulates in the target. For instance, the A_t/A_{eoi} ratio jumps from 0 to 0.6 after the first 5 days of activation of a stainless steel, whereas the same activation process of a copper results in a ratio of about 0.9. This can be explained by a different list of the induced fragments in a copper and a stainless steel targets. In reality, such effect is also visible within the same target material, where a miscellaneous balance of the relative activities of accumulated fragments leads to various time-evolution curves, as Figure 50 evidents.

Table 17: Tolerable beam-loss criteria for a short-term (100 days) using heavy-ion accelerators based on the investigated activation of a stainless steel bulk target. (The strikethrough values are improper for use)

	Scaling factor [W/m]												
Beam energy	1 GeV/u	900 MeV/u	800 MeV/u	700 MeV/u	600 MeV/u	500 MeV/u	400 MeV/u	300 MeV/u	200 MeV/u	150 MeV/u	100 MeV/u	50 MeV/u	25 MeV/u
^{1}H	1.00	1.00	1.01	1.02	1.05	1.09	1.20	1.38	1.78	2.17	~~2.94~~	~~4.92~~	~~8.63~~
^{4}He	0.93	0.92	0.92	0.93	0.96	1.02	1.13	1.37	1.94	2.63	~~3.84~~	~~6.79~~	~~16.47~~
^{12}C	1.23	1.28	1.36	1.48	1.66	1.95	2.47	3.48	6.09	9.48	~~15.58~~	~~30.69~~	~~59.48~~
^{20}Ne	1.55	1.66	1.82	2.05	2.39	2.93	3.85	5.69	10.32	16.05	~~26.50~~	~~54.01~~	~~109.36~~
^{40}Ar	1.99	2.18	2.45	2.82	3.37	4.22	5.69	8.56	15.61	23.48	~~38.17~~	~~79.11~~	~~173.62~~
^{84}Kr	3.01	3.37	3.84	4.52	5.52	7.03	9.71	14.71	26.48	38.19	~~58.75~~	~~122.83~~	~~267.97~~
^{132}Xe	3.80	4.26	4.91	5.78	7.11	9.12	12.47	18.81	33.02	45.63	~~68.05~~	~~137.52~~	~~285.58~~
^{197}Au	4.83	5.44	6.26	7.40	9.03	11.57	15.75	23.40	39.78	53.19	~~76.00~~	~~142.35~~	~~290.40~~
^{238}U	4.98	5.61	6.45	7.63	9.32	11.86	15.98	23.65	39.20	52.22	~~74.27~~	~~136.07~~	~~294.03~~

The independence of the scaling law from the bulk-target material was proven by the comparison of Table 16 and Table 17. The scaling factors in both tables do not differ remarkably from each other in the case of any beam species and energy. The result obtained from activation of the stainless steel bulk target confirmed again that the energy-threshold for nucleus-nucleus interactions does have an influence on activities calculated by FLUKA. At beam energies between 1 GeV/u and 150 MeV/u, the scaling law can be applied, but the simulations based on FLUKA 2011 lead to lower tolerable beam losses compared to FLUKA 2008. The scaling factors calculated for heavy ions with energies lower than 150 MeV/u are not qualified for practical use because the activation of the target is depending on the projectile species.

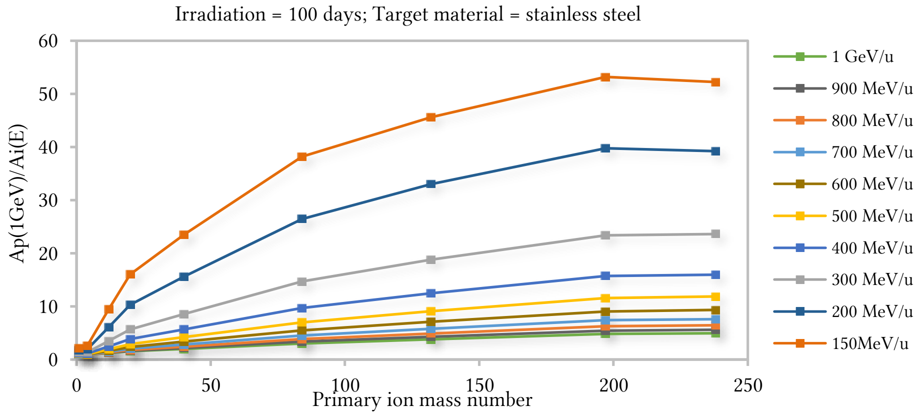

Figure 51: Scaling factor for the tolerable beam losses as a function of the ion mass for a stainless steel target

4.2 BEAM-LOSS CRITERIA CALCULATED FOR A LONG-TERM OPERATION

The evaluation of the original beam-loss criteria based on the calculations provided by FLUKA 2011 uncovered a limited applicability of the scaling law for some beam energies. This result raised another question related to the credibility of the whole idea of the predictability of the heavy-ion accelerators activation. In particular, the time dependency of the criterion became another investigated attribute, since the proton-based scaling law for heavy ions were defined only for 100 days long operation. Most of the accelerator facilities are working over a long period of time. This motivated us to repeat the calculations of the copper bulk target activation, where the only applied change was the irradiation time of 20 years. Corresponding detected decay times of the accumulated activity for up to 20 years are presented in Table 18. The beam losses were normalized to a beam power of 1 W and were delivered to the target permanently. A cylindrically shaped bulk target with a length of 60 cm and with a diameter of 20 cm was assumed. The activation of this target was similar to the previous approach described in Section 4.1; simulations of different projectiles (^{1}H, ^{4}He, ^{12}C, ^{20}Ne, ^{40}Ar, ^{84}Kr, ^{132}Xe, ^{197}Au and ^{238}U) with energies from 25 MeV/u up to 1 GeV/u were performed. This study was not provided for stainless steel because it was demonstrated already in the previous section, that the scaling law is independent from the target material.

Table 18: The list of the irradiation times (0-20 y) and the decay times (20.003-40 y) chosen for simulation of a long-term operation.

Scoring time points						
0 y	1 y	2 y	5 y	10 y	19 y	20 y
20.003 y	21 y	22 y	25 y	30 y	35 y	40 y

Time evolution of the activity induced in the target was determined as a ratio A_t/A_{eoi}, where A_t is the activity at a certain time t, and A_{eoi} is the activity at the end of the irradiation. The time evolution of total activity produced by different beams is supported by the nuclide inventory of main contributors with their determined relative activities. Examples of the time evolution of different activities produced by beams with energies of 500, 200 and 25 MeV/u are shown in Figure 52, Figure 53 and Figure 54, respectively.

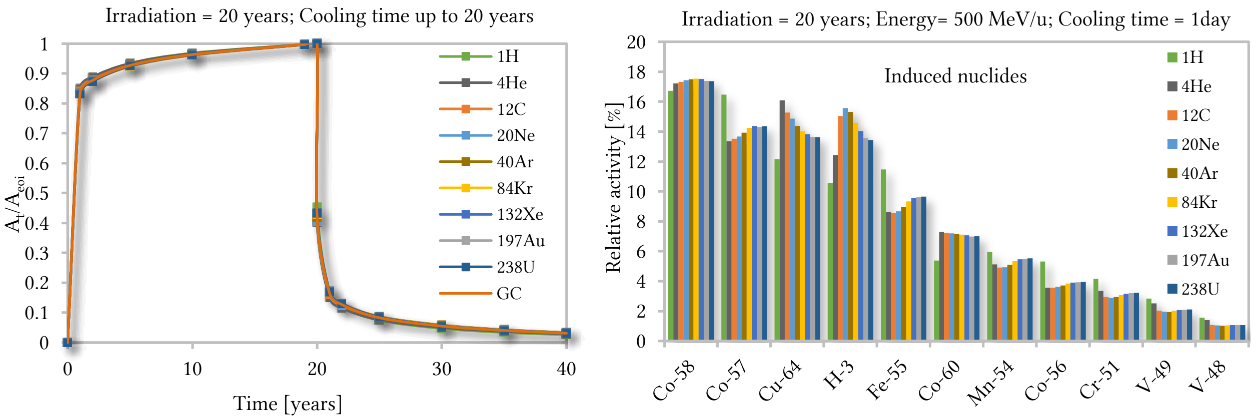

Figure 52: Time evolution of the induced activity in a copper bulk target irradiated by different projectiles with an energy of 500 MeV/u (left) and the relative activities of the most contributing nuclides (right).

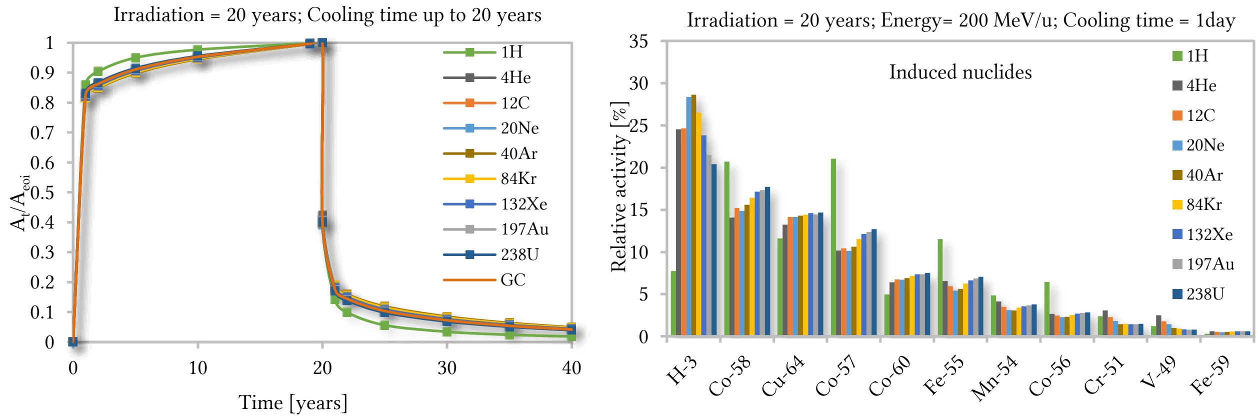

Figure 53: Time evolution of the induced activity in a copper bulk target irradiated by different projectiles with an energy of 200 MeV/u (left) and the relative activities of the most contributing nuclides (right).

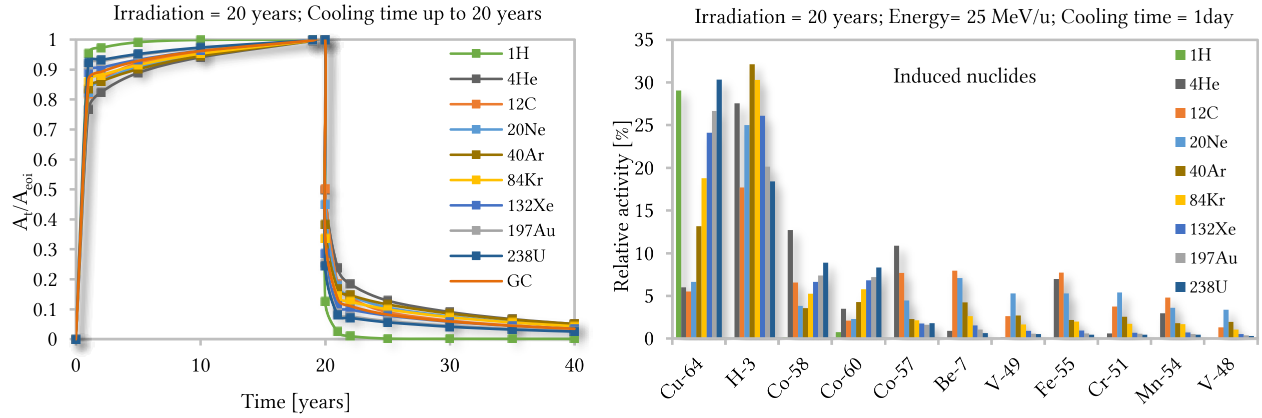

Figure 54: Time evolution of the induced activity in a copper bulk target irradiated by different projectiles with an energy of 25 MeV/u (left) and the relative activities of the most contributing nuclides (right).

The comparison of Figure 52, Figure 53 and Figure 54 is showing a remarkable difference between accumulations of the nuclides by beams of different energies. The normalized activities induced by different beams at a higher energy are almost identical, and their time evolution is satisfactorily similar to the generic curve. On the contrary, the time evolution of the normalized activities at a lower energy does depend significantly on the projectile species. The case of ^{1}H beam at 200 MeV/u is very outstanding for its unique list of included nuclides. For example, the relative activity of the ^{3}H is lower by a factor of 5 up to 8 compared to other beams, for which this isotope is the most dominating one. At the same time, the most dominant nuclides are ^{57}Co and ^{58}Co from the perspective of the ^{1}H beam, and their relative activities are higher by a factor of 2 compared to those of the same nuclides produced by other beams. A closer look at the same nuclides in the nuclide inventory of the ^{1}H at 25 MeV/u shows that ^{3}H, ^{57}Co, and ^{58}Co have a relative activity of 0% even though they were significant contributors for beams with higher energies. Moreover, the only nuclide produced by ^{1}H beam displayed in Figure 54 is ^{64}Cu with a relative activity of about 30%. One can ask, what are the other nuclides produced by ^{1}H at 25 MeV/u, which are responsible for the remaining 70% of the accumulated activity and why they are not presented in the nuclide inventory. The latter is explained by the ideology of a scaling law made for situations where the production ratio of the nuclides does not depend on beam energies and beam species. Based on this theoretical premise, the nuclide inventories were organised for one of the beam species. In this particular case, it was done from the perspective of a ^{238}U beam, and relative activities of the other beams were added in figure. This explains why relative activities of the nuclides produced by a uranium beam are ordered from highest to lowest, which is not necessarily the case of nuclide inventories for other beam species. As it was already mentioned, the initial expectation was that the relative activities of nuclides are comparable for all beam species. However, the interpretation of the nuclide inventory in Figure 54 can be understood as a proof of non-applicability of the scaling law at low beam energies. The production of nuclides differs so significantly that the qualitative comparison of numerical values of the relative activities is not possible since already the quantitative analysis dispose of the different list of produced nuclides for each beam species.

In the same manner as it was calculated in the case of a short-term operation, the scaling law for beam losses is expressed as a ratio of the normalized activity induced by 1 GeV protons, $A_{p\text{-}100d}$(1 GeV), and the normalized activity induced by particles of interest at a given energy, $A_{i\text{-}20y}$(E). The results for the scaling law are presented in Figure 55. It should be stressed that the ratio was determined between the activity produced by protons during 100 days long irradiation and the activity produced by heavy-ion beams during 20 years long irradiation. For this reason, the resultant scaling law of ^{1}H beam at 1 GeV/u is equal to 0.73 W/m (see Table 19), instead of 1 W/m as compared to the results of a short-term activation (see Table 16 or Table 17). The tolerable beam losses derived for a long-term operation are lower compared to the short-term operation. As an example, they are 30 W/m for a 20-years-long activation by a uranium beam with an energy of 200 MeV/u instead of 40 W/m calculated for a 100-days-long operation. The scaling factors calculated for heavy ions with energies of 100, 50 and 25 MeV/u are also presented in Table 19. Nevertheless, the time evolution and the partial relative activities of induced nuclides are becoming unique for each ion-beam species. This is not consistent with the conditions for a possible applicability of the generic-curve theory and therefore, the scaling law calculated for heavy-ion beams from this energy range is not recommended.

Table 19: Tolerable beam-loss criteria for a long-term (20 year) using heavy-ion accelerators based on the investigated activation of a copper bulk target. (The strikethrough values are improper for use).

Scaling factor [W/m]													
Beam energy	1 GeV/u	900 MeV/u	800 MeV/u	700 MeV/u	600 MeV/u	500 MeV/u	400 MeV/u	300 MeV/u	200 MeV/u	150 MeV/u	100 MeV/u	50 MeV/u	25 MeV/u
^{1}H	0.73	0.73	0.75	0.76	0.80	0.84	0.94	1.11	1.43	1.74	~~2.30~~	~~3.83~~	~~7.90~~
^{4}He	0.66	0.65	0.66	0.67	0.70	0.74	0.84	1.03	1.47	1.99	~~3.05~~	~~5.91~~	~~13.11~~
^{12}C	0.88	0.92	0.98	1.07	1.20	1.43	1.82	2.58	4.52	7.12	~~12.02~~	~~25.09~~	~~53.91~~
^{20}Ne	1.12	1.20	1.32	1.50	1.76	2.17	2.87	4.24	7.71	11.96	~~19.96~~	~~44.66~~	~~104.26~~
^{40}Ar	1.46	1.61	1.80	2.07	2.48	3.13	4.22	6.32	11.33	16.86	~~26.74~~	~~58.21~~	~~153.53~~
^{84}Kr	2.24	2.50	2.86	3.37	4.15	5.30	7.23	10.94	19.09	26.72	~~39.79~~	~~83.70~~	~~209.89~~
^{132}Xe	2.83	3.19	3.67	4.33	5.37	6.86	9.35	14.00	24.09	32.45	~~47.15~~	~~95.27~~	~~226.64~~
^{197}Au	3.60	4.07	4.69	5.61	6.89	8.85	12.03	17.83	30.14	40.08	~~56.50~~	~~104.58~~	~~233.77~~
^{238}U	3.74	4.23	4.86	5.76	7.13	9.12	12.34	18.18	29.99	39.44	~~54.59~~	~~97.71~~	~~217.96~~

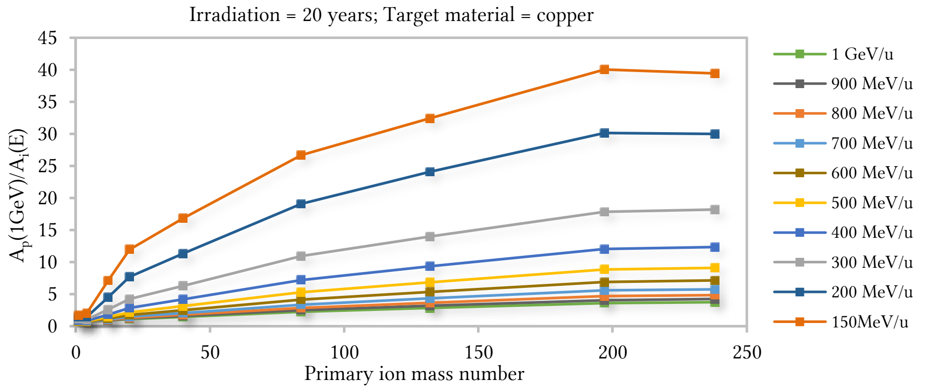

Figure 55: Scaling law for the tolerable beam losses as a function of ion mass after 20 years of operation. Calculated data were provided by FLUKA 2011 code.

4.3 SUMMARY OF THE TOLERABLE BEAM-LOSS CRITERIA CALCULATIONS

The recalculation of beam-loss criteria by the FLUKA 2011 software version brought several observations to light. The simulated results of the bulk-target activation changed depending on the application of the new nucleus-nucleus interaction model below 125 MeV/u, as compared to the results determined by FLUKA 2008 version. Acquiring the activity produced by the nuclides below this energy has influenced the ratio between the activity induced by protons at 1 GeV during 100 days and the activity induced by heavy-ion beams. The scaling law calculated from the activities determined by FLUKA 2011 is stricter than the results provided by FLUKA 2008, (Table 20). In other words, the new tolerable beam-loss criteria calculated for 100 days activation (corresponding to a short-term operation) are lower than the first criterion presented in Ref [4]. In the second step, the analysis of the simulated data of the copper bulk target irradiated with different beams during 20 years (corresponding to a long-term operation) with a normalized beam losses equal to a beam power of 1 W showed that the beam-loss criteria are becoming stricter also with the increasing operation time.

Table 20: Updates of the tolerable beam-loss criteria for heavy-ion accelerators obtained from different FLUKA versions and various simulated times of a machine-operation.

Activation by ^{238}U beam	FLUKA 2008.3.6 [4] 100 days	FLUKA 2011.2b.5 [34] 100 days	FLUKA 2011.2c.4 [33] 20 years
	Tolerable beam losses for the uranium beams [W/m]		
1GeV/u	5	5	4
500 MeV/u	12	12	9
200 MeV/u	60	40	30
150 MeV/u		52	39

Presented results of both long- and short-term activations of bulk targets proved that the relative activities of the nuclides with dominating contribution to the total activity do not depend on the projectile mass at high energies. On the contrary, the situation changes significantly in the case of heavy-ion beams at energies below 200 MeV/u, where the nuclide inventory showed a dependence of the production of the nuclides on the projectile mass.

Based on the presented observations and evidence, the extent of acceptation of the criteria failing in its essential idea is a question which cannot be answered in this thesis directly and must be open for a broader discussion with radiation protection experts and authorities. Taking into account the fact that a lot of accelerators are operating heavy-ion beams with energies below 200 MeV/u (e.g. accelerators for the tumour therapy using carbon ion beams) a specification for conditions of using the tolerable beam-loss criteria based on scaling of the criterion for proton machines or a defying a new approach for these special cases would be necessary. At this point, it is fair to remind the summary of Section 3.6, where some difficulties of the FLUKA calculations in the low energy range of heavy-ion beams interactions were concluded. Under these circumstances, it is correct to clarify that the beam-loss criteria are based on FLUKA 2011 calculations, and they can slightly change with new code versions which will solve the actual imperfections. Nevertheless, it can be proposed with confidence that no great changes of the scaling law will be determined in the future after debugging of the FLUKA modules. This argument is based on the adding of a missing interaction model for hadrons below 125 MeV/u, which can be considered as a very significant update creating a maximal difference with a factor of about 2 between the FLUKA 2008 and FLUKA 2011 results, determined for the uranium beam at 200 MeV/u.

As a solution for the actual situation of a non-reliability of the scaling law due to the nuclide production dependent on the projectile species additional calculations of the corresponding dose-rates induced by low-energy beams can be used.

CHAPTER FIVE

SUMMARY

5 DISCUSSION AND CONCLUSION

This work verified Monte Carlo transport codes for the estimation of radiation levels in order to define beam-loss criteria for heavy-ion accelerators important for operation of accelerator facilities causing a low activation of components and environment. For this, new experimental data for the activation by heavy ions with low to medium energies were collected and evaluated.

The irradiation of three aluminium targets was successfully conducted at GSI Darmstadt. The energies of the primary heavy-ion beams were chosen for benchmarking the physical models used by FLUKA at the low-energy range. The depth profiles of residual activity of ^{7}Be and ^{22}Na induced by ^{238}U at 125 MeV/u, ^{238}U at 200 MeV/u, and ^{124}Xe at 300 MeV/u showed similar issues in the region upstream of the primary particles. Detailed investigation of the accumulated target-nuclei fragments confirmed the discrepancies between the shapes of experimentally measured and numerically calculated depth profiles within the same energy ranges, where the transition between the Relativistic Quantum Mechanical Dynamics (RQMD) and the Boltzmann Master Equation (BME) nucleus-nucleus interaction models is located. Furthermore, it was demonstrated that different settings of the BME-RQMD transition band influence the shape of the depth profile. Nevertheless, none of the user-defined adjustments eliminated the observed deficiency. Another discrepancy of the FLUKA code was observed in the xenon-beam experiment, where an unfounded increase of the production-rate of intermediate-Z fragments was documented close to the range of the primary particles.

Existing limits for tolerable beam losses are based on the numerical calculations provided by FLUKA 2008, where a significant drawback of the interaction threshold at 100 MeV/u is affecting the activation results. Here, it was demonstrated that the broadened interaction-range due to the Boltzmann master equation model included in FLUKA 2011, leads to new and stricter limit. Short-term (100 days) and long-term (20 years) machine operations were simulated in order to monitor an impact of the accumulation of long-lived nuclides. In particular, the tolerable beam losses for 1 GeV/u uranium ions do not differ significantly for the chosen operation times and used FLUKA versions. They are 5 W/m according to activation determined by both FLUKA 2008 and FLUKA 2011 for 100 days of operation, and 4 W/m for 20 years of activation calculated by FLUKA 2011. A greater variance is visible at lower energies. Tolerable beam-loss criteria of 60 W/m were defined by FLUKA 2008 for uranium ions at 200 MeV/u during 100 days of machine operation. Lower tolerance limits were specified by FLUKA 2011, where tolerable losses of 40 W/m were determined for 100 days and only 30 W/m for 20 years operation of uranium beam at 200 MeV/u. The nuclide inventory and the time evolution of induced radioactivity exhibited a failing of the scaling law for heavy-ion beams with energies below 150 MeV/u. Therefore, the extension of the new criteria was not possible below this energy and they are not applicable in reliable way for radiation safety purposes at low energies.

Presented work fulfilled all assigned goals and achieved expected results. Relevant observations were published in journal publication [32], conference proceedings [33, 34, 35], or annual reports [36, 37, 38]. All evidences of the FLUKA code discrepancies were summarized and acquired experimental data were made available to the team of FLUKA developers for future consideration and application in code updates. The redefined tolerable beam losses were presented to the authors of both the first beam-loss criteria for heavy-ion accelerators and the original beam-loss criteria for proton machines as well as to the community of researchers specialised on the activation aspects of accelerators at the conferences of Shielding aspects of accelerators, Targets and Irradiation Facilities (SATIF-12 in Chicago, Illinois, USA [34] and SATIF-13 in Dresden, Germany [33]). The presented results have prompted a discussion which has created grounds for future study. Prospective activation experiments may be carried out within a closer collaboration with the FLUKA code developers. This is a great opportunity for benchmarking of experimental data with the developer version of the FLUKA code before the official discloser, which may have a direct impact on an improvement of physical models. The authors of MARS code expressed their interest in benchmarking as was performed in the case of FLUKA, which may additionally lead to intercomparison of transport codes in future experimental studies.

REFERENCES

BIBLIOGRAPHY

[1] O.E. KRIVOSHEEV, N.V. MOKHOV: “Tolerable Beam Loss at High-Intensity Proton Machines”, Proceedings of the 7th ICFA Mini-workshop on High Intensity High Brightness Hadron Beams, Wisconsin, USA, 13-15 September 1999 (2000) 85.

[2] J. ALONSO: “Beam loss working group report”, Proceedings of the 7th ICFA Mini-workshop on High Intensity High Brightness Hadron Beams, Wisconsin, USA, 13-15 September 1999 (2000) 51.

[3] FLUKA Team 2000-2016: “Release notes for FLUKA 2011.2”. Available: http://www.fluka.org/fluka.php?id=release_notes, [Jun. 10, 2014].

[4] I. STRAŠÍK, E. MUSTAFIN, M. PAVLOVIČ: “Residual activity induced by heavy ions and beam-loss criteria for heavy-ion accelerators”, Physical Review Special Topics - Accelerators and Beams 13 (2010) 071004.

[5] A. H. SULIVAN: “A Guide to Radiation and radioactivity levels near high energy particle accelerators”. Nuclear Technology Publishing (1992).

[6] M. GLORIS, R. MICHEL, F. SUDBROCK et al.: “Proton-induced production of residual radionuclides in lead at intermediate energies”. Nuclear Instruments and Methods in Physics Research A 463 (2001) 593-633.

[7] L. ULRICI, M. BRUGGER, T.H. OTTO et al.: “Radionuclide characterization studies of radioactive waste produced at high-energy accelerators”. Nuclear Instruments and Methods in Physics Research A 562 (2006) 569-600.

[8] N.V. MOKHOV, F. CERUTTI: “Beam-Material Interactions”, Proceedings of the Joint International Accelerator School: Beam Loss and Accelerator Protection, Newport Beach, US, November 2014, Ed. R. Schmidt, CERN-2016-002, CERN, Geneva (2016).

[9] G. BATTISTONI, J. BAUER, T.T. BOEHLEN et al.: “The FLUKA code: An Accurate Simulation Tool for Particle Therapy”, Front. Oncol. 6:116 (2016) DOI: http://dx.doi.org/10.3389/fonc.2016.00116.

[10] FAIR - FACILITY FOR ANTIPROTON AND ION RESEARCH IN EUROPE GMBH.: "FAIR - The universe in the laboratory", Available: http://www.fair-center.eu/, [Apr. 7, 2017].

[11] P. SPILLER, G. FRANCHETTI: "The FAIR accelerator project at GSI". Nuclear Instruments and Methods in Physics Research A 561 (2006) 305-309.

[12] O. BOINE-FRANKENHEIM: "The FAIR Accelerators: Highlights and Challenges", in proceedings of IPAC'10, Kyoto, Japan (2010) 2430-2434.

[13] J. ALONSO: "Review of Ion Accelerators", Proceedings of the 2nd European Particle Accelerator Conference, Nice (1990) 95-99.

[14] U.S. DEPARTMENT OF ENERGY: "Nuclear Physics and Reactor Theory", DOE Fundamentals Handbook, Volume 1 and 2 (1993).

[15] INTERNATIONAL ATOMIC ENERGY AGENCY: "Handbook on the photonuclear data for applications Cross-sections and spectra", IAEA-TECDOC-1178 (2000).

[16] A. FASSO, A.FERRARI, G. SMIRNOV et al.: "FLUKA Realistic modelling of radiation induced damage", Progress in Nuclear Science and Technology, Vol. 2 (2011) 769-775, DOI: http://dx.doi.org/ 10.15669/pnst.2.769.

[17] A. FERTMAN, E. MUSTAFIN, R.HINCA et al.: "First results of an experimental study of the residual activity induced by high-energy uranium ions in steel and copper", Nuclear Instruments and Methods in Physics Research B 260 (2007) 579-591.

[18] I. STRAŠÍK: "Activation Study of High-Energy Heavy-Ion Accelerators." PhD thesis, Slovak University of Technology in Bratislava, Bratislava (2009).

[19] V. CHETVERTKOVA: "Verification of Monte Carlo Transport Codes by Activation Experiments." PhD thesis, Johan Wolfgang Goethe - Universität, Frankfurt am Main (2012).

[20] I. STRAŠÍK, E. MUSTAFIN, A. FERTMAN et al.: "Experimental study of the residual activity induced by 950MeV/u uranium ions in stainless steel and copper", Nuclear Instruments and Methods in Physics Research B 266 (2008) 3443-33452, DOI: http://dx.doi.org/10.1016/j.nimb.2008.05.013.

[21] V. CHETVERTKOVA, I. STRAŠÍK, A. BELOUSOV et al.: "Activation of aluminum by argon: Experimental study and simulations". Nuclear Instruments and Methods in Physics Research B 269 (2011) 1336-1340.

[22] V. CHETVERTKOVA, U. RATZINGER, I. STRAŠÍK: "Activation of aluminium by uranium", in proceedings of HB2010, Morschach, Switzerland (2010) 250-253.

[23] I. STRAŠÍK, V. CHETVERTKOVA, E. MUSTAFIN et al.: "Depth profiling of residual activity of ^{237}U fragments as a range verification technique for ^{238}U primary ion beam". Physical Review Special Topics - Accelerators and Beams 15 (2012) 071001-1 – 13.

[24] I. STRAŠÍK, E. MUSTAFIN, T. SEIDL et al.: "Experimental study and simulation of the residual activity induced by high-energy argon ions in copper". Nuclear Instruments and Methods in Physics Research B 268 (2010) 573-580.

[25] E. MUSTAFIN, T. SEIDL, A. PLOTNIKOV et al.: "Ion Irradiation Studies of Construction Materials for High-Power Accelerators". Radiation Effects and Defects in Solids 164/7-8 (2009) 460-469.

[26] E. MUSTAFIN, E. FLOCH, A. PLOTNIKOV et al.: "Irradiation of superconducting magnet components for FAIR", in Proceedings of HIAT09, Venice, Italy (2009) 227-230.

[27] V.CHETVERTKOVA, E. MUSTAFIN, I. STRAŠÍK et al.: "Verification of Monte Carlo transport codes FLUKA, MARS and SHIELD", in Proceedings of the 10th Workshop on Shielding Aspects of Accelerators, Targets and Irradiation Facilities SATIF-10, CERN, Geneva, Switzerland (2010) 249-254.

[28] T. ENQVIST, J. BENLLIURE, E FARGET et al.: "Systematic experimental survey on projectile fragmentation and fission induced in collisions of ^{238}U at 1 A GeV with lead". Nuclear Physics A 658 (1999) 47-66.

[29] A.A. GLOBULEV, A.V. KANTSYREV, V.E. LUCKJASHIM et al.: "Measurement of the energy deposition profile for ^{238}U ions with specific energy 500 MeV/u and 950 MeV/u in stainless steel and copper target". Nuclear Instruments and Methods in Physics Research B 263 (2007) 339-344.

[30] A.D. FERTMAN, M. BASKO, R.HINCA et al.: "Activation method for measuring ranges of heavy ions in solids", in Proceedings of International Topical Meeting on Nuclear Research Applications and Utilization of Accelerators, Vienna, Austria (2009) AT/P5-09.

[31] I. STRAŠÍK, E. MUSTAFIN, M. PAVLOVIČ et al.: "Simulations of the activation of the beam pipe and bulky targets by FLUKA and SHIELD codes", GSI Technical report, Document ID: ACC_THEORY-report-2010-001 (2010).

[32] P. KATRÍK, E. MUSTAFIN, D.H.H. HOFFMANN et al.: "Activation of accelerator constructing materials by heavy ions", Nuclear Instruments and Methods in Physics Research B 365 (2012) 525-528, DOI: http://dx.doi.org/10.1016/j.nimb.2015.09.022

[33] P. KATRÍK, D.H.H. HOFFMANN, E. MUSTAFIN et al.: "Comparison of experimental data and FLUKA simulations, validation of beam-loss criteria after long term operation of heavy-ion accelerators", Proceedings of the 13th Workshop on Shielding Aspects of Accelerators, Targets and Irradiation Facilities SATIF-13, Dresden, Germany (Forthcoming 2017).

[34] P. KATRÍK, E. MUSTAFIN, D.H.H. HOFFMANN et al.: "New results on the beam-loss criteria for heavy-ion accelerators", Proceedings of the 12th Workshop on Shielding Aspects of Accelerators, Targets and Irradiation Facilities SATIF-12, Batavia, Illinois, US (2015) 124-134.

[35] P. KATRÍK, E. MUSTAFIN, I. STRAŠÍK et al.: "Some problems of residual activity measurement", Proceedings of the 19th international Conference on Applied Physics of Condensed Matter APCOM 2013, Štrbské Pleso, Slovakia (2013) 115-118.

[36] P. KATRÍK, D.H.H. HOFFMANN, E. MUSTAFIN et al.: "Beam-loss criteria for heavy-ion accelerators", Report No.: GSI-SR2015-FG-GENERAL-24 (2016) 339, DOI:10.15120/GR-2016-1.

[37] P. KATRÍK, D.H.H. HOFFMANN, E. MUSTAFIN et al.: "Beam-loss criteria for heavy-ion accelerators", News and Reports from High Energy Density Generated by Heavy ion and Laser Beam, GSI-2016-2 (2016) 51.

[38] P. KATRÍK, D.H.H. HOFFMANN, E. MUSTAFIN et al.: “Activation of the aluminium target by 200 MeV/u uranium beam”, Report No.: GSI-SR2014-FG-GENERAL-34, GSI Report 2015-1 (2015) 451, DOI:10.15120/GR-2015-1-FG-GENERAL-34.

[39] F. SOMMERER, F. CERUTTI, K. PARODI et al.: “In-beam PET monitoring of mono-energetic ^{16}O and ^{12}C beams: experiments and FLUKA simulations for homogeneous targets”, Physics in Medicine and Biology, Volume 54, Number 13 (2009) 3979-3996.

[40] F. CLAPIER, N. PAUWELS, J. PROUST et al.: “Activation of thick targets by energetic heavy ions and the resultant radiation levels”, Radiation and Environmental Biophysics 34 (1995) 213-216, DOI: http://dx.doi.org/10.1007/BF01209744

[41] A. FASSO, A. FERRARI, J. RANFT et al.: “FLUKA: a multi-particle transport code (Program version 2011)”, CERN-2005-10, INFT/TC_05/11, and SLAC-R-773.

[42] G. BATTISTONI, A. FERRARI, M. LANTZ et al.: “A neutrino-nucleon interaction generator for the FLUKA Monte Carlo code”, Proceedings of 12th International Conference on Nuclear Reaction Mechanisms, Varenna, Italy, 15-19 June 2009, CERN-Proceedings-2010-001, pp. 387-394.

[43] N.V. MOKHOV: “The Mars Code System User's Guide”, Fermilab-FN-628 (1995);

[44] O.E. KRIVOSHEEV, N.V. MOKHOV: “MARS Code Status”, Proc. Monte Carlo 2000 Conf., p. 943, Lisbon, October 23-26, 2000; Fermilab-Conf-00/181 (2000)

[45] N.V. MOKHOV: “Status of MARS Code”, Fermilab-Conf-03/053 (2003)

[46] N.V. MOKHOV, K.K. GUDIMA, C.C. JAMES et al.: “Recent Enhancements to the MARS15 Code”, Fermilab-Conf-04/053 (2004) Available: http://www-ap.fnal.gov/MARS/, [Sep. 9, 2016].

[47] A.V. DEMENTYEV, N.M. SOBOLEVSKY: “SHIELD – universal Monte Carlo hadron transport code: scope and applications”, Radiation Measurements 30 (1999) 553-557, DOI: http://dx.doi.org/10.1016/S1350-4487(99)00231-0

[48] A.V. DEMENTYEV, N.M. SOBOLEVSKY: “SHIELD, Monte-Carlo Code for Simulating Interaction of High Energy Hadrons with Complex Macroscopic Targets”, International Atomic Energy Agency, INIS repository: 39105840 (2002) Available: http://www.nea.fr/abs/html/iaea1287.html [Sep. 9, 2016]

[49] K. NIITA, N. MATSUDA, Y. IWAMOTO et al.: “PHITS: Particle and Heavy Ion Transport code System, Version 2.23”, JAEA-Data/Code 2010-022 (2010).

[50] H. IWASE, K. NIITA AND T. NAKAMURA: “Development of General-Purpose Particle and Heavy Ion Transport Monte Carlo Code” J. Nucl. Sci. Technol. 39 (2002) 1142.

[51] T. SATO, K. NIITA, N. MATSUDA et al.: “Particle and Heavy Ion Transport Code System PHITS, Version 2.52”, J. Nucl. Sci. Technol. 50:9, 913-923 (2013).

[52] X-5 MONTE CARLO TEAM: “MCNP - A General N-Particle Transport Code, Version 5” Volume I: Overview and Theory, LA-UR-03-1987 (2003, updated 2005). Available: https://laws.lanl.gov/vhosts/mcnp.lanl.gov/pdf_files/la-ur-03-1987.pdf, [Jul. 10, 2016].

[53] T. GOORLEY et al.: “Initial MCNP6 Release Overview”, Nuclear Technology, 180 (2012) 298-315.

[54] A. S. BOTVINA, A. V. DEMENTYEV, O. N. SMIRNOVA et al.: “MSDM - Multi Stage Dynamical Model. In International Codes and Model Intercomparison for Intermediate Energy Activation Yields, Eds. R.Michel and P.Nagel, NSC/DOC(97)-1, NEA/P&T No 14, OECD, Paris (1997) 307.

[55] S. AGOSTINELLI, J. ALLISON, K. AMAKO et al.: “GEANT4-a simulation toolkit”, Nucl. Instrum. Methods A 506 (2003) 250-303, DOI: http://dx.doi.org/10.1016/S0168-9002(03)01368-8.

[56] J. ALLISON, K. AMAKO, J. APOSTOLAKIS et al.: “Geant4 developments and applications”, IEEE Transactions on Nuclear Science, Vol. 53, No. 1 (2006) DOI: http://dx.doi.org/10.1109/TNS.2006.869826.

[57] H. HIRAYAMA, T. SANAMI: “Inter-comparison of particle production”, Proceedings of 12th Shielding Aspects of Accelerators, Targets and Irradiation Facilities SATIF-12, Batavia, Illinois, US (2014) 230-239.

[58] A. FASSO, A. FERRARI, A. FERRARI et al.: “Code inter-comparison and benchmark for muon fluence and absorbed dose induced by an 18 GeV electron beam after massive iron shielding” Proceedings of 12th Shielding Aspects of Accelerators, Targets and Irradiation Facilities SATIF-12, Batavia, Illinois, US (2014) 240-247.

[59] Irène Joliot-Curie - Biographical". Nobelprize.org. Nobel Media AB 2014. Available: http://www.nobelprize.org/nobel_prizes/chemistry/laureates/1935/joliot-curie-bio.html [Jan. 15, 2017]

[60] E.A. UEHLING: “Penetration of Heavy Charged Particles in Matter”, Annual Review of Nuclear Science, Vol. 4: 315-350 (1954) DOI: http://dx.doi.org/10.1146/annurev.ns.04.120154.001531

[61] H.A. BETHE, J. ASKIN: “Passage of Radiations Through Matter”, Experimental Nuclear Physics, Wiley, New York (1953–1959)

[62] H.A. BETHE: “Molière’s theory of multiple scattering”. Phys Rev (1953) 89:1256 66, DOI: http://dx.doi.org/10.1103/PhysRev.89.1256

[63] J.C. ASHLEY, R.H. RITCHIE, W. BRANDT: “Effect in the stopping power of matter for charged particles”. Phys Rev B (1972) 5(7):2393–7, DOI: http://dx.doi.org/10.1103/PhysRevB.5.2393

[64] J.C. ASHLEY, R.H. RITCHIE, W. BRANDT: “Z_1^3-dependent stopping power and range contributions”, Phys Rev A (1973) 8(5):2402–8. DOI: http://dx.doi.org/10.1103/PhysRevA.8.2402

[65] J.F. ZIEGLER: “Stopping of energetic light ions in elemental matter”, J. Appl. Phys. (1999) 85(3):1249–72, DOI: http://dx.doi.org/10.1063/1.369844

[66] W.H. BARKAS: “Mass-Ratio Method Applied to the Measurement of L-Meson Masses and the Energy Balance in Pion Decay”, Phys. Rev. 101 (1956) 778, DOI: http://dx.doi.org/10.1103/PhysRev.101.778

[67] W.H. BARKAS: “Resolution of the Σ^--Mass Anomaly”, Phys. Rev. Lett. 11, 138 (1963) DOI: http://dx.doi.org/10.1103/PhysRevLett.11.26

[68] F. BLOCH: “Zur Bremsung rasch bewegter Teilchen beim Durchgang durch Materie”, Ann Phys (1933) 16:285, DOI: http://dx.doi.org/10.1002/andp.19334080303

[69] N.F. MOTT: “The scattering of fast electrons by atomic nuclei”. Proc R Soc A (1929) 124:425–42, DOI: http://dx.doi.org/10.1098/rspa.1929.0127

[70] I. JUN, W. KIN, R. EVANS: “Electron Nonionizing Energy Loss for Device Applications”, IEEE Transactions on Nuclear Science 56: 6 (2009) 3229-3235, DOI: http://dx.doi.org/10.1109/TNS.2009.2033692.

[71] F. HUBERT, R. BIMBOT, H. GAUVIN et al.: “Semi-empirical formulae for heavy ion stopping powers in solids in the intermediate energy range”, Nucl Instrum Methods Phys Res B (1989) 36(4):357–63. DOI: http://dx.doi.org/10.1016/0168-583X(89)90339-X

[72] G. RAJ: “Advanced Inorganic Chemistry”, Meerut, India, GOEL Publishing house, 2008, ISBN: 81-87224-03-7.

[73] J. MAGILL, J. GALY: “Radioactivity Radionuclides Radiation”, Karlsruhe, Germany, Springer - Verlag Berlin Heidelberg and European Communities, 2005, ISBN: 3-540-21116-0.

[74] J.F. ZIEGLER: “SRIM (The Stopping and Range of Ions in Matter)”. Available: http://www.srim.org/, Mar. 1, 2014, [Jun. 10, 2014].

[75] J.F. ZIEGLER, J.P. BIERSACK: “The Stopping and Range of Ions in Matter”, Springer US, 1985, pp 93-129, ISBN: 978-1-4615-8105-5.

[76] COMMITTEE ON NUCLEAR SCIENCE, SUBCOMMITTEE ON PENETRATION OF CHARGED PARTICLES, NATIONAL ACADEMY OF SCIENCES: “Studies in Penetration of Charged Particles in Matter”, (Nuclear Science), Washington, DC (1964)

[77] H. NIFENECKER, O. MEPLAN, S. DAVID: “Accelerator Driven Subcritical Reactors.” Series in Fundamental and Applied Nuclear Physics, Institute of Physics Publishing, Bristol and Philadelphia, 2003.

[78] M. BRUGGER, A. FERRARI, S. ROESLER et al.: “Validation of the FLUKA Monte Carlo code for predicting induced radioactivity at high-energy accelerators”. Nuclear Instruments and Methods in Physics Research A 562 (2006) 814-818.

[79] P. CARBONEZ, F.P. LA TORRE, R. MICHAUD et al.: “Residual radioactivity at the CERN 600 MeV synchro-cyclotron”. Nuclear Instruments and Methods in Physics Research A 694 (2012) 234-245.

[80] L. ULRICI, Y. ALGOET, L. BRUNO et al.: “Radiation protection challenges in the management of radioactive waste from high-energy accelerators”. Radiation Protection Dosimetry, Vol 164, No. 1-2 (2015) 112-115.

[81] DEFENCE STANDARD 00-56: “Safety management requirements for defence systems”, Ministry of defence (2007).

[82] J. BERINGER et al.: (Particle Data Group), Phys. Rev. D 86, 010001 (2012).

[83] A.N. KALINOVSKII et al.: “Passage of High-Energy Particles through Matter”. New York: American Institute of Physics, 1989.

[84] A. FERRARI, P.R. SALA: “The Physics of High Energy Reactions”, Proc. Workshop on Nuclear Reaction Data and Nuclear Reactors Physics, Design and Safety, Trieste, April 1996, Ed. A. Gandini and G. Reffo (1998) p. 424.

[85] TECHNICAL REPORTS SERIES NO. 402: “Handling and processing of radioactive waste from nuclear applications”. Vienna: International Atomic Energy Agency, 2001.

[86] T.T. BÖHLEN, F. CERUTTI, M.P.W. CHIN et al.: “The FLUKA Code: Developments and Challenges for High Energy and Medical Applications”, Nuclear Data Sheets 120, 211-214 (2014).

[87] A. FERRARI, P.R. SALA: “The Physics of High Energy Reactions”, Proceedings of Workshop on Nuclear Reaction Data and Nuclear Reactors Physics, Design and Safety, Miramare Trieste, Italy, 15-17 April 1996.

[88] A. FERRARI, P.R. SALA, R. GUARALDI et al.: “An improved multiple scattering model for charged particle transport” Presented at the Int. Conf. on Radiation Physics, Dubrovnik, 1991 Nucl. Instr. Meth. B71, 412-426 (1992)

[89] A. FASSO, A. FERRARI, J. RANFT et al.: “New developments in FLUKA modelling of hadronic and EM interactions”, Proceedings of the 3rd workshop on simulating accelerator radiation environments SARE, KEK, Tsukuba, Japan (1997) 32-43, KEK-PROC—97-5.

[90] A. FASSO, A. FERRARI, P.R. SALA et al.: “Electron-photon transport in FLUKA”, Proceedings of the Monte Carlo 2000 Conference, Lisbon (2001) 159-164.

[91] L. LANDAU: “On the energy loss of fast particles by ionization”. J Phys USSR (1944) 8:201.

[92] P.V. VAVILOV: “Ionization losses of high-energy heavy particles”. Sov Phys JETP (1957) 5:749.

[93] F. COLLAMATI: “An Intraoperative Beta-Probe for Cancer Surgery”, Springer Theses, DOI: http://dx.doi.org/10.1007/978-3-319-33699-2_2

[94] THE CERN FLUKA TEAM: 6th FLUKA Course - CERN 2008: “Statistic and Sampling.” CERN, 23rd June 2008.

[95] G. BATTISTONI, F. CENTURI, A. FASSO et al.: “The FLUKA code: description and benchmarking”, Proceedings of the Hadronic Shower Simulation Workshop, Fermilab, AIP conference Proceeding 896 (2007) 31-49.

[96] T.T. BÖHLEN, F. CERUTTI, M. DOSANJH et al.: ”Benchmarking nuclear models of FLUKA and GEANT4 for carbon ion therapy”, Phys. Med. Bio 55 (2010) 5833-5847, DOI: http://dx.doi.org/10.1088/0031-9155/55/19/014.

[97] G. MOLIÈRE: “Theorie der streuung schneller geladener teilchen. iii. die vielfachstreuung von bahnspuren unter berücksichtigung der statistischen kopplung”. Z Naturforsch A (1955) 10:177

[98] J. F. ZIEGLER, M. D.ZIEGLER, J. P. BIERSACK: “SRIM – The stopping and range of ions in matter (2010)” Nucl. Instrum. Methods Phys. Res., Sect. B 268 (2010) 1818, DOI: http://dx.doi.org/10.1016/j.nimb.2010.02.091.

[99] J. F. ZIEGLER, J. P.BIERSACK, M. D. ZIEGLER: “SRIM–The Stopping and Range of Ions in Matter”, Lulu Press Co., Morrisville, NC (2008) Available: http://www.srim.org/, Mar. 1, 2014, [Jun. 10, 2014].

[100] W. BRANDT, M. KITAGAWA: “Effective stopping-power charges of swift ions in condensed matter”, Physical Review 25B (1982) 5631, DOI: http://dx.doi.org/10.1103/PhysRevB.25.5631.

[101] N. BOHR: Kgl. Danske Videnskab Selskab., Mat.-Fys. Medd, 18 (1948) 581.

[102] J. F. ZIEGLER: “Stopping of energetic light ions in elemental matter” J. Appl. Phys., 85 (1999) 1249-1272, DOI: http://dx.doi.org/10.1063/1.369844

[103] H. WEICK: “ATIMA (Energy loss of ions penetrating matter)”. Available: http://www-linux.gsi.de/~weick/atima.html, Mar. 13, 2014, [Dec. 1, 2014].

[104] A. PROCHAZKA: “WebAtima”. Available: http://web-docs.gsi.de/~aprochaz/webatima/about.html, Dec. 12, 2016, [Apr. 10, 2017].

[105] J. LINDHARD, A.H. SOERENSEN: “Relativistic theory of stopping for heavy ions”, Phys. Rev. A53 (1996) 2443, DOI: http://dx.doi.org/10.1103/PhysRevA.53.2443

[106] W.H. BARKAS, M.J. BERGER: “Tables of energy losses and ranges of heavy charged particles”, Scientific report NASA Report SP-3013 (1964).

[107] J.D. JACKSON, R.L. MCCARTHY: “Z^3 Corrections to Energy Loss and Range”, Phys.Rev. B6 (1972) 4131-4141, DOI: http://dx.doi.org/10.1103/PhysRevB.6.4131

[108] J. LINDHARD: “The Barkas effect - or Z_1^3, Z_1^4-corrections to stopping of swift charged particles”, Nucl. Instr. and Meth. 132 (1976) 1-5, DOI: http://dx.doi.org/10.1016/0029-554X(76)90702-3.

[109] R.M. STERNHEIMER, R.F. PEIERLS: “General Expression for the Density Effect for the Ionization Loss of Charged Particles”, Phys. Rev. B3 (1971) 3681, DOI: http://dx.doi.org/10.1103/PhysRevB.3.3681

[110] T.E. PIERCE, M. BLANN: “Stopping Powers and Ranges of 5-90-MeV S^{32}, Cl^{35}, Br^{79}, and I^{127} Ions in H_2, He, N_2, Ar, and Kr: A Semiempirical Stopping Power Theory for Heavy Ions in Gases and Solids”, Phys. Rev. B 1 173 (1968) 390, DOI: http://dx.doi.org/10.1103/PhysRev.173.390.

[111] H.A. BETHE: “Bremsformel für Elektronen relativistischer Geschwindigkeit“ Z. Phys. 76 (1932) 293-299, DOI: http://dx.doi.org/10.1007/BF01342532.

[112] O.B. FIRSOV: “Interaction Energy of Atoms for Small Nuclear Separations”, SOV. PHYS. JETP 5 (1957) 1192.

[113] P. HVELPLUND: “Energy Loss and Straggling of 100-500 keV Atoms with 2 ó Z1 ó 12 in Various Gases” Kgl. Danske Videnskab. Selskab Mat. Fys. Medd., 38, No. 4, P. 1-25 (1971).

[114] C. SCHEIDENBERGER, H. GEISSEL, H. H. MIKKELSEN et al.: “Direct observation of systematic deviations from the Bethe stopping theory for relativistic heavy ions”, Phys. Rev. Lett. 73 (1994) 50, DOI: http://dx.doi.org/10.1103/PhysRevLett.73.50.

[115] C. SCHEIDENBERGER, H. GEISSEL, H.H. MIKKELSEN et al.: “Energy-Loss-Straggling Experiments with Relativistic Heavy Ions in Solids” Phys. Rev. Lett. 77 (1996) 3987, DOI: http://dx.doi.org/10.1103/PhysRevLett.77.3987.

[116] H. GEISSEL, C. SCHEIDENBERGER: “Slowing Down of Relativistic Heavy Ions and New Applications”, Nucl. Instr. and Meth. B136-138 (1998) 114-124.

[117] C. SCHEIDENBERGER, H. GEISSEL: “Penetration of relativistic heavy ions through matter”, Nucl. Instr. and Meth. B135 (1998) 25, DOI: http://dx.doi.org/10.1016/S0168-583X(97)00639-3.

[118] H. GEISSEL, H. WEICK, C. SCHEIDENBERGER et al.: “Experimental studies of heavy-ion slowing down in matter”, Nucl. Instr. and Meth. B195 (2002) 3, DOI: http://dx.doi.org/10.1016/S0168-583X(02)01311-3.

[119] H. WEICK, H. GEISSEL, C. SCHEIDENBERGER et al.: “Drastic Enhancement of Energy-Loss Straggling of Relativistic Heavy Ions due to Charge-State Fluctuations”, Phys. Rev. Lett. 85 (2000) 2725, DOI: http://dx.doi.org/10.1103/PhysRevLett.85.2725.

[120] H. WEICK, A.H. SOERENSEN et al.: “Energy-loss straggling of (200–1000) MeV/u uranium ions”, Nucl. Instr. and Meth. B 193 (2002) 1-7, DOI: http://dx.doi.org/10.1016/S0168-583X(02)00718-8.

[121] H. WEICK et al.: “Slowing down of relativistic few-electron heavy ions”, Nucl. Instr. and Meth. B 164-165 (2000) 168-179, DOI: http://dx.doi.org/10.1016/S0168-583X(99)01025-3.

[122] J. PAWELKE, W. ENGHARDT, T. HABERER et al.: “In-beam PET imaging for the control of heavy-ion tumour therapy”. IEEE Transactions on nuclear science, vol. 44, No. 4 (1997) 1492-1498, DOI: http://dx.doi.org/10.1109/23.632694.

[123] K. PARODI, T. BORTFELD, W. ENGHARDT et al.: “PET imaging for treatment verification of ion therapy: Implementation and experience at GSI Darmstadt and MGH Boston”, Nucl. Instrum. Methods A 591 (2008) 282-286, DOI: http://dx.doi.org/10.1016/j.nima.2008.03.075 .

[124] W. ENGHARDT, P. CRESPO, F. FIEDLER et al.: “Charged hadron tumour therapy monitoring by means of PET”, Nucl. Instrum. Methods A 525 (2004) 284-288, DOI: http://dx.doi.org/10.1016/j.nima.2004.03.128.

[125] “Verordnung über den Schutz vor Schäden durch ionisierende Strahlen” (BGBl. I S. 1714; 2002 I S. 1459) (2001) Available: http://www.gesetze-im-internet.de/strlschv_2001/

[126] H. REEG, N. SCHNEIDER: Current transformers for GSI’s keV/u to GeV/u ion beams – an overview, Proceedings of DIPAC 2001, ESRF, Grenoble, France (2001) 120-122.

[127] GSI HELMHOLTZZENTRUM FÜR SCHWERIONENFORSCHUNG GMBH.: “Heavy ion synchrotron SIS18 – Beam properties”, Available: https://www.gsi.de/en/work/accelerator/heavy_ion_synchrotron _sis18 /beam_properties.htm, [Apr. 7, 2017].

[128] M. SCHWICKERT, T. HOFFMANN, F. KURIAN et al.: “Diagnostic devices for beam intensity measurement at FAIR”, Proceedings of IPAC2011, San Sebastian, Spain (2011) 1174-1176.

[129] E. SOLIMAN, K. HOFFMANN, H. REEG et al.: “Sensor studies for DC current transformer application”, Proceedings of IBIC2014, Monterey, CA, USA (2014) 624-628.

[130] “Secondary Electron TRAnsmission Monitor”. Available: https://www-win.gsi.de/charms/ seetraminfo/ seetram2.htm, Dec. 10, 2008, [Feb. 14, 2014].

[131] A. JUNGHANS, H.G. CLERC, A. GREWE et al.: “A self-calibrating ionisation chamber for the precise intensity calibration of high-energy heavy-ion beam monitors”, Nucl. Instrum. Methods A 370 (1996) 312-314.

[132] B. JURADO, K. SCHMIDT, K. BEHR: “Application of a secondary-electron transmission monitor for high-precision intensity measurements of relativistic heavy-ion beams”, Nuclear Instruments and Methods in Physics Research Section A: Accelerators, Spectrometers, Detectors and Associated Equipment 483 (2002) 603-610, DOI: http://dx.doi.org/10.1016/S0168-9002(01)01931-3.

[133] C. ZIEGLER, T. BROHM, H.G. CLERC et al.: “Performance of the secondary-electron transmission Monitor at the FRS”. GSI Scientific Report 1990 (1991) 291.

[134] B. WALASEK-HOHNE, C. ANDRE, P. FORCK et al.: “Scintillating screen applications in accelerator beam diagnostics”. IEEE Transactions on nuclear science, vol. 59, No. 5 (2012) 2307-2312.

[135] A. LIEBERWIRTH, W. ENSINGER, P. FORCK et al.: “Response of scintillating screens to fast and slow extracted ion beams”, Proceedings of IBIC2013, Oxford, UK (2013) 553-556.

[136] S. DEVASAHAYAM, D. J.T. HILL, J. CONNELL.: “A comparative study of the radiation resistance of four optically transparent polyimides”. Radiation Physics and Chemistry 62 (2001) 189-194.

[137] N. SERTOVA, E. BALANZAT, M. TOULEMONDE, C. TRAUTMANN: “Investigation of initial stage of chemical etching of ion tracks in polycarbonate”. The Seventh International Symposium on Swift Heavy Ions in Matter, Lyon, France (2008).

[138] G.R. GILMORE: “Practical Gamma-Ray Spectroscopy”. Warrington, UK, 2008, ISBN: 978-0-470-86196-7.

[139] CANBERRA INDUSTRIES, INC.: “Germanium Detectors – User’s Manual”, Available: https://www1.aps.anl.gov/files/download/DET/Detector-Pool/Spectroscopic- Detectors/Canberra /Germanium_Detectors_Manual.pdf, [Jul. 7, 2016].

[140] ADVANCED MEASUREMENT TECHNOLOGY “DSP^{EC} LF – High-Performance, Digital Signal Processor for Gamma Spectroscopy”, Available: www.ortec-online.com/download/dspec-lf.pdf, [Jul. 7, 2016].

[141] ADVANCED MEASUREMENT TECHNOLOGY “GammaVision – Gamma Spectroscopy Software”, Available: http://www.ortec-online.com/download/GammaVision.pdf, [Jul. 7, 2016].

[142] L.P. REEG, R.B. FIRESTONE: “WWWTable of Radioactive Isotopes”. Database version 2/28/99. Available: http://ie.lbl.gov/toi/index.htm. [Feb. 14, 2014].

[143] S.Y.F. CHU, L.P. REEG, R.B. FIRESTONE: “The Lund/LBNL Nuclear Data Search”. Version 2.0, February 1999. Available: http://nucleardata.nuclear.lu.se/toi/ . [Jul. 25, 2016].

[144] C.L. DUNFORD AND T.W. BURROWS: “Online Nuclear Data Service, Report IAEA-NDS-150” (NNDC Informal Report NNDC/ONL-95/10), Rev. 12/01 (2012) International Atomic Energy Agency, Vienna, Austria

[145] “General User's Guide to the NEA Online Services”, Report DBG-030.11, NEA Data Bank, Paris, France (1993).

[146] M.F. L’Annuziata: “Handbook of Radioactivity Analysis”. 3rd edition, Academic Press, 2012. ISBN: 978-0-12-384873-4

[147] R.H. CROWELL, W.E. SLESNICK: “Calculus with Analytic Geometry (3rd ed.)”. W.W. Norton & Company Inc., 2008, Available: https://math.dartmouth.edu/~doyle/docs/calc/calc.pdf [Jun 11, 2016].

[148] G.B. THOMAS, R.L. FINNEY: “Calculus and Analytic Geometry (9th ed.)”. Addison-Wesley Publishing Company, 1996, ISBN: 0-201-53174-7

[149] S.S. KAPOOR, V.C. RAMAMURTHY: “Nuclear Radiation Detectors”. New Age International (P) Ltd. Publishers, First Edition: 1986, Reprint: 2005, ISBN: 0-85226-496-8

[150] U.S. DEPARTMENT OF ENERGY, DOE Standard: DOE-STD-1098-99 Radiological control, 2004.

APPENDIX 1 – ALUMINIUM ACTIVATED BY ^{238}U AT 200 MeV/u

The depth profiles of the residual activity induced in aluminium target irradiated by uranium beam with an energy of 200 MeV/u are collected in this section (Figure 56 - Figure 112). The depth profiles of residual activity are sorted from low atomic number (^{7}Be) to higher atomic number (^{237}U). The depth profiles of metastable nuclides are presented without their simulated version due to the lack of capability of the FLUKA code. Nevertheless, publishing the experimental data in this form is meaningful because of their uniqueness. There are some conventions used in presented graphs. Experimental data from the 1st set of measurement (6 – 22 days after the end of the irradiation) are labelled as "(1st)" in the legends and they are marked with "circle" shape in the graphical interpretation. Data obtained from the 2nd set of measurement (133 – 180 days after the end of the irradiation) are labelled as "(2nd)" and with "square" shape of markers. Results of the FLUKA simulations are labelled as "(FLUKA)" in the legends of the graphs and they are graphically represented as the "square" shaped markers of orange colour.

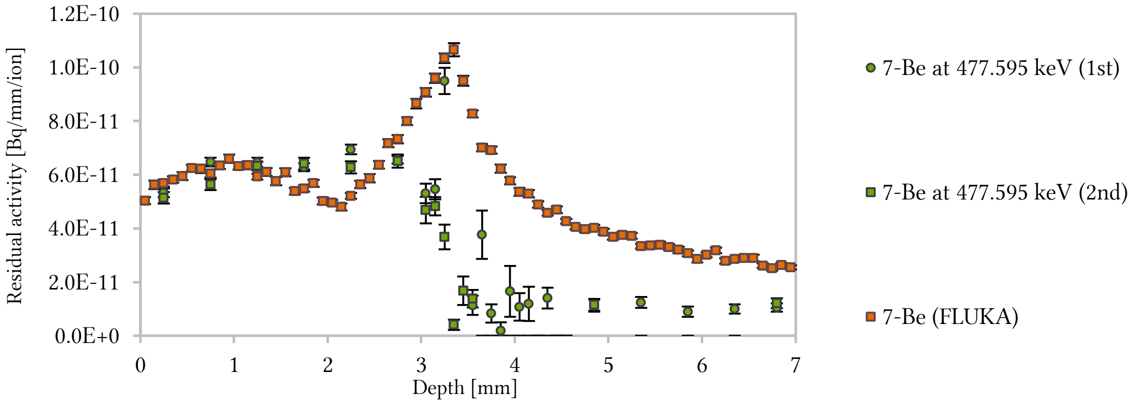

Figure 56: The depth profile of ^{7}Be in the aluminium target irradiated by 200 MeV/u ^{238}U beam.

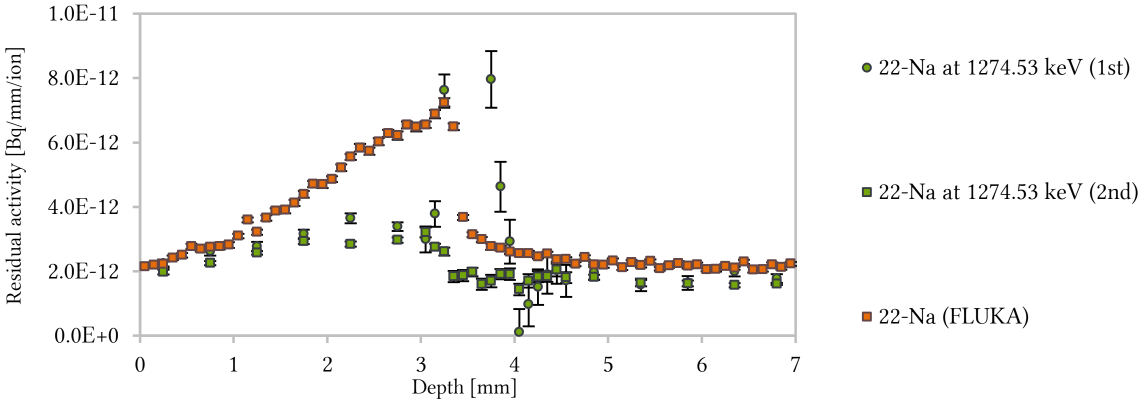

Figure 57: The depth profile of ^{22}Na in the aluminium target irradiated by 200 MeV/u ^{238}U beam.

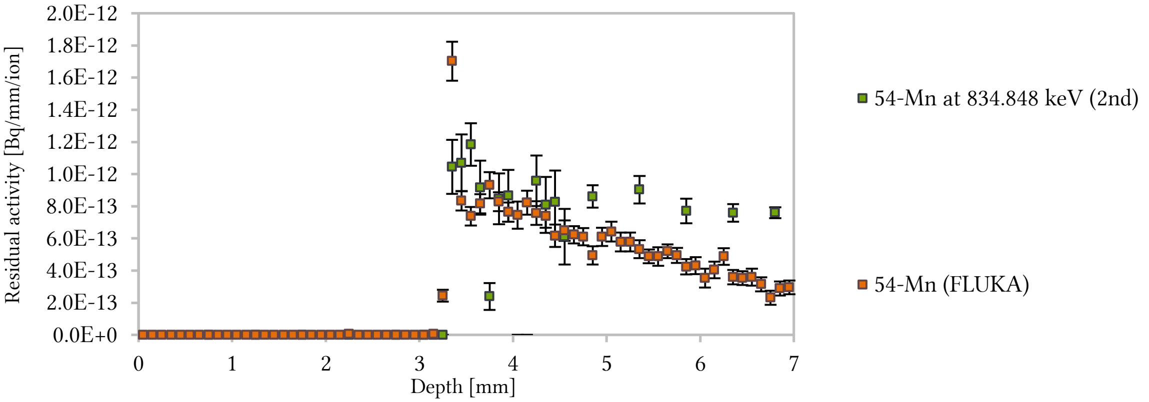

Figure 58: The depth profile of ^{54}Co in the aluminium target irradiated by 200 MeV/u ^{238}U beam.

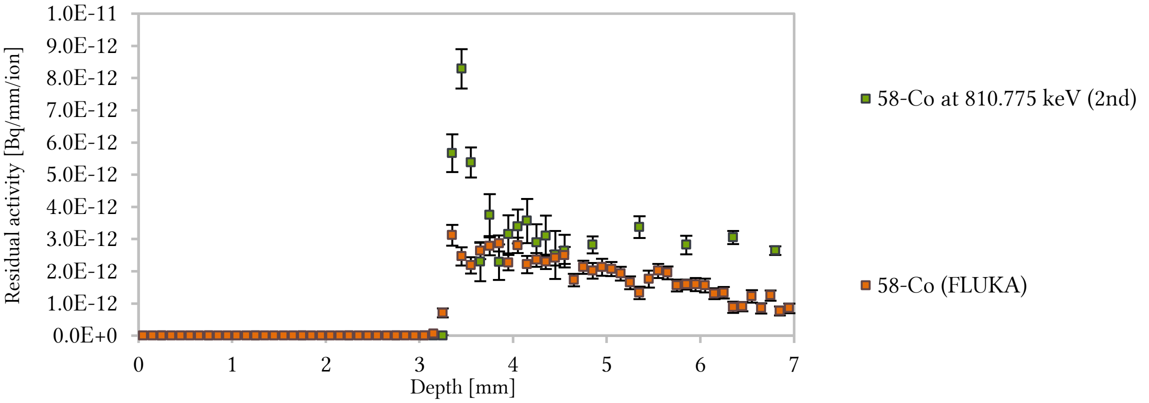

Figure 59: The depth profile of ^{58}Co in the aluminium target irradiated by 200 MeV/u ^{238}U beam.

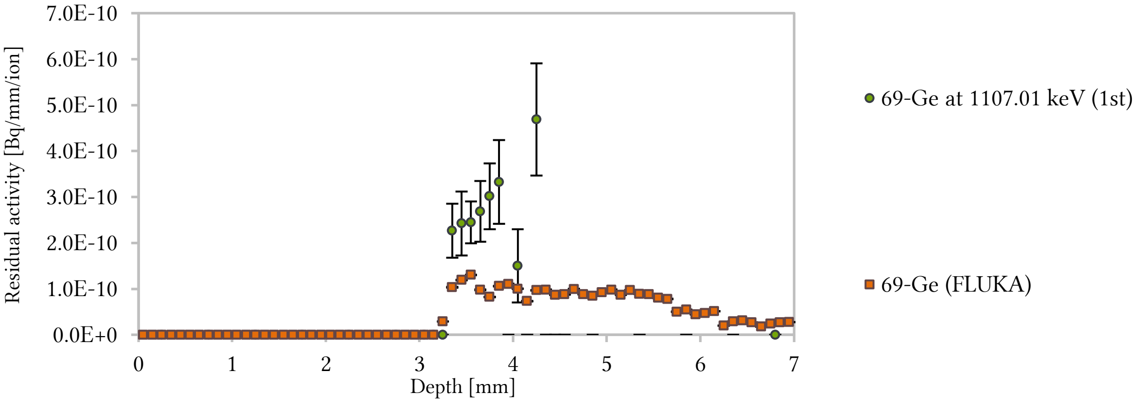

Figure 60: The depth profile of ^{69}Ge in the aluminium target irradiated by 200 MeV/u ^{238}U beam.

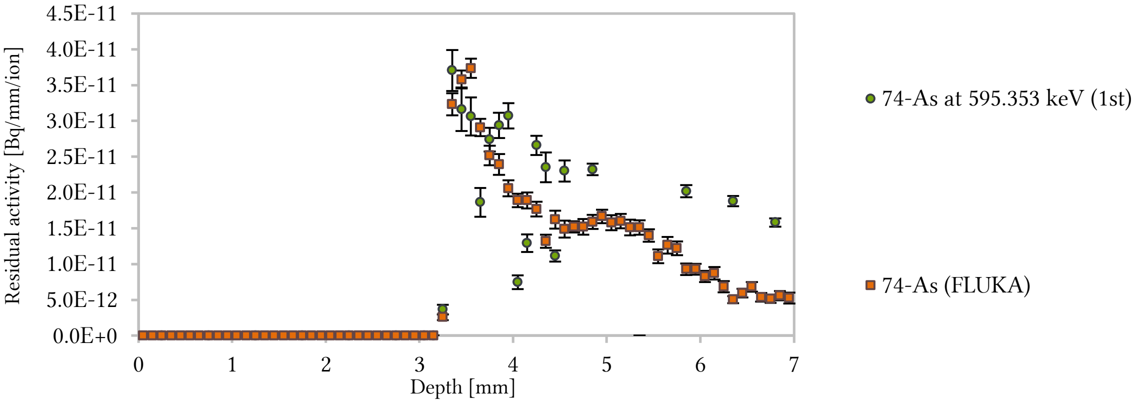

Figure 61: The depth profile of ^{74}As in the aluminium target irradiated by 200 MeV/u ^{238}U beam.

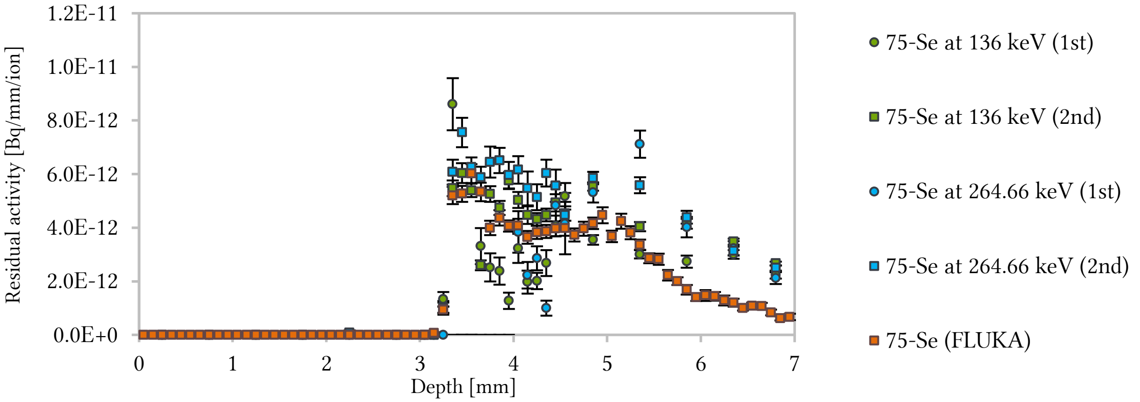

Figure 62: The depth profile of ^{75}Se in the aluminium target irradiated by 200 MeV/u ^{238}U beam.

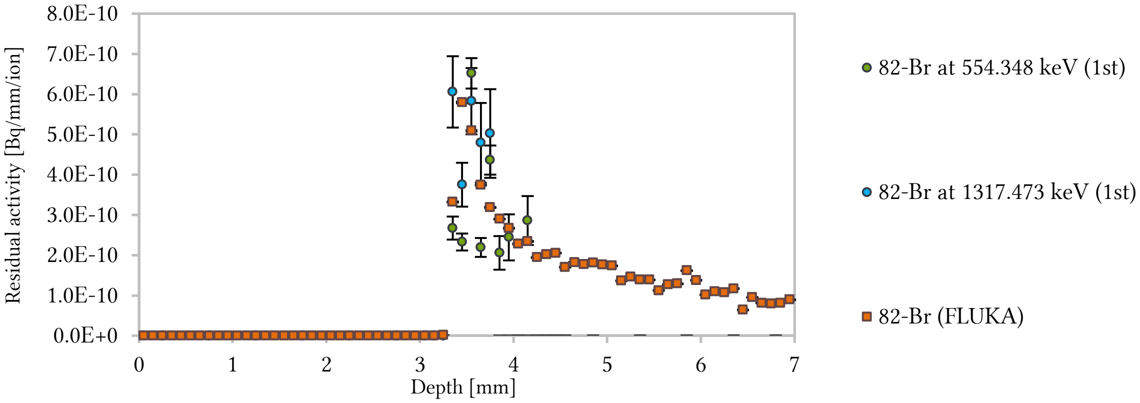

Figure 63: The depth profile of ^{82}Br in the aluminium target irradiated by 200 MeV/u ^{238}U beam.

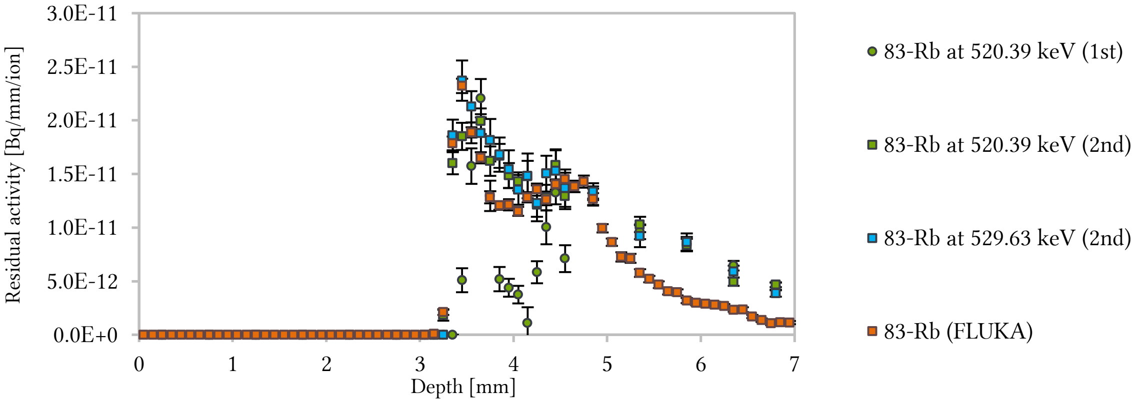

Figure 64: The depth profile of ^{83}Rb in the aluminium target irradiated by 200 MeV/u ^{238}U beam.

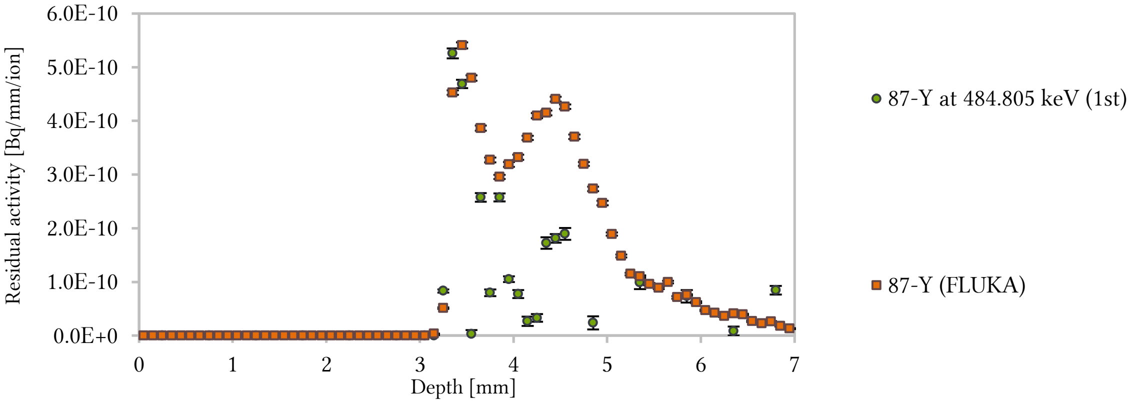

Figure 65: The depth profile of ^{87}Y in the aluminium target irradiated by 200 MeV/u ^{238}U beam.

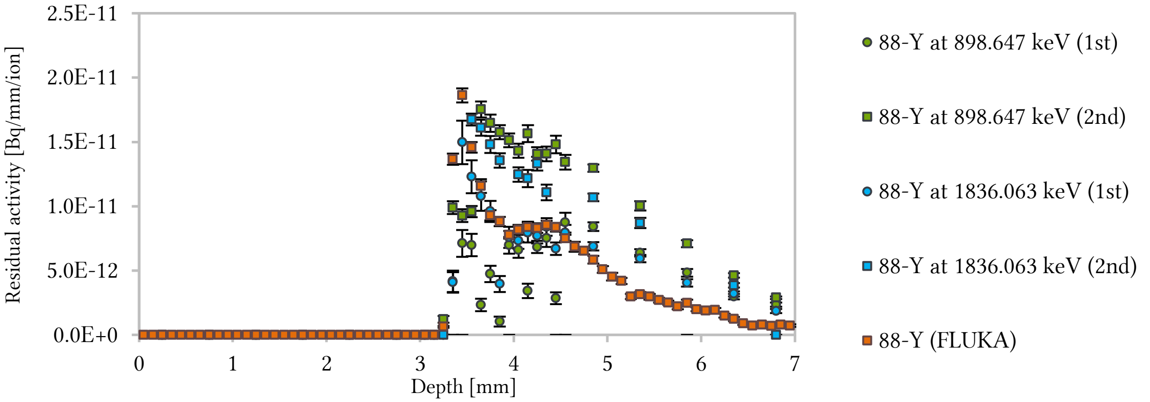

Figure 66: The depth profile of ^{88}Y in the aluminium target irradiated by 200 MeV/u ^{238}U beam.

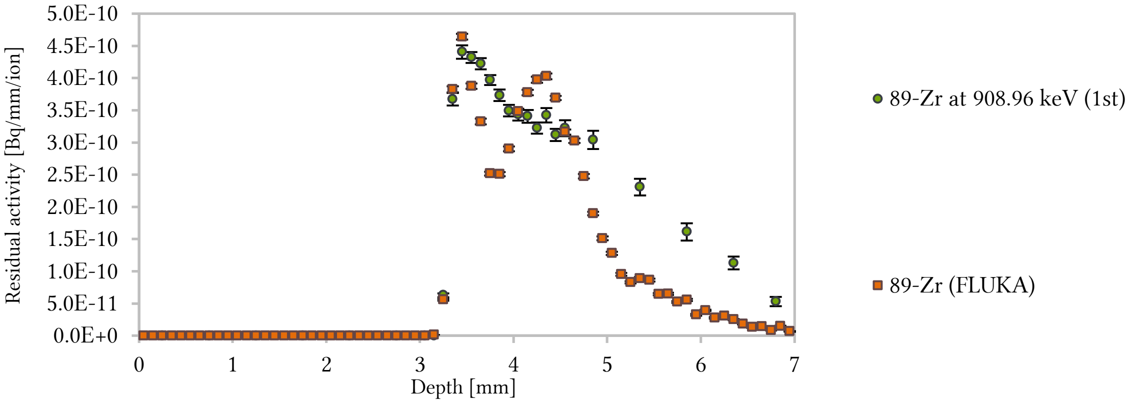

Figure 67: The depth profile of ^{89}Zr in the aluminium target irradiated by 200 MeV/u ^{238}U beam.

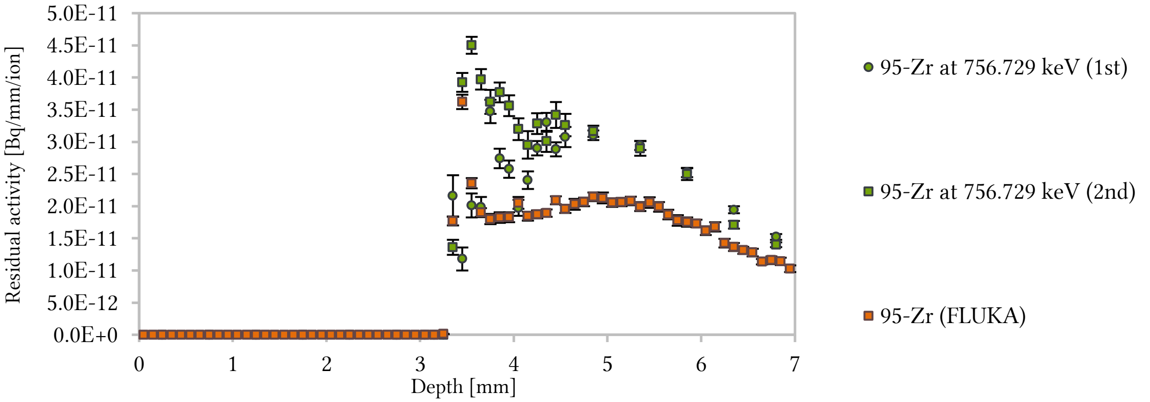

Figure 68: The depth profile of ^{95}Zr in the aluminium target irradiated by 200 MeV/u ^{238}U beam.

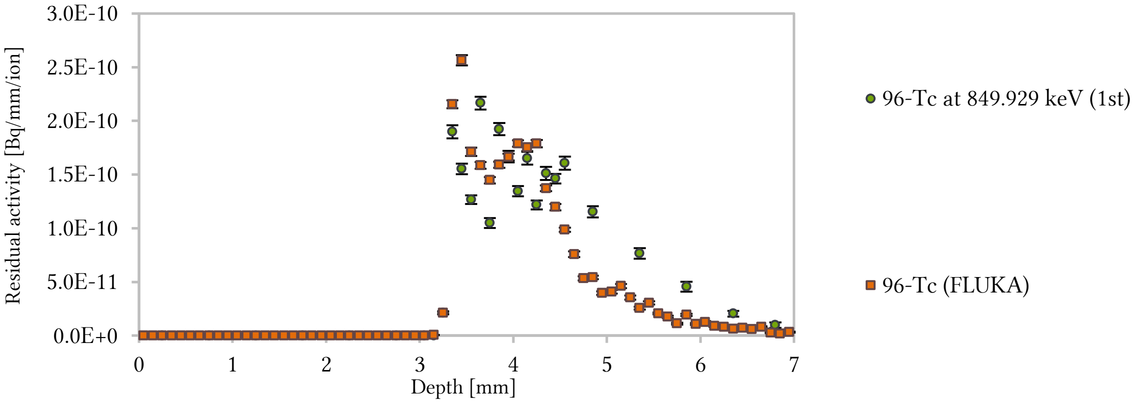

Figure 69: The depth profile of ^{96}Tc in the aluminium target irradiated by 200 MeV/u ^{238}U beam.

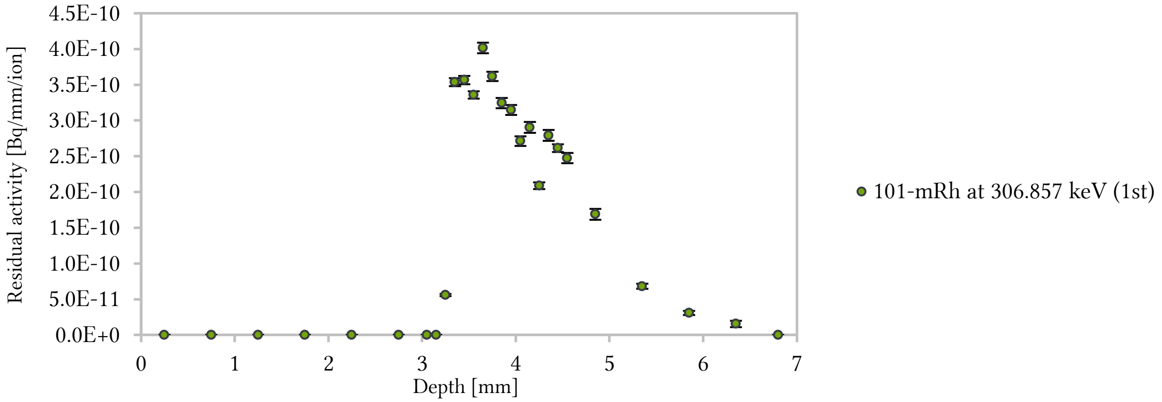

Figure 70: The depth profile of ^{101m}Rh in the aluminium target irradiated by 200 MeV/u ^{238}U beam.

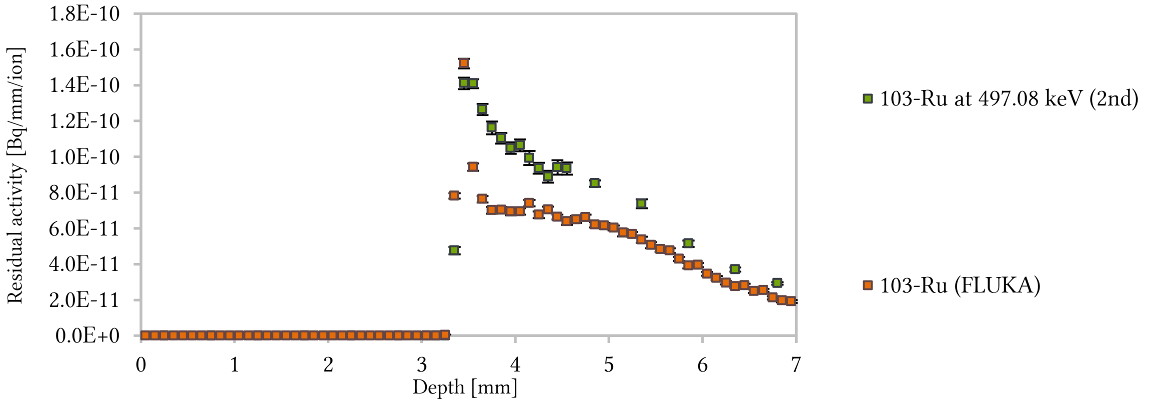

Figure 71: The depth profile of ^{103}Ru in the aluminium target irradiated by 200 MeV/u ^{238}U beam.

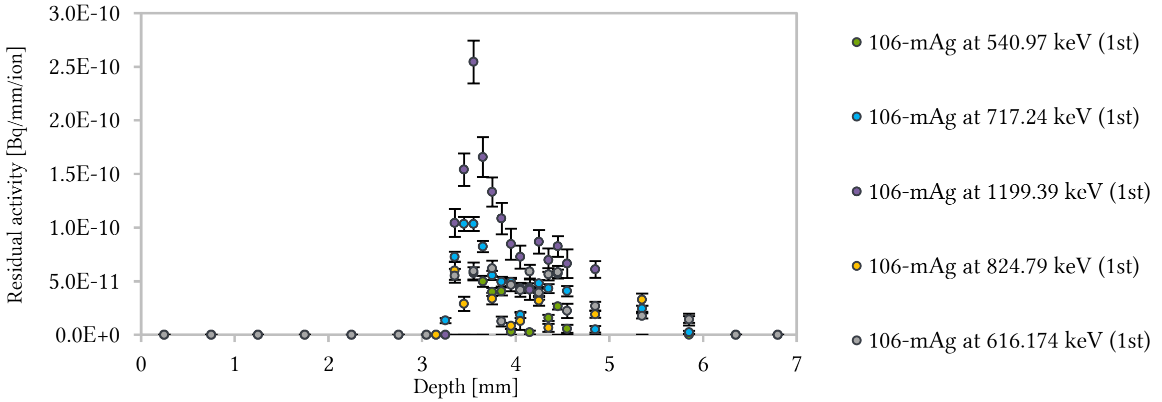

Figure 72: The depth profile of ^{106m}Ag in the aluminium target irradiated by 200 MeV/u ^{238}U beam.

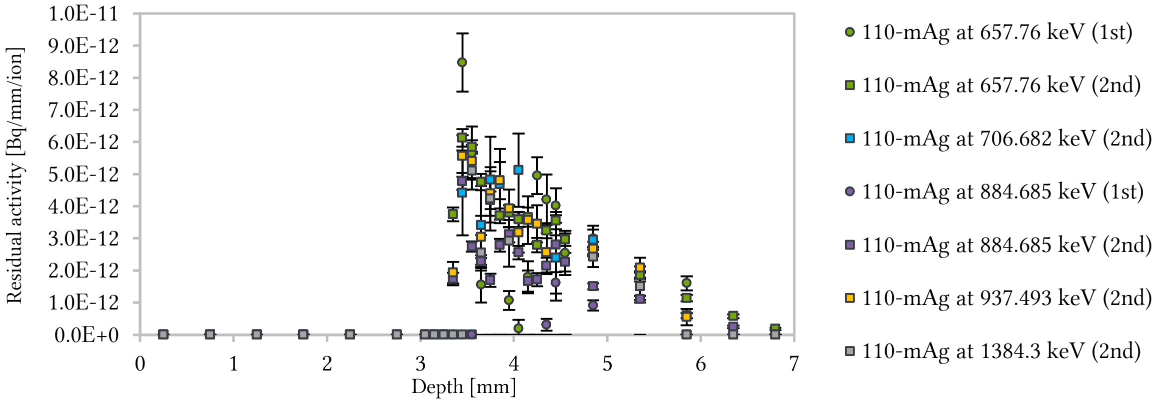

Figure 73: The depth profile of ^{110m}Ag in the aluminium target irradiated by 200 MeV/u ^{238}U beam.

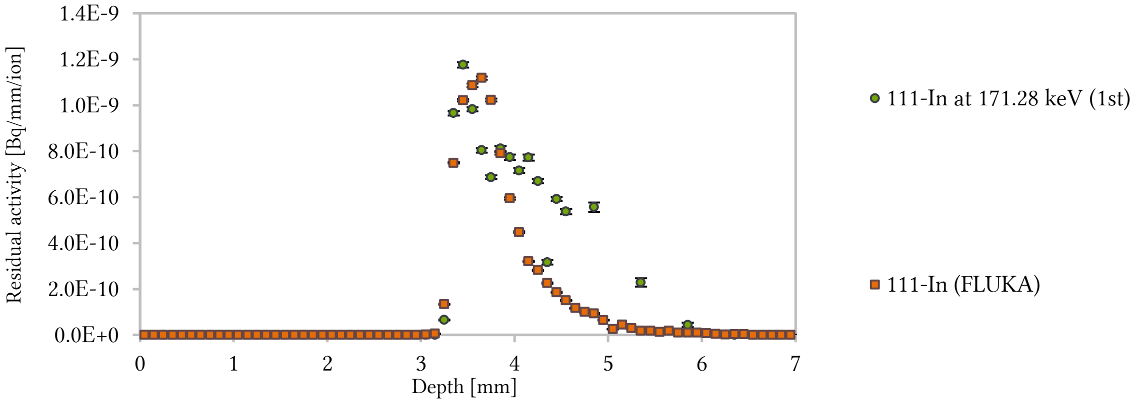

Figure 74: The depth profile of ^{111}In in the aluminium target irradiated by 200 MeV/u ^{238}U beam.

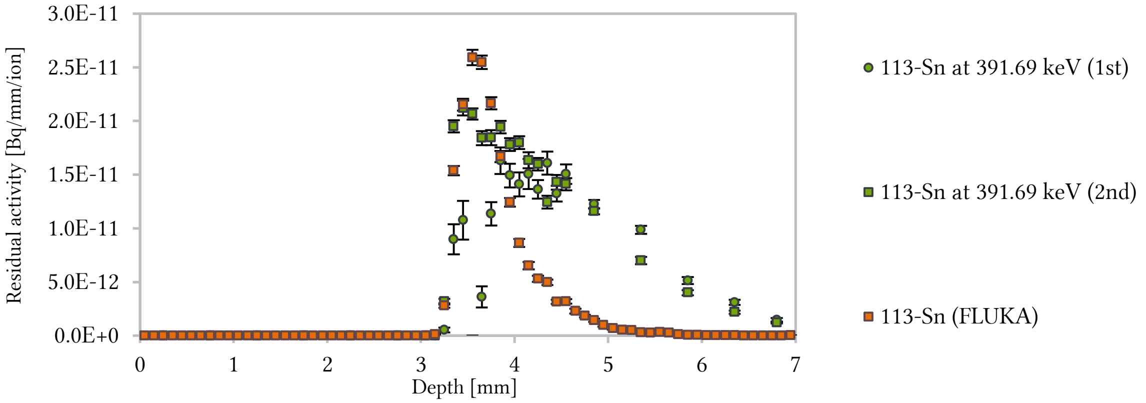

Figure 75: The depth profile of ^{113}Sn in the aluminium target irradiated by 200 MeV/u ^{238}U beam.

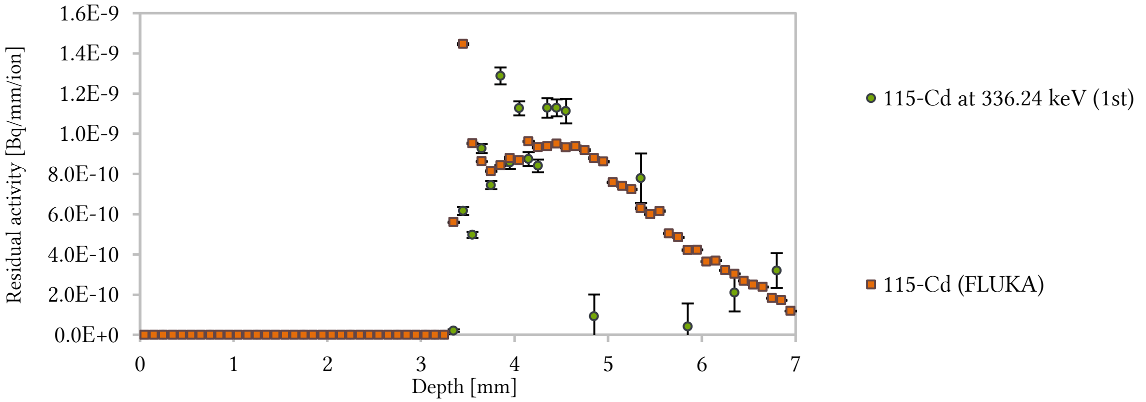

Figure 76: The depth profile of ^{115}Cd in the aluminium target irradiated by 200 MeV/u ^{238}U beam.

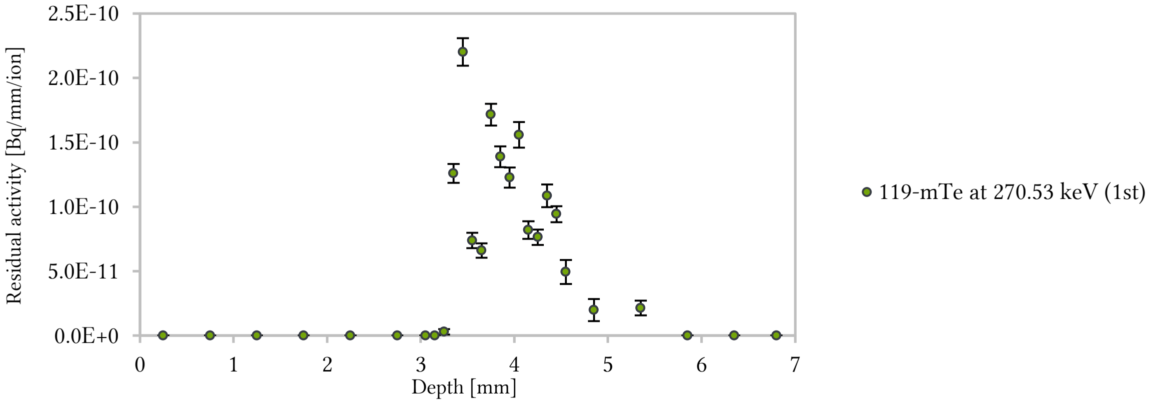

Figure 77: The depth profile of ^{119m}Te in the aluminium target irradiated by 200 MeV/u ^{238}U beam.

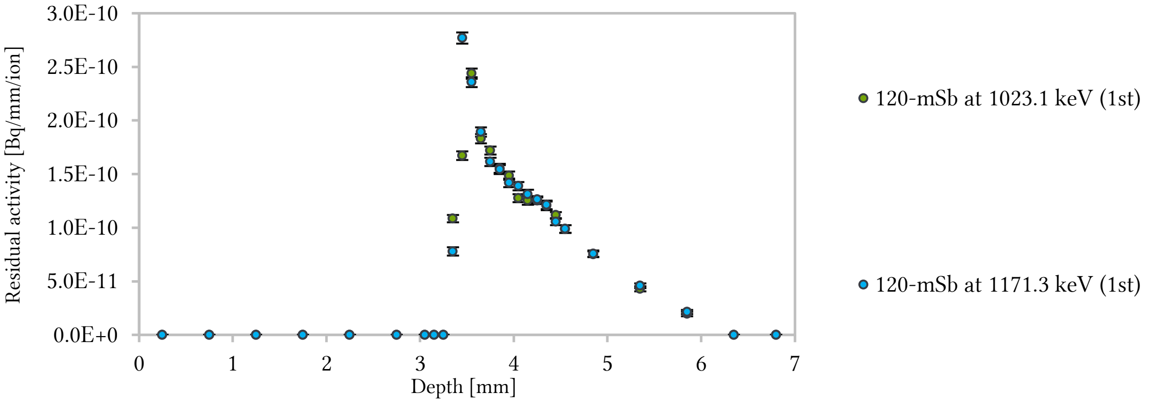

Figure 78: The depth profile of ^{120m}Sb in the aluminium target irradiated by 200 MeV/u ^{238}U beam.

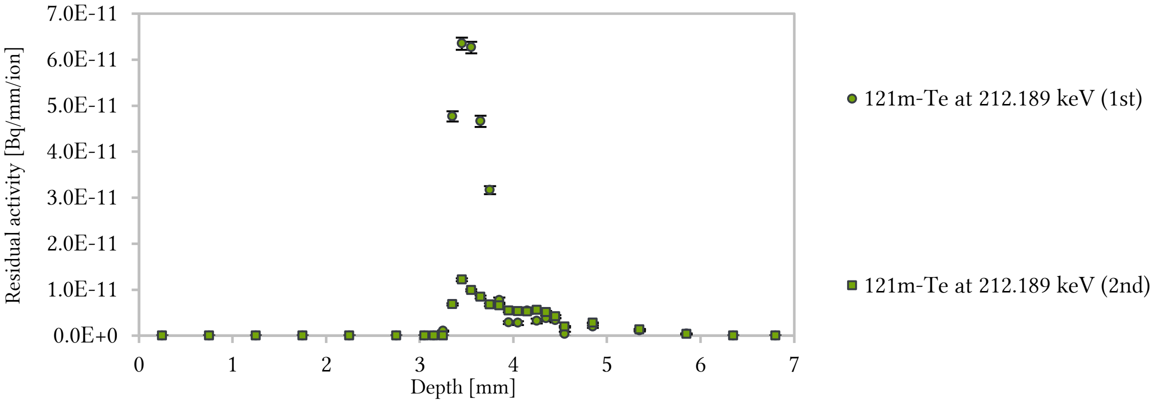

Figure 79: The depth profile of ^{121m}Te in the aluminium target irradiated by 200 MeV/u ^{238}U beam.

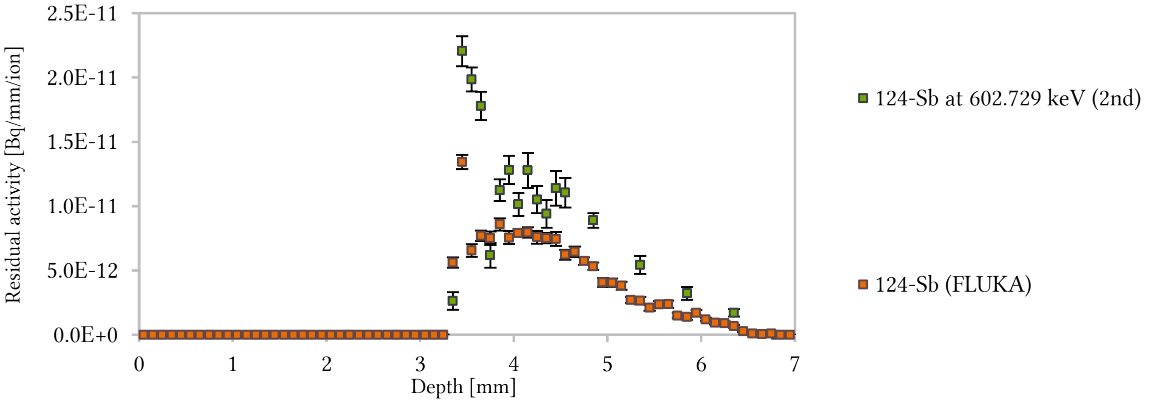

Figure 80: The depth profile of ^{124}Sb in the aluminium target irradiated by 200 MeV/u ^{238}U beam.

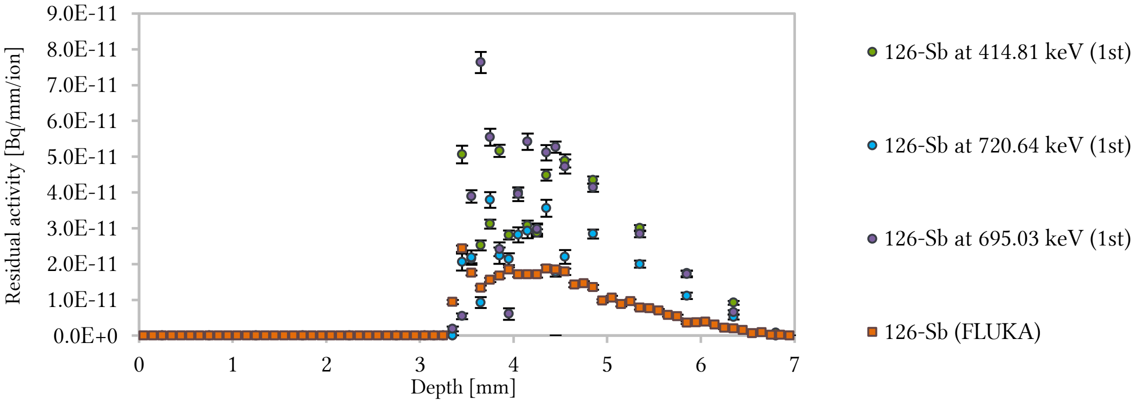

Figure 81: The depth profile of ^{126}Sb in the aluminium target irradiated by 200 MeV/u ^{238}U beam.

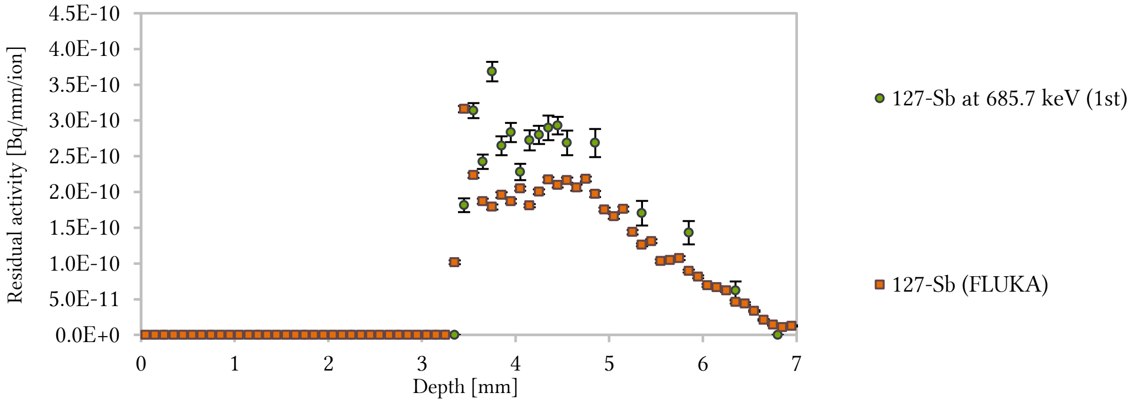

Figure 82: The depth profile of ^{127}Sb in the aluminium target irradiated by 200 MeV/u ^{238}U beam.

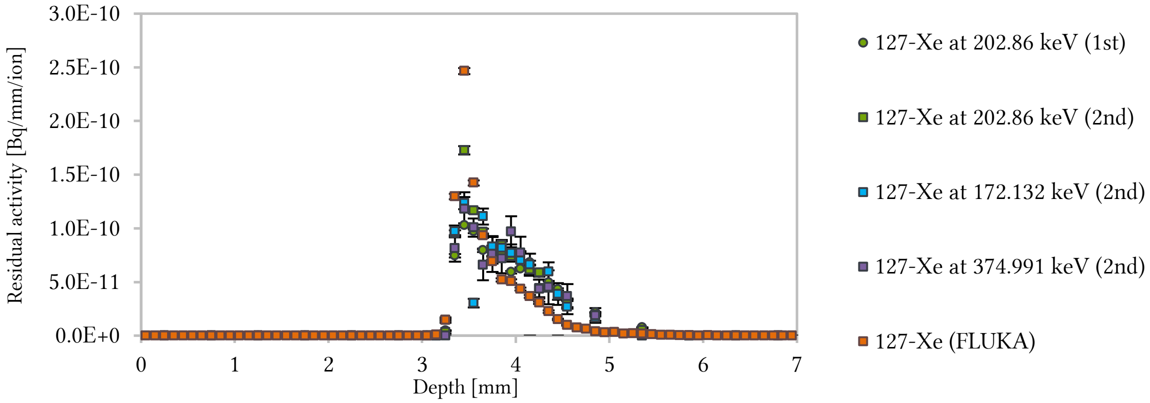

Figure 83: The depth profile of ^{127}Xe in the aluminium target irradiated by 200 MeV/u ^{238}U beam.

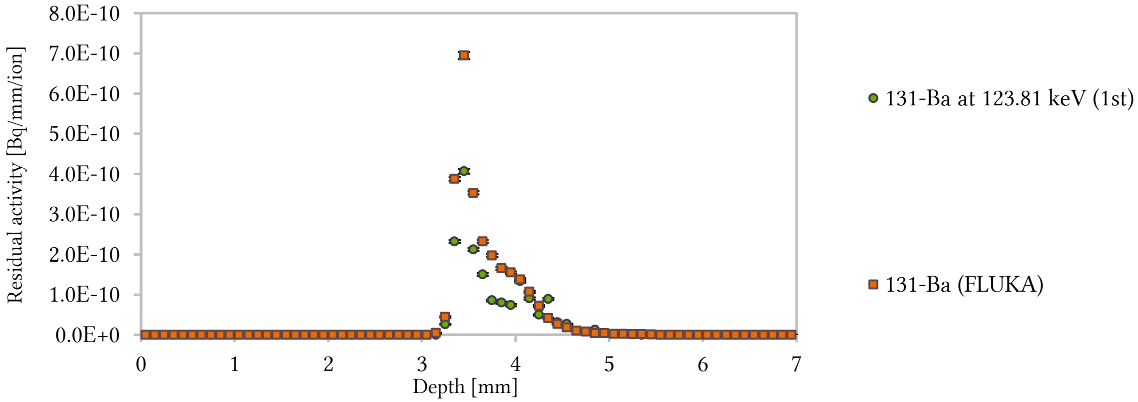

Figure 84: The depth profile of ^{131}Ba in the aluminium target irradiated by 200 MeV/u ^{238}U beam.

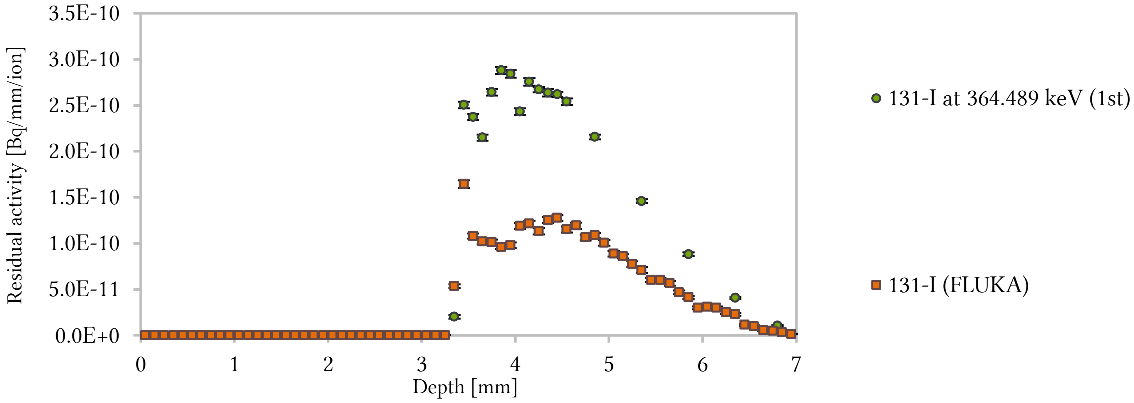

Figure 85: The depth profile of ^{131}I in the aluminium target irradiated by 200 MeV/u ^{238}U beam.

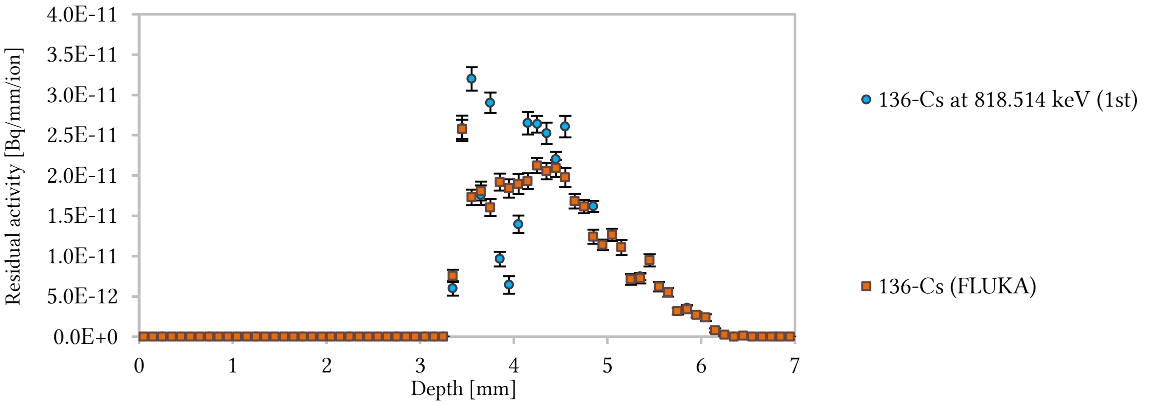

Figure 86: The depth profile of ^{136}Cs in the aluminium target irradiated by 200 MeV/u ^{238}U beam.

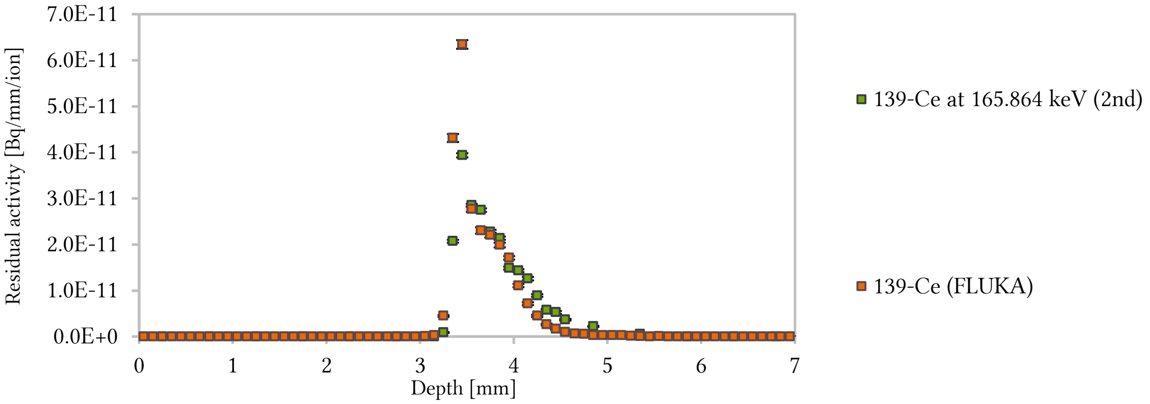

Figure 87: The depth profile of ^{139}Ce in the aluminium target irradiated by 200 MeV/u ^{238}U beam.

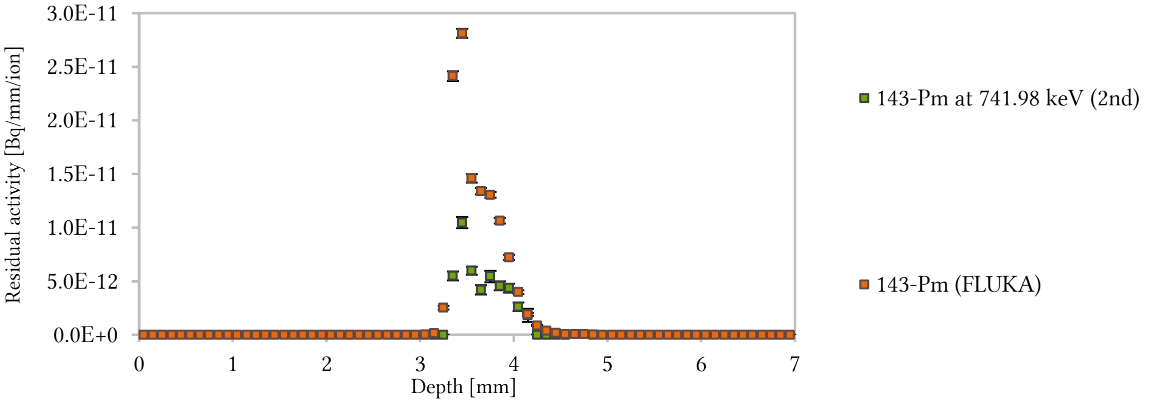

Figure 88: The depth profile of ^{143}Pm in the aluminium target irradiated by 200 MeV/u ^{238}U beam.

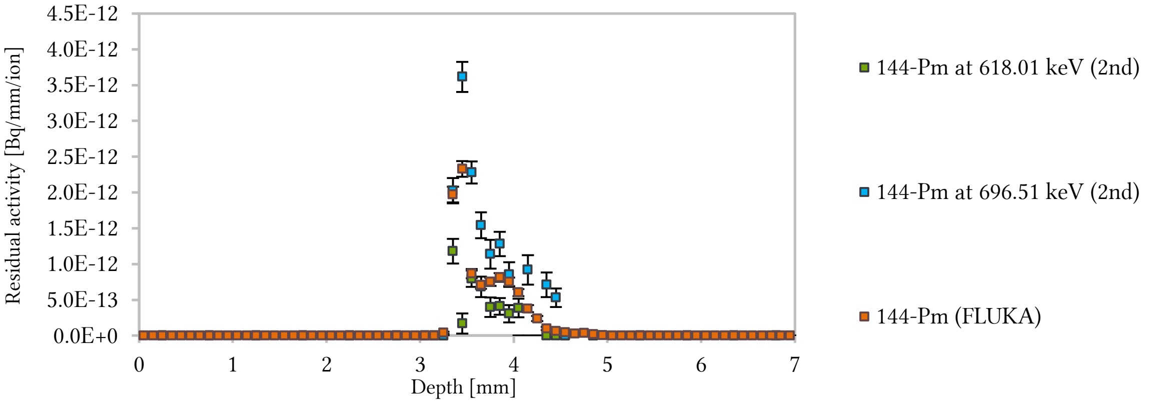

Figure 89: The depth profile of ^{144}Pm in the aluminium target irradiated by 200 MeV/u ^{238}U beam.

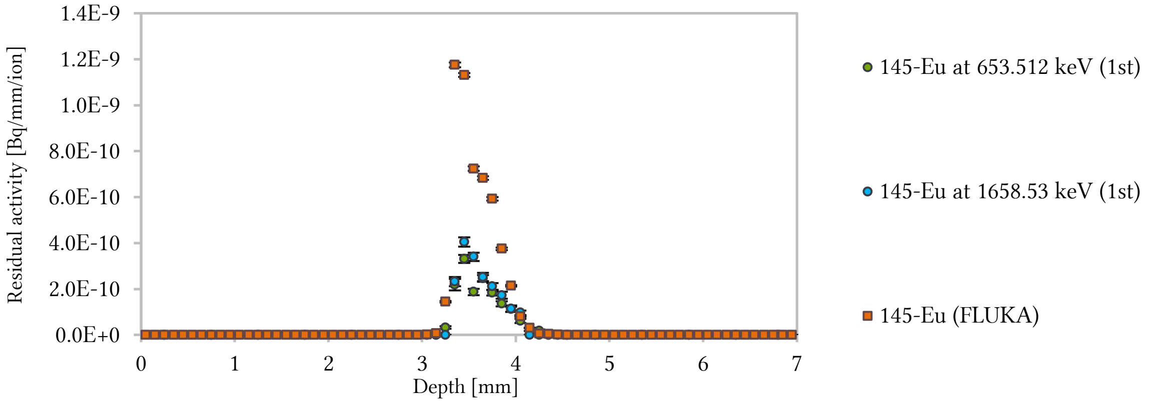

Figure 90: The depth profile of ^{145}Eu in the aluminium target irradiated by 200 MeV/u ^{238}U beam.

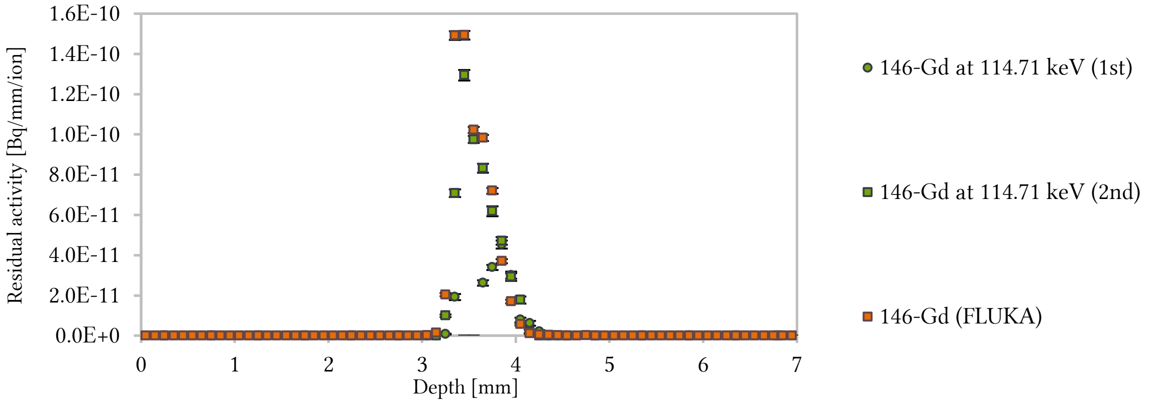

Figure 91: The depth profile of ^{146}Gd in the aluminium target irradiated by 200 MeV/u ^{238}U beam.

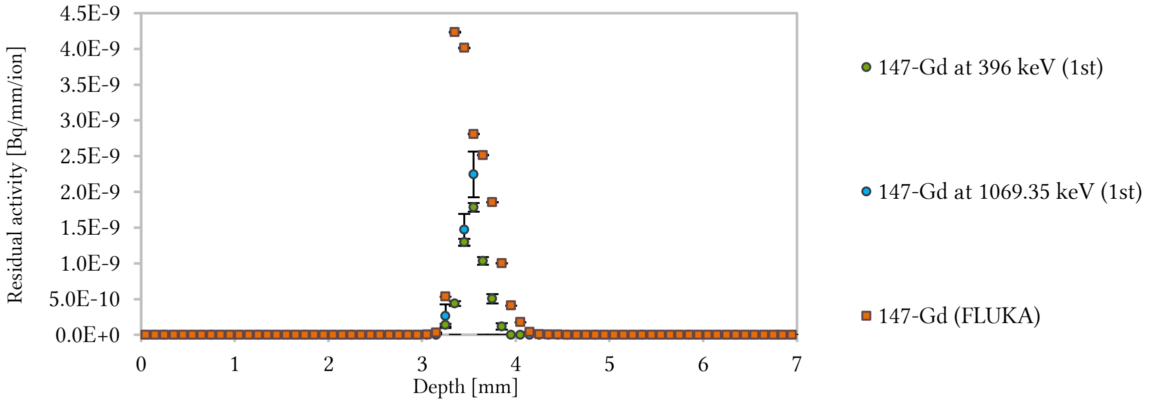

Figure 92: The depth profile of ^{147}Gd in the aluminium target irradiated by 200 MeV/u ^{238}U beam.

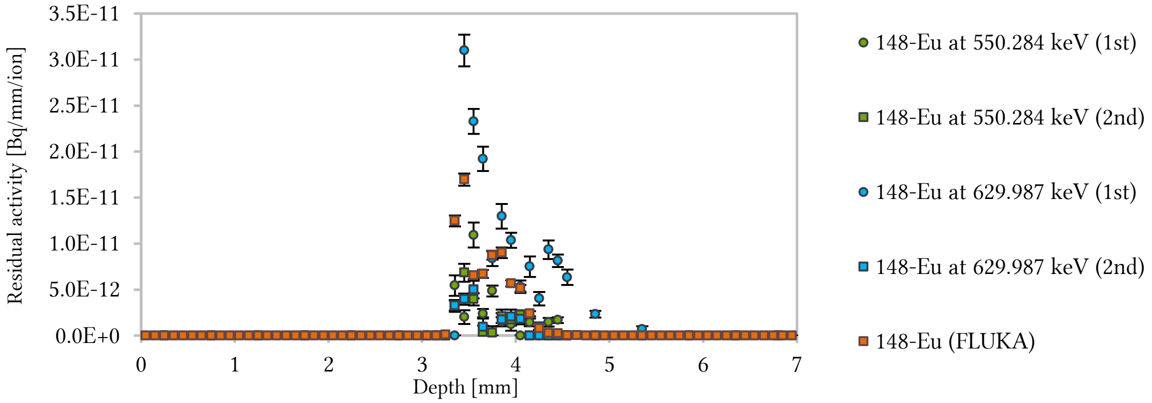

Figure 93: The depth profile of ^{148}Eu in the aluminium target irradiated by 200 MeV/u ^{238}U beam.

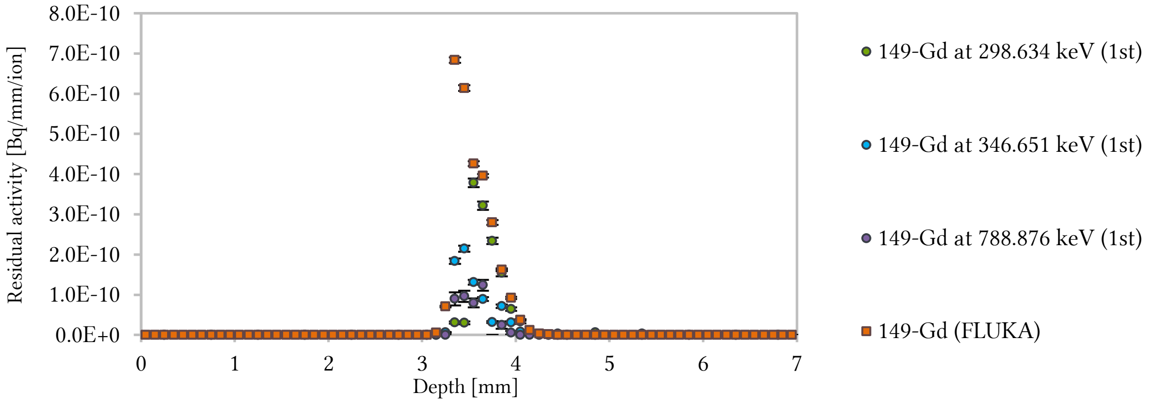

Figure 94: The depth profile of ^{149}Gd in the aluminium target irradiated by 200 MeV/u ^{238}U beam.

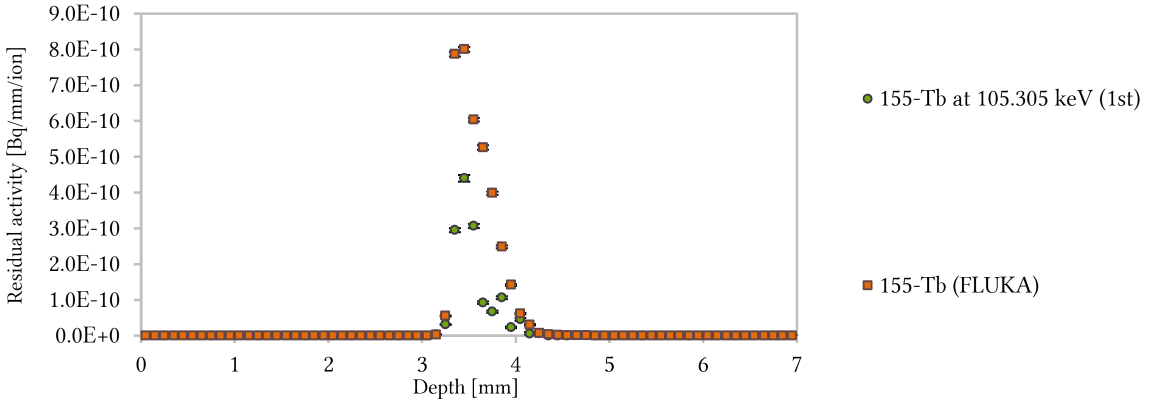

Figure 95: The depth profile of ^{155}Tb in the aluminium target irradiated by 200 MeV/u ^{238}U beam.

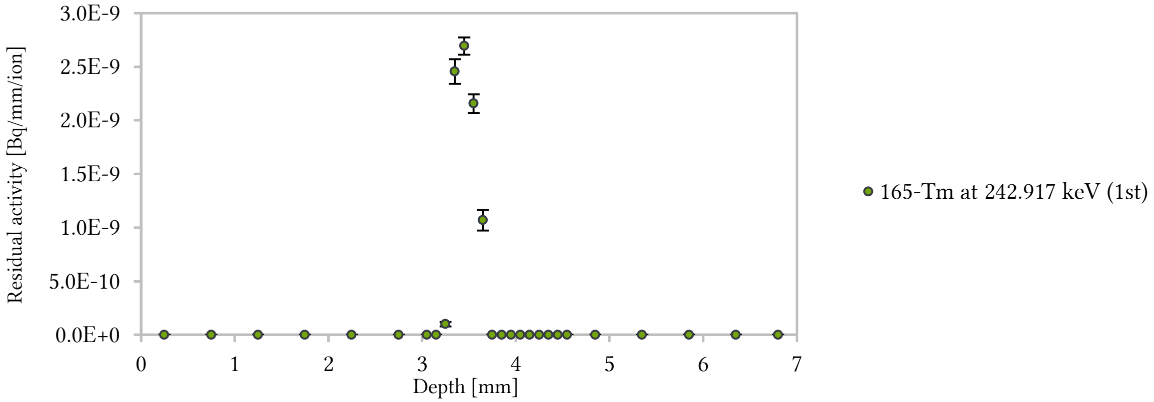

Figure 96: The depth profile of ^{165}Tm in the aluminium target irradiated by 200 MeV/u ^{238}U beam.

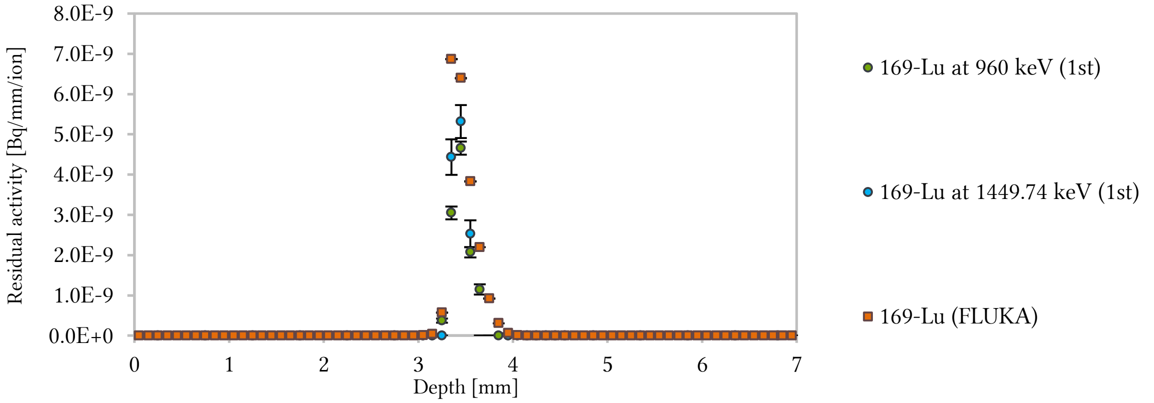

Figure 97: The depth profile of ^{169}Lu in the aluminium target irradiated by 200 MeV/u ^{238}U beam.

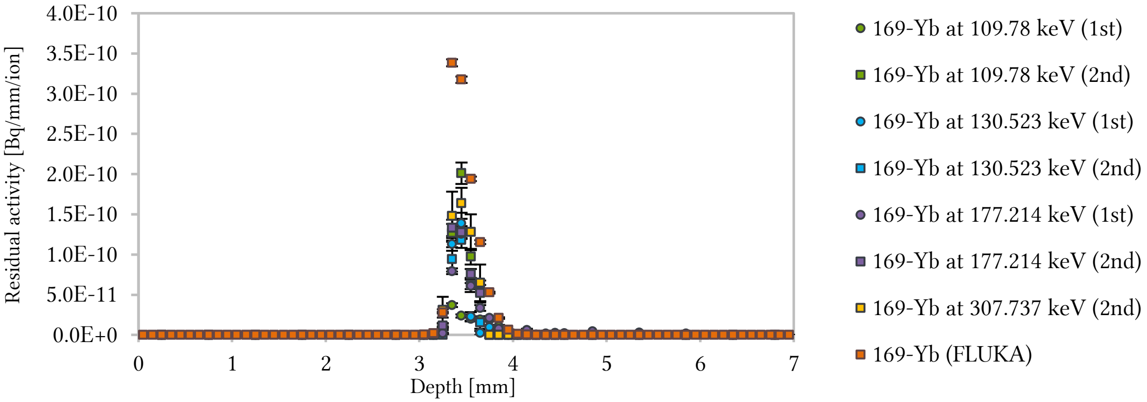

Figure 98: The depth profile of ^{169}Yb in the aluminium target irradiated by 200 MeV/u ^{238}U beam.

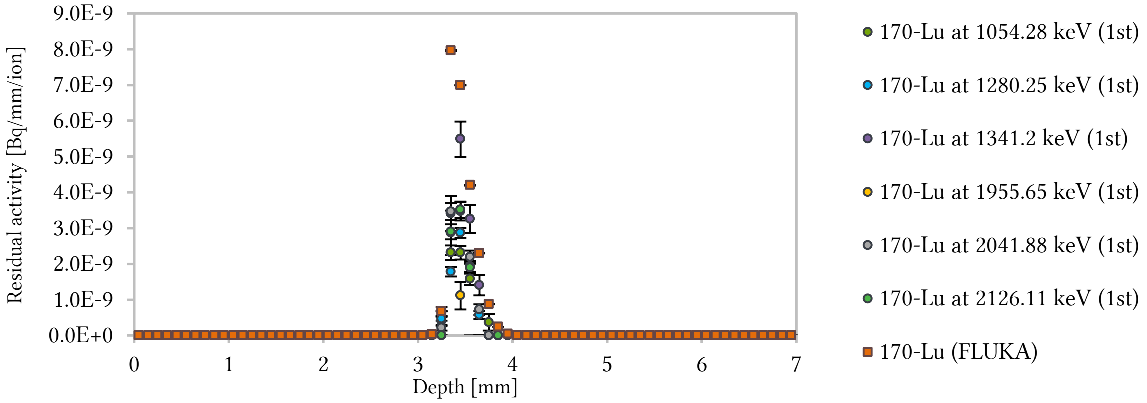

Figure 99: The depth profile of ^{170}Lu in the aluminium target irradiated by 200 MeV/u ^{238}U beam.

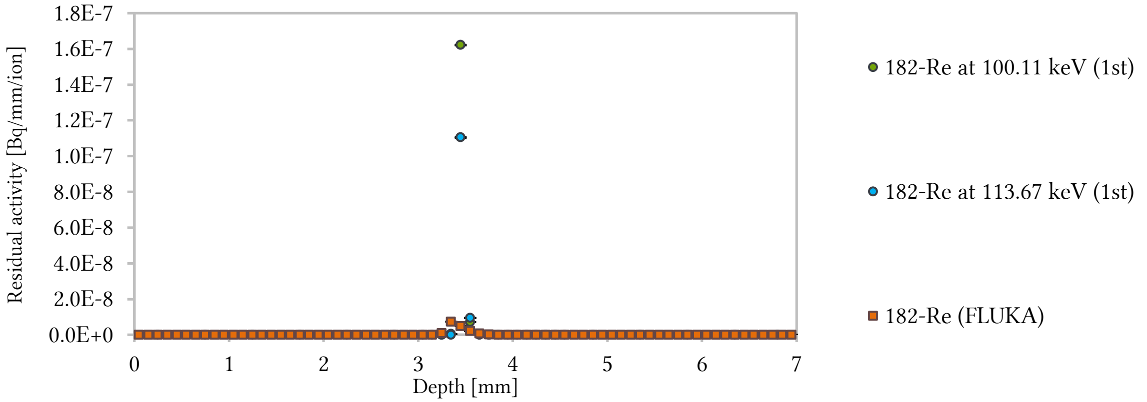

Figure 100: The depth profile of ^{182}Re in the aluminium target irradiated by 200 MeV/u ^{238}U beam.

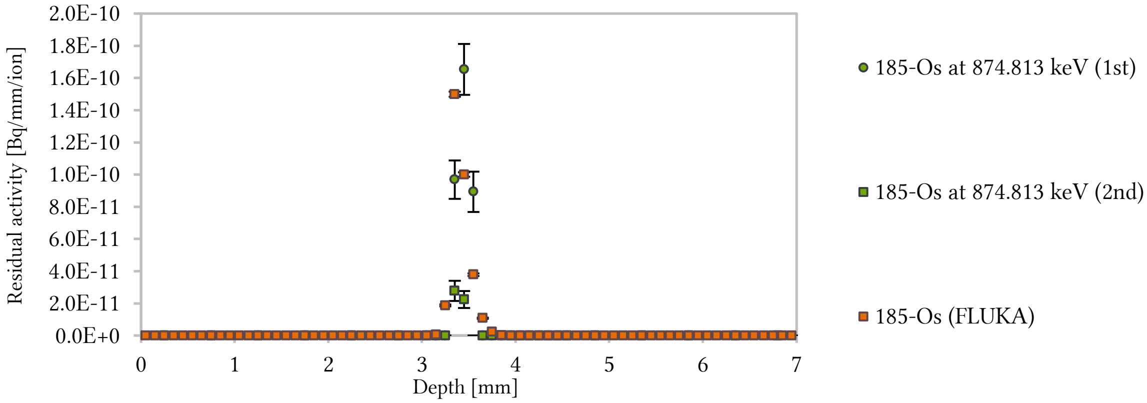

Figure 101: The depth profile of ^{185}Os in the aluminium target irradiated by 200 MeV/u ^{238}U beam.

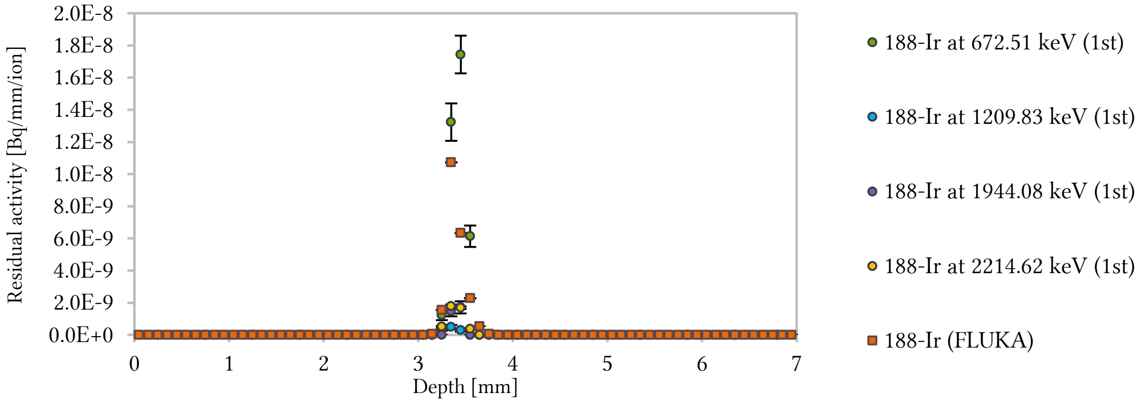

Figure 102: The depth profile of ^{188}Ir in the aluminium target irradiated by 200 MeV/u ^{238}U beam.

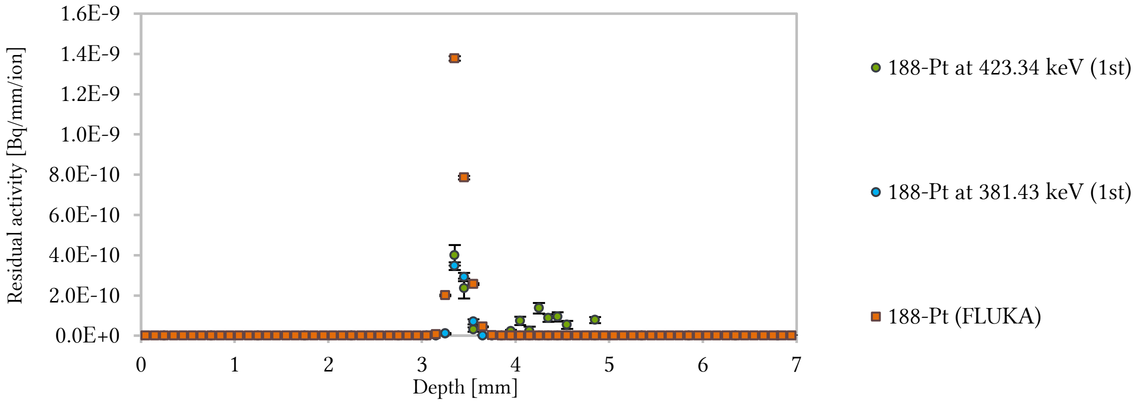

Figure 103: The depth profile of ^{188}Pt in the aluminium target irradiated by 200 MeV/u ^{238}U beam.

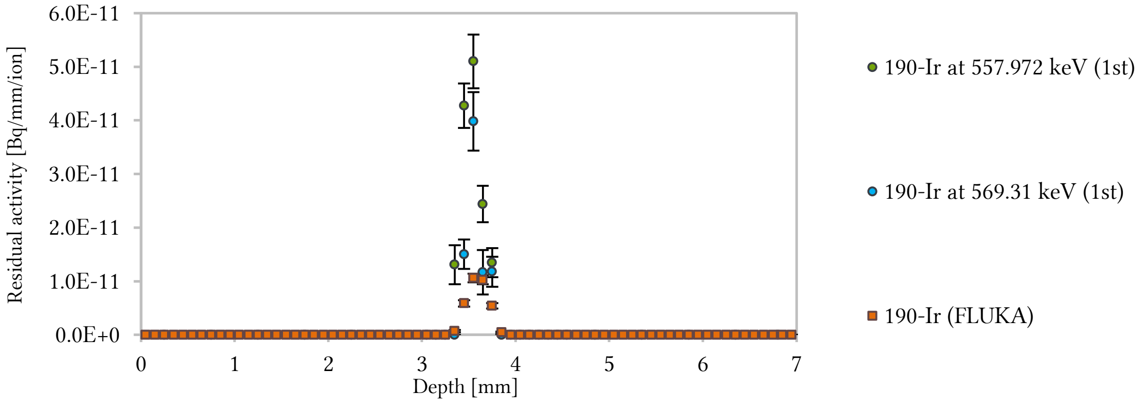

Figure 104: The depth profile of ^{190}Ir in the aluminium target irradiated by 200 MeV/u ^{238}U beam.

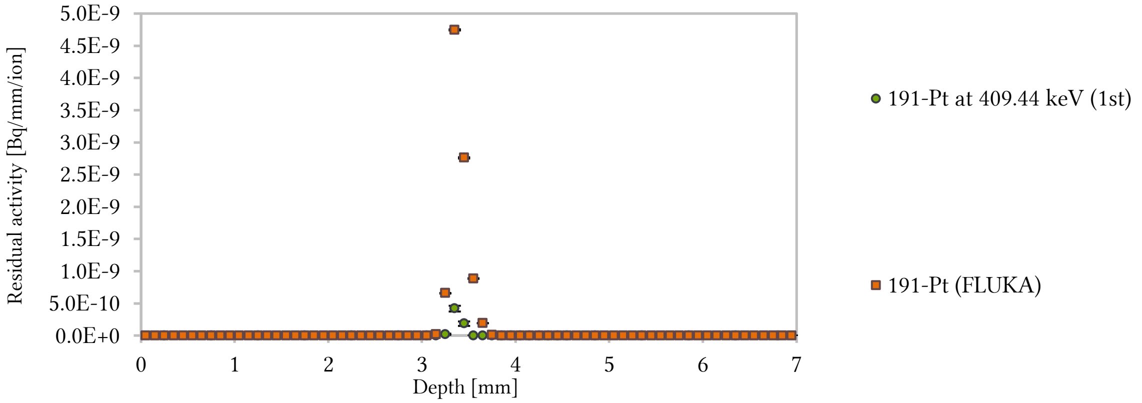

Figure 105: The depth profile of ^{191}Pt in the aluminium target irradiated by 200 MeV/u ^{238}U beam.

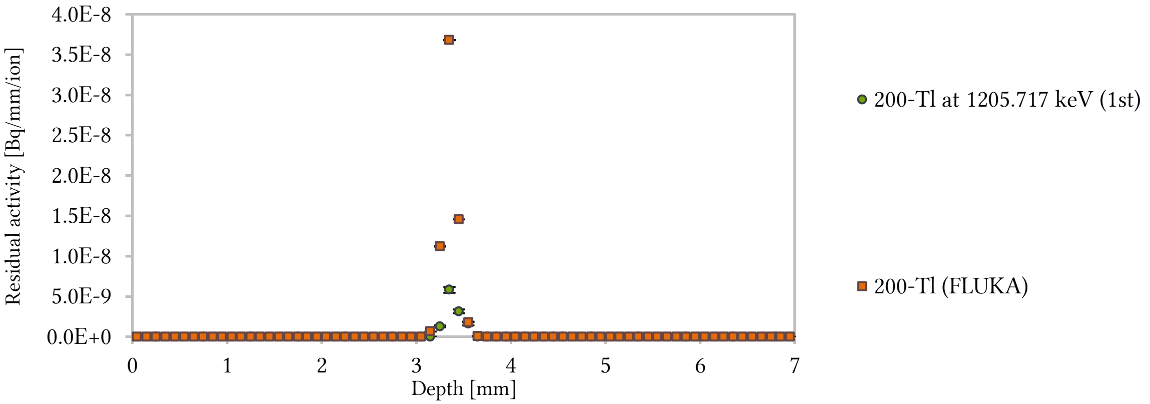

Figure 106: The depth profile of ^{200}Tl in the aluminium target irradiated by 200 MeV/u ^{238}U beam.

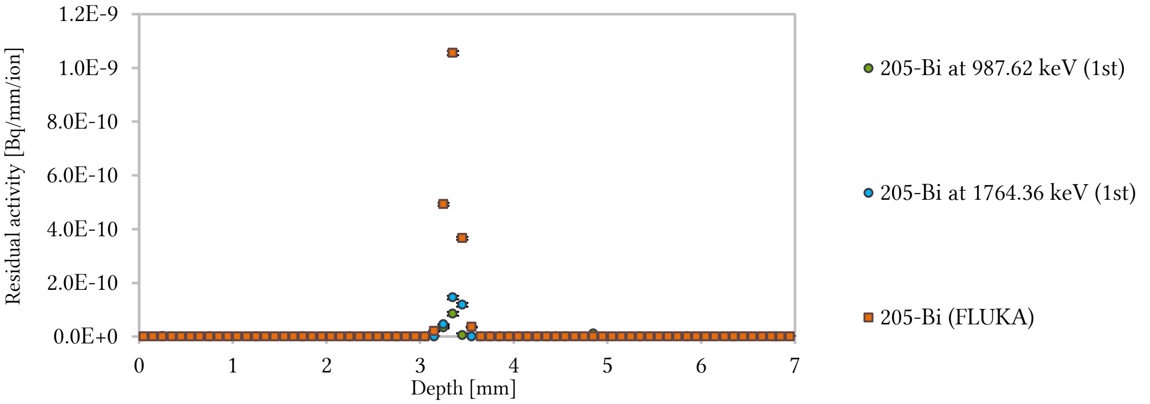

Figure 107: The depth profile of ^{205}Bi in the aluminium target irradiated by 200 MeV/u ^{238}U beam.

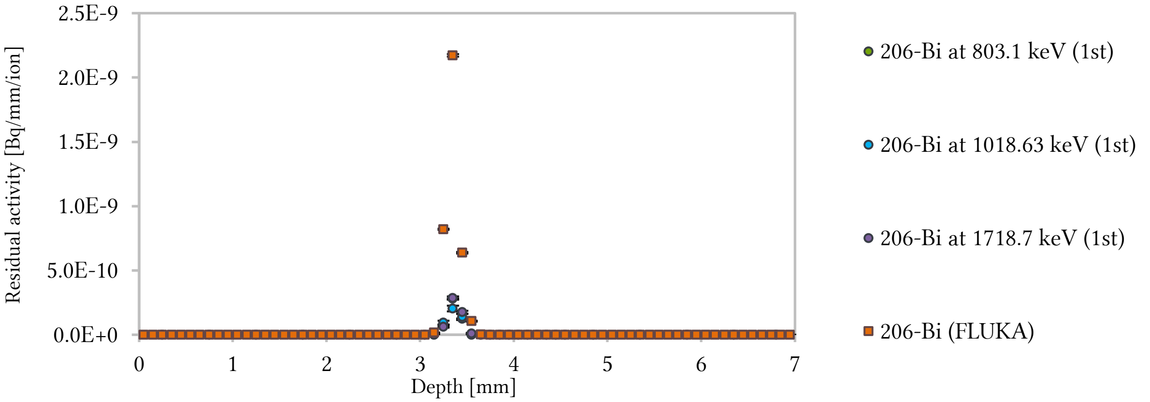

Figure 108: The depth profile of ^{206}Bi in the aluminium target irradiated by 200 MeV/u ^{238}U beam.

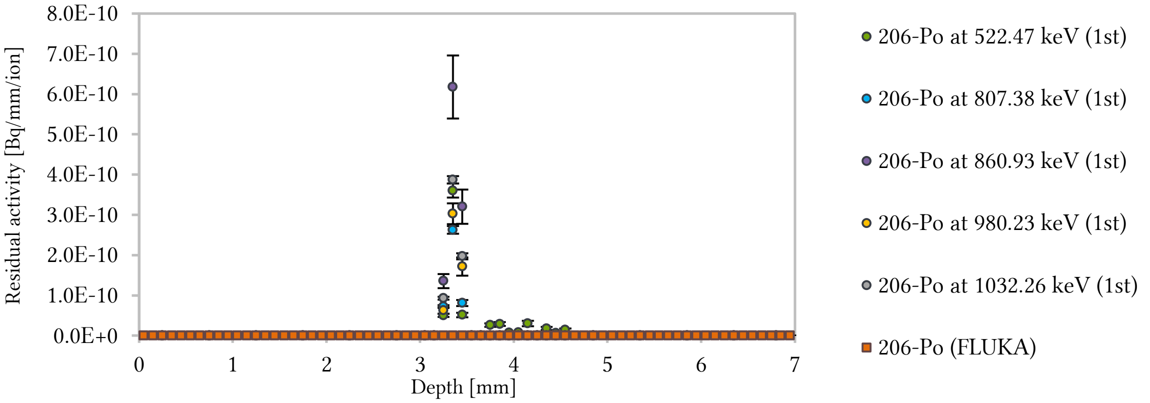

Figure 109: The depth profile of ^{206}Po in the aluminium target irradiated by 200 MeV/u ^{238}U beam.

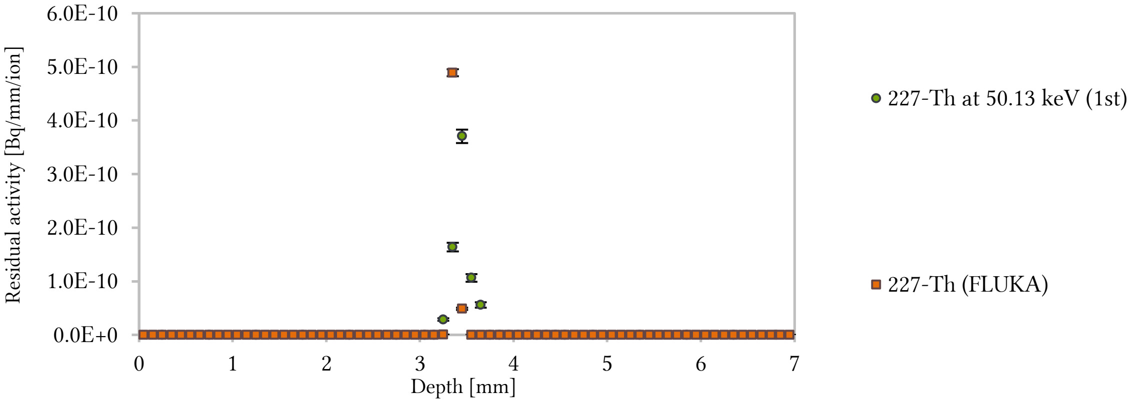

Figure 110: The depth profile of ^{227}Th in the aluminium target irradiated by 200 MeV/u ^{238}U beam.

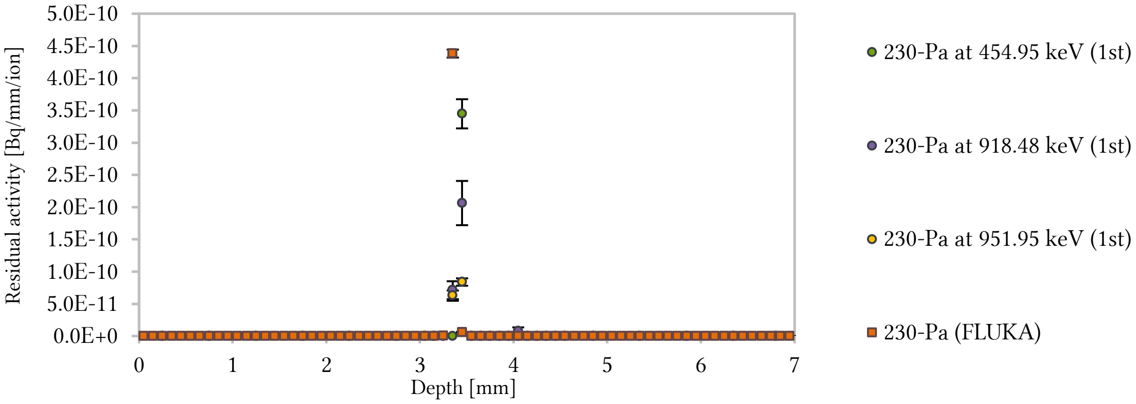

Figure 111: The depth profile of ^{203}Pa in the aluminium target irradiated by 200 MeV/u ^{238}U beam

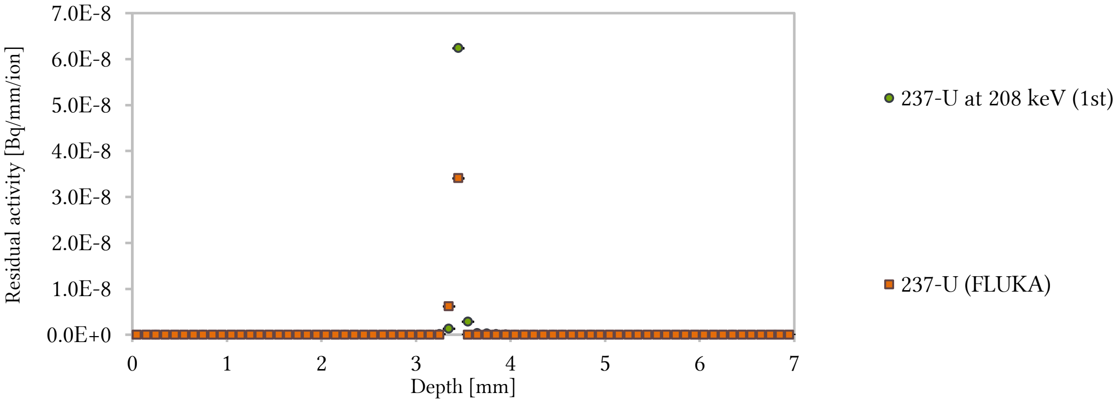

Figure 112: The depth profile of ^{237}U in the aluminium target irradiated by 200 MeV/u ^{238}U beam.

APPENDIX 2 – ALUMINIUM ACTIVATED BY ^{238}U AT 125 MeV/u

The depth profiles of the residual activity induced in aluminium target irradiated by uranium beam with an energy of 125 MeV/u are collected in this section (Figure 113 - Figure 120). Experimental data from the first set of measurement (16 – 34 days after the end of the irradiation) are labelled as "(1st)" in the legends and they are marked with "circle" shape in the graphical interpretation. Data obtained from the second set of measurement (128 – 144 days after the end of the irradiation) are labelled as "(2nd)" with "square" shape of markers and the third set of measurement (260 – 285 days after the end of the irradiation) are labelled as "(3rd)" of the "triangle" shape of the markers. Results of the FLUKA simulations are labelled as "(FLUKA)" in the legends of the graphs and they are graphically represented as the "square" shaped markers of orange colour.

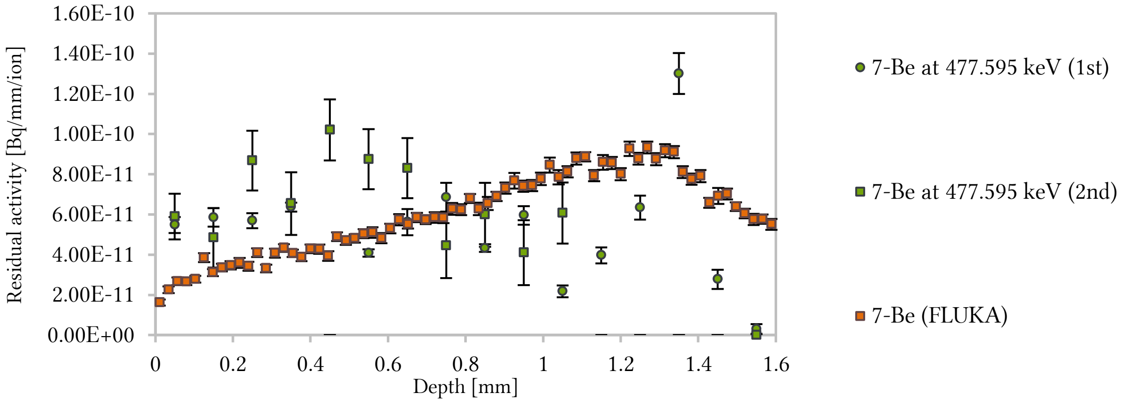

Figure 113: The depth profile of ^{7}Be in the aluminium target irradiated by 125 MeV/u ^{238}U beam.

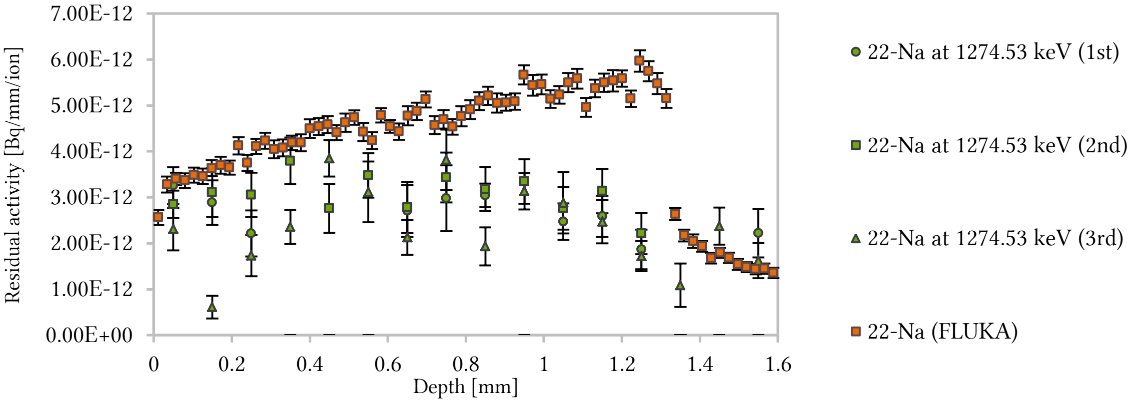

Figure 114: The depth profile of ^{22}Na in the aluminium target irradiated by 125 MeV/u ^{238}U beam.

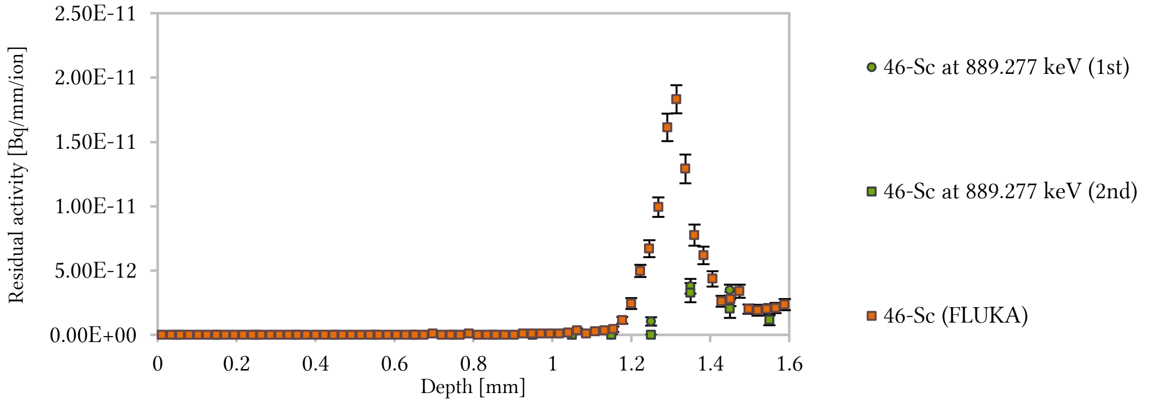

Figure 115: The depth profile of ^{46}Sc in the aluminium target irradiated by 125 MeV/u ^{238}U beam.

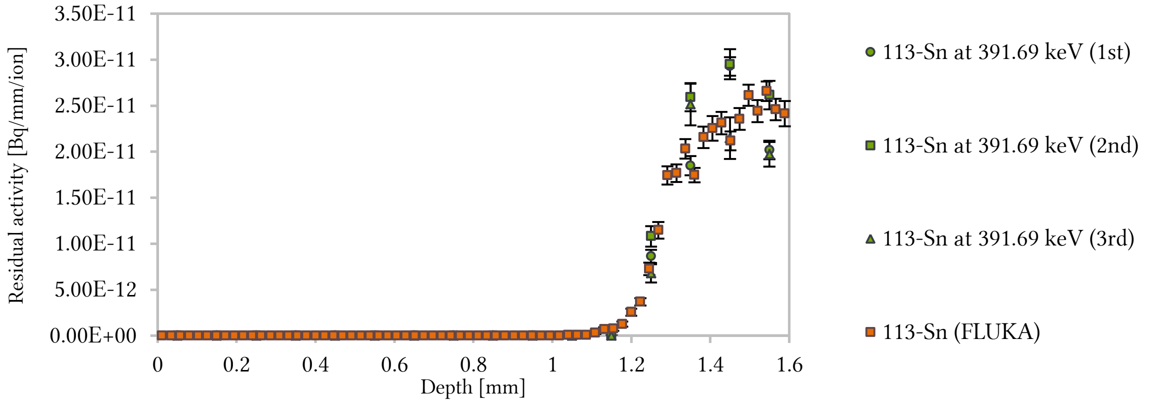

Figure 116: The depth profile of ^{113}Sn in the aluminium target irradiated by 125 MeV/u ^{238}U beam.

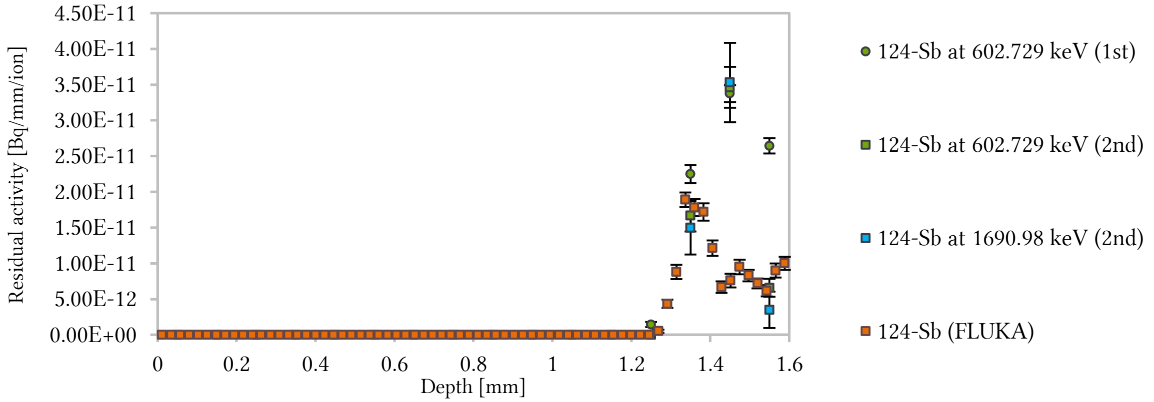

Figure 117: The depth profile of ^{124}Sb in the aluminium target irradiated by 125 MeV/u ^{238}U beam.

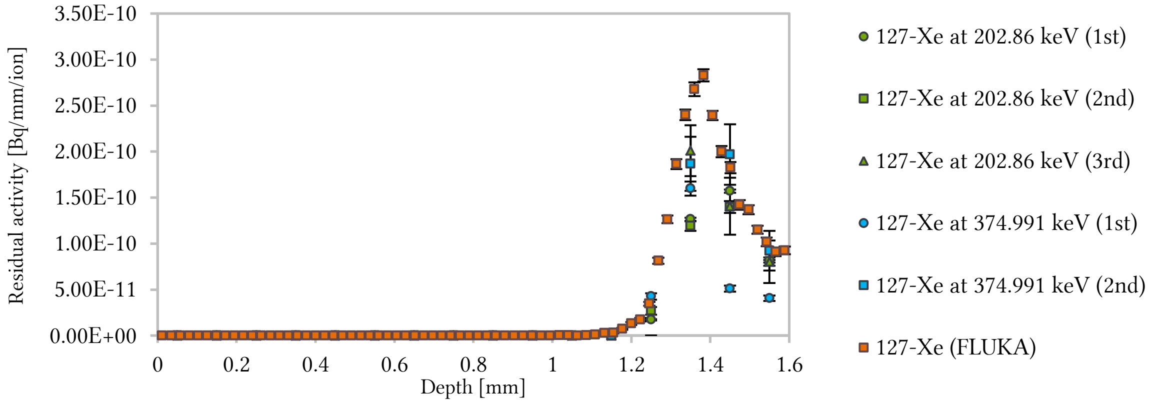

Figure 118: The depth profile of ^{127}Xe in the aluminium target irradiated by 125 MeV/u ^{238}U beam.

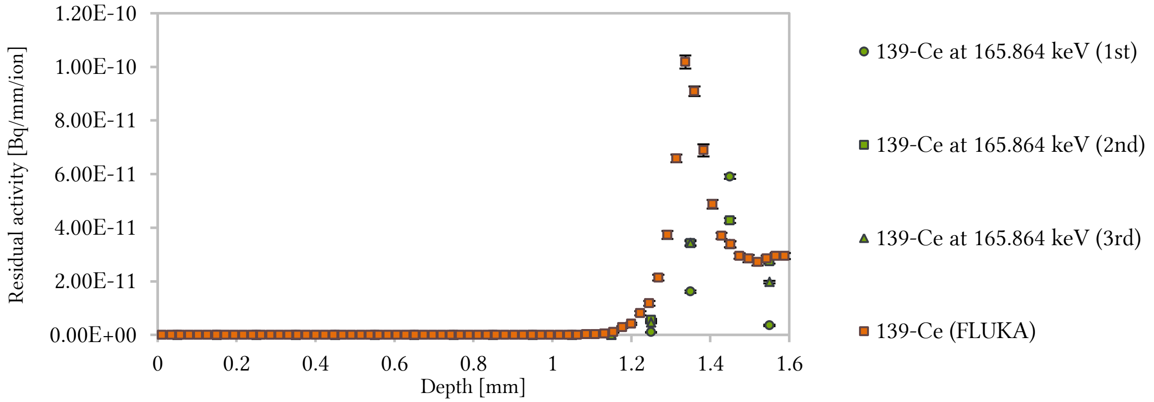

Figure 119: The depth profile of ^{139}Ce in the aluminium target irradiated by 125 MeV/u ^{238}U beam.

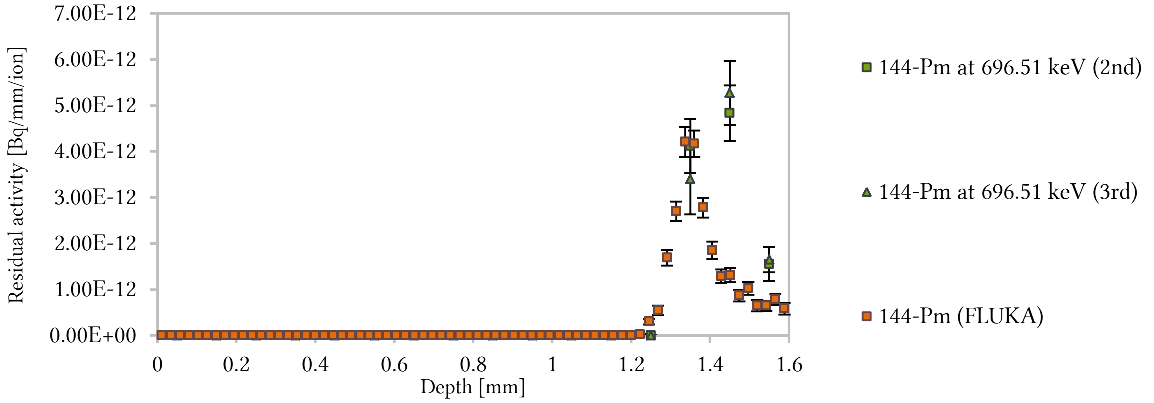

Figure 120: The depth profile of ^{144}Pm in the aluminium target irradiated by 125 MeV/u ^{238}U beam.

APPENDIX 3 – ALUMINIUM ACTIVATED BY ^{124}Xe AT 300 MeV/u

The depth profiles of the residual activity induced in aluminium target irradiated by xenon beam with an energy of 300 MeV/u are collected in this section (Figure 121 - Figure 159). Experimental data from the first set of measurement (9 – 38 days after the end of the irradiation) are labelled as "(1st)" in the legends and they are marked with "circle" shape in the graphical interpretation. Data obtained from the second set of measurement (218 – 293 days after the end of the irradiation) are labelled as "(2nd)" with "square" shape of markers and the third set of measurement (378 – 505 days after the end of the irradiation) are labelled as "(3rd)" of the "triangle" shape of the markers. Results of the FLUKA simulations are labelled as "(FLUKA)" in the legends of the graphs and they are graphically represented as the "square" shaped markers of orange colour.

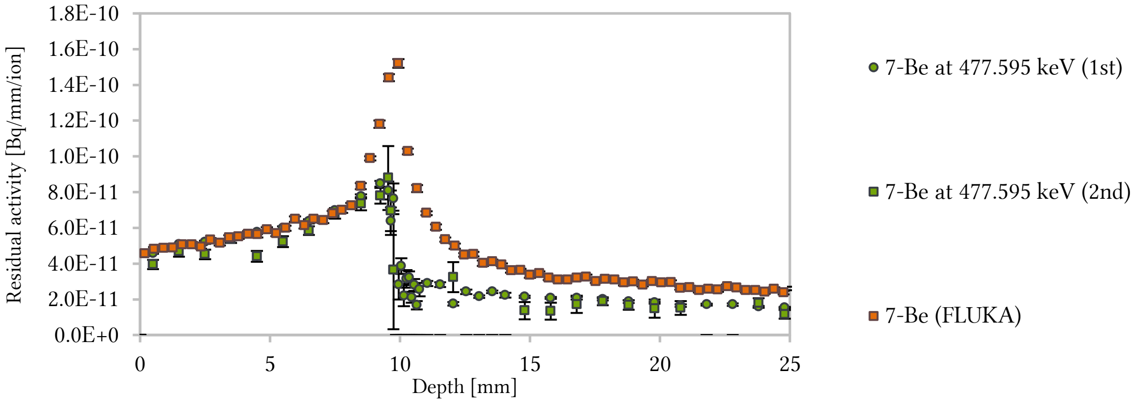

Figure 121: The depth profile of ^{7}Be in the aluminium target irradiated by 300 MeV/u ^{124}Xe beam.

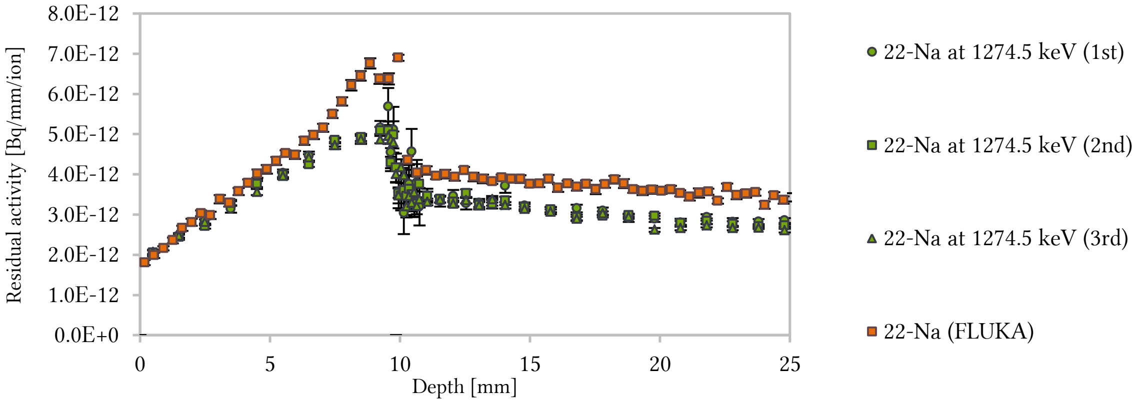

Figure 122: The depth profile of ^{22}Na in the aluminium target irradiated by 300 MeV/u ^{124}Xe beam.

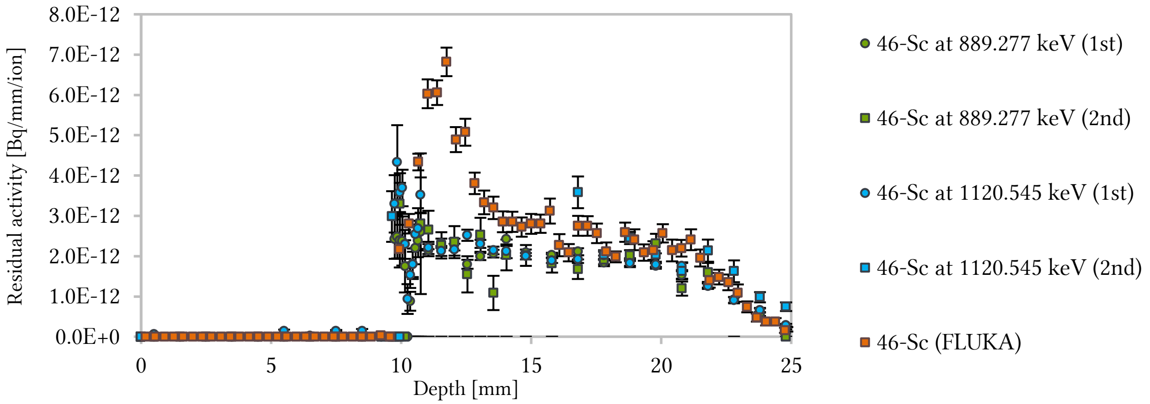

Figure 123: The depth profile of ^{46}Sc in the aluminium target irradiated by 300 MeV/u ^{124}Xe beam.

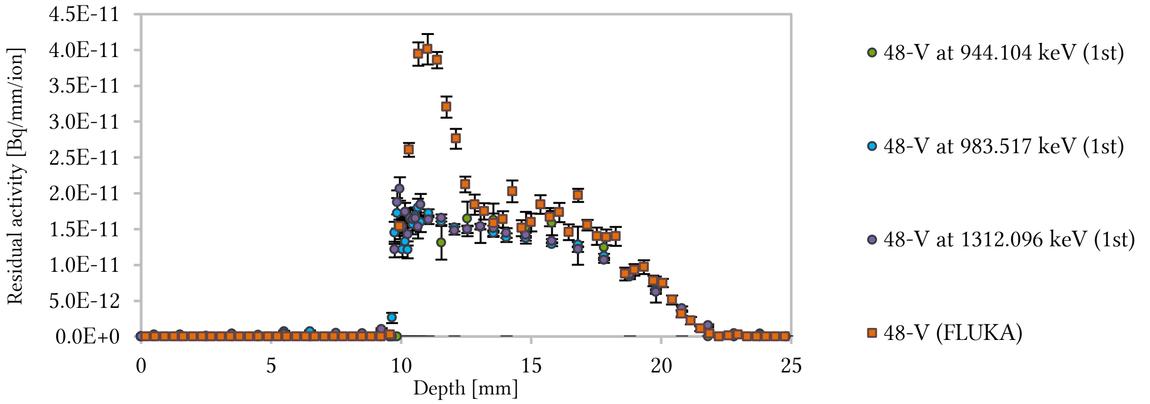

Figure 124: The depth profile of ^{48}V in the aluminium target irradiated by 300 MeV/u ^{124}Xe beam.

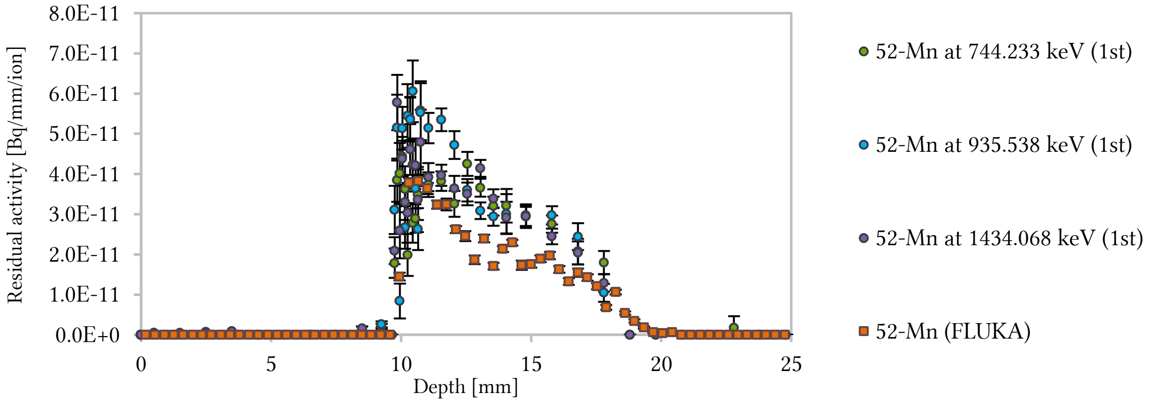

Figure 125: The depth profile of ^{52}Mn in the aluminium target irradiated by 300 MeV/u ^{124}Xe beam.

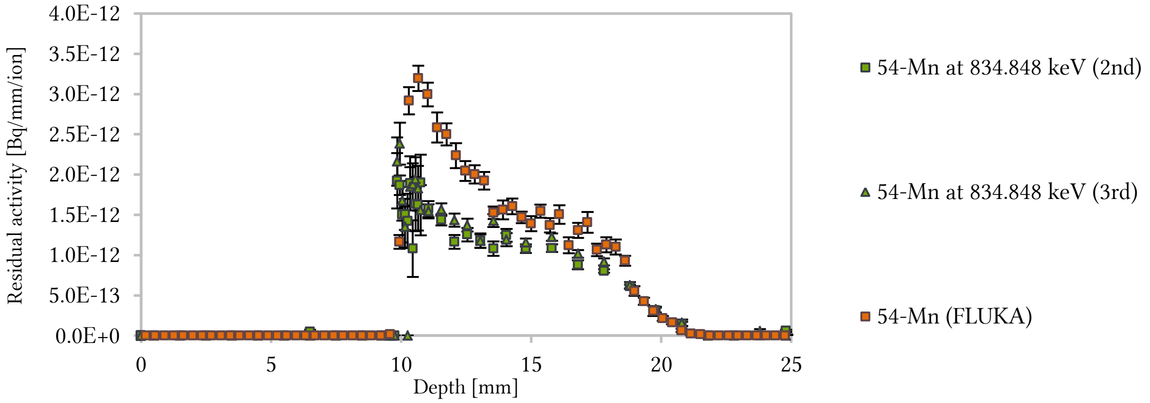

Figure 126: The depth profile of ^{54}Mn in the aluminium target irradiated by 300 MeV/u ^{124}Xe beam.

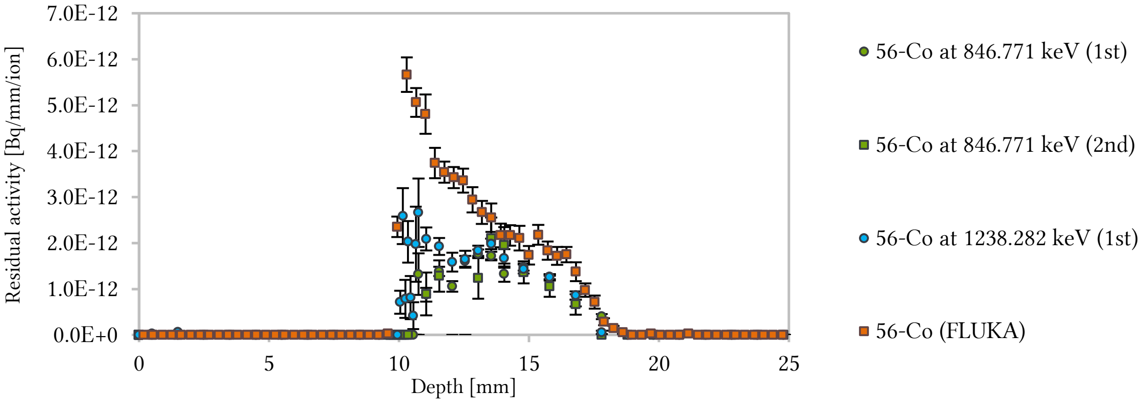

Figure 127: The depth profile of ^{56}Co in the aluminium target irradiated by 300 MeV/u ^{124}Xe beam.

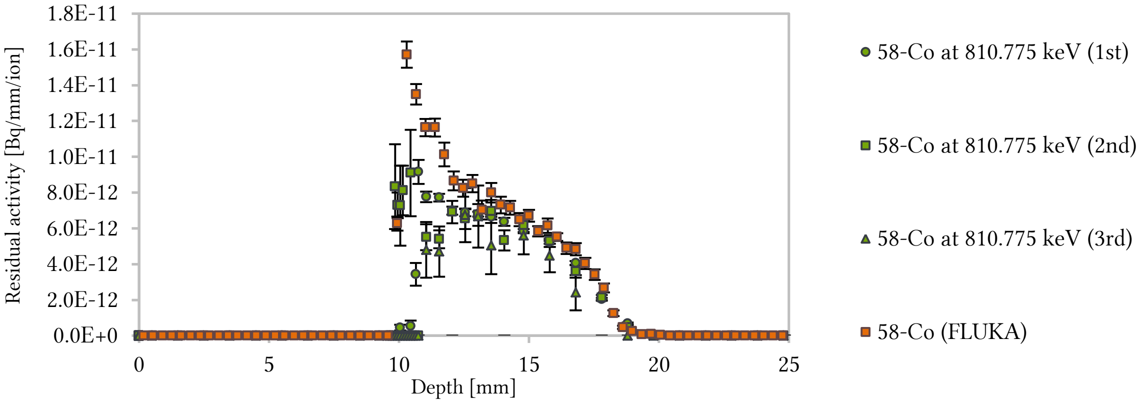

Figure 128: The depth profile of ^{58}Co in the aluminium target irradiated by 300 MeV/u ^{124}Xe beam.

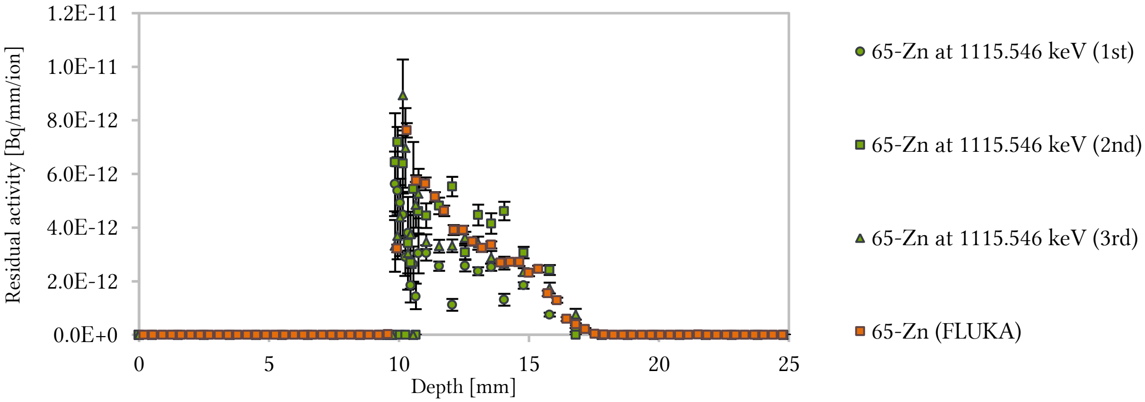

Figure 129: The depth profile of ^{65}Zn in the aluminium target irradiated by 300 MeV/u ^{124}Xe beam.

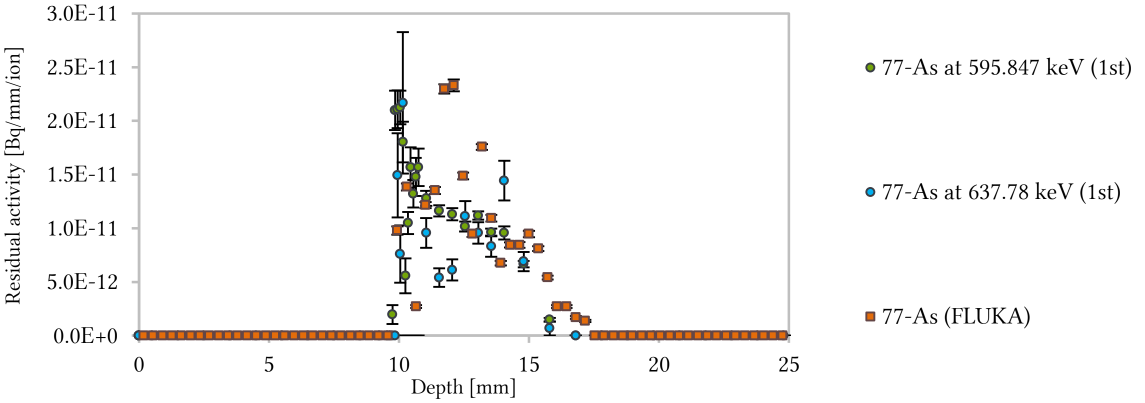

Figure 130: The depth profile of ^{77}As in the aluminium target irradiated by 300 MeV/u ^{124}Xe beam.

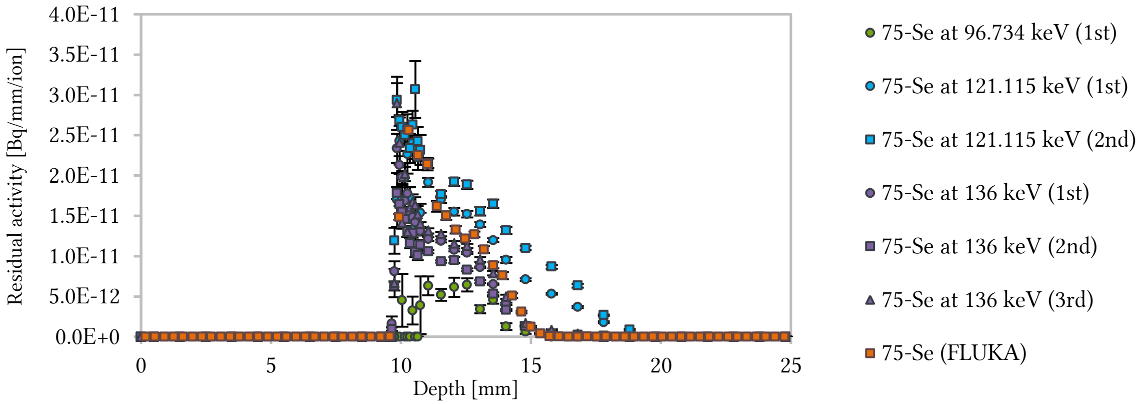

Figure 131: The depth profile of ^{75}Se in the aluminium target irradiated by 300 MeV/u ^{124}Xe beam (1/2).

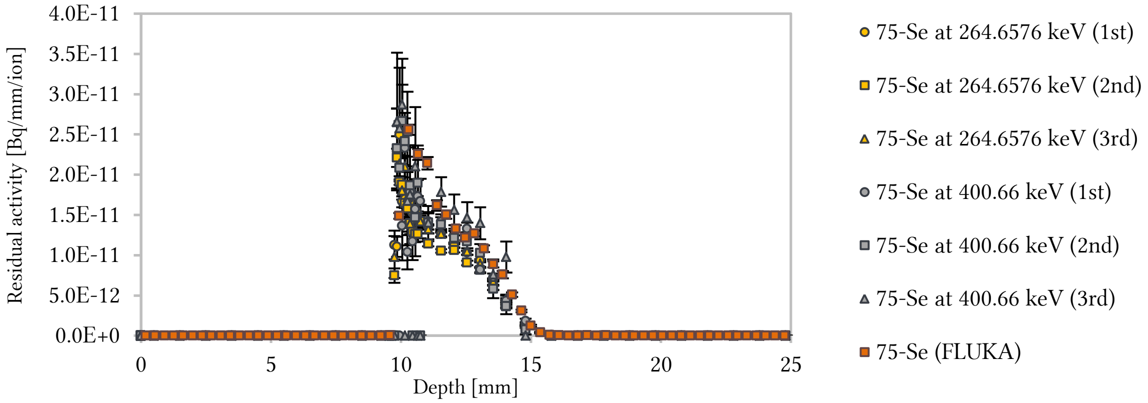

Figure 132: The depth profile of ^{75}Se in the aluminium target irradiated by 300 MeV/u ^{124}Xe beam (2/2).

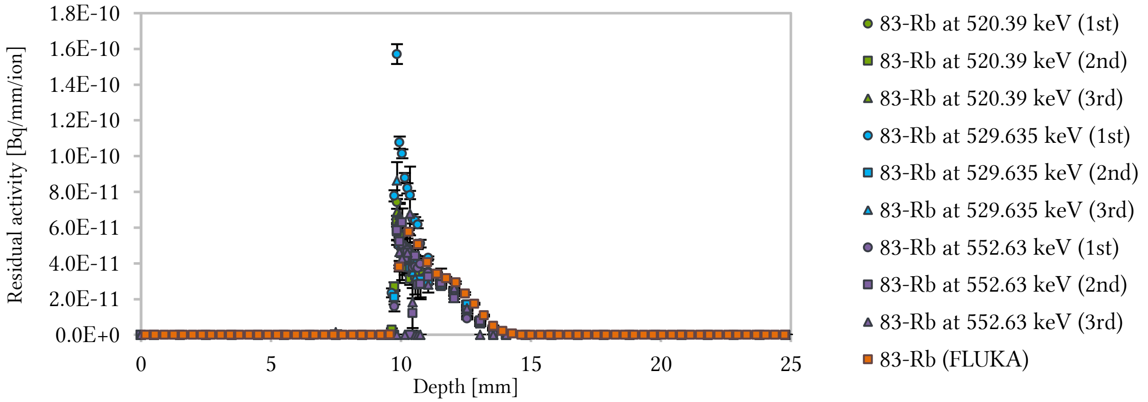

Figure 133: The depth profile of ^{83}Rb in the aluminium target irradiated by 300 MeV/u ^{124}Xe beam.

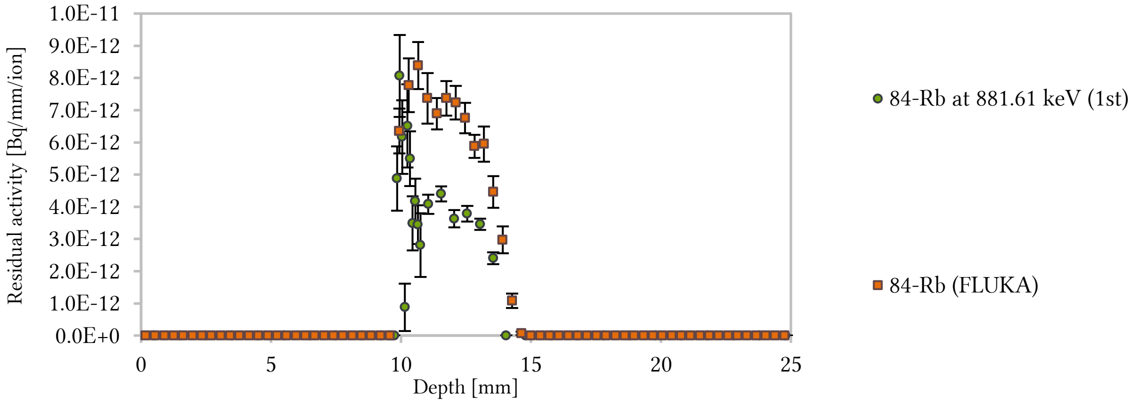

Figure 134: The depth profile of ^{84}Rb in the aluminium target irradiated by 300 MeV/u ^{124}Xe beam.

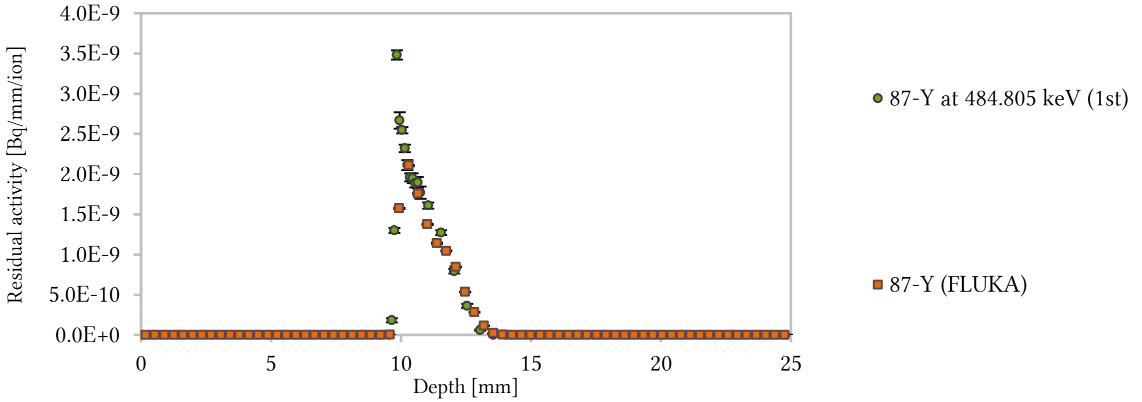

Figure 135: The depth profile of ^{87}Y in the aluminium target irradiated by 300 MeV/u ^{124}Xe beam.

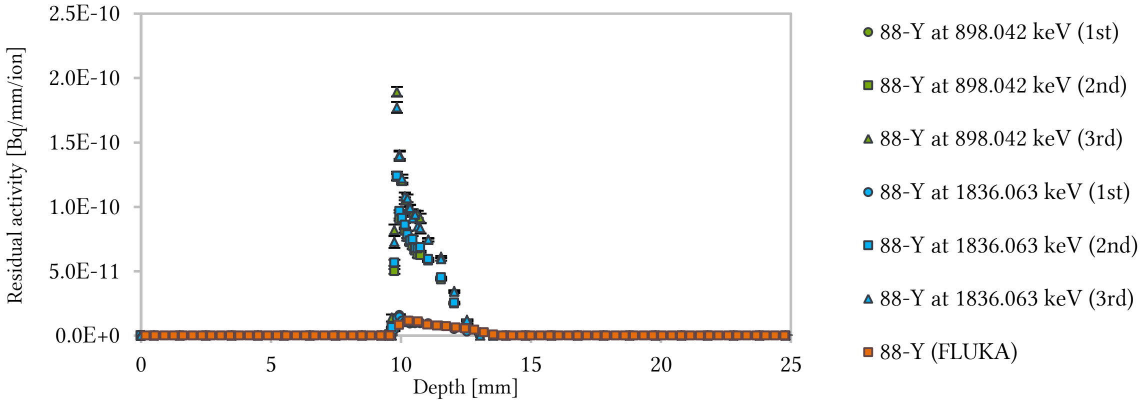

Figure 136: The depth profile of ^{88}Y in the aluminium target irradiated by 300 MeV/u ^{124}Xe beam.

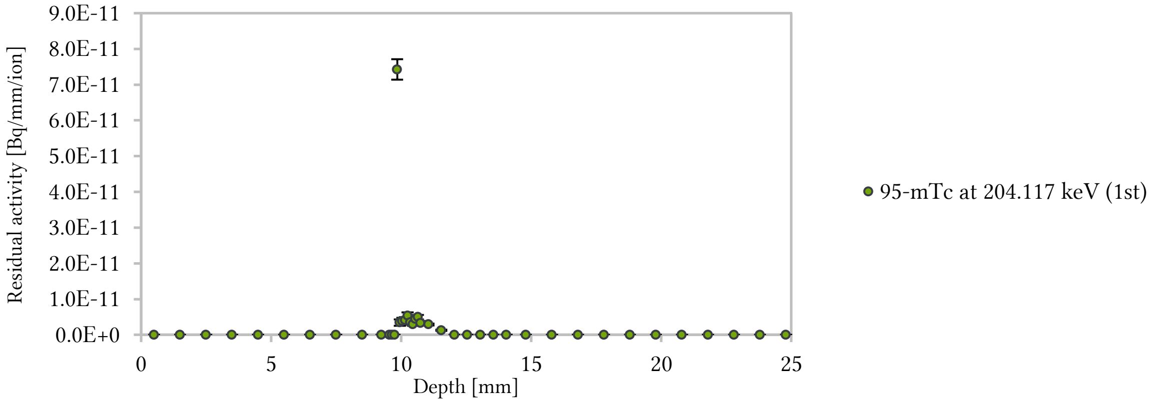

Figure 137: The depth profile of ^{95m}Tc in the aluminium target irradiated by 300 MeV/u ^{124}Xe beam.

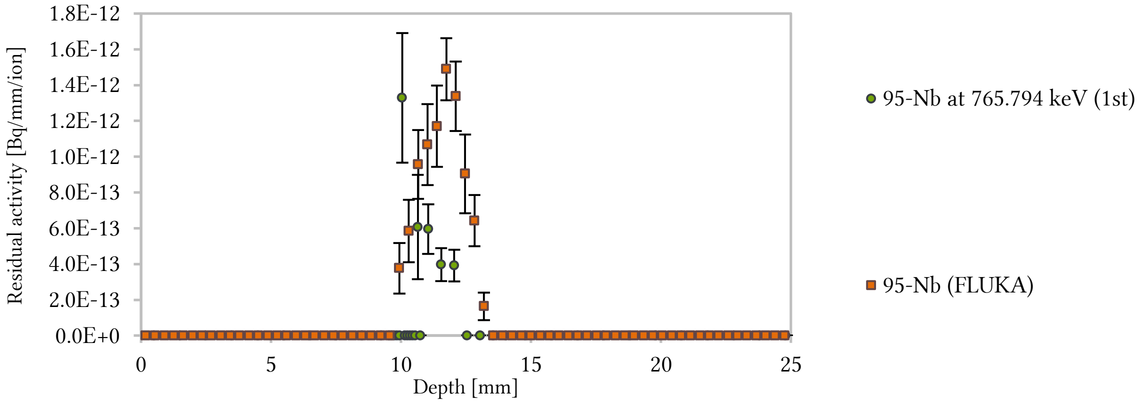

Figure 138: The depth profile of ^{95}Nb in the aluminium target irradiated by 300 MeV/u ^{124}Xe beam.

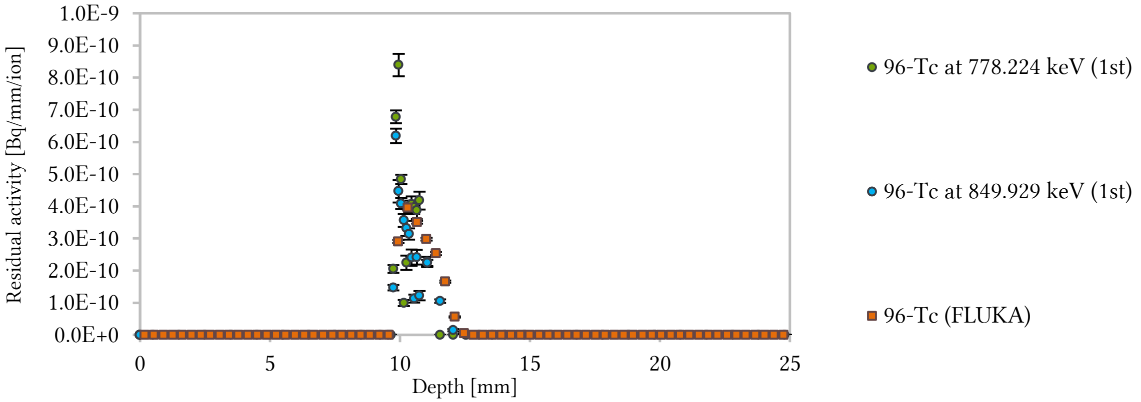

Figure 139: The depth profile of ^{96}Tc in the aluminium target irradiated by 300 MeV/u ^{124}Xe beam.

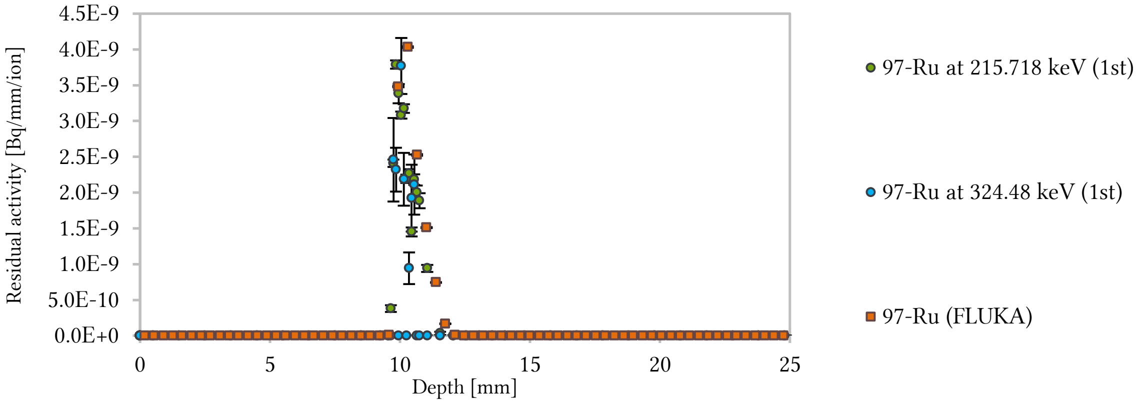

Figure 140: The depth profile of ^{97}Ru in the aluminium target irradiated by 300 MeV/u ^{124}Xe beam.

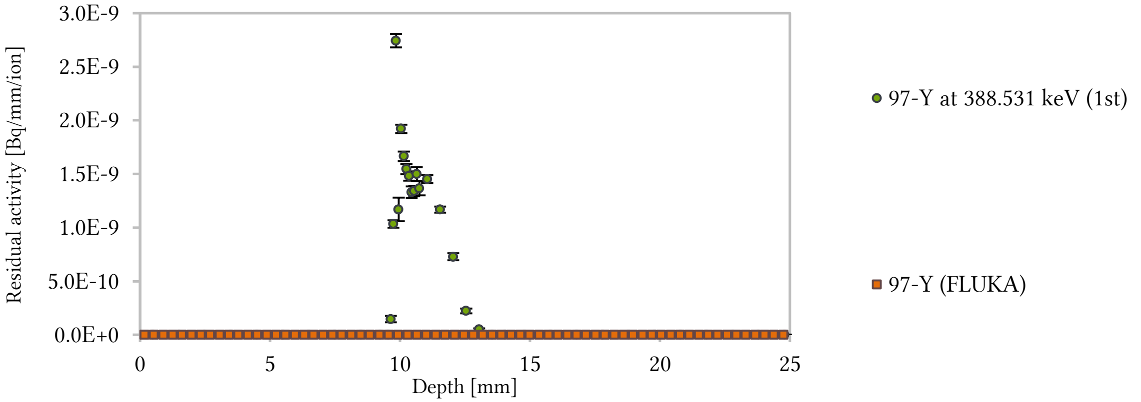

Figure 141: The depth profile of ^{97}Y in the aluminium target irradiated by 300 MeV/u ^{124}Xe beam.

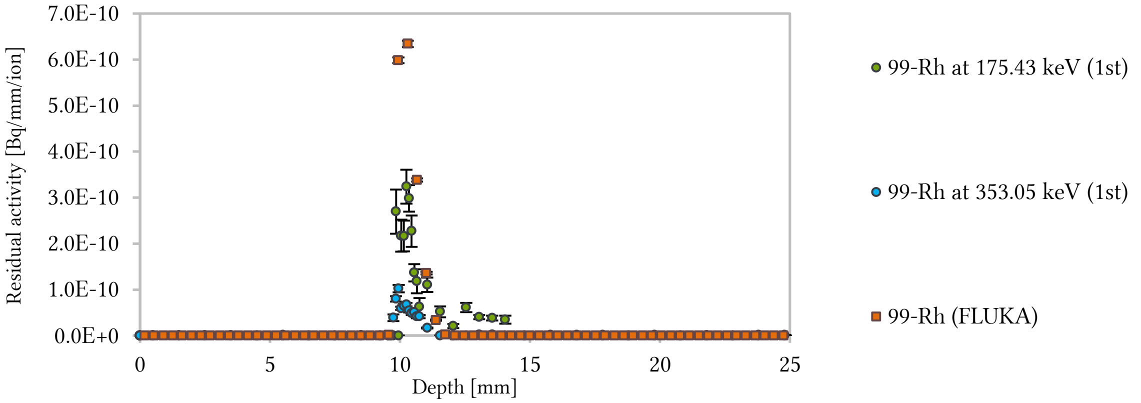

Figure 142: The depth profile of ^{99}Rh in the aluminium target irradiated by 300 MeV/u ^{124}Xe beam.

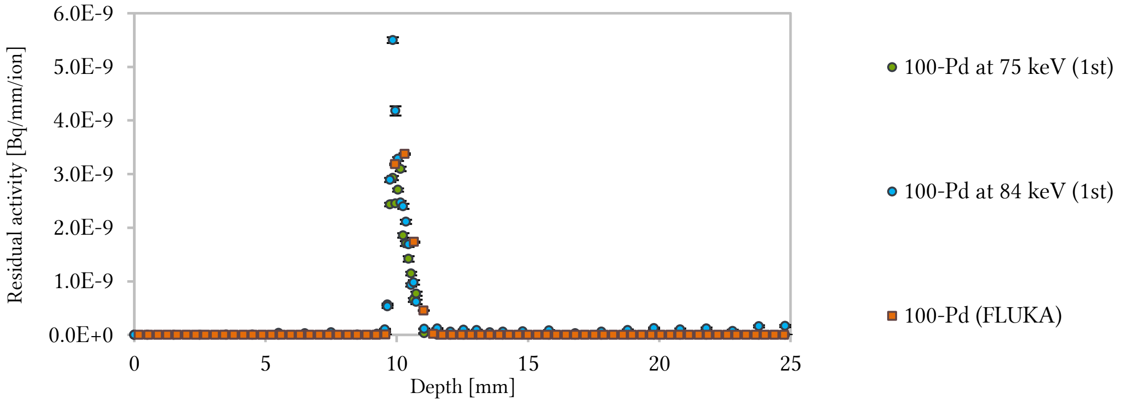

Figure 143: The depth profile of ^{100}Pd in the aluminium target irradiated by 300 MeV/u ^{124}Xe beam.

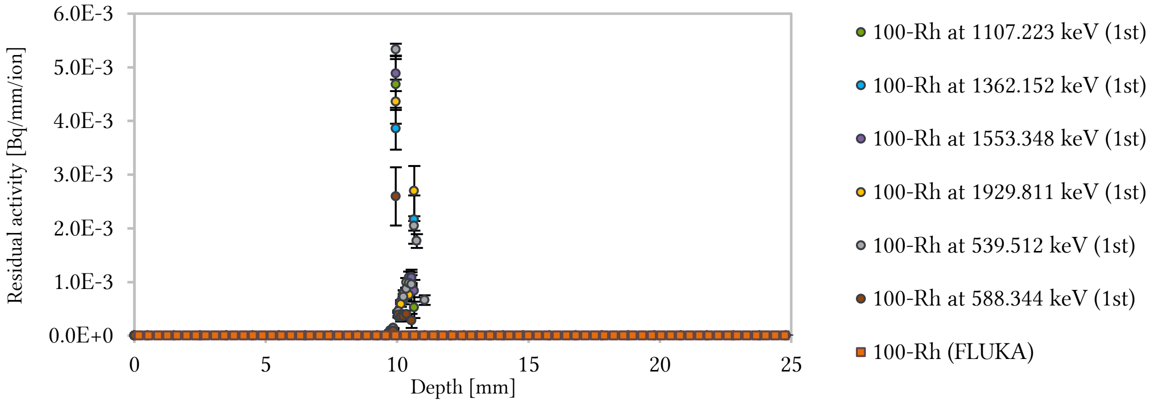

Figure 144: The depth profile of ^{100}Rh in the aluminium target irradiated by 300 MeV/u ^{124}Xe beam.

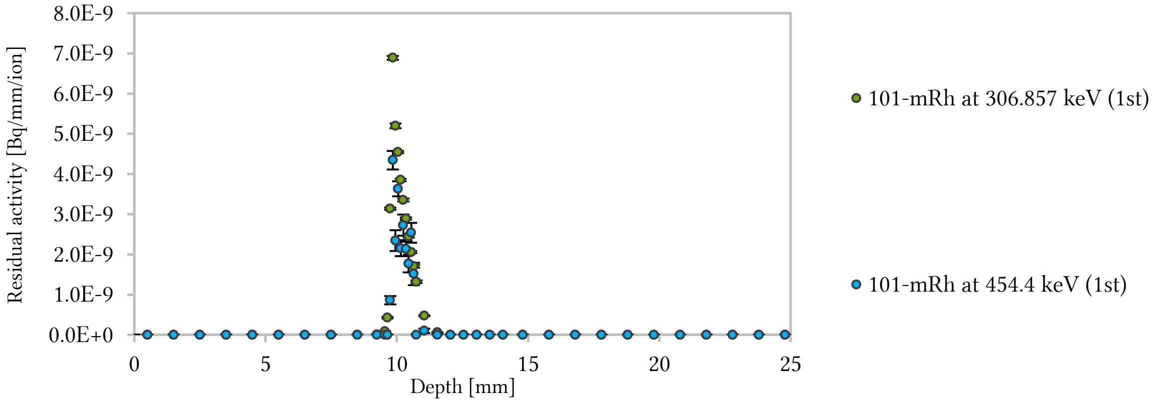

Figure 145: The depth profile of ^{101m}Rh in the aluminium target irradiated by 300 MeV/u ^{124}Xe beam.

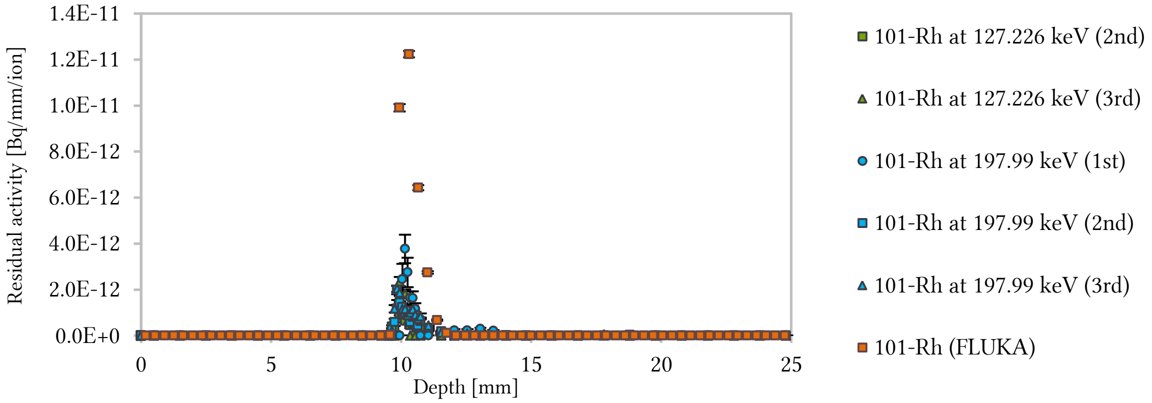

Figure 146: The depth profile of ^{101}Rh in the aluminium target irradiated by 300 MeV/u ^{124}Xe beam.

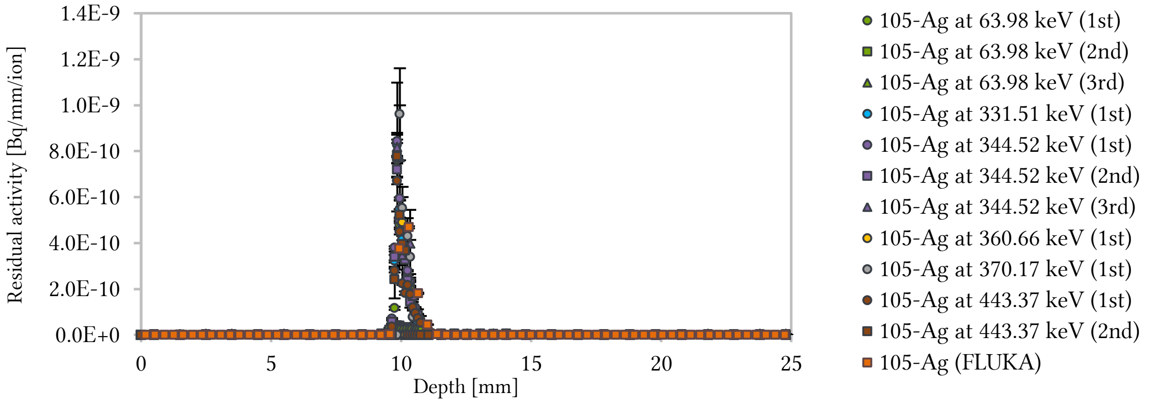

Figure 147: The depth profile of ^{105}Ag in the aluminium target irradiated by 300 MeV/u ^{124}Xe beam (1/2).

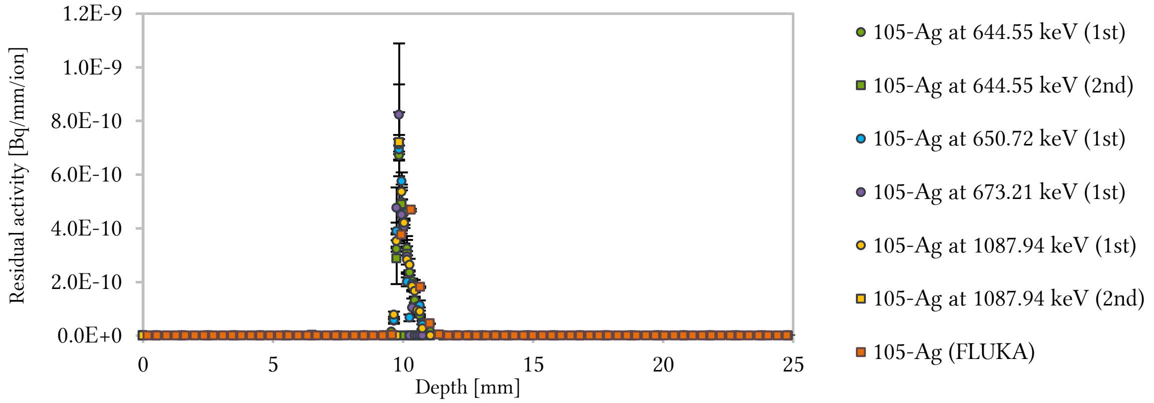

Figure 148: The depth profile of ^{105}Ag in the aluminium target irradiated by 300 MeV/u ^{124}Xe beam (2/2).

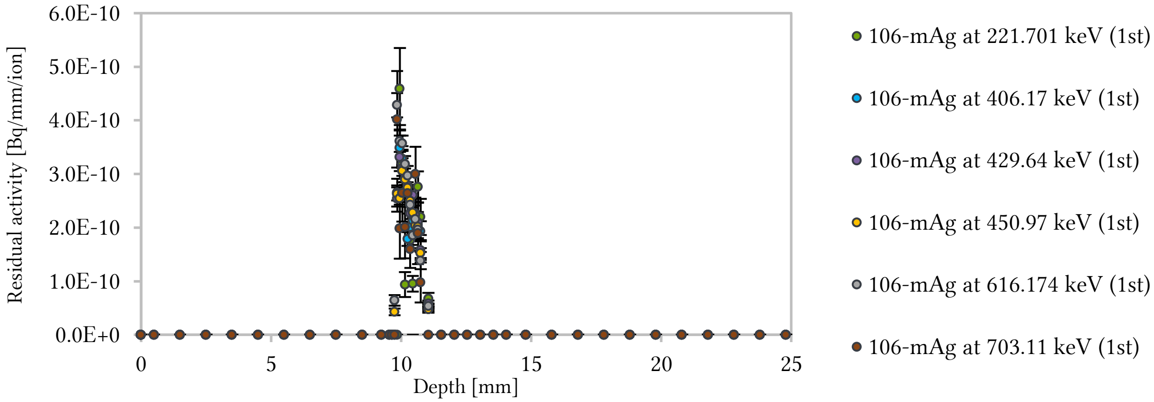

Figure 149: The depth profile of ^{106m}Ag in the aluminium target irradiated by 300 MeV/u ^{124}Xe beam (1/2).

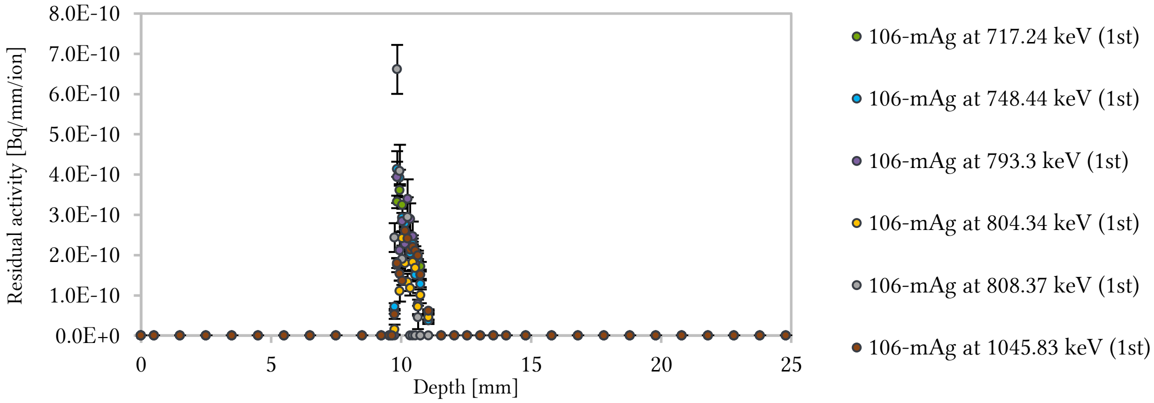

Figure 150: The depth profile of ^{106m}Ag in the aluminium target irradiated by 300 MeV/u ^{124}Xe beam (2/2).

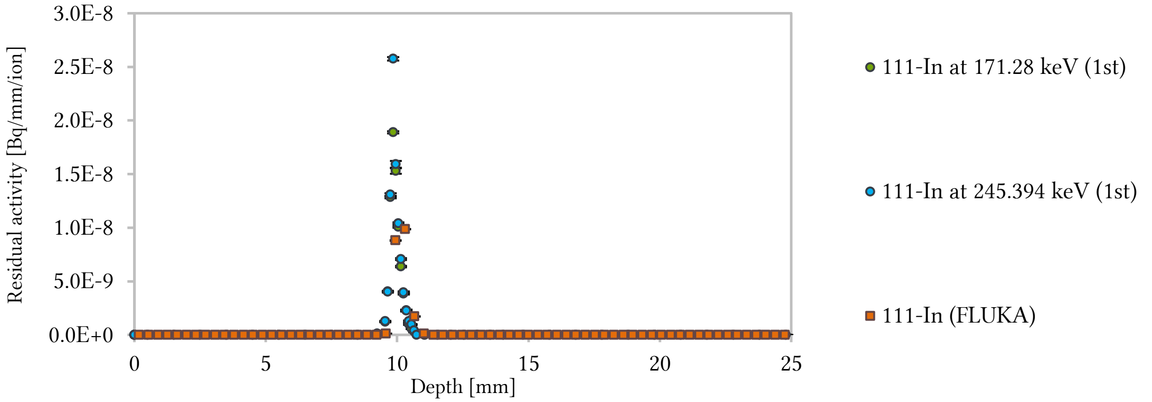

Figure 151: The depth profile of ^{111}In in the aluminium target irradiated by 300 MeV/u ^{124}Xe beam.

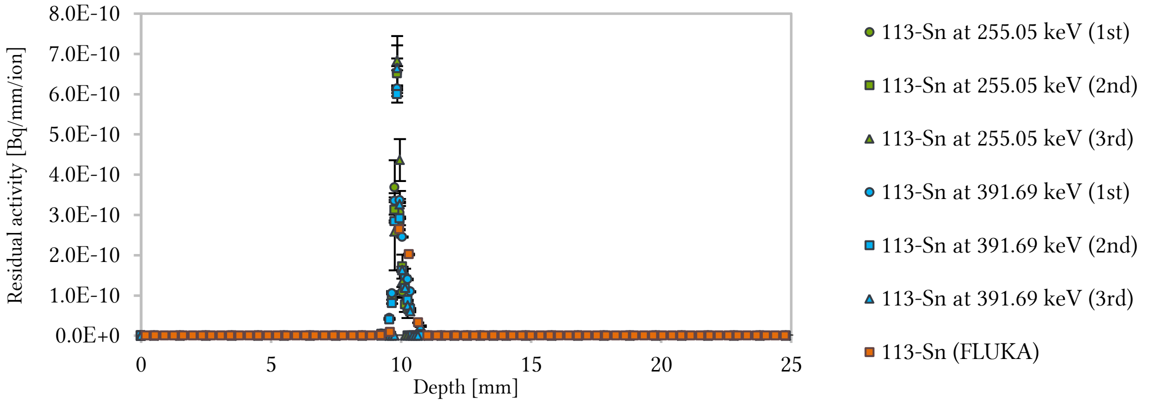

Figure 152: The depth profile of ^{113}Sn in the aluminium target irradiated by 300 MeV/u ^{124}Xe beam.

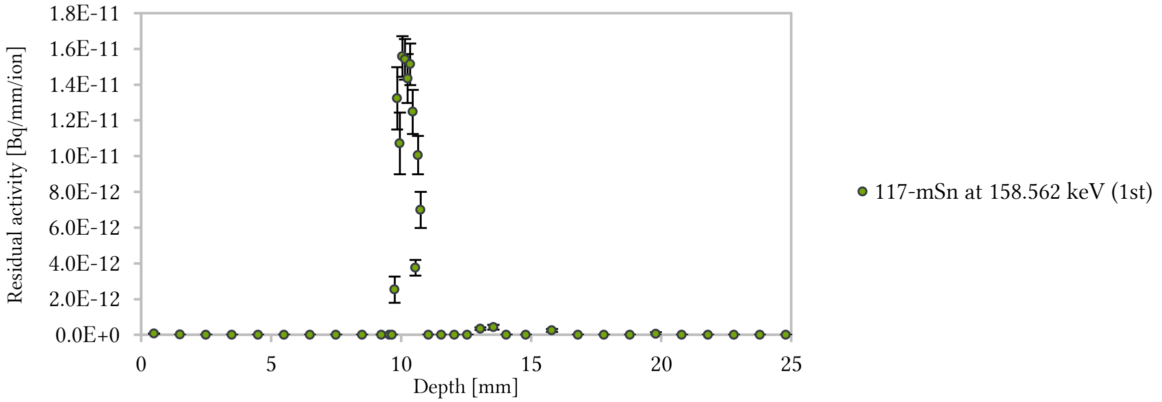

Figure 153: The depth profile of ^{117m}Sn in the aluminium target irradiated by 300 MeV/u ^{124}Xe beam.

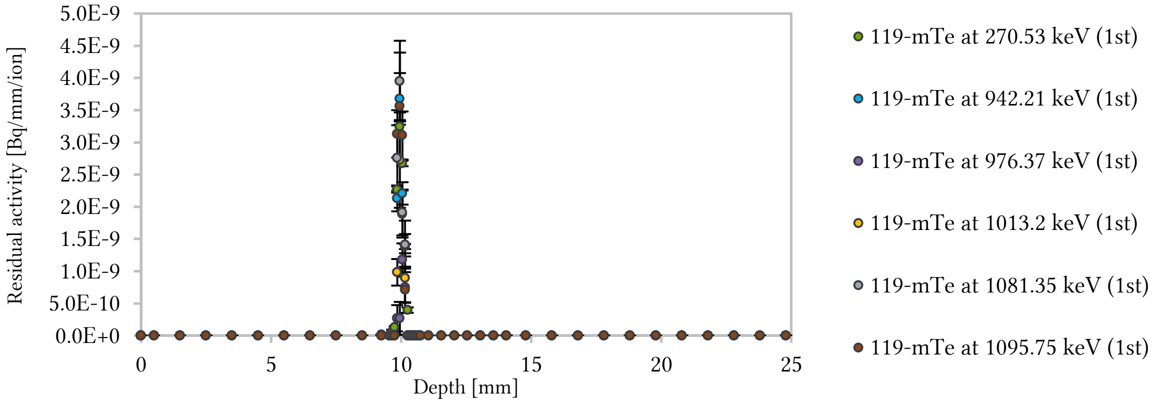

Figure 154: The depth profile of ^{119m}Te in the aluminium target irradiated by 300 MeV/u ^{124}Xe beam (1/2).

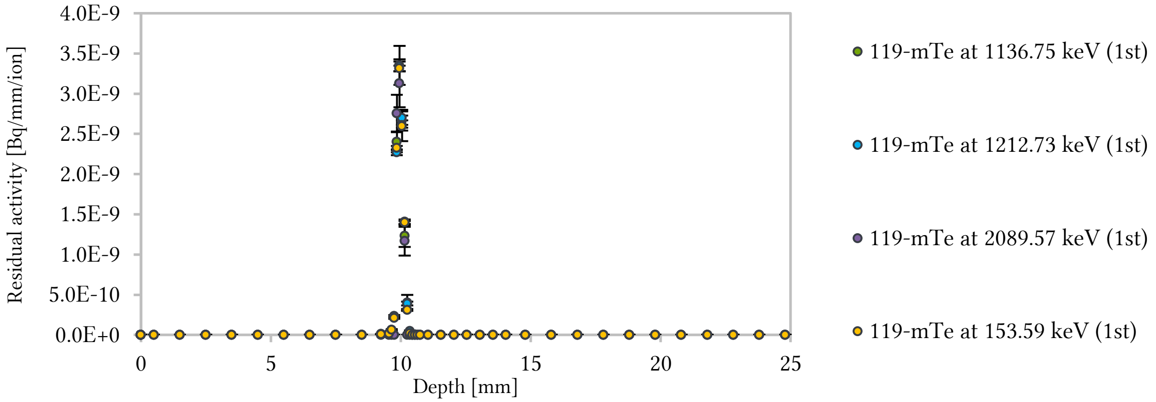

Figure 155: The depth profile of ^{119m}Te in the aluminium target irradiated by 300 MeV/u ^{124}Xe beam (2/2).

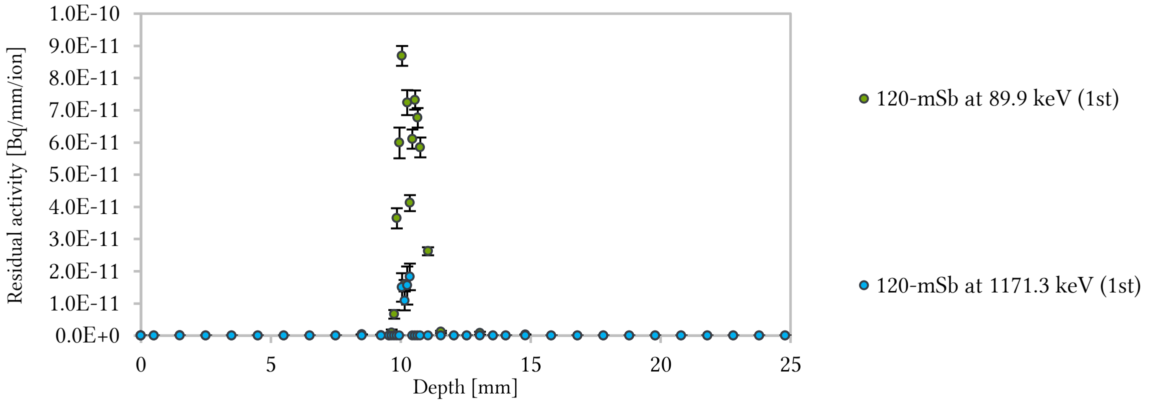

Figure 156: The depth profile of ^{120m}Sb in the aluminium target irradiated by 300 MeV/u ^{124}Xe beam.

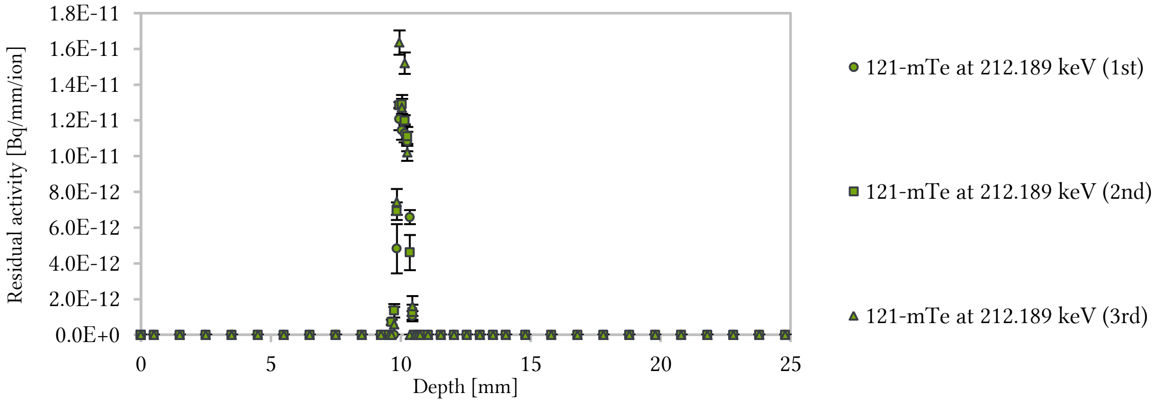

Figure 157: The depth profile of ^{121m}Te in the aluminium target irradiated by 300 MeV/u ^{124}Xe beam.

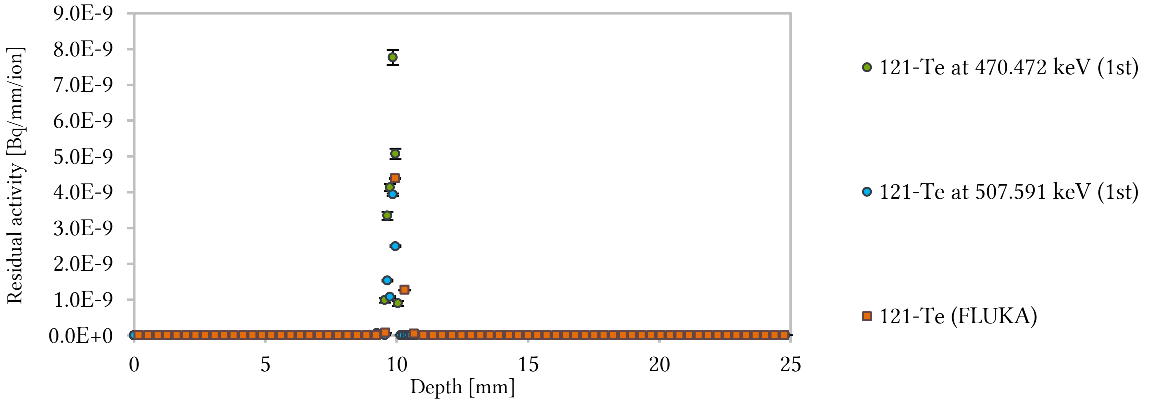

Figure 158: The depth profile of ^{121}Te in the aluminium target irradiated by 300 MeV/u ^{124}Xe beam.

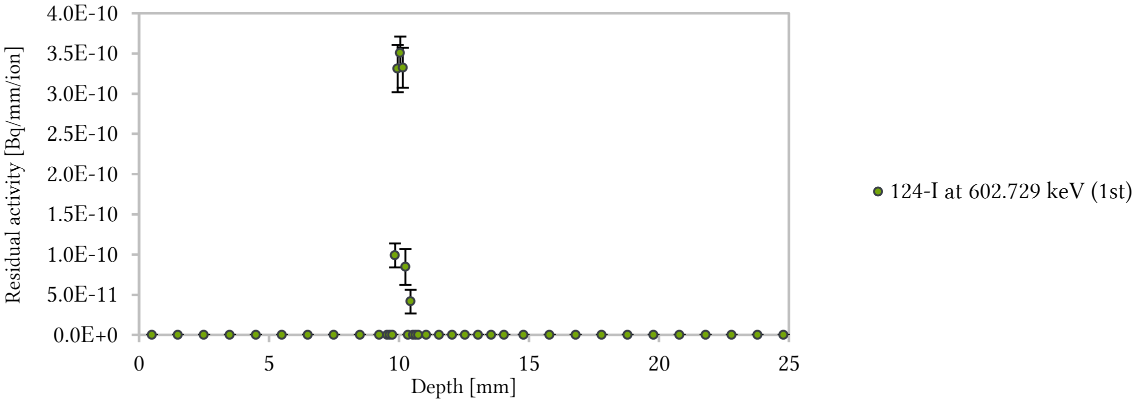

Figure 159: The depth profile of ^{124}I in the aluminium target irradiated by 300 MeV/u ^{124}Xe beam.

ACKNOWLEDGMENTS

Firstly, I would like to express my sincere gratitude to my advisor Prof. Dr. Dr. h.c./RUS Dieter H. H. Hoffmann for the continuous support of my doctoral study and related research as well as for his patience, motivation, and immense knowledge. His guidance helped me during all the time of research and writing of this thesis. I cannot imagine having a better advisor and mentor for my PhD study.

My sincere thanks also go to Dr. Edil Mustafin, Dr. Ivan Strašík, Prof. Márius Pavlovič, and Dr. Vera Chetvertkova who gave me the opportunity to join their team, and who provided me access to the laboratory and research facilities. Without their precious support it would not have been possible to conduct this research. I would like to thank you for encouraging my research and for allowing me to grow as a research scientist. Your advice on both research as well as on my career have been priceless.

Besides my advisors, I would like to thank my thesis committee: Prof. Dr. Christina Trautmann, Prof. Dr. Dr. h.c./RUS Dieter H.H. Hoffmann, Prof. Dr. Dr. h.c. Norbert Pietralla, and Prof. Dr. Reinhold Walser, for their insightful comments and encouragement, but also for the hard questions which stimulated me to widen my research from various perspectives.

I would also like to thank all of my friends who supported me in writing, and helped me to reach my goals. I am grateful to Ing. Slavomír Bebjak, Ing. Jozef Bokor, PhD., Ing. Amine Bouhaddanne, PhD., Fatima Boui, Dr. Loïc Burr, Dr. Marco Cassanelli, Dr. Giulia Guastalla, Dr. Christian Hubert, Dr. Frederik Kesting, Dr. Dimitri Khaghani, Janina Krieg, Dr. Katharina Kupka, Dr. Wouter Maijenburg, Gonzalo Pérez-Mitta, Dr. Liana Movsesyan, Ing. Patrik Novák, Alexey Prosvetov, Dr. Damian Ralet, Dr. Anton Romanenko, Dr. Anne Spende and Michael Wagner. All of you have been there to support me when I collected data for my PhD, when I needed to confront my observations or when I needed to find new solutions in stimulating discussions. Of course you have been there for all the fun we have had in the last few years. Very special thanks go to Loïc and Jani. Guys, I am still not decided if you are the best or the worst thing which could possibly happen to me during my study. I do know that I would take that crazy ride with you again without regrets and I would laugh at all those jokes which were meant to be for us only and always left the crowd around us awkwardly confused. Thank you for being serious when I needed, for all trips we made, all talks we had and sunsets we watched together and for all moments saved in my memory. It was great time with you, "It was so crazy that it cannot be a fake!"

I cannot express by words how grateful I am for a spiritual support and all sacrifices that my family made on my behalf. Your prayers for me were what sustained me thus far. My respect and my appreciation belong to Zuzka for her continual support also in the moments unlike those we planned or imagined. The major portion of successful finishing of my thesis was stimulated by my son Jakub. He literally always kicked me out of the bed when I was lazy after a night writing session and he shared with me great amount of his energy. Jakub, thank you for taking long walks with me in all kinds of weather, showing me that sliding down the slide and hands in hot sand may bring peace into the mind of an adult man. Now I see that I needed that probably more than you. I know, your memories of this period will be completely different than my own, and it will still take some time until you will learn English and learn to read, but one thing you should know. I love you, I believe in you and in your great future!

CURRICULUM VITAE

ABOUT THE AUTHOR

Ing. Peter Katrík

1st December 1987

Považská Bystrica, Slovakia

EDUCATION

09/2012–Present

Doctoral Study

EQF level 8

Technische Unversität Darmstadt, Darmstadt (Germany)
Department of Physics
Thesis: Activation analysis of heavy-ion accelerator constructing materials and validation of beam-loss criteria

- independent designing and constructing of experimental setup
- planning of 5 beam-times and successfully conducting 8 experiments
- presenting and publishing results on international conferences and in peer-reviewed journals

09/2010–06/2012

Ing. (M. Eng.) (Physical engineering)

EQF level 7

Slovak University of Technology in Bratislava, Bratislava (Slovakia)
Faculty of Electrical Engineering and Information Technology
Thesis: Activation of constructing materials of accelerators by high-energy heavy-ions

09/2007–07/2010

Bc. (B. Eng.) (Electrotechnology)

EQF level 6

Slovak University of Technology in Bratislava, Bratislava (Slovakia)
Faculty of Electrical Engineering and Information Technology
Thesis: Using of MOSFET transistors as detectors in radiology

WORK EXPERIENCES

10/2016–Present

GSI Helmholtzzentrum für Schwerionenforschung GmbH

Physicist
P-linac / P-bar target group

- designing the collimation system for the p-linac
- preparation of the p-bar target prototype
- optimisation of the beam dumps for the p-linac and APPA experiment at FAIR

AWARDS

07/2011

Czech and Slovak student science conference

1st place in international competition in section Nuclear and subnuclear physics and biophysics

06/2010

Slovak academy of science

Institute of Electrical Engineering
2nd place in the category "Best bachelor thesis"

LIST OF PUBLICATIONS

REFEREED JOURNAL PUBLICATION

Activation of accelerator constructing materials by heavy ions

P. Katrík, E. Mustafin, D.H.H. Hoffmann, M. Pavlovič, I. Strašík
Nuclear Instruments and Methods in Physics Research B 365 (2015) 525-528
http://dx.doi.org/10.1016/j.nimb.2015.09.022

CONFERENCE PROCEEDINGS

Comparison of experimental data and FLUKA simulations, validation of beam-loss criteria after long-term operation of heavy-ion accelerators

P. Katrík, D.H.H. Hoffmann, E. Mustafin, I. Strašík, M. Pavlovič
Proceedings of the 13th Shielding Aspects of Accelerators, Targets and Irradiation Facilities SATIF 13, Dresden, Germany, 10-12 October 2016, (Forthcoming 2017)

New results on the beam-loss criteria for heavy-ion accelerators

P. Katrík, E. Mustafin, D.H.H. Hoffmann, I. Strašík, M. Pavlovič
Proceedings of the 12th Shielding Aspects of Accelerators, Targets and Irradiation Facilities SATIF 12, Batavia, Illinois, US, 28-30 April 2014, (June 2015), 124-134

Some problems of residual activity measurement

P. Katrík, E. Mustafin, I. Strašík, M. Pavlovič
Proceedings of the 19th international Conference on Applied Physics of Condensed Matter APCOM 2013, Štrbské Pleso, Slovakia, 19-21 June 2013, 115 -118, ISBN 978-80-2273956-6

TECHNICAL AND ANNUAL REPORTS

Beam-loss criteria for heavy-ion accelerators

P. Katrík, D.H.H. Hoffmann, E. Mustafin, I. Strašík, M. Pavlovič
Report No.: GSI-SR2015-FG-GENERAL-24, (2016), p. 339, DOI:10.15120/GR-2016-1

Beam-loss criteria for heavy-ion accelerators

P. Katrík, D.H.H. Hoffmann, E. Mustafin, I. Strašík, M. Pavlovič
News and Reports from High Energy Density Generated by Heavy ion and Laser Beam, GSI-2016-2, (2016), p. 51.

Activation of the aluminium target by 200 MeV/u uranium beam

P. Katrík, E. Mustafin, D.H.H. Hoffmann, I. Strašík
Report No.: GSI-SR2014-FG-GENERAL-34, GSI Report 2015-1, (2015), p. 451, DOI:10.15120/GR-2015-1-FG-GENERAL-34

Experimental study of the residual activity induced by high-energy Uranium ions in Aluminium

P. Katrík, E. Mustafin
Journal of final reports, GSI - Summer student program (2010), p. 54.

e